Exploring Extended Higgs Sectors from Colliders to the Early Universe

Dissertation

zur Erlangung des Doktorgrades

an der Fakultät für Mathematik, Informatik und Naturwissenschaften

Fachbereich Physik der Universität Hamburg

Vorgelegt Von

Alain Verduras Schaeidt

Hamburg

2026

Gutachter/innen der Dissertation:	Dr. Johannes Braathen Prof. Dr. Gudrid Moortgat-Pick
Zusammensetzung der Prüfungskommission:	Dr. Johannes Braathen Prof. Dr. Gudrid Moortgat-Pick Prof. Dr. Jochen Liske Prof. Dr. Timo Weigand Dr. Jenny List
Vorsitzende/r der Prüfungskommission:	Prof. Dr. Jochen Liske
Datum der Disputation:	29.05.2026
Vorsitzender des Fach-Promotionsausschusses PHYSIK:	Prof. Dr. Johannes Haller
Leiter des Fachbereichs PHYSIK:	Prof. Dr. Markus Drescher
Dekan der Fakultät MIN:	Prof. Dr.-Ing. Norbert Ritter

Dedicado a
la abuela Maripaz
y la tía Bego

Abstract

The discovery of the Higgs boson completed the particle content of the Standard Model (SM), but it also reinforced the need to understand some of the caveats of the model, such as the baryon asymmetry of the universe and to look for possible solutions like Beyond Standard Model (BSM) models that modify the scalar sector of the SM. In particular, extended Higgs sectors can modify collider observables and the thermal history of the early Universe, thereby opening the possibility of a strong first-order electroweak phase transition and an associated stochastic gravitational-wave signal. This thesis investigates these connections by focusing on the scalar potential as the common origin of Higgs self-interactions, di-Higgs production, electroweak phase-transition dynamics, and gravitational-wave phenomenology.

The main phenomenological analysis is performed in the most general real singlet extension of the Standard Model without an imposed $\mathbb{Z}_2$ symmetry. Firstly, di-Higgs production is studied at the High-Luminosity Large Hadron Collider and at a future 1 TeV e^+e^- collider, with particular emphasis on the sensitivity to BSM trilinear scalar couplings and on the importance of using the full production cross section rather than simplified resonant approximations. A central part of the thesis is devoted to higher-order corrections to trilinear scalar couplings. A fully on-shell renormalisation scheme is constructed for the non Z_2 symmetric real singlet model for the first time, allowing renormalisation-scale-independent predictions for the loop-corrected couplings relevant to di-Higgs production. The one-loop analysis shows that radiative corrections can be sizeable and can alter Higgs-pair production rates in a phenomenologically relevant way, demonstrating that higher-order effects are indispensable for a realistic interpretation of Higgs self-interactions in extended scalar sectors.

The cosmological implications of the model are then investigated through a dedicated implementation in `BSMPT`. By studying the one-loop finite-temperature effective potential, different thermal histories are studied, and scenarios featuring a strong first-order electroweak phase transition are identified. For those scenarios the corresponding stochastic gravitational-wave spectra are evaluated, with particular attention to their observability at LISA. Combining these results with the collider analysis shows that collider signatures and gravitational-wave signals provide genuinely complementary probes of extended Higgs sectors.

Finally, the thesis extends the study of Higgs self-interactions to two-loop order in the CP-conserving Two-Higgs-Doublet Model. In the alignment limit, a consistent on-shell treatment of the parameter controlling departures from exact alignment is developed, and the two-loop corrections to the trilinear couplings are computed using both diagrammatic and effective-potential methods. Overall, this thesis shows that a coherent understanding of extended Higgs sectors requires combining collider phenomenology, higher-order quantum corrections, phase-transition dynamics, and gravitational-wave signals, and that such an approach is essential for providing reliable answers to open questions in particle physics and cosmology.

Zusammenfassung

Die Entdeckung des Higgs-Bosons vervollständigte den Teilcheninhalt des Standardmodells (SM), machte jedoch zugleich deutlich, dass einige seiner offenen Probleme, wie etwa die Baryonasymmetrie des Universums, weiterhin ungelöst sind und nach möglichen Erklärungen im Rahmen von Modellen jenseits des Standardmodells (BSM) gesucht werden muss, die den skalaren Sektor des SM erweitern. Insbesondere können erweiterte Higgs-Sektoren sowohl Observablen an Kollidern als auch die thermische Geschichte des frühen Universums verändern und damit die Möglichkeit eines starken elektroschwachen Phasenübergangs erster Ordnung sowie eines damit verbundenen stochastischen Gravitationswellensignals eröffnen. In dieser Dissertation werden diese Zusammenhänge untersucht, wobei das skalare Potential als gemeinsamer Ursprung von Higgs-Selbstwechselwirkungen, Di-Higgs-Produktion, der Dynamik des elektroschwachen Phasenübergangs und der Phänomenologie von Gravitationswellen im Mittelpunkt steht.

Die phänomenologische Hauptanalyse wird im allgemeinsten reellen Singulettmodell des Standardmodells ohne auferlegte $\mathbb{Z}_2$-Symmetrie durchgeführt. Zunächst wird die Di-Higgs-Produktion am High-Luminosity Large Hadron Collider sowie an einem zukünftigen 1 TeV-e^+e^--Kollider untersucht, mit besonderem Augenmerk auf die Sensitivität gegenüber trilinearen skalaren BSM-Kopplungen sowie auf die Bedeutung der vollständigen Produktionswirkungsquerschnitte im Vergleich zu vereinfachten resonanten Näherungen. Ein zentraler Teil der Dissertation ist höheren Ordnungen in den Korrekturen der trilinearen skalaren Kopplungen gewidmet. Für das reelle Singulettmodell ohne $\mathbb{Z}_2$-Symmetrie wird erstmals ein vollständig On-Shell-renormiertes Schema konstruiert, das von der Renormierungsskala unabhängige Vorhersagen für die schleifenkorrigierten Kopplungen ermöglicht, die für die Di-Higgs-Produktion relevant sind. Die Ein-Schleifen-Analyse zeigt, dass diese Strahlungskorrekturen groß sein können und die Higgs-Paarproduktionsraten in phänomenologisch relevanter Weise verändern, was verdeutlicht, dass höhere Ordnungen für eine realistische Interpretation von Higgs-Selbstwechselwirkungen in erweiterten skalaren Sektoren unverzichtbar sind.

Die kosmologischen Implikationen des Modells werden anschließend mithilfe einer speziellen Implementierung in `BSMPT` untersucht. Durch die Analyse des effektiven Potentials bei endlicher Temperatur auf Ein-Schleifen-Niveau werden verschiedene thermische Entwicklungen untersucht und Szenarien mit einem starken elektroschwachen Phasenübergang erster Ordnung identifiziert. Für diese Szenarien werden die entsprechenden stochastischen Gravitationswellenspektren berechnet, wobei besonderes Augenmerk auf ihre Nachweisbarkeit mit LISA gelegt wird. Die Kombination dieser Resultate mit der Kollidersanalyse zeigt, dass Kollidersignaturen und Gravitationswellensignale tatsächlich komplementäre Sonden erweiterter Higgs-Sektoren darstellen.

Abschließend erweitert die Dissertation die Untersuchung von Higgs-Selbstwechselwirkungen auf Zwei-Schleifen-Ordnung im CP-erhaltenden Zwei-Higgs-Dublett-Modell. Im Alignment-Limes wird eine konsistente On-Shell-Behandlung des Parameters entwickelt, der Abweichungen vom exakten Alignment kontrolliert, und die Zwei-Schleifen-Korrekturen der trilinearen Kopplungen werden sowohl mit diagrammatischen Methoden als auch mithilfe des effektiven Potentials berechnet. Insgesamt zeigt diese Dissertation, dass ein kohärentes Verständnis erweiterter Higgs-Sektoren die Kombination aus Kollierphänomenologie, höheren Quantenkorrekturen, der

Dynamik von Phasenübergängen und Gravitationswellensignalen erfordert und dass ein solcher Ansatz wesentlich ist, um verlässliche Antworten auf offene Fragen der Teilchenphysik und Kosmologie zu liefern.

List of Publications

This thesis is based on the following scientific articles:

Published in journal:

1. F. Arco, S. Heinemeyer, M. Mühlleitner, A. Parra Arnay, N. Rivero González and A. Verduras Schaeidt,
   "Sensitivity to Triple Higgs Couplings via Di-Higgs Production in the RxSM at the (HL-)LHC and future e^+e^- Colliders",
   arXiv:2502.03878 [hep-ph].

2. J. Braathen, S. Heinemeyer, A. Parra Arnay and A. Verduras Schaeidt,
   "Impact of one-loop corrections to trilinear scalar couplings on di-Higgs production in the RxSM",
   Eur. Phys. J. C **85** (2025) 1153,
   arXiv:2507.02569 [hep-ph].

Accepted for publication:

1. J. Braathen, S. Heinemeyer, C. Pulido Boatella and A. Verduras Schaeidt,
   "Complementarity of gravitational wave analyses and di-Higgs production in the exploration of the Electroweak Phase Transition dynamics in the RxSM",
   arXiv:2510.12569 [hep-ph].

In preparation:

1. J. Braathen, F. Egle and A. Verduras Schaeidt,
   "Two-loop corrections to trilinear scalar couplings in the 2HDM".

Declaration on oath

I hereby declare and affirm that this doctoral dissertation is my own work and that I have not used any aids and sources other than those indicated. If electronic resources based on generative artificial intelligence (gAI) were used in the course of writing this dissertation, I confirm that my own work was the main and value-adding contribution and that complete documentation of all resources used is available in accordance with good scientific practice. I am responsible for any erroneous or distorted content, incorrect references, violations of data protection and copyright law or plagiarism that may have been generated by the gAI.

Acknowledgments

First of all, I would like to thank my supervisors, Johannes Braathen and Sven Heinemeyer, for their support and guidance throughout this thesis. I would especially like to express my gratitude to Johannes Braathen, first of all, for giving me the opportunity to pursue this PhD, for trusting me as his first PhD student, for his mentorship, and for always looking after both my present and my future. I greatly appreciate all the time, care, and patience he has given me throughout these years. Without him, this thesis would not have been possible. I would also like to thank his wife, Luna, for always making me feel welcome in their home, and of course their son, Lukas, for helping with the review of this thesis in his own way. I would also like to thank Sven Heinemeyer for giving me the opportunity to begin this journey by carrying out my Bachelor's thesis with him in Santander and, later, also my Master's thesis in Madrid. I am also grateful to him for looking after me during these years and for always keeping my future in mind.

I would like to express my gratitude to Gudrid Moortgat-Pick for co-supervising this thesis, and also to Prof. Dr. Jochen Liske, Prof. Dr. Timo Weigand, and Dr. Jenny List for agreeing to take part in the examination committee for this thesis. This work would not have been possible without Maggie Mühlleitner and her help, especially regarding the di-Higgs production cross-section computations and the use of HPAIR, which has been a valuable contribution to this thesis. I am also grateful to Martin Gabelmann for his mentorship during my first months at DESY as a summer student, and for all the time he spent together with Johannes Braathen explaining the renormalisation procedure in QFT to Jonas Scheibler and myself.

I would now like to acknowledge my colleagues and collaborators, starting with Kateryna Radchenko, who has always been one step ahead of me, guiding and helping me since my Bachelor's thesis, the beginning of this journey. I am very grateful to her for all her support and help during these years, but also for all the good moments that we spent together in Spain, Germany, and Italy. I would also like to thank my colleague Fran Arco for his valuable input in different projects and, by extension, to this thesis, but above all, for the time we spent together outside the office and for all the conversations and fun we shared, again in Spain, Germany, and Italy, but also in Japan. I would also like to thank Jonas Scheibler for the time we shared during the DESY Summer Student Programme, for all the hours we spent working together while we were barely understanding anything, for the lunches in the fourth-floor kitchen, and for all the moments we enjoyed together outside the office. I owe a great deal to Felix Egle for agreeing to review part of this thesis, but also for all his work and effort on the two-loop computations. Finally, I would like to express my gratitude to all my colleagues at DESY for their help with different technical aspects of this thesis and for all the good times we shared inside and outside DESY: Panos, Andrii, Guilherme, Mathias, Julia, Max, Jonas, Jacopo, Carlo, Romal, Monika, Marten, Mohamed, Rebecca, Deniz, Jayita, and many others.

Now I would like to mention all the people who, although they did not contribute directly to the content of this thesis or to my work at DESY, have had a significant impact on my life, and without whom I would not have made it here. Let me begin with the people who were there during my first steps in physics, back when I was doing my Bachelor's degree in Santander.

I have to start with my longest-standing flatmate, Hugo. Together, we developed a deep love for cooking and grocery shopping, and we shared many film nights. I must continue with Sergio, who spent many Thursdays sleeping on a mattress on the floor of my room after our long nights together. Speaking of nights out, I should also mention Edu, who never backed down when the night was calling. He also taught me everything I know about basketball, and together we won the university 3x3 championship. Now that I have mentioned basketball, I also have to acknowledge Fran, the organiser of our matches, not only for that, but also for still making the effort to keep us all in touch. I am also grateful to him for hosting me whenever I am in Santander and for always reaching out to me, even though I am not always the easiest person to stay in touch with. I would also like to thank Duje for all the fun moments we shared at university, but especially for letting me drive his car on the day I got my driving licence, even though we nearly died. I am grateful to Jose for being my surfing partner in Santander, for showing me all the surf spots I know in Cantabria, and for sharing my love for food. I also need to thank Fer, not only for sharing Agave Azul with us, but more importantly for ringing Jose's doorbell on one of our first nights out together. I would like to thank Ana for being the most cheerful person I met in Santander, for sharing that joy with all of us, and for never saying no to a plan. I am also grateful to Alex for sharing my love of cycling and running, and for showing us some amazing hikes in Cantabria. I would also like to thank Juan for sharing with us his deep love for Torrelavega and its basketball team, and Pablo for showing us that geography is also a fascinating subject. Finally, I would like to thank Alba, Bea, Angela and Jose for making Santander feel like a second home to me during those years. Of course I did not forget about Miguel, who I met in Santander but later on became my flatmate in Madrid.

After those years, I moved to Madrid to do my Master's degree. Once again, I will begin with my flatmate, Miguel. I would like to thank him for all the good moments and conversations we shared in that house about our lives and our future and also for taking care of our little pet Mauricio also in its worst moments. More importantly, however, he should thank me for teaching him how to cook rice without dying in the process. I would particularly like to thank Maria for all her support and help from the very first moment we met, for all the hours we spent in the library working through exercises together, and, more importantly, for the breaks outside the library. I should also thank her for showing me how not to play mus. I am also grateful to Mikel, first of all, for sharing with me his love of running and trail running, for being my loyal companion on so many nights out in Madrid, my mus partner, my running partner, and of course for the week we happened to spend together in Japan. I would also like to thank Miguel for all the time he spent explaining the AQFT exercises to me, and for all the beers we shared in the polytechnic canteen. I would like to thank Manu for all the good moments and conversations we shared on his terrace. I am especially grateful to both of them, Miguel and Manu, for hosting me in Madrid over the last few years and for all the FIFA matches we played in that living room. I would also like to acknowledge Sergi, for never saying no to a drink, always saying yes to a panettone, and, more importantly, for thinking he could hide a backpack under his jacket without anyone noticing. I am also grateful to Marta for welcoming us to her city, showing us the best places in Madrid, for all the enjoyable lunches we shared on campus, and for letting Mikel and me show her the proper way to play mus. Finally, I would like to thank Tere for sharing all her board games with me, teaching me how to play them, and, of course, for all the conversations and fun moments we shared together.

Once I completed my Master's degree, I moved to Hamburg to pursue my PhD, where I met all the people mentioned above. There is, however, a small group of people with whom I have spent most of my time in Hamburg. *Ai miei amici italiani, tra i quali ero l'unico non italiano e che spesso hanno dovuto parlare in inglese per me: mi dispiace, ma vi sono davvero molto grato per questo.* First of all, I would like to thank Margherita, the host of our Sunday lunches, where I discovered true *cucina italiana* — even if she was not the one doing the cooking — for always opening her home to us and for never ceasing to come up with new and crazy things to do in

Hamburg. I would also like to thank Lorenzo for welcoming me when I arrived at DESY, for all the coffee breaks we shared in the kitchen, for showing me the traditions behind the Christmas party, and for introducing me to the Italian community in Hamburg. I am especially grateful to Davide for letting me stay in his living room for two months when we were unable to find a place to live, for the fun moments we shared sleeping in a van in the Black Forest, and, of course, for all the memes. Finally, I would like to thank my two flatmates, Sara and Simone. Without their constant company and support during these years, this thesis would not have been possible. They made my days easier, more enjoyable, and brighter. I would like to thank Sara for our conversations about the PhD and about life in general, and for all the wonderful moments we shared in Germany, Spain, and Italy. Without her, this journey would not have been the same. I would now like to express my gratitude to Simone, for showing me the secrets of pasta, for all the chats we had at the end of the day that always made things feel easier, for watching *How I Met Your Mother* together from beginning to end, for sharing my love for food and digestifs, for opening the doors of what was, at one point, his home to me and for all the wonderful moments we spent together. Without him, this experience would not have been the same.

I would now like to turn to those back home and thank all those who have stood by me there, without whom this would not have been possible. I would like to begin with my *kuadrilla*, for all these years of friendship. Mikel, for all those "funny" ideas that skirted the edge of legality when we were children, and which gave us unforgettable stories. Pombo, for leading so many of our bad ideas when we were kids, and for continuing to do so even now. Urban, for all the hours we spent together in the library at Andra Mari, even if, to this day, we still do not understand his schedules or how he manages to stay so toned. Nico, for his spontaneity and natural charm; I should also mention that we started our driving lessons together, and he only managed to get his licence a few months before the completion of this thesis. Juaris, for always believing in me, often more than I believed in myself, and for showing us that there are many different ways to live a life, though none quite like his. Magu, for all the discussions we have had over the years on all kinds of topics, for disagreeing on 75% of them, and yet remaining friends since we were three years old. Lucia, for showing us how to pursue your ambitions, even if that means moving to another city with barely anything in your purse and leaving friends and family behind. Aisha, for sharing with us her deep love of techno music, for never saying no to a plan, even if it means "climbing" a mountain, or at least half of it, and that amazing week we spent in Hamburg. Paupe, for being unique, for all your joyfulness, and for sharing my deep love for the sea, she is also known as *la chica de la playa*. Mikelats, for sharing with me for so many years the position between the goalposts, a lonely position that we made our own together, and for all the training sessions, conversations, and good moments we shared. Ionmi, for being the first chauffeur among us, for all the stories we have from that car, but also for always being there when I needed you and for making the effort to see each other even when it was not easy.

Gallu, for never saying no to a night out; although he is hard to spot in daylight, you can always count on finding him by your side at night. I also have to thank him for being with me in the thick bone club when we were kids and for always being there for me. Paul, for always being there for me, for helping me whenever I needed it, and, more recently, for also letting me help you. Also known as "the voice of reason", although after a couple of ginkases the tornado appears and he forgets all about his reasoning; however, thanks to that, we have many funny stories together. James, first of all for always trying to keep us together, for those years when we were both living in Cantabria and could understand each other, for always being by my side in the good moments as well as in the bad ones, and for being my BJJ partner, even though I am 30 kilos heavier than you and you will always have that as an excuse. Maitane, for showing me that sometimes your best friends appear later in life, for never judging me and for giving me a space in which I have always felt safe, for always backing me up no matter what happened or whether it was my fault, and for being there during some of my worst moments, but of course

also during the best ones. Alvis, for being my oldest friend; I think we have known each other since we were born. We grew up together and went through all the stages of life side by side. He has seen me at my best and at my worst, and I have seen the same of him, and he has always been there for me from the very beginning. I always like to tell this story: at school, they put us in different classes because we were spending too much time together and they thought we needed to make other friends. Thank you for all these years; without you, I would not be who I am. Jaco, we were not friends from the first day we met, but I am sure we will be friends until the very end. First of all, I have to thank you for teaching me how to surf, which has been one of the greatest gifts I have ever received, for sharing with me your deep knowledge of the sea and of the coastline we both call home, but also for sharing your family with me and making me feel part of it. Thank you for always believing in me, often more than I believed in myself, and for all your support, company, advice, and friendship throughout all these years, and for always being there whenever I needed you. Without you, none of these years would have been the same.

Finally, I am deeply grateful to my family for all their love and support throughout these years. I would like to begin with my partner, Nerea, whom I must thank for reviewing these acknowledgments. I also want to thank her for being my personal coach, for teaching me how to ride a bicycle properly, for showing me all the cycling routes I know, and for being my loyal companion in every crazy idea I have had. Thank you as well for all your unconditional support during this time; you have gone through the worst days of this process with me, only you know how difficult they have been, and you have also celebrated the best ones by my side. You made this whole journey easier with your care, love and support, and a part of this thesis is yours. To my aunt Elena and my uncle Sergio, for giving me my love of travelling and discovering new cultures, for always encouraging my curiosity, and for supporting me in every possible way whenever it was needed. To my brother, for being my most unconditional supporter, for being my partner in crime at home, and for always betraying me and claiming it was my fault, just as I was claiming it was yours, for being the greatest fan of my cooking, for never letting me take the biggest piece of any meal, and for celebrating every time I came back home. I only hope that one day I can give you back at least one part of all you have given me, and yes, we will do that surf trip together. To my father, for giving me the best advice one could receive, for waking me up so that we could watch MotoGP together, for sharing with me your regrets in life so that I would not repeat them, for driving me on your bus, for taking me on your motorcycle, and for showing me the coastal route that saved me so many times, for passing on to me your love and madness for cycling, running, and swimming, and, above all, for loving me. To my mother, for taking care of me my whole life, for never stop calling me, for not letting me do whatever I wanted every time, for making me study when I did not want to, for punishing me when I was not kind to others, for telling me what I did not want to hear, for pushing me when I thought I was not enough, for holding me back when I overestimated myself, for supporting me in every decision I had to make, for being an example to follow, for raising me to be who I am, for being there in all the bad moments, and also in all the good ones, and for always loving me. And finally, to my aunt Bego and my grandmother Maripaz, for always believing in me, for giving me their unconditional love, for being the best grandparents one could wish for, and for teaching me through their example to never give up.

Contents

Chapter 1

Introduction

¿Ya me va a querer?

– Abuela Maripaz

The discovery in 2012 of a scalar particle with a mass around 125 GeV by the ATLAS and CMS collaborations [1–3] at the Large Hadron Collider (LHC) marked a turning point in particle physics, establishing the Brout-Englert-Higgs (BEH) mechanism [4–8] as the origin of electroweak symmetry breaking (EWSB) and completing the particle content of the Standard Model (SM) [1–6]. Since then, increasingly precise measurements of the properties of the observed Higgs boson have shown remarkable agreement with the SM expectations. At present, the couplings of the 125 GeV Higgs boson to gauge bosons and third-generation fermions are known with a precision at the level of roughly 10–20%, and no conclusive evidence for additional scalar states has yet emerged. Nevertheless, the present experimental accuracy still leaves substantial room for physics beyond the Standard Model (BSM), in particular in the scalar sector, where sizeable deviations may still be realised consistently with all current data [9–14].

In spite of its extraordinary phenomenological success, the Standard Model cannot be regarded as a complete description of Nature. It does not explain several fundamental observations, including the origin of the baryon asymmetry of the Universe (BAU) [15–23], the nature of dark matter [24–27], the neutrino masses [28–34], or the hierarchy of physical scales. Among these open questions, the origin of the BAU is especially compelling because it points directly towards new dynamics in the early Universe. A particularly attractive framework is electroweak baryogenesis [16–23], in which the asymmetry is generated during the electroweak phase transition (EWPT) [16, 17, 21, 23]. For this mechanism to work, the three Sakharov conditions must be satisfied, including a departure from thermal equilibrium [15]. In electroweak baryogenesis, this requires the EWPT to proceed as a strong first-order electroweak phase transition (SFOEWPT), during which bubbles of the broken-symmetry phase nucleate and expand within the surrounding symmetric phase [35–42]. This highly violent event in the early Universe can also give rise to a stochastic gravitational-wave (GW) background [43–48]. However, within the SM for the measured Higgs-boson mass, the electroweak transition is known to be a smooth crossover rather than first order, so that the SM fails to explain the BAU through this mechanism [49].

This provides a strong motivation for considering theories with extended Higgs sectors. Such models can modify the scalar potential both at zero and finite temperature, opening the possibility of a SFOEWPT and thereby offering a route towards electroweak baryogenesis [21, 23, 35–42]. At the same time, extended scalar sectors can lead to rich collider phenomenology through modified Higgs couplings, additional scalar states, additional scalar couplings, and non-trivial vacuum structures. They therefore provide a particularly appealing and well motivated class of BSM theories in which collider physics, early-Universe cosmology and GW signals become deeply intertwined. A central theme of this thesis is precisely to explore this interplay.

An especially interesting window to the scalar potential is provided by the trilinear Higgs couplings. In the SM, the trilinear self-coupling of the observed Higgs boson, λ_{hhh}, which experimental determination is still loosely constrained. It directly probes the shape of the Higgs potential away from the electroweak vacuum and is therefore closely related to the dynamics of the EWPT [50–57]. It is customary to quantify deviations from its SM prediction through the modifier $\kappa_\lambda \equiv \lambda_{hhh}/\lambda_{hhh}^{\mathrm{SM},(0)}$, where $\lambda_{hhh}^{\mathrm{SM},(0)}$ is the tree level SM prediction for the coupling. Current direct limits from di-Higgs searches still allow broad ranges for this quantity [9,10], and future improvements are expected at the HL-LHC and at possible future lepton colliders [58–63]. In BSM scalar theories, not only λ_{hhh} but also genuinely new trilinear couplings can appear, and measuring them would be essential for reconstructing the scalar potential realised in Nature [55, 59, 64–69].

A remarkable feature of extended scalar sectors is that their trilinear couplings can receive very large radiative corrections. This is particularly well known in scenarios with sizeable differences between BSM mass scales, where so-called mass-splitting effects first arise at loop level and can induce corrections to Higgs self-couplings of several hundred percent, even in situations where other couplings of the observed Higgs boson remain close to their SM values [70–91]. Explicit two-loop studies have furthermore shown that these large BSM effects are compatible with perturbative convergence in the relevant parameter regions [92–97]. The same mechanism can also generate large corrections to BSM trilinear scalar couplings [98, 99]. This makes higher-order calculations indispensable for a reliable phenomenological interpretation of extended Higgs sectors.

Experimentally, the most direct access to the trilinear Higgs couplings is through Higgs-pair production. At hadron colliders, the dominant channel is gluon fusion, $gg \to hh$, while at high-energy e^+e^- colliders the channels $e^+e^- \to Zhh$ and $e^+e^- \to \nu\bar{\nu}hh$ become available [60–62, 100–104]. In all these processes, the diagrams involving trilinear Higgs couplings interfere with the other contributions, and the sign and size of this interference can dramatically alter the total and differential cross sections. In the SM, the interference is destructive in $gg \to hh$, resulting in a very small production rate. This also implies that BSM deviations in the Higgs self-coupling can induce large changes in the di-Higgs production cross section, making it a particularly sensitive probe of new scalar dynamics. A central line of investigation of this thesis is to exploit this sensitivity in order to test extended Higgs sectors at present and future colliders.

The simplest non-minimal scalar extension of the SM is obtained by adding a real singlet field. In this thesis, particular emphasis is put on the most general real singlet extension of the SM, denoted RxSM, in which no additional $\mathbb{Z}_2$ symmetry is imposed [105–111]. After electroweak symmetry breaking, the model contains two physical CP-even Higgs bosons, one of which is identified with the observed 125 GeV state while the second, have assigned

to be heavier. The absence of a $\mathbb{Z}_2$ symmetry allows linear and cubic singlet interactions and enlarges the parameter space compared to the symmetric variants of the model. These additional degrees of freedom can have important consequences both for the shape of the scalar potential and for the size of the trilinear scalar couplings. The RxSM without a $\mathbb{Z}_2$ symmetry is known to be one of the most minimal Higgs-sector extensions capable of realising a SFOEWPT, and the simplest one in which this may occur already through a one-step transition [35]. Previous studies have shown that a first-order transition in this setup favors relatively light extra Higgs states, below the TeV scale, which makes the model particularly attractive from the point of view of collider searches [23,37,40,108,112].

The dynamics of the electroweak transition and the related phenomenology in singlet models, and in the RxSM in particular, have been studied intensively in the literature. The occurrence of a first-order transition, the possible production of GW, and the associated collider signatures have been analysed from different perspectives [37, 38, 112–125]. Likewise, resonant and non-resonant di-Higgs phenomenology in the RxSM and related models have received growing attention at hadron, e^+e^-, and muon colliders [108, 126–130]. However, a recurring lesson from these studies is that no single observable is sufficient to cover the full parameter space of phenomenologically viable scenarios, especially once thermal-history considerations are imposed.

This thesis is devoted to a systematic exploration of these questions, with particular emphasis on the interplay between collider observables, radiative corrections, and the thermal history of the scalar potential. The first part of the thesis reviews the current status of particle physics and the main shortcomings of the SM, and introduces the cosmological framework needed to discuss the thermal history of the Universe, the BAU, electroweak phase transitions, and the generation of stochastic GW backgrounds. This is followed by an introduction to the extended Higgs sectors that constitute the main theoretical framework of this work: the general real singlet extension of the SM and the CP-conserving Two-Higgs-Doublet Model (2HDM) [131–135]. Particular attention is paid to the role of loop corrections and to the methods used to compute them, both in the effective-potential and in the diagrammatic approach.

The central phenomenological part of the thesis begins in Chapter 5 with an analysis of di-Higgs production in the RxSM at the HL-LHC and at a future 1 TeV e^+e^- collider. The focus there is on the sensitivity to the BSM trilinear coupling λ_{hhH} through resonant heavy-Higgs exchange, and on the impact of including the full set of contributing diagrams rather than relying on simplified resonant approximations [108, 136–140]. The aim of this chapter is to assess the importance of computing the full di-Higgs production cross section in a simple BSM scenario, rather than considering only the resonant contribution, as is commonly done in phenomenological studies of such models. A further objective is to understand how this approximation may affect the extraction of a possible BSM trilinear scalar coupling.

As discussed above, trilinear scalar couplings can receive sizeable radiative corrections in BSM models with extended scalar sectors, and these corrections can in turn have an important impact on di-Higgs production cross sections. Chapter 6 presents a detailed one-loop analysis of the trilinear scalar couplings in the RxSM. For this purpose, a fully on-shell renormalisation scheme is constructed for the model for the first time, allowing renormalisation-scale independent predictions for the loop-corrected couplings relevant to di-Higgs production. These couplings are then used to evaluate the impact of one-loop BSM effects on Higgs-pair production at the HL-LHC and at high-energy e^+e^-

colliders [89, 99, 141, 142]. The goal of this chapter is thus to determine how large the impact of the one-loop corrections to the trilinear scalar couplings can be on di-Higgs production cross sections in a simple BSM model.

All the efforts devoted in this thesis to investigating precise experimental features of BSM models are ultimately motivated by the goal of addressing the BAU problem through the identification of experimental signatures of scenarios capable of realising a SFOEWPT. Chapter 7 therefore explores the thermal history of a simple BSM model such as the RxSM, with the aim of understanding the different cosmological scenarios that may arise within the model. Using a dedicated implementation of the model into the public code `BSMPTv3` [83, 85, 91], the one-loop finite-temperature effective potential is studied in order to classify the different thermal histories of the model and to identify scenarios with a SFOEWPT. The associated stochastic GW spectra and signal-to-noise ratios at future space-based interferometers, in particular LISA [48, 143–145], are then evaluated. One of the main objectives of this part of the thesis is to study, for the first time in the RxSM, the GW signal from the phase transition simultaneously with the collider signatures at the HL-LHC and at future e^+e^- colliders, using in the collider analysis the full di-Higgs cross sections and including the relevant one-loop corrections to the trilinear scalar couplings. This makes it possible to assess, in a unified way, the complementarity between cosmological and collider probes of the model.

Finally, the thesis pushes the study of extended Higgs sectors one step further in perturbative precision by considering two-loop corrections in the 2HDM. In that part, the trilinear couplings λ_{hhh} and λ_{hhH} are studied in the alignment limit, with particular emphasis on the consistent renormalisation of the parameter controlling the departure from exact alignment. A correct on-shell treatment of this issue is developed, and the two-loop corrections are computed simultaneously using both the diagrammatic and the effective-potential approaches, providing a non-trivial cross-check of the calculation. Their impact on di-Higgs production at the HL-LHC is then investigated. This final step places the phenomenological study of extended Higgs sectors in a broader precision context and illustrates how the program developed throughout the thesis can be extended to yet higher perturbative orders.

Overall, the purpose of this thesis is to investigate how BSM models with extended Higgs sectors can address open questions in particle physics and cosmology, and how they can be tested through a combination of collider and early-Universe observables. The emphasis is placed on the scalar potential as the common origin of these phenomena: it determines Higgs self-interactions, shapes di-Higgs production rates and distributions, governs the dynamics of the electroweak phase transition, and controls the production of cosmological relics such as GW. By combining tree-level analyses, one-loop and two-loop calculations, collider phenomenology, and finite-temperature field theory, this thesis aims to provide a coherent and quantitative picture of how the Higgs sector may offer clues towards physics beyond the SM.

Chapter 2

State of the art of Particle Physics

Nunca digas nunca jamás.

– Aita

Particle physics aims to explain and understand the smaller bricks of our universe and their behaviour using a framework that allows us to make precise predictions of different phenomena in nature. To do so it identifies the fundamental degrees of freedom of nature and the principles governing their interactions, from laboratory energies up to the conditions of the early Universe. Over the past decades this programme has converged into a remarkably successful theoretical framework: the Standard Model (SM), a renormalisable quantum field theory based on local gauge symmetries. The SM provides a unified description of strong, weak, and electromagnetic interactions and has been tested with high precision across a wide range of experiments, culminating in the discovery of the Higgs boson in 2012.

Despite this success, the SM is still incomplete. For example it does not explain the origin of the electroweak scale, the nature of dark matter, the observed matter–antimatter asymmetry, or the pattern of fermion masses and mixings, and it does not incorporate quantum gravity. These shortcomings motivate the exploration of physics beyond the SM, often through extensions of the Higgs sector. Such extensions are particularly compelling because they can simultaneously modify collider observables and alter the thermal history of the Universe, potentially enabling a strongly first-order electroweak phase transition and an observable stochastic gravitational-wave background.

This chapter provides the necessary context for the rest of the thesis. We begin with a concise review of the theoretical foundations of the SM, emphasising the gauge principle, the path-integral formulation, and the role of renormalisation. We then summarise the structure of QCD and the electroweak theory, and discuss electroweak symmetry breaking via the Higgs mechanism. Having established the SM framework, we highlight its main phenomenological and conceptual limitations, focusing on the open problems most relevant to the themes of this thesis. Finally, we review the current experimental status of Higgs physics at the LHC and outline the prospects for future measurements that motivate the study of extended scalar sectors pursued in the subsequent chapters.[1]

[1] A large part of this chapter is based on the book [146] and on personal notes from QFT and advanced

2.1 The Standard Model

The Standard Model of particle physics is the result of many years of theoretical and experimental efforts and successes in understanding the fundamental building blocks of matter and how they interact. Its origin was in the pursuit of a consistent theory able to unify special relativity and the quantum theory representing the nature of our universe.

The first major breakthrough in this direction were the works of the late 1940s on quantum electrodynamics (QED). A local $U(1)$ gauge theory which describes electromagnetic interactions with really high precision. The renormalizability and predictive power of QED established gauge symmetry as a powerful tool to organize fundamental field-theoretic models.

By the 1950s and 1960s, key experimental features of the weak interaction—such as parity violation in beta decay and the existence of the neutrino—had been established, and the effective $V-A$ description was in place. A fully unified and renormalisable framework, however, had to wait for the electroweak theory of Glashow, Weinberg, and Salam, which predicts the $W^{\pm}$ and Z mediators. They demonstrated that the electromagnetic and the weak interactions could be unified into a common gauge theory, which symmetry group was $SU(2)_L \times U(1)_Y$. Yet this unification was not complete: gauge invariance implies no explicit mass terms for the weak gauge bosons, which contradicted the masses of the these bosons from an experimental viewpoint.

This problem was solved by the BEH mechanism, developed independently in 1964 [4–8]. The Higgs mechanism allows to give mass to gauge bosons by applying a spontaneous symmetry breaking to a gauge theory with scalar fields. This also explains the fermion mass generation via Yukawa interactions and therefore completing theoretically the electroweak sector.

At the same time, the strong interaction was being understood thanks to the development of quantum chromodynamics (QCD), a non-Abelian gauge theory, which symmetry group is the $SU(3)_C$. The discovery of asymptotic freedom and the gluon discovered at DESY in 1979, predicted by QCD, gave it the status of the correct theory for the strong interactions, explaining the confinement of quarks at low energies with their behaviour as nearly free particles at high energies.

By the mid 70's these various results conclude into a unified theoretical picture for strong, weak and electromagnetic interactions, what is known today as the Standard Model. In subsequent decades its predictions have been confirmed with great accuracy, including the discoveries of the W and Z bosons, the top quark, and most recently, the Higgs boson in 2012.

Despite its extraordinary success, the Standard Model is known to be an effective theory valid up to a certain energy scale. It still leaves fundamental questions without an answer, including the origin of the electroweak scale, the nature of dark matter, and the mechanism responsible for the matter–antimatter asymmetry of the Universe. These open problems motivate the study of physics beyond the Standard Model.

QFT courses at the Instituto de Física Teórica de Madrid (IFT).

2.1.1 Quantum Field Theory and the Path Integral Formalism

A theoretical formulation of the Standard Model as a consistent quantum field theory requires a quantization procedure capable of handling relativistic fields, internal symmetries, and gauge redundancies in a systematic way. In quantum field theory, physical models are organized in terms of a Lagrangian density, which encodes the particle content, the interactions, and symmetries of the theory. The reason for using a Lagrangian formulation is that, in practical calculations, quantum field theory is most naturally formulated within the path integral approach. In this framework, the Lagrangian serves as the fundamental building block from which all quantum information of the theory can be extracted through the generating functional.

In the path integral formulation of quantum field theory, quantum amplitudes are obtained by summing over all possible field configurations connecting given initial and final states and each configuration is weighted by the exponential of the classical action. Schematically, the transition amplitude between two field configurations can be written as

$$\mathscr{A} \;\sim\; \int \mathscr{D}\phi_i \;\exp(iS[\phi_i])\,, \tag{2.1}$$

where $S[\phi_i] = \int d^4x\, \mathscr{L}(\phi_i)$ represents the classical action and the functional integration runs over all field configurations consistent with the boundary conditions and $\mathscr{D}\phi_i$ denotes the functional integration measure, that is, the integration over all field configurations $\phi_i(x)$ consistent with the prescribed boundary conditions. This formulation provides a direct link between the classical dynamics represented by the Lagrangian and the quantum theory.

In practice, it is convenient to introduce external sources in order to systematically extract physical information from the theory. For a generic set of fields $\{\phi_i\}$, this is achieved by defining the generating functional

$$Z[J] = \int \mathscr{D}\phi_i \;\exp\!\left[i \int d^4x\; \left(\mathscr{L}(\phi_i) + J_i(x)\,\phi_i(x)\right)\right], \tag{2.2}$$

where $J_i(x)$ are classical source fields coupled to the quantum fields. The generating functional encodes the full quantum dynamics of the theory and serves as the central object from which all correlation functions can be derived. Correlation functions, also known as Green's functions, describe the quantum correlations between field excitations at different spacetime points and constitute the basic building blocks of perturbative quantum field theory. They are obtained by functional differentiation of $Z[J]$ with respect to the sources,

$$\langle 0|T\{\phi_{i_1}(x_1)\cdots\phi_{i_n}(x_n)\}|0\rangle = \frac{1}{Z[0]}\,\frac{\delta^n Z[J]}{i^n\,\delta J_{i_1}(x_1)\cdots\delta J_{i_n}(x_n)}\bigg|_{J=0}, \tag{2.3}$$

where T denotes time ordering. The time-ordering prescription ensures a causal description of quantum propagation by arranging field operators according to their time coordinates, with later times appearing to the left. This is essential for consistency with relativistic causality and for establishing the connection between Green's functions and physically measurable quantities.

The path integral formulation is especially well suited for gauge theories. In the presence of a local gauge symmetry, the naive functional integral overcounts physically equivalent

field configurations related by gauge transformations. This redundancy must be properly removed in order to define the quantum theory consistently, a procedure that will be discussed in the following in the context of gauge fixing and ghost fields. The standard procedure to address this issue is gauge fixing, implemented through the Faddeev–Popov method. By inserting a suitable identity into the path integral, one introduces a gauge-fixing condition together with additional ghost fields that compensate for the Jacobian arising from the change of variables. These ghost fields are unphysical but play a crucial role in preserving unitarity and gauge invariance at the quantum level.

Beyond tree level, the path integral formalism provides the natural framework for computing loop corrections, renormalization group effects, and effective actions. In particular, the effective potential, obtained by integrating out quantum fluctuations around a background field configuration, plays a central role in the study of symmetry breaking and phase transitions. At finite temperature, the extension of the path integral to imaginary time allows for a unified description of thermal effects in quantum field theory.

For these reasons, the path integral formalism underlies the theoretical tools employed throughout this thesis, from the description of gauge theories in the Standard Model to the analysis of extended scalar sectors and electroweak phase transitions beyond it. Having established this formal framework and the technical language of quantum field theory, we can now proceed to identify and discuss the fundamental building blocks of the Standard Model, namely its gauge structure, field content, and symmetry-breaking mechanism.

2.1.2 QCD

Quantum Chromodynamics (QCD) is the quantum field theory describing the strong interaction, one of the four fundamental interactions of nature. It governs the dynamics of quarks and gluons and is formulated as a non-Abelian gauge theory based on the local symmetry group $SU(3)_C$. Together with the electroweak theory, QCD forms the theoretical foundation of the Standard Model of particle physics.

Gauge structure and field content

The fundamental degrees of freedom of QCD consist of quark fields, which transform under the fundamental representation of the color gauge group $SU(3)_C$, and gluon fields, which transform under the adjoint representation. The local gauge invariance uniquely fixes the interaction structure of the theory.

The QCD Lagrangian is given by

$$\mathscr{L}_{\text{QCD}} = -\frac{1}{4} G^a_{\mu\nu} G^{a\,\mu\nu} + \sum_f \bar{q}_f \left(i\gamma^\mu D_\mu - m_f\right) q_f \,, \tag{2.4}$$

where the sum runs over all quark flavors f, m_f denotes the quark masses, and the gluon field strength tensor is defined as

$$G^a_{\mu\nu} = \partial_\mu G^a_\nu - \partial_\nu G^a_\mu + g_s f^{abc} G^b_\mu G^c_\nu \,. \tag{2.5}$$

Here, g_s is the strong coupling constant and f^{abc} are the structure constants of the $SU(3)_C$ algebra. The covariant derivative acting on quark fields reads

$$D_\mu = \partial_\mu - i g_s T^a G^a_\mu \,, \tag{2.6}$$

with T^a the generators of the fundamental representation.

A characteristic feature of QCD, in contrast to Abelian gauge theories such as quantum electrodynamics, is the presence of gluon self-interactions. These arise directly from the non-Abelian gauge structure and play a central role in determining the qualitative behavior of the theory.

Renormalization and asymptotic freedom

The renormalization properties of QCD reveal one of its most remarkable features: asymptotic freedom. The running of the strong coupling constant is governed by the renormalization group equation

$$\mu \frac{dg_s}{d\mu} = \beta(g_s)\,, \tag{2.7}$$

where, at one-loop order, the beta function is given by

$$\beta(g_s) = -\frac{g_s^3}{16\pi^2}\left(11 - \frac{2}{3}n_f\right)\,, \tag{2.8}$$

with n_f denoting the number of active quark flavors. The negative sign of the beta function implies that the strong coupling decreases at high energies, rendering the theory weakly coupled in the ultraviolet regime.

The discovery of asymptotic freedom provided a crucial theoretical justification for the parton model and established QCD as the correct description of strong interactions at high energies [147, 148]. It also allows for precise perturbative predictions in processes involving large momentum transfers, such as those probed at modern collider experiments.

Infrared dynamics and confinement

In the infrared regime, the running coupling becomes large and perturbation theory ceases to be applicable. This strongly coupled regime is associated with the phenomenon of color confinement, according to which colored states such as quarks and gluons do not appear as free asymptotic particles. Instead, only color-singlet bound states, known as hadrons, are observed experimentally.

While confinement is a well-established empirical fact, a complete analytic derivation from first principles remains an open problem. Non-perturbative methods, including lattice gauge theory, have provided compelling numerical evidence for confinement and have enabled quantitative studies of hadronic properties. From a theoretical standpoint, confinement highlights the intrinsically non-perturbative nature of QCD at low energies and represents one of the most profound challenges in quantum field theory.

Role of QCD within the Standard Model

Within the Standard Model, QCD is responsible for the dominant contributions to hadron-collider observables and provides the theoretical framework for understanding strong-interaction backgrounds. While it does not directly participate in electroweak symmetry breaking, QCD effects enter precision predictions through radiative corrections and significantly impact the interpretation of experimental data. Moreover, in the limit of vanishing quark masses the QCD Lagrangian exhibits an approximate chiral symmetry, under which

explicit fermion mass terms are forbidden; in the Standard Model such masses arise instead from Yukawa interactions after electroweak symmetry breaking.

In the context of physics beyond the Standard Model without new particles with colour charge, QCD remains unmodified at the energy scales relevant for electroweak symmetry breaking. Consequently, extensions of the scalar sector primarily affect the electroweak interactions, while the strong sector serves as a robust and well-tested component of the theoretical framework. For this reason, the following sections will focus on the electroweak theory and the Higgs mechanism, which are central to the models and phenomena investigated in this thesis.

2.1.3 Electroweak Sector

The electroweak sector of the Standard Model provides a unified quantum field theoretical description of electromagnetic and weak interactions. This unification is realized through a non-Abelian gauge theory based on the local symmetry group

$$SU(2)_L \times U(1)_Y \,, \tag{2.9}$$

and constitutes one of the central conceptual achievements of modern particle physics. The electroweak theory successfully explains a wide range of phenomena, from beta decay to precision collider observables, and its structure is deeply intertwined with the mechanism of spontaneous symmetry breaking.

Gauge structure and field content

The gauge sector of the electroweak theory consists of four gauge fields: three $SU(2)_L$ gauge bosons W^a_μ $(a = 1, 2, 3)$ associated with the weak isospin symmetry, and one $U(1)_Y$ gauge boson B_μ corresponding to weak hypercharge. The dynamics of these fields are governed by the field strength tensors

$$W^a_{\mu\nu} = \partial_\mu W^a_\nu - \partial_\nu W^a_\mu + g\,\epsilon^{abc} W^b_\mu W^c_\nu \,, \tag{2.10}$$

$$B_{\mu\nu} = \partial_\mu B_\nu - \partial_\nu B_\mu \,, \tag{2.11}$$

where g and g' denote the $SU(2)_L$ and $U(1)_Y$ gauge couplings, respectively.

The pure gauge part of the electroweak Lagrangian is given by

$$\mathscr{L}^{\text{gauge}}_{\text{EW}} = -\frac{1}{4} W^a_{\mu\nu} W^{a\,\mu\nu} - \frac{1}{4} B_{\mu\nu} B^{\mu\nu} \,. \tag{2.12}$$

Fermions are assigned to representations of the gauge group according to their chirality. Left-handed fermions transform as doublets under $SU(2)_L$, while right-handed fermions are singlets. For example, the leptonic fields are arranged as

$$L_L = \begin{pmatrix} \nu_L \\ \ell_L \end{pmatrix} , \qquad \ell_R \,, \tag{2.13}$$

with analogous assignments for quarks. This chiral structure leads to maximal parity violation in weak interactions, a defining experimental signature of the electroweak force.

Gauge invariance uniquely fixes the interaction structure through the covariant derivative

$$D_\mu = \partial_\mu - i g \frac{\sigma^a}{2} W^a_\mu - i g' \frac{Y}{2} B_\mu \,, \tag{2.14}$$

where σ^a are the Pauli matrices and Y denotes the weak hypercharge.

Renormalization and theoretical consistency

A crucial requirement for the viability of any quantum field theory is renormalizability. In the electroweak theory, explicit mass terms for gauge bosons would violate gauge invariance and spoil renormalizability. The introduction of spontaneous symmetry breaking via the Higgs mechanism allows gauge bosons to acquire masses while preserving the renormalizable structure of the theory.

The proof of renormalizability of spontaneously broken non-Abelian gauge theories, established by 't Hooft and Veltman, represented a major theoretical breakthrough and firmly established the electroweak theory as a consistent quantum field theory [149]. Gauge fixing and the introduction of Faddeev–Popov ghost fields [150] are essential ingredients in this construction and ensure the unitarity and gauge independence of physical observables.

Infrared behavior and symmetry breaking

In contrast to QCD, the electroweak theory does not exhibit confinement. Instead, its infrared behavior is dominated by spontaneous symmetry breaking, which generates a mass gap for the weak gauge bosons. The breaking of

$$SU(2)_L \times U(1)_Y \longrightarrow U(1)_{\mathrm{em}} \tag{2.15}$$

leads to the emergence of massive $W^{\pm}$ and Z bosons, while the photon remains massless.

The presence of massive gauge bosons suppresses infrared divergences and allows for a well-defined perturbative expansion at energies above the electroweak scale. At energies well below the weak scale, the heavy gauge bosons can be integrated out, yielding effective four-fermion interactions such as those originally described by Fermi theory.

Charged and neutral currents

The electroweak theory predicts both charged-current and neutral-current interactions. Charged currents are mediated by the $W^{\pm}$ bosons and induce transitions between members of the same $SU(2)_L$ doublet. Neutral currents, mediated by the Z boson, were a striking prediction of the electroweak theory and their experimental discovery in the 1970s provided decisive confirmation of the unified framework.

The precise structure of these interactions is fixed by the gauge symmetry and has been tested with high precision at collider and low-energy experiments, forming one of the strongest empirical pillars of the Standard Model.

Role of the electroweak sector within the Standard Model

Within the Standard Model, the electroweak sector plays a central role in connecting the gauge structure to the mechanism of mass generation. While QCD governs the strong dynamics of quarks and gluons, electroweak interactions fix the chiral structure of the fermions and their gauge couplings, and they determine how fermion masses arise through Yukawa interactions once electroweak symmetry is broken. In theories beyond the Standard Model, the details of this connection can be altered, depending on the choice of field content and symmetry structure (for instance through extended scalar sectors, additional gauge symmetries, or vector-like fermions), even though the low-energy theory must reproduce the observed electroweak phenomenology.

Moreover, the electroweak sector provides the theoretical framework in which extensions of the scalar sector are naturally embedded. Modifications of electroweak symmetry-breaking dynamics, such as those studied in singlet extensions or multi-Higgs-doublet models, can affect electroweak precision observables and play a crucial role in the phenomenology explored in this thesis.

2.1.4 Higgs Sector and Electroweak Symmetry Breaking

The BEH sector provides the mechanism by which the electroweak gauge symmetry is spontaneously broken, generating masses for gauge bosons and fermions while preserving gauge invariance and renormalizability. The central idea is that the Lagrangian is fully symmetric under $SU(2)_L \times U(1)_Y$, but the ground state (vacuum) is not. This phenomenon, known as spontaneous symmetry breaking (SSB), was developed in the context of gauge theories in the 1960s [4–6, 8] and forms a cornerstone of the Standard Model.

Scalar field content and Higgs potential

The Standard Model contains one complex scalar doublet transforming under $SU(2)_L$ with hypercharge $Y_\Phi = 1$,

$$\Phi(x) = \begin{pmatrix} \phi^+(x) \\ \phi^0(x) \end{pmatrix}, \qquad \Phi \sim (\mathbf{2}, 1)\,. \tag{2.16}$$

The most general renormalizable, gauge-invariant scalar potential is

$$V(\Phi) = -\mu^2\, \Phi^\dagger\Phi + \lambda\, (\Phi^\dagger\Phi)^2\,, \qquad \lambda > 0\,, \tag{2.17}$$

with real parameters μ^2 and λ. The sign choice $\mu^2 > 0$ triggers a non-trivial vacuum structure: the potential is minimized for field configurations satisfying

$$\Phi^\dagger\Phi = \frac{\mu^2}{2\lambda} \equiv \frac{v^2}{2}\,. \tag{2.18}$$

The parameter v is identified with the electroweak vacuum expectation value (vev), fixed experimentally through the Fermi constant (G_F), $v \simeq 246\,\mathrm{GeV}$.

Spontaneous symmetry breaking and vacuum choice

The set of minima of $V(\Phi)$ forms a continuous manifold related by gauge transformations. Choosing one specific vacuum corresponds to selecting a gauge orbit representative, and does not imply that the underlying gauge symmetry is explicitly broken. A convenient choice is

$$\langle\Phi\rangle = \frac{1}{\sqrt{2}} \begin{pmatrix} 0 \\ v \end{pmatrix}. \tag{2.19}$$

This vacuum breaks the electroweak gauge group as

$$SU(2)_L \times U(1)_Y \;\longrightarrow\; U(1)_\mathrm{em}\,, \tag{2.20}$$

leaving the electromagnetic subgroup unbroken. In other words, the vacuum is invariant under the generator of electric charge $Q = T^3 + Y/2$, while it is not invariant under the remaining three broken generators.

It is important to emphasize the distinction between global and gauge SSB. For a global continuous symmetry, Goldstone's theorem implies the presence of massless physical scalars. In a gauge theory, the would-be Goldstone modes are gauge artifacts: they can be removed by a gauge transformation, and their degrees of freedom reappear as longitudinal polarizations of massive gauge bosons. This is the essence of the Higgs mechanism [4–6,8].

Spectrum after symmetry breaking: degrees of freedom

Before symmetry breaking, the scalar doublet contains four real degrees of freedom. Expanding around the vacuum,

$$\Phi(x) = \frac{1}{\sqrt{2}} \begin{pmatrix} \chi^+(x) \\ v + h(x) + i\chi^0(x) \end{pmatrix}, \tag{2.21}$$

we identify one real scalar field h (the physical Higgs boson) and three real fields $\chi^\pm, \chi^0$ corresponding to would-be Goldstone modes.

The gauge kinetic term $(D_\mu \Phi)^\dagger (D^\mu \Phi)$ generates mass terms for the gauge bosons once Φ acquires a vev. Defining the charged fields

$$W_\mu^\pm = \frac{1}{\sqrt{2}} \left(W_\mu^1 \mp i W_\mu^2 \right), \tag{2.22}$$

and the neutral mass eigenstates

$$\begin{pmatrix} Z_\mu \\ A_\mu \end{pmatrix} = \begin{pmatrix} \cos\theta_W & -\sin\theta_W \\ \sin\theta_W & \cos\theta_W \end{pmatrix} \begin{pmatrix} W_\mu^3 \\ B_\mu \end{pmatrix}, \qquad \tan\theta_W = \frac{g'}{g}, \tag{2.23}$$

one obtains the tree-level gauge boson masses

$$m_W = \frac{1}{2} g v, \qquad m_Z = \frac{1}{2} \sqrt{g^2 + g'^2}\, v, \qquad m_A = 0. \tag{2.24}$$

The Higgs boson mass follows from the curvature of the potential at the minimum,

$$m_h^2 = 2\lambda v^2 \,. \tag{2.25}$$

The degrees-of-freedom counting provides an intuitive picture. Before SSB, we have:

- 4 scalar d.o.f. from Φ,
- 4 gauge bosons, each with 2 transverse polarizations $\Rightarrow$ 8 gauge d.o.f.

After SSB:

- 1 physical scalar (h),
- $W^\pm$ and Z become massive and each acquire a longitudinal mode (3 polarizations),
- the photon remains massless (2 polarizations).

The three Goldstone d.o.f. are precisely "eaten" to provide the longitudinal polarizations of $W^\pm$ and Z.

Yukawa interactions and fermion masses

Gauge invariance also allows Yukawa interactions between Φ and fermions, schematically

$$\mathscr{L}_Y = -y_d\,\bar{Q}_L\Phi\,d_R - y_u\,\bar{Q}_L\tilde{\Phi}\,u_R - y_\ell\,\bar{L}_L\Phi\,\ell_R + \text{h.c.}, \qquad \tilde{\Phi} = i\sigma^2\Phi^*\,. \tag{2.26}$$

After SSB, these interactions generate fermion masses $m_f = y_f v/\sqrt{2}$ and predict Higgs-fermion couplings proportional to the fermion masses. This structure explains why fermion masses are not arbitrary parameters in the Lagrangian but arise from gauge-invariant interactions with the Higgs field.

Gauge fixing and R_ξ gauges

Beyond tree level, quantization requires fixing the gauge to remove redundancies from gauge-equivalent field configurations. After SSB, the kinetic term $(D_\mu\Phi)^\dagger(D^\mu\Phi)$ contains mixing terms between gauge bosons and Goldstone fields, e.g. of the form $m_W\,W_\mu\,\partial^\mu\chi$, which complicates perturbation theory. A convenient and widely used class of renormalizable gauges is provided by the R_ξ gauge-fixing functions,

$$\mathscr{F}^\pm = \partial^\mu W_\mu^\pm \mp i\xi_W m_W \chi^\pm\,, \tag{2.27}$$

$$\mathscr{F}^Z = \partial^\mu Z_\mu - \xi_Z m_Z \chi^0\,, \tag{2.28}$$

$$\mathscr{F}^A = \partial^\mu A_\mu\,, \tag{2.29}$$

leading to the gauge-fixing Lagrangian

$$\mathscr{L}_{\text{GF}} = -\frac{1}{\xi_W}\,\mathscr{F}^+\mathscr{F}^- - \frac{1}{2\xi_Z}(\mathscr{F}^Z)^2 - \frac{1}{2\xi_A}(\mathscr{F}^A)^2. \tag{2.30}$$

This choice cancels gauge–Goldstone mixing and yields propagators suitable for loop calculations. In R_ξ gauges, the Goldstone fields acquire gauge-dependent masses,

$$m^2_{\chi^\pm} = \xi_W m_W^2, \qquad m^2_{\chi^0} = \xi_Z m_Z^2. \tag{2.31}$$

Although unphysical, these masses are essential for maintaining a renormalizable perturbative expansion.

Faddeev–Popov ghosts and their role

Gauge fixing introduces an overcounting of gauge-equivalent field configurations in the path integral. The Faddeev–Popov procedure [150] resolves this by introducing ghost fields c and $\bar{c}$. Ghosts are Lorentz scalars but obey fermionic (Grassmann) statistics and therefore cannot appear as external physical states.

In a broken gauge theory, ghosts couple not only to the gauge fields but also to the scalar sector, and in R_ξ gauges they acquire gauge-dependent masses analogous to the Goldstone masses,

$$m^2_{c_W} = \xi_W m_W^2, \qquad m^2_{c_Z} = \xi_Z m_Z^2. \tag{2.32}$$

While ghosts do not correspond to observable particles, they are indispensable: they ensure the cancellation of unphysical polarization contributions and guarantee the gauge independence and unitarity of physical S-matrix elements. This structure is a key ingredient in the proof of renormalizability of the electroweak theory [149].

2.2 Limitations of the Standard Model

Despite its remarkable success in describing a vast range of experimental data, the Standard Model (SM) is widely regarded as an incomplete theory. While it provides a consistent and predictive quantum field theoretical framework for strong, weak and electromagnetic interactions, it fails to address several fundamental questions concerning the structure of matter, the origin of mass scales, and the evolution of the early Universe. These shortcomings strongly motivate the existence of new physics beyond the Standard Model (BSM).

In this section we discuss the main theoretical and phenomenological limitations of the SM and highlight the open problems that are particularly relevant for extensions of the scalar sector, electroweak phase transition dynamics, and gravitational-wave phenomenology.

Dark matter

A wealth of astrophysical and cosmological observations provides compelling evidence for the existence of dark matter (DM), which constitutes approximately 25% of the energy density of the Universe [151]. These observations include galactic rotation curves [152], gravitational lensing [153], large-scale structure formation, and precise measurements of the cosmic microwave background [151].

The Standard Model, however, does not contain a viable dark matter candidate. While neutrinos are electrically neutral and weakly interacting, their small masses render them relativistic at the time of structure formation, excluding them as the dominant component of cold dark matter [154].

This strongly motivates the existence of new stable or long-lived particles beyond the SM. Many BSM scenarios introduce dark matter candidates whose stability is ensured by discrete symmetries. In particular, scalar extensions of the Higgs sector often naturally accommodate dark matter candidates, for example through singlet scalars stabilised by a $\mathbb{Z}_2$ symmetry [155, 156]. These scenarios tightly connect dark matter phenomenology to electroweak symmetry breaking and Higgs physics.

Baryon asymmetry of the Universe

One of the most striking failures of the Standard Model is its inability to explain the observed matter–antimatter asymmetry of the Universe. The baryon asymmetry is conventionally expressed in terms of the baryon-to-photon ratio,

$$\eta_B = \frac{n_B - n_{\bar{B}}}{n_\gamma} \simeq 6 \times 10^{-10}, \tag{2.33}$$

as inferred from Big Bang nucleosynthesis and cosmic microwave background measurements [151, 157].

Any successful explanation of this asymmetry must be a dynamical mechanism it can not be an initial condition of the universe. And to do so any possible explanation must satisfy the Sakharov conditions: baryon number violation, C and CP violation, and a departure from thermal equilibrium [15]. While the SM contains baryon number violating sphaleron processes [158] and CP violation through the CKM matrix, these ingredients are insufficient in practice [159, 160]. In particular, the electroweak phase transition in

the SM is a smooth crossover for $m_h \simeq 125$ GeV [49, 161], preventing the necessary out-of-equilibrium dynamics at the time of the EWPT.

Electroweak baryogenesis provides an appealing framework in which the baryon asymmetry is generated at the electroweak scale [16, 17, 21]. However, its realisation requires a strongly first-order electroweak phase transition, sources of C violation and additional sources of CP violation, both of which necessitate physics beyond the SM. Extensions of the scalar sector can modify the finite-temperature effective potential, render the phase transition first order, and thereby play a crucial role in addressing the baryon asymmetry problem [19, 37].

Neutrino masses and flavor structure

Neutrino oscillation experiments have conclusively demonstrated that neutrinos possess non-zero masses and mix between flavour eigenstates [162, 163]. In the Standard Model, neutrinos are exactly massless, as no neutrino mass term is present in the Lagrangian.

The simplest extension involves higher-dimensional operators, such as the Weinberg operator [164],

$$\mathscr{L}_5 = \frac{c_{\alpha\beta}}{\Lambda}(\bar{L}^c_\alpha \tilde{\Phi}^*)(\tilde{\Phi}^\dagger L_\beta) + \text{h.c.}, \tag{2.34}$$

which generates Majorana masses after electroweak symmetry breaking. The origin of this operator and the scale Λ point towards new degrees of freedom and potentially high-energy dynamics, such as seesaw mechanisms [28–31].

More broadly, the flavour structure of the SM remains unexplained. The theory contains three generations of fermions with hierarchical masses and mixing angles spanning many orders of magnitude. Understanding the origin of this structure constitutes one of the major open problems in particle physics.

The strong CP problem

The QCD Lagrangian allows for a CP-violating term proportional to

$$\mathscr{L}_\theta = \theta \frac{g_s^2}{32\pi^2} G^a_{\mu\nu} \tilde{G}^{a\,\mu\nu}. \tag{2.35}$$

However, the parameter θ appearing in the Lagrangian is not itself directly physical, since chiral rephasings of the quark fields shift θ and simultaneously affect the phase of the quark mass matrix. The observable CP-violating parameter is the invariant combination

$$\bar{\theta} \;=\; \theta \;+\; \arg\det M_q \,, \tag{2.36}$$

where M_q denotes the quark mass matrix. Experimental bounds on the neutron electric dipole moment require this effective parameter to be extremely small, $\bar{\theta} \lesssim 10^{-10}$ [165,166]. The absence of a natural explanation for why $\bar{\theta}$ is so tiny constitutes the strong CP problem [167].

Proposed solutions typically involve extending the SM, most notably through the Peccei–Quinn mechanism [168, 169], which predicts the existence of a light pseudoscalar axion [170, 171]. Axions are also well-motivated dark matter candidates, illustrating how different open problems of the SM may be interconnected [172–174].

Gravity and the ultraviolet completion of the Standard Model

The Standard Model does not include gravity, and its quantisation within the framework of perturbative quantum field theory is not possible in a renormalisable way. At energies approaching the Planck scale, gravitational interactions are expected to become important, requiring a more fundamental ultraviolet completion.

Moreover, the observed value of the cosmological constant is many orders of magnitude smaller than naive quantum field theory estimates, posing an extreme naturalness problem. While this issue extends beyond particle physics, it highlights the limitations of the SM as a complete description of nature [175].

Vacuum stability and the structure of the Higgs potential

Another fundamental question concerns the stability of the electroweak vacuum. Renormalisation group analyses of the SM reveal that the Higgs quartic coupling $\lambda(\mu)$ decreases with increasing energy scale and may turn negative at scales far above the electroweak scale, depending sensitively on the values of the Higgs and top masses [176, 177].

If $\lambda(\mu)$ becomes negative, the effective Higgs potential develops a deeper minimum at large field values, implying that the electroweak vacuum is only metastable [177, 178]. Current data suggest that the SM lies close to the boundary between absolute stability and metastability [177]. Although a metastable vacuum is phenomenologically acceptable if its lifetime exceeds the age of the Universe, the proximity to instability is theoretically intriguing [176].

This behaviour suggests that additional degrees of freedom may modify the running of λ and stabilise the Higgs potential at high energies. Scalar extensions of the SM are particularly effective in this regard, as additional bosonic states can contribute positively to the beta function of λ, thereby altering the vacuum structure. As a result, vacuum stability considerations provide strong motivation for extending the Higgs sector [179,180].

The hierarchy problem and the stability of the electroweak scale

A central conceptual issue of the SM is the apparent instability of the electroweak scale under radiative corrections. The Higgs mass parameter μ^2 in the scalar potential receives quantum corrections that are sensitive to the ultraviolet (UV) completion of the theory. Schematically, at one loop one finds contributions of the form

$$\delta m_h^2 \sim \frac{1}{16\pi^2}\left(6\lambda + \frac{9}{4}g^2 + \frac{3}{4}g'^2 - 6y_t^2\right)\Lambda^2 + \cdots , \tag{2.37}$$

where Λ denotes a UV cutoff, λ is the quartic Higgs self-coupling, and y_t the top Yukawa coupling [181]. If the SM is assumed to remain valid up to very high scales (e.g. a grand-unified or Planck scale), the physical Higgs mass requires an enormous cancellation between the bare parameter and the radiative corrections. This tension is commonly referred to as the hierarchy problem or naturalness problem [182].

While naturalness is not an experimental inconsistency, it strongly motivates scenarios that protect the Higgs mass parameter from large corrections (e.g. supersymmetry, compositeness, extra dimensions), as well as more minimal extensions of the scalar sector in which the electroweak scale can be stabilised or its origin can be dynamically connected to other phenomena.

2.3 Experimental Status

High-energy collider experiments play a central role in testing the SM and in understanding how to solve the limitations of the SM. By comparing precise theoretical predictions with experimental measurements, colliders allow us to study the SM over a wide range of energy scales and to search for deviations that may point to new physics beyond the SM. In this context, the absence of significant discrepancies is also highly informative, as it constrains viable extensions of the SM and guides us in the construction of consistent BSM scenarios. In this section, we review the current experimental status of these searches, focusing on the latest collider measurements related to the Higgs sector. Before speaking about the measurements, we have to introduce the most powerful collider that exists until today and the one that has given the most accurate measurements of the Higgs sector, the LHC.

2.3.1 The Large Hadron Collider

The Large Hadron Collider (LHC) at CERN is currently the most powerful particle accelerator in operation and constitutes the primary experimental facility for testing the SM at the highest available energies. It is a proton–proton collider with a design center-of-mass energy of $\sqrt{s} = 14$ TeV, it has operated in several runs with increasing luminosity and energy since its first collisions in 2010. The LHC has done precision measurements of SM processes as well as direct searches for BSM physics, and between them the most important achievement is the discovery of the Higgs boson in 2012 by the ATLAS and CMS collaborations simultaneously.

The LHC hosts several experiments, among which ATLAS and CMS are the two general-purpose detectors designed to explore a broad range of physics topics, including Higgs physics, electroweak measurements, top-quark physics, and searches for BSM physics. Despite employing different detector technologies and design philosophies, ATLAS and CMS achieve comparable performance and provide independent and complementary measurements, which is crucial for the robustness of the results.

The LHC accelerates two counter-rotating proton beams in a 27 km circular tunnel using superconducting dipole magnets operating at cryogenic temperatures. Protons are injected through a chain of pre-accelerators and brought into collision at four interaction points, two of which host the ATLAS and CMS detectors. The collider performance is characterized by the instantaneous and integrated luminosity, with the latter determining the total size of the data sample available for physics analyses.

Following the successful completion of Run 2, the LHC is currently operating in Run 3, with increased collision energy and improved detector performance. In the longer term, the High-Luminosity LHC (HL-LHC) upgrade aims to deliver an integrated luminosity of approximately 3 ab^{-1}, enabling high-precision measurements of Higgs couplings and significantly extending the sensitivity to rare processes and new physics scenarios [100, 183].

The ATLAS detector

ATLAS is a multi-purpose detector with a forward–backward symmetric cylindrical geometry and nearly full solid-angle coverage around the interaction point. Its design emphasizes a large volume and robust tracking and calorimetry systems. From the interaction

point outwards, ATLAS consists of an inner tracking detector immersed in a solenoidal magnetic field, electromagnetic and hadronic calorimeters for energy measurements, and a muon spectrometer embedded in a large toroidal magnetic field system.

The inner detector provides precise reconstruction of charged-particle trajectories and interaction vertices, which is essential for identifying heavy-flavor jets and leptons. The calorimeter system allows accurate measurements of electrons, photons, and jets over a wide kinematic range, while the muon spectrometer offers high-resolution muon momentum measurements. This combination enables ATLAS to perform precision measurements of Higgs production and decay modes, as well as searches for resonances and deviations from Standard Model predictions [184, 185].

The CMS detector

CMS follows a more compact design centered around a high-field superconducting solenoid providing a magnetic field of 3.8 T. Within this magnetic field volume are located the silicon pixel and strip trackers, the electromagnetic calorimeter based on lead tungstate crystals, and the hadronic calorimeter. Outside the solenoid, a muon system based on gas-ionization detectors provides efficient muon identification and momentum measurements.

The strong magnetic field and high-granularity tracking system give CMS excellent momentum resolution for charged particles, particularly at high transverse momentum. The electromagnetic calorimeter achieves outstanding energy resolution for electrons and photons, which is especially advantageous for Higgs measurements in channels such as $H \to \gamma\gamma$. CMS has produced a wide range of precision measurements and searches that closely mirror those of ATLAS, providing crucial cross-checks and combined results [186, 187].

Complementarity and combined results

The parallel operation of ATLAS and CMS is a defining strength of the LHC physics program. Independent analyses using different detector technologies reduce systematic uncertainties and increase confidence in experimental discoveries. Many of the most important results, including Higgs property measurements and limits on new physics scenarios, are obtained through statistical combinations of ATLAS and CMS data, leading to significantly improved precision.

In the context of Higgs physics, the combined measurements of production cross sections, decay rates, and coupling modifiers provide the most stringent tests of the Standard Model Higgs sector to date. These results serve as essential inputs for constraining extensions of the scalar sector and motivate the detailed phenomenological studies presented in this thesis.

2.3.2 Current measurements

We focus on experimental measurements in the Higgs sector of the Standard Model. With the discovery of the Higgs boson in 2012, the particle content of the Standard Model was completed. However, this does not imply that the Standard Model itself is complete. Several Higgs couplings have not yet been measured experimentally, such as the Higgs coupling to muons, the charm Yukawa coupling, or the Higgs self-coupling. In particular, the lack of a direct measurement of the Higgs self-interaction means that the shape

of the Higgs potential remains largely unknown. Nevertheless, all Higgs measurements performed at the LHC to date are in agreement with the Standard Model predictions.

As an illustration, in fig. 2.1 we show the latest CMS results [14] for the main Higgs boson production and decay modes. These results are presented using the signal strength framework. In this approach, the measured cross section times branching ratio is normalized to the corresponding Standard Model prediction. Consequently, a signal strength value $\mu = 1$ indicates perfect agreement with the Standard Model. Inspecting the results shown in fig. 2.1, one observes that all measured signal strengths are compatible with unity within uncertainties, and no significant deviation from the Standard Model is found.

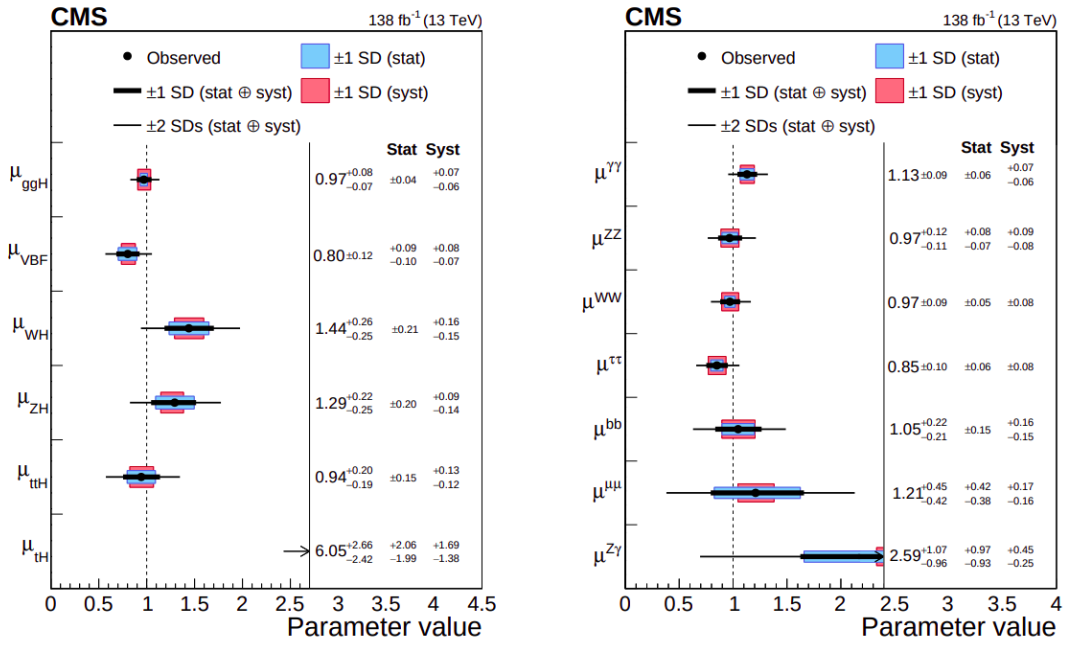

Figure 2.1: Results obtained by CMS [14] for the Higgs production and decay rates.

Deviations from the Standard Model can also be probed using the κ framework. In this approach, coupling modifiers κ_i are introduced, rescaling the Higgs couplings with respect to their Standard Model values. By computing Higgs production and decay processes while allowing selected κ_i parameters to vary and comparing the predictions with experimental measurements, constraints on possible deviations from the Standard Model are obtained. The Standard Model limit is recovered for all $\kappa_i = 1$. In fig. 2.2, we present the latest results from CMS [14] and ATLAS [188]. All measured coupling modifiers are found to be consistent with the Standard Model within current uncertainties.

Some coupling modifiers are not included in fig. 2.2. Among them are the quartic coupling between two Higgs bosons and two vector bosons, usually denoted as κ_{2V}, and the Higgs self-coupling modifier, which is the main focus of this thesis. The latter is commonly denoted as κ_λ or κ_3. Sensitivity to κ_λ arises from EW precision observables, single-Higgs and double-Higgs production. In single-Higgs processes, the trilinear coupling contributes through loop effects at next-to-leading order, whereas in double-Higgs production it enters already at leading order and provides the dominant sensitivity.

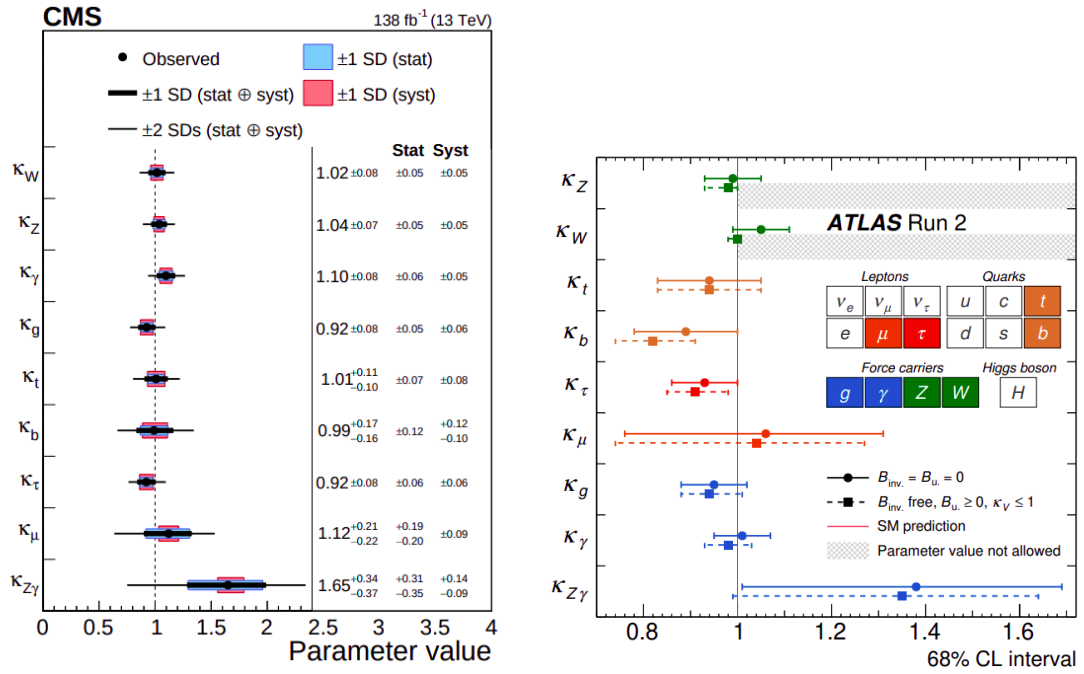

Figure 2.2: Experimental limits of the SM-like Higgs boson modifiers. *Left:* Results obtained by CMS [14]. *Right:* Results obtained by ATLAS [188].

To date, double-Higgs production has not been observed experimentally, and therefore the Higgs self-coupling has not been measured. Current constraints on κ_λ from Run 2 of the LHC are obtained by comparing theoretical predictions for Higgs-pair production, allowing κ_λ to vary, with the experimental upper limits on the corresponding cross section. The resulting bounds are $-1.4 < \kappa_\lambda < 7.8$ for CMS [10] and $-1.2 < \kappa_\lambda < 7.2$ for ATLAS [9]. These limits are illustrated in fig. 2.3 for both experiments.

The large uncertainties in the current determination of κ_λ make it one of the most promising observables for probing extensions of the scalar sector, motivating the detailed phenomenological studies presented in the following chapters.

2.3.3 Future prospects: HL-LHC

Despite the remarkable success of the LHC program, the precision of many Higgs-sector measurements is still limited by statistical and systematic uncertainties. In particular, several Higgs couplings remain poorly constrained or entirely unmeasured, with the Higgs self-coupling representing one of the most prominent open targets. Addressing these limitations requires a substantial increase in luminosity, which will be provided by the High-Luminosity Large Hadron Collider (HL-LHC).

The HL-LHC constitutes the next major upgrade of the LHC and is designed to extend its physics reach by delivering an integrated luminosity of up to 3 ab^{-1} at a center-of-mass energy of $\sqrt{s} = 14$ TeV while in the LHC Run 2it was obtained an integrated luminosity of 140 fb^{-1} at a center-of-mass energy of $\sqrt{s} = 13$ TeV. In the context of the Higgs sector, the HL-LHC is expected to reduce the uncertainties on most Higgs couplings to the percent level and to provide meaningful improvements to the constraints on the Higgs self-coupling through measurements of double-Higgs production.

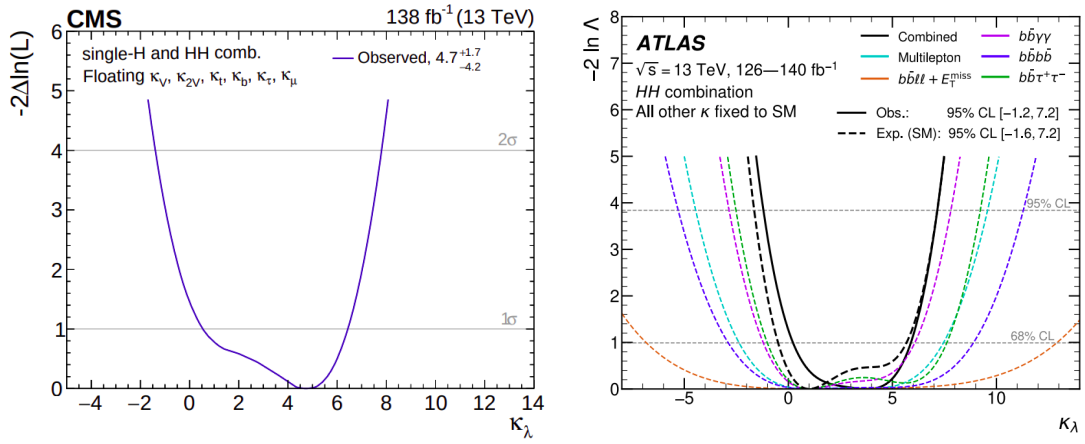

Figure 2.3: Experimental limits of the κ_λ modifier. *Left:* Results obtained by CMS [10]. *Right:* Results obtained by ATLAS [9].

In fig. 2.4, the projected combined sensitivity of the CMS and ATLAS experiments to the Higgs self-coupling modifier κ_λ at the HL-LHC is shown [63]. The projected limits are $0.5 < \kappa_\lambda < 1.7$ for a 95% C.L. which represent a significant improvement with respect to current constraints.

This limit is obtained assuming a value of $\kappa_\lambda = 1$ as an hypothesis and this affects to the obtained limits. In [63] the authors also present how this limit depend on the realized value of κ_λ and these results are shown in fig. 2.5. This is particularly helpful for the BSM scenarios studied in this thesis, in which κ_λ typically deviates from its SM value. It should also be kept in mind that, as soon as a non-zero BSM coupling enters the di-Higgs production calculation, the applicability of these limits could be affected.

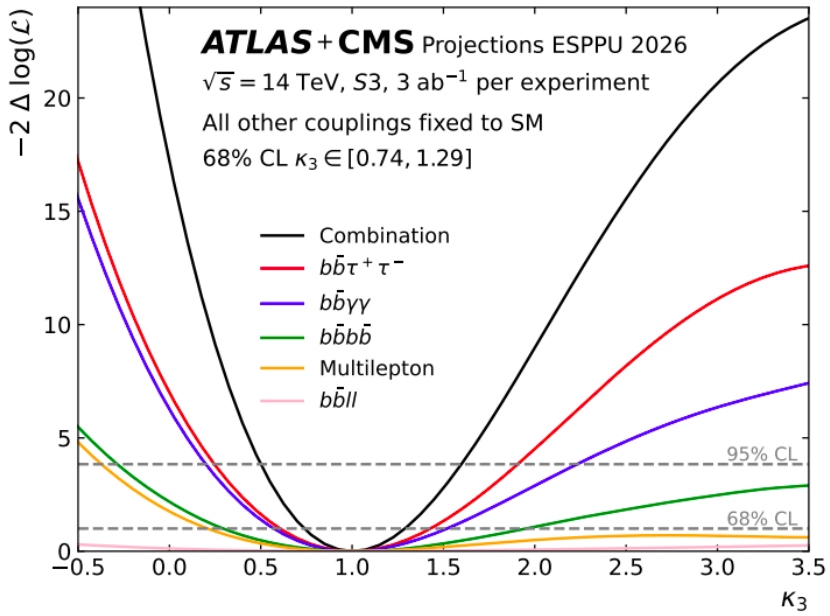

Figure 2.4: Future prospects for experimental limits of the κ_λ modifier at the HL-LHC by combining the CMS and ATLAS prospects [63].

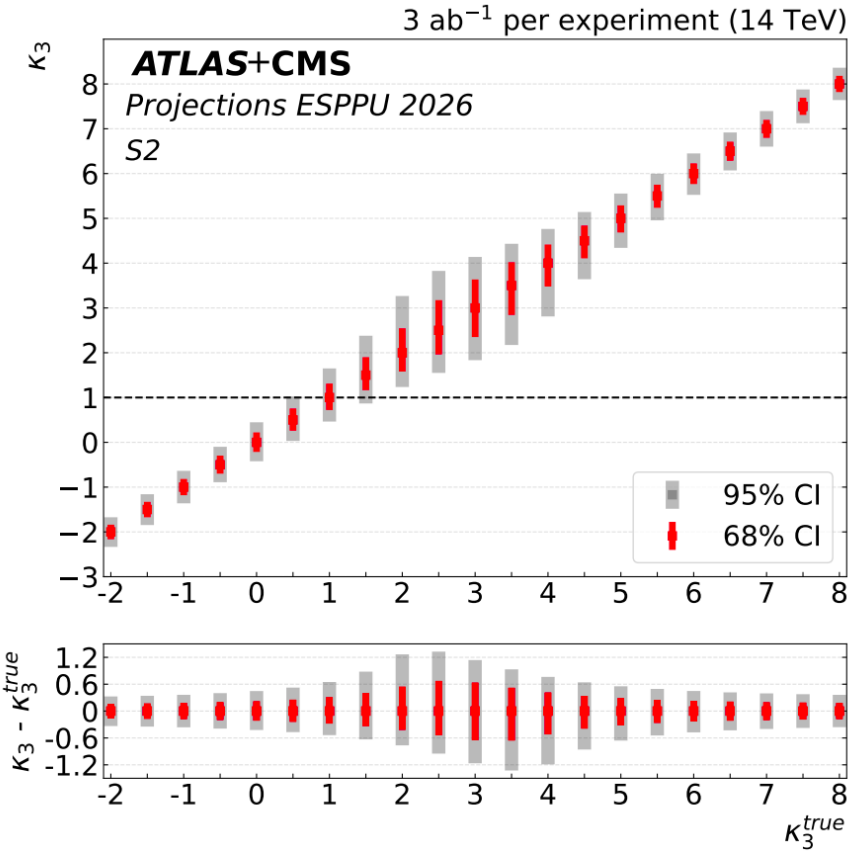

Figure 2.5: Future prospects for experimental limits of the κ_λ modifier at the HL-LHC by combining the CMS and ATLAS prospects assuming different values of κ_λ [63].

Chapter 3

Early Universe and finite temperature

Aprovecha ahora que están aquí
para no arrepentirte cuando falten.

– Ama

The previous chapter established the Standard Model as a remarkably successful quantum field theory of particle interactions and outlined the key open problems that motivate physics beyond it. Several of these shortcomings are intrinsically cosmological: the nature of dark matter, the origin of the baryon asymmetry, and the possibility that new degrees of freedom modify the thermal evolution of the early Universe. In this sense, collider measurements and precision tests constrain the microphysics, but the Universe itself provides an additional, complementary arena in which the same microscopic ingredients are at work. To connect extensions of the Higgs sector to phenomena such as electroweak baryogenesis and stochastic gravitational-wave production, one must embed the particle-physics model into a dynamical cosmological background and specify the thermal history in which phase transitions and out-of-equilibrium processes take place.

This chapter therefore introduces the cosmological standard model, ΛCDM, which offers an effective description of the Universe on large scales based on homogeneity and isotropy, General Relativity, and a present-day energy budget dominated by cold dark matter and a cosmological constant. Within this framework, the expansion rate links cosmological evolution to microscopic physics through the energy density of the plasma, while finite-temperature quantum field theory provides the tools to describe symmetry breaking and phase transitions in an expanding spacetime. After reviewing the Friedmann–Lemaître–Robertson–Walker geometry and the Friedmann equations, we summarise the sequence of cosmological epochs that structure the thermal history. This sets the stage for the subsequent discussion of the baryon asymmetry, the electroweak phase transition dynamics that form the central focus of this thesis and, ultimately, for the computation of the stochastic GW background generated during the PT.

3.1 The Cosmological Standard Model

The *cosmological standard model*, commonly referred to as ΛCDM, provides an effective description of the Universe on large scales. For the construction of the model, three basic assumptions are made. Firstly, the Universe at large-scales is homogenous and isotropic, secondly it assumes General Relativity as the theory of gravity on cosmological scales, and lastly it assumes a matter-energy budget dominated today by cold dark matter (CDM) and a cosmological constant Λ, with ordinary (baryonic) matter and radiation composing subdominant fractions. Within this framework, early-Universe dynamics is governed by thermal quantum field theory in an expanding background and the thermal history can be organized into a sequence of epochs characterized by the dominant component of the cosmic energy density. Modern high-precision cosmological observations—most notably the cosmic microwave background (CMB) anisotropies—pin down the parameters of ΛCDM at the percent level [151].

In General Relativity to describe an specific space-time, like ours, we need to define a metric. The metric that describes an expanding homogeneous and isotropic Universe is the Friedmann–Lemaître–Robertson–Walker (FLRW) metric [189, 190],

$$ds^2 = -dt^2 + a^2(t)\left[\frac{dr^2}{1-kr^2} + r^2\left(d\theta^2 + \sin^2\theta, d\varphi^2\right)\right], \tag{3.1}$$

where $a(t)$ is the scale factor, which encodes the expansion of the Universe, and $k = 0, \pm 1$ denotes the spatial curvature corresponding to flat, closed, or open geometries, respectively.

To now understand how this kind of Universe behaves we need to solve the Einstein's equation for the FLRW metric. When we solve this equation assuming that the Universe is a perfect fluid, with an equation of state $p = w\rho$, we obtain the Friedmann equations [191, 192],

$$H^2(t) \equiv \left(\frac{\dot{a}}{a}\right)^2 = \frac{8\pi G}{3}\rho(t) - \frac{k}{a^2(t)}, \tag{3.2}$$

$$\frac{\ddot{a}}{a} = -\frac{4\pi G}{3}\left[\rho(t) + 3p(t)\right], \tag{3.3}$$

where $H(t)$ is the Hubble parameter, and $\rho(t)$ and $p(t)$ are the total energy density and pressure of the cosmic fluid, respectively. The first Friedmann equation relates the expansion rate of the Universe, encoded in the Hubble parameter $H = \dot{a}/a$, to the total energy density ρ and the spatial curvature k [189–193]. It therefore determines whether the Universe is expanding or contracting and fixes the relation between the expansion rate and the microscopic particle content through $\rho(T)$ [191, 194]. The second Friedmann equation describes the acceleration or deceleration of the expansion and shows explicitly that not only energy density but also pressure contributes to the gravitational dynamics [191–193]. In particular, components with sufficiently negative pressure can drive accelerated expansion [193, 194].

Together with the energy–momentum conservation equation [191, 193],

$$\dot{\rho} + 3H(\rho + p) = 0, , \tag{3.4}$$

the Friedmann equations determine how different components of the cosmic plasma dilute with the expansion and thereby define the sequence of radiation-dominated, matter-dominated, and dark-energy-dominated epochs that structure the thermal history of the

Universe [191, 193, 194]. The conservation equation implies a simple scaling of the energy density with the scale factor [191, 193, 194],

$$\rho \propto a^{-3(1+w)}, . \tag{3.5}$$

In particular, relativistic species ($w = 1/3$) scale as

$$\rho_{rad} \propto a^{-4}, \tag{3.6}$$

non-relativistic matter ($w = 0$) as

$$\rho_{\mathrm{m}} \propto a^{-3}, \tag{3.7}$$

and a cosmological constant ($w = -1$) remains constant,

$$\rho_{\Lambda} = \text{const.} \tag{3.8}$$

These distinct scaling behaviors describe the radiation-dominated (RD), matter-dominated (MD), and dark-energy-dominated (Λ-dominated) epochs, which structure the thermal and dynamical history of the Universe and provide the cosmological backdrop for early-Universe phenomena such as phase transitions and baryogenesis [191, 194].

After inflation and reheating (which we do not discuss in detail here), the Universe rapidly enters a radiation-dominated (RD) epoch [191]. During this phase, the expansion rate is high and the cosmic plasma is close to thermal equilibrium [191, 194]. As the temperature decreases, a sequence of physical processes takes place, including particle annihilations, decouplings, and phase transitions [191]. One of the most important of these is the electroweak phase transition, which occurs at temperatures of order $T \sim 100$ GeV and marks the breaking of the electroweak gauge symmetry [195]. This epoch is of particular interest, as it provides a potential setting for the generation of the baryon asymmetry of the Universe [17, 21, 49, 196].

At much later times, when the energy density of non-relativistic matter exceeds that of radiation, the Universe enters a matter-dominated (MD) era [191, 194]. This transition enables the growth of cosmological structures through gravitational instability [193, 194]. Eventually, at redshift $z \simeq 1100$, electrons and protons combine to form neutral hydrogen during recombination, and photons decouple from the plasma [193, 197]. These photons constitute the Cosmic Microwave Background (CMB), observed today as an almost perfect blac-kbody spectrum with small anisotropies [193, 197].

The CMB encodes precise information about the early Universe and, in particular, provides stringent constraints on the baryon density. As a result, it allows for an accurate determination of the baryon-to-photon ratio, which quantifies the observed matter–antimatter asymmetry and serves as a key benchmark to reproduce for any baryogenesis mechanism [151]. The striking mismatch between this observed value and the prediction of the SM lies at the heart of the baryon asymmetry problem, which we discuss in detail in the following.

3.2 Baryon Asymmetry of the Universe

One of the most discussed open problems of particle physics and cosmology is the origin of the baryon asymmetry of the Universe (BAU) [21, 22, 198]. Observations indicate that the

present Universe is dominated by matter, with only a small abundance of antimatter [22]. This asymmetry is conventionally quantified by the baryon-to-photon ratio,

$$\eta_B \equiv \frac{n_B - n_{\bar{B}}}{n_\gamma}, \tag{3.9}$$

[22, 151, 198] whose value has been measured experimentally in two independent ways.

3.2.1 Experimental measurements

Firstly it can be determined from the CMB. Temperature and polarization anisotropies of the CMB are sensitive to the baryon content of the Universe [151, 197]. In particular, the relative heights and positions of the acoustic peaks in the CMB power spectrum depend on the baryon density through its effect on the photon–baryon plasma before the recombination [151, 197]. These observations allow for a precise determination of the baryon density parameter [151, 197],

$$\Omega_b h^2, \tag{3.10}$$

where Ω_b is the baryon energy density in units of the critical density and h is the reduced Hubble parameter [191]. Once $\Omega_b h^2$ is known, it can be converted into the baryon-to-photon ratio [151, 191]. The parameter $\Omega_b h^2$ fixes the present baryon mass density ρ_b [191],

$$\rho_b = \Omega_b \rho_{crit}, \tag{3.11}$$

where ρ_{crit} denotes the critical energy density of the Universe, defined as the density for which the spatial geometry is flat and from which the baryon number density n_B follows dividing by the proton mass. On the other hand, the present photon number density n_γ is determined by the measured CMB temperature, $T_{CMB} \simeq 2.725$ K, assuming a blackbody spectrum. Since both quantities are known with high precision, their ratio can be computed reliably. Using the Planck measurement of $\Omega_b h^2$, one finds

$$\eta_B^{CMB} \simeq 6.1 \times 10^{-10}, \tag{3.12}$$

with percent-level uncertainty [151]. This value reflects the baryon asymmetry frozen in at early times and conserved during the expansion of the Universe.

Secondly, an independent determination of η_B is obtained from Big Bang nucleosynthesis. In order of decreasing temperature, nuclear reactions in the hot primordial plasma during the first few minutes after the Big Bang led to the synthesis of light nuclei, with deuterium forming first, followed by helium and lithium.The predicted abundances of these elements depend sensitively on the baryon density, which controls the nuclear reaction rates and the expansion rate of the Universe at that epoch.

By comparing theoretical BBN predictions with observed primordial abundances, most notably the deuterium, one can infer the baryon-to-photon ratio. Remarkably, this procedure yields a value of η_B fully consistent with the CMB determination,

$$\eta_B^{BBN} \simeq \eta_B^{CMB}, \tag{3.13}$$

within uncertainties [199]. This agreement provides a powerful cross-check of the hot Big Bang picture and demonstrates that the baryon asymmetry was already established well before the onset of nucleosynthesis.

The existence of a non-zero η_B implies that baryon number was dynamically generated in the early Universe, because any kind on initial baryon asymmetry would be washed out by inflation. In the following we summarize the general requirements that a theory need to fulfil for generating the BAU dynamically, which are known as the Sakharov conditions. And we will briefly review the main theoretical scenarios, with particular emphasis on electroweak baryogenesis.

3.2.2 Sakharov conditions

Any viable mechanism for generating the baryon asymmetry of the Universe must satisfy a set of necessary criteria formulated by Sakharov in 1967 [15]. These general conditions apply independently of the energy scale or the specific particle physics model under consideration. They provide a framework for understanding why baryogenesis is non-trivial and serve as a guiding principle for the construction of baryogenesis scenarios.

The three Sakharov conditions are:

1. Baryon number violation,
2. Violation of charge conjugation (C) and charge–parity (CP) symmetries,
3. Departure from thermal equilibrium.

In the following, we briefly discuss the physical meaning of each condition and explain why all three are necessary for the generation of the baryon asymmetry.

Baryon number violation

The first condition requires that the baryon number (B) is not an exact symmetry of the fundamental theory. If the baryon number was strictly conserved, any initial baryon asymmetry would be preserved, but it would be impossible to dynamically generate a net baryon excess starting from a baryon-symmetric initial state.

In the Standard Model, the baryon number is an accidental global symmetry at the classical level, but it is violated non-perturbatively through electroweak sphaleron processes [16, 158]. These transitions change baryon and lepton numbers according to

$$\Delta B = \Delta L = 3\,, \tag{3.14}$$

while conserving $B-L$. As a result, sphalerons provide a realization of the baryon number violation and play a central role in several baryogenesis scenarios.

C and CP violation

The second Sakharov condition requires the violation of charge conjugation (C) and charge–parity (CP) symmetries. If C and CP were exact symmetries, processes producing baryons would occur at the same rate as those producing antibaryons, washing out any kind of asymmetry generated by another process.

While the Standard Model violates C maximally through its chiral gauge structure and contains sources of CP violation in the quark sector via the Cabibbo–Kobayashi–Maskawa (CKM) [200] matrix, these effects are quantitatively insufficient for successful baryogenesis [159,160]. In particular, the amount of CP violation induced by the CKM phase is strongly suppressed in baryon-number-violating processes and leads to an asymmetry many orders of magnitude smaller than the observed value [159, 160, 201, 202].

Departure from thermal equilibrium

The third Sakharov condition requires a departure from thermal equilibrium. In a Universe in thermal equilibrium, any baryon-producing process is exactly compensated by its inverse process, leading to no net asymmetry even in the presence of baryon number and CP violation.

A departure from equilibrium can be achieved in several ways, such as the out-of-equilibrium decay of heavy particles in the early Universe or during a first-order phase transition. In the context of electroweak baryogenesis, this condition is fulfilled by the dynamics of the expanding bubble walls of the broken phase during a first-order electroweak phase transition.

3.2.3 Theoretical mechanisms for generating the BAU

The Sakharov conditions are individually necessary but not sufficient to explain the observed baryon asymmetry of the Universe. Only their simultaneous realization allows for its dynamical generation. In the following, we briefly review the main theoretical frameworks proposed to satisfy these conditions and to account for the observed baryon asymmetry. We will put particular emphasis on electroweak baryogenesis, which is the mechanism considered in the phenomenological studies presented in this thesis.

GUT baryogenesis

One of the earliest proposals for baryogenesis arises in the context of Grand Unified Theories (GUTs). In these theories, the baryon number is not an exact symmetry and can be violated through the out-of-equilibrium decays of heavy gauge or scalar bosons at very high temperatures, typically close to the GUT scale, $T \sim 10^{15}$–$10^{16}\,\text{GeV}$ [191].

Although GUT baryogenesis is theoretically appealing, it suffers from severe phenomenological challenges. Such as the rapid proton decay, the fact that the generated baryon asymmetry can be washed out by sphaleron processes if $B - L$ is not conserved, and the required energy scales are far beyond direct experimental reach.

Affleck–Dine baryogenesis

Affleck–Dine baryogenesis exploits the existence of flat directions in the scalar potential of supersymmetric theories [203]. During inflation, scalar fields carrying the baryon or lepton number can acquire large vacuum expectation values along these flat directions. As the Universe cools and supersymmetry-breaking effects become relevant, the scalar condensate evolves dynamically and can generate a net baryon asymmetry through coherent oscillations.

This mechanism naturally produces large asymmetries and operates at relatively high temperatures. However, it relies on specific properties of supersymmetric models and is sensitive to details of the scalar potential and inflationary dynamics.

Leptogenesis

Leptogenesis provides a well-motivated explanation of the baryon asymmetry by linking it to the origin of neutrino masses [204]. In this framework, a lepton asymmetry is

first generated and later is converted into a baryon asymmetry by electroweak sphaleron processes, which violate $B + L$ but conserve $B - L$.

In its simplest realization, leptogenesis occurs via the out-of-equilibrium decays of heavy right-handed Majorana neutrinos [205], as predicted by the seesaw mechanism [28,29,204]. CP-violating decay asymmetries generate a net lepton number, while the expansion of the Universe provides the required departure from equilibrium. Sphaleron transitions then partially convert the lepton asymmetry into a baryon asymmetry before the electroweak phase transition.

Leptogenesis is theoretically attractive because it connects cosmology, neutrino physics, and the Standard Model in a minimal way. Its main problem is that it typically operates at very high energy scales, well above those accessible at current or foreseeable experiments, making direct tests challenging.

Electroweak baryogenesis

Electroweak baryogenesis is one of the most studied mechanisms to explain the observed baryon asymmetry of the Universe. It exploits the dynamics of the electroweak phase transition to generate the asymmetry during the symmetry-breaking, at temperatures of order $T \sim 100\,\text{GeV}$. As a result, it operates at experimentally accessible energy scales and can be directly linked to extensions of the Standard Model scalar sector.

Within the electroweak theory, baryon number violation is provided by sphaleron processes. A departure from thermal equilibrium can be realized if the electroweak phase transition is of first order, proceeding through the nucleation and expansion of bubbles of the broken phase within the symmetric plasma.

In this picture, expanding bubble walls separate regions of phases of the EW vacuum preserving or breaking the symmetry. In the presence of additional sources of CP violation, interactions of particles with the bubble walls generate CP-asymmetric charge densities in front of the wall. These asymmetries bias sphaleron transitions in the symmetric phase and lead to the production of a net baryon asymmetry. The generated asymmetry can then be preserved if sphaleron processes are sufficiently suppressed inside the broken phase. Otherwise the asymmetry is washed out.

The suppression of sphaleron transitions inside of the broken phase imposes a quantitative condition on the strength of the electroweak phase transition. The requirement for a sufficiently SFOEWPT is imposing that the sphaleron transitions are sufficiently suppressed inside the bubble walls in order to avoid the washout of the asymmetry and a commonly used criterion for this purpose is

$$\frac{v(T_n)}{T_n} \gtrsim 1, \tag{3.15}$$

where $v(T_n)$ denotes the Higgs vacuum expectation value at the nucleation temperature T_n, which is the temperature at which the probability of nucleating at least one critical bubble of the true vacuum within one Hubble volume becomes of order unity. In the Standard Model this condition is not satisfied for the measured Higgs boson mass, which is o big to accommodate a FOEWPT and give rise to a smooth crossover for the EWPT. Consequently, extensions of the scalar sector are required to realize a SFOEWPT if they want to be compatible with an electroweak baryogenesis scenario.

3.2.4 Failure of the SM and the need of BSM physics

Electroweak baryogenesis is an attractive framework because it operates at the electroweak scale and relies on SM dynamics such as sphaleron-induced baryon number violation. However, despite satisfying the first two Sakharov conditions at a qualitative level (although not enough CP violation), the SM fails quantitatively to generate the observed baryon asymmetry of the Universe. This failure can be traced to two fundamental shortcomings: the nature of the electroweak phase transition and the insufficiency of CP violation.

In the SM, the nature of the electroweak phase transition is governed mainly by the Higgs potential at finite temperature. Non-perturbative lattice studies have demonstrated that, for a Higgs boson mass above approximately 70–80 GeV, the electroweak phase transition is not first order but rather a smooth crossover [49, 196]. Given the experimentally measured Higgs mass of $m_h \simeq 125\,\text{GeV}$, the SM electroweak phase transition is firmly in the crossover regime.

As a consequence, there is no departure from thermal equilibrium associated with bubble nucleation, and sphaleron transitions remain active throughout the transition. Any baryon asymmetry that might be generated would therefore be efficiently erased.

The second major obstacle for electroweak baryogenesis in the SM is the smallness of CP violation. The only source of CP violation in the SM resides in the complex phase of the CKM matrix. While this phase successfully accounts for CP-violating phenomena observed in the quark sector, its impact on baryogenesis is extremely suppressed.

Quantitatively, CP-violating effects in the SM relevant for baryogenesis are proportional to the Jarlskog invariant and involve products of quark Yukawa couplings. This leads to an enormous suppression of the baryon asymmetry, yielding estimates many orders of magnitude below the observed value,

$$\eta_B^{SM} \sim 10^{-20} \; - \; 10^{-18}, \tag{3.16}$$

to be compared with the experimental value $\eta_B \simeq 6 \times 10^{-10}$.

Taken together, the absence of a first-order electroweak phase transition and the insufficiency of CP violation render electroweak baryogenesis ineffective in the SM. These shortcomings are robust and persist even when higher-order corrections are taken into account. As a result, the SM cannot account for the observed baryon asymmetry of the Universe through electroweak dynamics alone.

The failure of the SM to realize electroweak baryogenesis provides strong motivation for extensions of the scalar sector and the introduction of new sources of CP violation. Additional scalar degrees of freedom can strengthen the electroweak phase transition, while new complex couplings can enhance CP-violating effects. Such extensions can simultaneously address the baryon asymmetry problem and lead to testable signatures at colliders and in gravitational wave observables. In this thesis we are going to focus on how to fulfil the third Sakharov condition and for this we are going to focus on the electroweak phase transition.

3.3 Electroweak Phase Transition

3.3.1 Effective potential calculations

The study of cosmological phase transitions relies on the finite-temperature effective potential, which encodes the thermodynamic properties of the quantum field theory. In thermal field theory, calculations are performed in Euclidean spacetime, obtained by a Wick rotation of the time coordinate, $t \to -i\tau$ [206, 207]. At finite temperature, the partition function is given by $Z = \mathrm{Tr}\, e^{-\beta H}$, with $\beta = 1/T$. In the imaginary-time formalism, this trace is represented as a path integral over field configurations evolving in Euclidean time from $\tau = 0$ to $\tau = \beta$. The trace requires the final field configuration to be identified with the initial one, which makes the Euclidean time direction compact. As a result, bosonic fields satisfy periodic boundary conditions and fermionic fields antiperiodic boundary conditions in the Euclidean time direction, giving rise to a discrete set of frequencies known as Matsubara modes.

For bosonic and fermionic fields, the Matsubara frequencies are given by

$$\omega_n = \begin{cases} 2\pi n T\,, & \text{bosons,} \\ (2n+1)\pi T\,, & \text{fermions,} \end{cases} \tag{3.17}$$

and the corresponding field-dependent Matsubara masses read

$$m_n^2(\phi, T) = m^2(\phi) + \omega_n^2. \tag{3.18}$$

Meaning that we have a tower of states depending on n. A well-known difficulty arises from the bosonic zero Matsubara mode ($n = 0$). When the tree-level bosonic mass becomes small or vanishes, since the zero bosonic mode is not dressed by temperature corrections it leads to infrared (IR) divergences in the perturbative expansion [208]. Moreover, higher-order daisy (or ring) diagrams involving this mode become parametrically of the same size as the one-loop contribution, leading to a breakdown of the perturbation theory. Therefore the effective potential can not be constructed in a straightforward way because the theory would have uncured IR divergences. There are two main approaches to compute the finite-temperature effective potential curing the IR problem: the so-called four-dimensional approach and the dimensional reduction approach.

Four-dimensional approach

In the four-dimensional formulation of thermal field theory, the finite-temperature effective potential is computed using the original four-dimensional theory by summing over all Matsubara modes. The separation of scales is implicit and governed by the Matsubara frequencies for bosonic fields. In this thesis, we work at the one-loop level for the finite-temperature effective potential. Within the four-dimensional approach, this leads to the following expression for the effective potential:

$$V_{\text{eff}}(\phi, T) = V_{\text{tree}}(\phi) + V_{\text{CW}}(\phi) + V_{\text{CT}}(\phi) + V_T(\phi, T), \tag{3.19}$$

where $V_{\text{tree}}(\phi)$ is the tree-level potential, $V_{\text{CW}}(\phi)$ is the one-loop Coleman–Weinberg contribution [209], $V_{\text{CT}}(\phi)$ is the counterterm to renormalize the $V_{\text{CW}}(\phi)$ term and it's definition depends on the renormalisation scheme choice. And finally $V_T(\phi, T)$ denotes the finite-temperature correction.

Modes with non-zero Matsubara frequencies, $\omega_n \neq 0$, have typical energies of order πT and are referred to as hard modes. Their contribution to the effective potential is perturbative and is captured by the one-loop thermal functions.

The bosonic zero Matsubara modes, $\omega_0 = 0$, correspond to soft modes with characteristic momenta of order gT or smaller. When the field-dependent bosonic masses become small, these modes generate infrared divergences in perturbation theory. In particular, higher-order daisy (ring) diagrams scale as

$$V_{\text{daisy}}^{(L)} \sim g^{2L-2}T^4\,, \tag{3.20}$$

where L is the loop order of the diagram. These contributions become parametrically of the same order as the one-loop term, signaling a breakdown of naive perturbation theory.

To cure it, the contribution of the soft bosonic modes is reorganized by resumming thermal self-energy insertions in the propagators. Thermal resummation is commonly implemented by dressing bosonic propagators with leading thermal self-energies (Debye masses) $\Pi_b(T) \sim g^2T^2$. Basically we are dressing the bosonic mass to avoid the IR divergence. There are different ways of dressing the mass and of introducing it in the potential, which correspond to different resummation schemes.

In the Parwani scheme [210], one performs the replacement of the bosonic zero-modes

$$m_b^2(\phi) \;\longrightarrow\; m_{b,\text{eff}}^2(\phi,T) \equiv m_b^2(\phi) + \Pi_b(T) \tag{3.21}$$

everywhere in the one-loop effective potential, i.e. both in the Coleman–Weinberg and thermal pieces. Schematically,

$$V_{\text{eff}}(\phi,T)\Big|_{\text{Parwani}} = V_{\text{CW}}\big(m^2 \to m_{\text{eff}}^2\big) + V_T\big(m^2 \to m_{\text{eff}}^2\big)\ . \tag{3.22}$$

This cures the leading IR divergences, but it also introduces a partial resummation of higher-loop effects in all thermal and zero-temperature terms. As a result, Parwani dressing typically mixes perturbative orders and may induce overcounting, since higher-order contributions are included without consistently adding the corresponding higher-loop diagrams and counterterms [211].

In the Arnold–Espinosa (AE) scheme [211], one resums only the IR-sensitive part associated with the bosonic zero modes, which are the mass cubic terms $m_b^3(\phi)$. In practice, this corresponds to substitute the tree level mass in the cubic terms by the dressed mass o to keeping the standard one-loop potential with tree-level masses and adding a term that counteracts the cubic terms which is know as daisy or ring contribution.

$$V_{\text{eff}}(\phi,T)\Big|_{\text{AE}} = V_{\text{tree}}(\phi) + V_{\text{CW}}(\phi) + V_T(\phi,T) + V_{\text{daisy}}(\phi,T)\,, \tag{3.23}$$

with

$$V_{\text{daisy}}(\phi,T) = -\frac{T}{12\pi}\sum_b n_b\left[\big(m_b^2(\phi)+\Pi_b(T)\big)^{3/2} - \big(m_b^2(\phi)\big)^{3/2}\right], \tag{3.24}$$

where the sum runs over bosonic degrees of freedom (typically including longitudinal gauge modes and scalars) and n_b are their multiplicities [211, 212]. Eq. (3.24) is precisely the resummation of the daisy diagrams that correct the cubic bosonic term responsible for the leading IR divergences.

The AE scheme is often more convenient for phenomenological studies at fixed perturbative order because it preserves the loop counting more transparently: only the subset of diagrams that is parametrically enhanced in the IR is resummed, while the remaining contributions are kept at the intended loop order [211]. In contrast, Parwani dressing effectively resums parts of higher-loop contributions in a non-uniform way across the potential, which can complicate comparisons between different truncations (e.g. when adding explicit two-loop corrections) and may lead to scheme-dependent shifts in the phase transition properties. For these reasons, the AE (daisy-improved) potential is a standard default choice in many modern analyses and reviews [48, 213–215].

Three-dimensional effective field theory approach

Dimensional reduction (DR) provides a systematic way of exploiting the thermal scale hierarchy by constructing a sequence of effective theories for the static ($\omega_n = 0$) sector [216–220]. At high temperature, bosonic theories exhibit the parametric separation

$$\pi T \gg gT \gg g^2 T, \tag{3.25}$$

where πT is the hard scale set by non-zero Matsubara modes, gT is the so-called electric (Debye) scale, and g^2T is the so-called magnetic scale (non-perturbative in non-Abelian gauge sectors).

The first step in DR is to integrate out the hard modes, i.e. all non-zero Matsubara frequencies $\omega_n \neq 0$ (and typically also heavy fermionic modes which have no zero mode). This is performed perturbatively by matching static ($\omega_n = 0$) n-point functions (or the static 1PI effective action) between the full four-dimensional theory and a three-dimensional EFT [218, 219]. The resulting three-dimensional Lagrangian contains only bosonic zero modes and has temperature-dependent parameters:

$$\mathscr{L}_{\rm 3d} = \frac{1}{4}F^a_{ij}F^a_{ij} + \frac{1}{2}(D_i\Phi)^\dagger(D_i\Phi) + \frac{1}{2}m_3^2(T)\,\Phi^\dagger\Phi + \lambda_3(T)(\Phi^\dagger\Phi)^2 + \cdots, \tag{3.26}$$

where the ellipsis denotes higher-dimensional operators suppressed by powers of $1/(\pi T)$, and additional fields (e.g. extra scalars) are included as required by the underlying BSM model.

The matching yields explicit power counting for the 3D parameters. For instance, for a generic weakly-coupled theory one finds parametrically

$$g_3^2 \sim g^2 T, \qquad m_3^2(T) \sim g^2 T^2, \qquad \lambda_3(T) \sim \lambda\, T, \tag{3.27}$$

where λ is an arbitrary 4-dimensional coupling and with analogous relations for additional scalar self-couplings and portal couplings. In gauge theories one must also treat the temporal gauge field components A_0^a (which *do* have a bosonic zero mode): after integrating out hard modes, A_0^a becomes an adjoint scalar with a Debye mass $m_D^2 \sim g^2T^2$ in the intermediate 3D theory [218–220]. If one integrates out this electric scale, one obtains a purely magnetostatic 3D gauge theory at the g^2T scale, which is intrinsically non-perturbative in non-Abelian sectors.

The key point for phase-transition studies is that the infrared-sensitive bosonic zero modes are treated *within* the three-dimensional theory, while the hard sector has been integrated out consistently in perturbation theory. In particular, the thermal mass corrections that are introduced by hand in 4D resummation schemes arise automatically through the

matching, i.e. the 3D mass parameters are thermal masses by construction. Therefore, the resummation of daisy diagrams is not an additional prescription but a consequence of the EFT construction, which reorganizes the perturbative expansion in a gauge-consistent manner at the order of matching [49, 196, 218, 219].

Within the DR framework, the thermodynamics relevant for the phase transition (e.g. the effective potential or, more generally, the free energy difference between phases) is computed in the 3D EFT. This separates the treatment of hard and soft physics and improves perturbative control over the IR sector. The main limitation is that DR relies on a high-temperature expansion when matching the hard modes; consequently, the accuracy may deteriorate if some BSM degrees of freedom have masses comparable to or larger than πT in the temperature range of interest, enhancing the impact of higher-dimensional operators neglected in the truncated 3D EFT [49, 196, 220]. This can for example happen in the 2HDM or the RxSM which are studied later in this thesis in this kind of scenario where the models have heavier scales.

3.3.2 Electroweak Phase Transition dynamics

Once we have defined the temperature dependent effective potential we can use it to understand the electroweak phase transition of our specific model. As has been discussed before, we are interested in the realization of a FOEWPT to fulfil the third Sakharov condition. However, FOEWPTs by themselves are not sufficient to explain the origin of the BAU — they must be a strong FOEWPT (SFOEWPT). We consider a FOEWPT to be strong if the suppression of the sphaleron transitions [158] in the broken-phase vacuum is large enough to avoid the wash-out of the generated baryon asymmetry

$$\Gamma_{sph}(v_n, T_n) < H(T_n), \tag{3.28}$$

this leads to the following condition

$$\xi_n \equiv \frac{v_n}{T_n} \gtrsim 1, \tag{3.29}$$

where $v_n \equiv v(T_n)$. Thus, the first step to determine whether we have an SFOEWPT is to compute T_n, which is the temperature at which the tunnelling decay rate from the false to the EW minima per Hubble volume matches the Hubble rate

$$\frac{\Gamma(T_n)}{H^4(T_n)} \overset{!}{=} 1\,, \tag{3.30}$$

where the tunnelling decay rate is given by [221]

$$\Gamma(T) = A(T)\, e^{-S_E(T)}\,. \tag{3.31}$$

In this expression, $A(T)$ is a temperature-dependent prefactor (discussed below) and $S_E(T)$ is the Euclidean action (expressed in terms of the Euclidean time τ),

$$S_E(T) = \int d\tau d^3x \left[\frac{1}{2}(\partial_\mu \phi)(\partial^\mu \phi) + V(\phi, \tau)\right]\,. \tag{3.32}$$

In finite-temperature field theory, the Euclidean time evolution replaces the T evolution, and there are periodic boundary conditions for this coordinate, i.e. $\tau \in [0, \frac{1}{T}]$. Thus, by

integrating over this coordinate and performing a change of variables to spatial spherical coordinates, with $\rho = \sqrt{\sum_{i\leq 3} x_i^2}$, one can obtain a three-dimensional action that is known as the bounce action [222, 223]

$$S_3(T) = 4\pi \int_0^\infty d\rho\, \rho^2 \left[\frac{1}{2} \left(\frac{d\phi}{d\rho} \right)^2 + V(\phi, T) \right] , \tag{3.33}$$

in terms of which the tunnelling decay rate is expressed as

$$\Gamma(T) = A(T)\, e^{-S_3(T)/T} . \tag{3.34}$$

In this equation, the prefactor $A(T)$ can be computed, following Ref. [224], as

$$A(T) = T^4 \left(\frac{S_3(T)}{2\pi T} \right)^{3/2} . \tag{3.35}$$

Imposing that, far from the true vacuum bubble, the false vacuum remains unaffected by the phase transition, and that the transition occurs at $\rho = 0$ as boundary conditions to solve the equations of motion of the bounce action, one can find the bounce solution for the fields ϕ_B, which describes a bubble of the true vacuum nucleating and expanding within the false vacuum.

With the computed bounce solution one can calculate the transition rate for different temperatures and thereby determine the nucleation temperature. The problem is that one has to trace the real and the false vacua for different temperatures because the potential is a thermodynamic quantity, and so are the minima obtained by solving the equations of motion. Since this cannot be done analytically, one resorts to use numerical methods to solve the bounce action each time.

The idea is to compute the different vacua for each temperature, then compute the tunnelling rates and check the nucleation condition. Doing this by hand is really an impossible task therefore there have been different efforts from the community to create codes that allow to do this in an automatic way. Some of these codes are public such as `CosmoTransitions` [225] or `BSMPT` [83, 85, 91]. In this thesis we have used the public tool `BSMPTv3` [91]. In comparison to earlier versions [83,85], `v3` additionally allows the computation of the background spectrum of stochastic GWs produced during the SFOEWPT and features improved numerical stability.

3.3.3 Stochastic GW background

The nucleation of the bubbles during a SFOEWPT would have been a very violent event in the early Universe, giving rise to a stochastic background of primordial GWs that could potentially be detectable nowadays. In this section we briefly review the computation of the spectrum of GWs created during the SFOEWPT and verify whether it would be observable in a future GW observatory, such as the space-based GW interferometer LISA [48, 143]. However, since GWs are a macroscopic phenomenon, the first step is to characterize the phase transition dynamics at the thermodynamical level [46].

There are four main macroscopic parameters that characterise the GW spectrum generated during a phase transition. The first of them is the transition temperature, T_*, at which the transition takes place. In the literature, two temperatures are usually used:

the first is the nucleation temperature T_n, which was defined in the previous section. However, we use here instead the more appropriate percolation temperature T_p, which represents the temperature at which at least 29% of the Universe has tunnelled to the true vacuum. At this fraction of the false vacuum, a macroscopic cluster of true vacuum bubbles has formed, irreversibly driving the system to the true vacuum phase [226]. This choice is motivated by the nature of the phenomena that give rise to the GW background, which will be discussed below [46]. Once the transition temperature has been defined, a second parameter, α, measures the strength of the phase transition,

$$\alpha = \frac{30}{g_* \pi^2 T_*^4} \left[V(\phi_f) - V(\phi_t) - \frac{T}{4} \left(\frac{\partial V(\phi_f)}{\partial T} - \frac{\partial V(\phi_t)}{\partial T} \right) \right]_{T=T_*} , \tag{3.36}$$

where g_* is the effective number of relativistic degrees of freedom and is a function of T and ϕ_t and ϕ_f are the true and false phases respectively (the false phase being the one where the transition begins and the true phase the one where it finishes) [46, 227]. The third parameter characterizing the phase transition is the inverse duration of the phase transition in units of the Hubble rate H_* at the moment of the transition,

$$\frac{\beta}{H_*} = T_* \frac{d}{dT} \left(\frac{S_3(T)}{T} \right) \Bigg|_{T_*} . \tag{3.37}$$

In this case, H_* is the Hubble parameter in a radiation-dominated Universe, i.e.

$$H_* \equiv T_*^2 \sqrt{\frac{g_* \pi^2}{90 \widetilde{M}_{\rm Pl}^2}} , \tag{3.38}$$

where $\widetilde{M}_{\rm Pl}$ is the reduced Planck mass which is defined as $\widetilde{M}_{\rm Pl} \equiv \frac{M_{\rm Pl}}{\sqrt{8\pi}}$. Finally, the last parameter to be computed is the wall velocity, $v_{\rm w}$. There exist several approaches to compute the bubble dynamics [228–232], however, all of them suffer from large theoretical uncertainties (for a general discussion of theoretical uncertainties in studies of EWPT dynamics, see e.g. Ref. [233]) that can have a considerable impact on final results for the produced GW spectrum. In several studies of SFOEWPT in models with extended Higgs sectors [114, 234, 235], the value has been shown to be typically within the range of $v_{\rm w} \in [0.2, 1]$. In this work, we will assume for the first approach that the bubble wall velocity is equal to 0.95, which is a pessimistic choice for the observability of the GW spectrum. Later, in section 7.2.3, we will study the dependence of the observability of the GW signal on the velocity of the bubble wall.

Once the phase transition is characterized the GW spectrum can be computed. First of all there are three main sources during the SFOEWPT [46, 48] that can produce a GW signal. First, there are collisions of the bubbles: this happens when bubbles of the true vacuum nucleate and expand into the false vacuum, until they collide with each other generating GWs [236, 237]. Secondly, the dynamics of the EWPT can create pressure waves in the plasma around the bubble walls, which act like sound waves and propagate leading to a GW signal, this source is known as sound waves [238–240]. Finally, the sound waves induce magnetohydrodynamical turbulence in this plasma. The plasma is then far from equilibrium during the SFOEWPT and, similarly to how turbulence in fluids can generate waves, GWs are generated by turbulence after sound-wave decay [45, 241]. The total GW spectrum can be described as

$$h^2 \Omega_{\rm GW}(f) = h^2 \Omega_{\rm col}(f) + h^2 \Omega_{\rm SW}(f) + h^2 \Omega_{\rm turb}(f) , \tag{3.39}$$

where

$$h^2\Omega_{\rm GW}(f) \equiv \frac{h^2}{\rho_c}\frac{\partial\rho_{\rm GW}}{\partial\log f}\,, \tag{3.40}$$

$\rho_{\rm GW}$ being the energy density of the stochastic background of GWs, h the reduced Hubble constant, and f denotes the frequency of the GWs [242].

To understand which contribution is more relevant for the total spectrum we need to know if we have runaway bubble walls. There are different criteria to determine if a benchmark point exhibits runaway bubble wall like the Bödecker-Moore criterion [243] or [244]. In the scenarios studied in this thesis we did not find runaway bubble walls. Therefore, the energy stored in the scalar field is negligible and the main sources of gravitational waves are related to the fluid dynamics, namely sound waves and plasma turbulence. On the other hand, for these scenarios, collisions can be neglected in $\Omega_{\rm GW}$.

We can express the spectrum of each type of source in terms of its peak amplitude (Ω^{peak}) and peak frequency (f^{peak}), which leads to the following expression for the total GW spectrum [46, 48, 91],

$$\begin{aligned} h^2\Omega_{\rm GW}(f) \approx\; & h^2\Omega_{\rm SW}^{\rm peak}\left(\frac{4}{7}\right)^{-\frac{7}{2}}\left(\frac{f}{f_{\rm SW}^{\rm peak}}\right)^3\left[1+\frac{3}{4}\left(\frac{f}{f_{\rm SW}^{\rm peak}}\right)^2\right]^{-\frac{7}{2}} \\ & + h^2\Omega_{\rm turb}^{\rm peak}\left(\frac{(f/f_{\rm turb}^{\rm peak})^3}{(1+f/f_{\rm turb}^{\rm peak})^{11/3}(1+8\pi f/H_*)}\right), \end{aligned} \tag{3.41}$$

where the first and second terms correspond to the contributions from sound waves and magnetohydrodynamic turbulence, respectively [48, 239, 240].

The peak amplitudes are given by [46, 48],

$$h^2\Omega_{\rm SW}^{\rm peak} = 2.65\times10^{-6}\left(\frac{H_*}{\beta}\right)\left(\frac{\kappa_{\rm sw}\alpha}{1+\alpha}\right)^2\left(\frac{100}{g_*}\right)^{1/3} v_w, \tag{3.42}$$

$$h^2\Omega_{\rm turb}^{\rm peak} = 3.35\times10^{-4}\left(\frac{H_*}{\beta}\right)\left(\frac{\kappa_{\rm turb}\alpha}{1+\alpha}\right)^{3/2}\left(\frac{100}{g_*}\right)^{1/3} v_w, \tag{3.43}$$

where H_* is the Hubble parameter at the time of GW production, β^{-1} characterizes the duration of the phase transition, g_* is the effective number of relativistic degrees of freedom, and v_w is the bubble wall velocity.

The peak frequencies redshifted to today are given by [46, 48],

$$f_{\rm SW}^{\rm peak} = 1.9\times10^{-5}\,{\rm Hz}\,\frac{1}{v_w}\left(\frac{\beta}{H_*}\right)\left(\frac{T_*}{100\,{\rm GeV}}\right)\left(\frac{g_*}{100}\right)^{1/6}, \tag{3.44}$$

$$f_{\rm turb}^{\rm peak} = 2.7\times10^{-5}\,{\rm Hz}\,\frac{1}{v_w}\left(\frac{\beta}{H_*}\right)\left(\frac{T_*}{100\,{\rm GeV}}\right)\left(\frac{g_*}{100}\right)^{1/6}, \tag{3.45}$$

where T_* denotes the temperature at which the GWs are predominantly generated (typically close to the percolation temperature).

The efficiency factors κ_i in eq. (3.43) quantify the fraction of the released vacuum energy that is converted into a given source of gravitational waves. For non-runaway walls, the

dominant channel is sound waves, with efficiency [48, 227]

$$\kappa_{\rm sw} \simeq \frac{\alpha}{0.73 + 0.083\sqrt{\alpha} + \alpha}. \tag{3.46}$$

The turbulence efficiency factor is commonly taken as a fixed fraction of the sound-wave efficiency [46, 48],

$$\kappa_{\rm turb} \simeq \epsilon\, \kappa_{\rm sw}, \qquad \epsilon \simeq 0.05\text{–}0.1, \tag{3.47}$$

reflecting the partial conversion of bulk fluid motion into turbulent flows.

Observability of GWs

After having derived the power spectrum of the GW background, we can compare it with the sensitivity of different planned GW observatories to test if this signal could be detected. If we check the characteristic frequency range of the potential signals coming from a SFOEWPT, they lie within the frequency range of the future GW observatory LISA. Therefore, in this work, we have focused on this observatory. To determine whether the signal is observable, we compare the power spectrum of the signal with the sensitivity of LISA. To do so, we define a signal-to-noise ratio (SNR) following Ref. [48],

$$\mathrm{SNR} = \sqrt{\tau \int_{f_{\rm min}}^{f_{\rm max}} df \left[\frac{h^2\Omega_{\rm GW}(f)}{h^2\Omega_{\rm sens}(f)}\right]^2}, \tag{3.48}$$

where τ is the data-taking time of LISA and $h^2\Omega_{\rm sens}$ [48] is the nominal sensitivity of LISA to stochastic sources like phase transitions. Throughout this work, we have made the conservative assumption of a data-taking period of three years.

Chapter 4

Extended Higgs sectors

Sé bueno.

– Aita

In the previous chapters, we have outlined the two main theoretical pillars that motivate the present work. On the one hand, we reviewed the current status of particle physics and emphasised that, despite its extraordinary experimental success, the SM cannot be regarded as a complete description of fundamental interactions. In particular, it does not provide a satisfactory explanation for the origin of the baryon asymmetry of the Universe. On the other hand, we discussed the thermal history of the early Universe and showed that cosmology offers a natural arena in which such shortcomings become especially relevant.

These considerations motivate the study of simple extensions of the scalar sector of the SM. Extended Higgs sectors provide a particularly well-motivated and economical framework in which to investigate whether new scalar degrees of freedom can modify the electroweak phase transition, enhance Higgs self-interactions, and open new phenomenological scenarios at colliders. From this perspective, they constitute a natural class of models with which to explore possible solutions to the problems discussed in the previous chapters, while remaining close enough to the SM to allow for precise and testable predictions.

In this chapter we focus on two representative and widely studied examples: the real singlet extension of the SM and the Two Higgs Doublet Model. These models illustrate two different ways of enlarging the Higgs sector. The former extends the scalar content through an additional gauge-singlet degree of freedom, while the latter introduces a second electroweak doublet, leading to a richer spectrum and interaction structure. Despite their relative simplicity, both frameworks can give rise to sizeable modifications of the scalar potential, non-trivial vacuum structures, and strong departures from the SM expectations for Higgs self-couplings and finite-temperature dynamics.

A further reason why these models are particularly relevant for this thesis is that the observables of interest are not controlled exclusively by tree-level effects. In extended scalar sectors, loop corrections can be numerically important and, in some regions of parameter space, even qualitatively alter the predictions obtained at leading order. This is especially true for trilinear Higgs couplings and for the effective potential governing the phase transition. A consistent analysis therefore requires not only a definition of

the models and their allowed parameter space, but also a careful treatment of radiative corrections and renormalisation.

First, we introduce the structure of the extended Higgs sectors that will be studied throughout this thesis, together with the main theoretical consistency conditions and experimental constraints that shape their viable parameter space. Second, we present the loop framework that will later be used to compute radiative corrections to scalar self-couplings, both from the effective-potential and diagrammatic points of view. This will provide the theoretical basis for the phenomenological and cosmological analyses developed in the following chapters.

4.1 The Real Singlet extension of the Standard Model

4.1.1 The model

The real singlet extension of the SM is one of the simplest extensions of the SM that can be constructed, and it has several different versions. In this thesis, it is consider the most general real singlet extension of the SM, which is denoted as RxSM [23,107,108,245,246]. This model adds a real singlet S to the Higgs sector of the SM, and unlike other singlet extension variants (like the $\mathbb{Z}_2$ symmetric version or the one with a spontaneously broken $\mathbb{Z}_2$ symmetry), does not contain any $\mathbb{Z}_2$ symmetry of the Lagrangian. After EWSB, the SM-like doublet Φ and the singlet S can be expanded as

$$\Phi = \frac{1}{\sqrt{2}} \begin{pmatrix} \sqrt{2}G^+ \\ v + \phi + iG^0 \end{pmatrix}, \qquad S = s + v_S, \tag{4.1}$$

where s is the new scalar field and v_S is the singlet vev, while ϕ is the CP-even component of the doublet, G^0 ($G^\pm$) is the neutral (charged) would-be Goldstone boson, and v is the EW (or SM) vev. The scalar potential of the RxSM reads, at the tree level,

$$V(\Phi, S) = \mu^2(\Phi^\dagger\Phi) + \frac{\lambda}{2}(\Phi^\dagger\Phi)^2 + \kappa_{SH}(\Phi^\dagger\Phi)S + \frac{\lambda_{SH}}{2}(\Phi^\dagger\Phi)S^2 + \frac{M_S^2}{2}S^2 + \frac{\kappa_S}{3}S^3 + \frac{\lambda_S}{2}S^4. \tag{4.2}$$

Since no $\mathbb{Z}_2$ symmetry has been imposed on the model, there would in principle be terms linear and cubic in the singlet field. However, the RxSM offers the freedom to redefine the singlet vev v_S to absorb one of these terms [40], which has been used here to remove the linear (tadpole) term. Furthermore, since the singlet S is real, CP-violation cannot be included in the scalar potential of the RxSM (like in the case for the SM), so that all the parameters in eq. (4.2) are real.

Taking into account the two mass parameters and five couplings in the Lagrangian, as well as the vevs of the doublet and the singlet, the model contains nine free parameters, without taking into account the measurement of the 125 GeV Higgs boson and it's width. This number can be reduced to seven using the minimisation conditions of the potential (i.e. the tadpole equations),

$$\left.\frac{\partial V}{\partial \phi}\right|_{\phi=0,s=0} = t_\phi = 0, \qquad \left.\frac{\partial V}{\partial s}\right|_{\phi=0,s=0} = t_S = 0, \tag{4.3}$$

which lead to two relations among the Lagrangian parameters

$$\begin{aligned}\mu^2 &= -\frac{\lambda v^2}{2} - \kappa_{SH} v_S - \frac{\lambda_{SH} v_S^2}{2} + \frac{t_\phi}{v}\,,\\ M_S^2 &= -2\lambda_S v_S^2 - \kappa_S v_S - \frac{\kappa_{SH} v^2}{2 v_S} - \frac{\lambda_{SH} v^2}{2} + \frac{t_S}{v_S}\,.\end{aligned} \tag{4.4}$$

Next, expanding the potential using the definitions from eq. (4.1), the mass matrix can be computed as

$$\mathscr{M}^2 = \begin{pmatrix} \frac{\partial^2 V}{\partial \phi^2} & \frac{\partial^2 V}{\partial \phi \partial s} \\ \frac{\partial^2 V}{\partial \phi \partial s} & \frac{\partial^2 V}{\partial s^2} \end{pmatrix} = \begin{pmatrix} \mathscr{M}_\phi^2 & \mathscr{M}_{\phi s}^2 \\ \mathscr{M}_{\phi s}^2 & \mathscr{M}_s^2 \end{pmatrix}, \tag{4.5}$$

where

$$\begin{aligned}\mathscr{M}_\phi^2 &= \mu^2 + \frac{3\lambda v^2}{2} + \kappa_{SH} v_S + \frac{\lambda_{SH} v_S^2}{2}\,,\\ \mathscr{M}_s^2 &= M_S^2 + \frac{\lambda_{SH} v^2}{2} + 2 v_S(\kappa_S + 3\lambda_S v_S)\,,\\ \mathscr{M}_{\phi s}^2 &= (\kappa_{SH} + \lambda_{SH} v_S) v\,.\end{aligned} \tag{4.6}$$

The CP-even gauge eigenstates can be rewritten in terms of mass eigenstates h and H through a mixing matrix R_α, defined by,

$$\begin{pmatrix} \phi \\ s \end{pmatrix} = R_\alpha \begin{pmatrix} h \\ H \end{pmatrix} = \begin{pmatrix} \cos\alpha & -\sin\alpha \\ \sin\alpha & \cos\alpha \end{pmatrix} \begin{pmatrix} h \\ H \end{pmatrix}. \tag{4.7}$$

For the rest of this thesis, it will assumed that h corresponds to the detected Higgs boson with a mass around 125 GeV, while H is a BSM Higgs boson, assumed to be always heavier than h, as we want to allow the decay $H \to hh$ in the studies in chapters 5, 6, 7 and 8. After the diagonalisation of the mass matrix, the CP-even scalar mass eigenvalues and corresponding mixing angle α are found to be

$$\begin{aligned} m_h^2 &= \mathscr{M}_\phi^2 \cos^2\alpha + \mathscr{M}_s^2 \sin^2\alpha + \mathscr{M}_{\phi s}^2 \sin 2\alpha\,,\\ m_H^2 &= \mathscr{M}_\phi^2 \sin^2\alpha + \mathscr{M}_s^2 \cos^2\alpha - \mathscr{M}_{\phi s}^2 \sin 2\alpha\,,\\ \tan 2\alpha &= \frac{2\mathscr{M}_{\phi s}^2}{\mathscr{M}_\phi^2 - \mathscr{M}_s^2}\,.\end{aligned} \tag{4.8}$$

For the renormalisation of the RxSM Higgs sector, it is especially helpful to employ quantities defined in terms of the following nine parameters if we also consider the tadpole parameters

$$m_h^2,\, m_H^2,\, \alpha,\, v,\, v_S,\, \kappa_S,\, \kappa_{SH}, t_\phi, t_s, \tag{4.9}$$

which we will refer to as "*mass basis*". Among these parameters, $m_h \simeq 125$ GeV and $v \simeq 246$ GeV, are fixed, i.e., one is left with five free BSM parameters.

Therefore, the Lagrangian mass parameters and quartic couplings can be reexpressed in terms of m_h, m_H, α, and the tadpole parameters t_ϕ and t_S. While $t_\phi = t_S = 0$ in the minimum of the potential, it is useful to keep the dependence on these parameters

for the sake of properly including tadpole counterterms in our radiative calculations, see section 6.1. It is found

$$\begin{aligned}
\lambda &= \frac{c_\alpha^2 m_h^2 + s_\alpha^2 m_H^2}{v^2} - \frac{t_\phi}{v^3}\,, \\
\lambda_{SH} &= \frac{(m_h^2 - m_H^2)c_\alpha s_\alpha}{v v_S} - \frac{\kappa_{SH}}{v_S}\,, \\
\lambda_S &= \frac{(m_h^2 + m_H^2)v_S + (m_H^2 - m_h^2)v_S c_{2\alpha} - 2t_S - 2\kappa_S v_S^2 + \kappa_{SH} v^2}{8 v_S^3}\,, \\
M_S^2 &= \frac{6t_S - \kappa_{SH} v^2 - 2\kappa_S v_S^2 - (m_h^2 + m_H^2)v_S + (m_H^2 - m_h^2)(v s_{2\alpha} - v_S c_{2\alpha})}{4 v_S}\,, \\
\mu^2 &= \frac{3}{2}\frac{t_\phi}{v} - \frac{1}{2}\kappa_{SH} v_S - \frac{1}{2}\big(m_h^2 c_\alpha^2 + m_H^2 s_\alpha^2\big) - \frac{v_S}{2v}\big(m_h^2 - m_H^2\big)c_\alpha s_\alpha\,,
\end{aligned} \tag{4.10}$$

where the shorthand notations $c_x \equiv \cos x$ and $s_x \equiv \sin x$.

Finally, using the relations of eq. (4.10), the following expressions can be obtained at the tree level for the trilinear Higgs couplings in the mass basis (keeping once again the parametric dependence on the tadpoles),

$$\begin{aligned}
\lambda_{hhh} = \frac{1}{4v^2 v_S^2}\Big\{ & -3v_S\left[\kappa_{SH} v^3 + 3(t_\phi - m_h^2 v)v_S\right] c_\alpha + 3v_S\left[\kappa_{SH} v^3 - t_\phi v_S + m_h^2 v v_S\right] c_{3\alpha} \\
& + 2v^2\left[-6t_S + 3\kappa_{SH} v^2 + 6m_h^2 v_S - 2\kappa_S v_S^2\right] s_\alpha^3 \Big\}\,, \\
\lambda_{hhH} = \frac{1}{4v^2 v_S^2} s_\alpha \Big\{ & -2v_S\left[\kappa_{SH} v^3 - 3t_\phi v_S + (2m_h^2 + m_H^2)v v_S\right] \\
& - 2v_S[3\kappa_{SH} v^3 - 3t_\phi v_S + (2m_h^2 + m_H^2)v v_S]c_{2\alpha} \\
& + v^2\left[-6t_S + 3\kappa_{SH} v^2 + 2v_S\left(2m_h^2 + m_H^2 - \kappa_S v_S\right)\right] s_{2\alpha} \Big\}\,, \\
\lambda_{hHH} = \frac{1}{4v^2 v_S^2} c_\alpha \Big\{ & 2v_S\left[\kappa_{SH} v^3 - 3t_\phi v_S + (m_h^2 + 2m_H^2)v v_S\right] \\
& - 2v_S[3\kappa_{SH} v^3 - 3t_\phi v_S + (m_h^2 + 2m_H^2)v v_S]c_{2\alpha} \\
& + v^2\left[-6t_S + 3\kappa_{SH} v^2 + 2v_S\left(m_h^2 + 2m_H^2 - \kappa_S v_S\right)\right] s_{2\alpha} \Big\}\,, \\
\lambda_{HHH} = \frac{1}{8v^2 v_S^2} \Big\{ & 3v^2\left[-6t_S + 3\kappa_{SH} v^2 + 6m_H^2 v_S - 2\kappa_S v_S^2\right] c_\alpha \\
& + v^2[-6t_S + 3\kappa_{SH} v^2 + 6m_H^2 v_S - 2\kappa_S v_S^2]c_{3\alpha} \\
& + 12v_S\left[\kappa_{SH} v^3 + t_\phi v_S - m_H^2 v v_S + \left(\kappa_{SH} v^3 - t_\phi v_S + m_H^2 v v_S\right) c_{2\alpha}\right] s_\alpha \Big\}\,.
\end{aligned} \tag{4.11}$$

4.1.2 Theoretical and experimental constraints

This section briefly summarizes the various theoretical and experimental constraints on the RxSM that have to be considered in its analysis. It should be noted that constraints arising from di-Higgs measurements at the LHC are not mentioned at this stage, but are instead a central part of the later phenomenological investigations in section 6.3.

Boundedness from below and vacuum stability.

First, on the theoretical side, it has to be ensured that boundedness-from-below of the potential is fulfilled. For the scalar potential to be bounded from below, the quartic

couplings must be positive in all field directions. To ensure this, one has to demand that the determinant of the Hessian matrix of the potential is positive, which leads to

$$\lambda > 0, \quad \lambda_S > 0, \quad \text{and} \quad \lambda_{SH} > -2\sqrt{\lambda\,\lambda_S}\,. \tag{4.12}$$

These boundedness-from-below conditions are necessary to avoid runaway directions at large field values. However, they are not sufficient to guarantee that the electroweak vacuum is the global minimum: additional (deeper) minima can exist, in which case the EW one may be only metastable. The issue of metastability is already present in the SM, where the running Higgs quartic can become negative at high scales. State-of-the-art analyses of SM vacuum stability and its RG improvement can be found in [106, 177, 247–250]. In models with extended scalar sectors, analogous considerations apply, and vacuum metastability can provide additional bounds that are complementary to collider constraints. A conservative practical criterion is to require that the electroweak vacuum is either the global minimum or sufficiently long-lived on cosmological timescales. In semiclassical tunnelling, the vacuum decay probability is controlled by the bounce action [251], and metastability requirements can be implemented by requiring that the bounce action remains above the approximate critical value used in the literature [252].

Perturbative unitarity. The S-matrix must be unitary, implying that the partial-wave amplitudes for $2 \to 2$ scattering processes remain within the perturbative regime. A classic illustration is longitudinal gauge-boson scattering in the SM, which yields an upper bound on the Higgs mass from unitarity considerations [253, 254]. To ensure perturbative unitarity in the RxSM, one can compute the scalar $2 \to 2$ scattering amplitude matrix in the high-energy limit, using results from [255], and demand that the eigenvalues are below 1.

Perturbativity. Closely related to unitarity is the requirement that the quartic couplings remain within a range where perturbation theory is reliable. A common working criterion is to demand that all $|\lambda_i|$ are sufficiently smaller than 4π, and that loop-corrected observables do not exhibit signs of a breakdown of the perturbative expansion. To ensure it, we require that [23, 116]

$$\frac{\lambda}{2},\ \frac{\lambda_S}{2},\ \frac{|\lambda_{SH}|}{2} < 4\pi. \tag{4.13}$$

Experimental measurements. Finally, one has to check compatibility with experimental measurements. To do so, it has to be considered on the one hand constraints from direct Higgs-boson searches at colliders. The exclusion limits at the 95% C.L. of all relevant BSM Higgs boson searches (including Run 2 data from the LHC) are included in the public code `HiggsBounds v.6` [256–261], which is included in the public code `HiggsTools` [261]. For a parameter point in a particular model, `HiggsBounds` determines on the basis of expected limits which is the most sensitive channel to test each BSM Higgs boson. Then, based on this most sensitive channel, `HiggsBounds` determines whether the point is allowed or not at the 95% CL. As input `HiggsBounds` requires some specific predictions from the model, like branching ratios or Higgs-boson couplings.

Any model beyond the SM has to accommodate a Higgs boson with mass and signal strengths as they were measured at the LHC. For the parameter points used, the compatibility of the CP-even scalar h with a mass of 125.09 GeV with the measurements of

signal strengths at the LHC is tested with the code `HiggsSignals v.3` [261–264], which is included in the code `HiggsTools`. The code provides a statistical χ^2 for the h_{125} predictions of a given model in comparison to the measurements of the Higgs-boson signal rates and masses from the LHC. Specifically, we demand that $\chi^2_{h_{125},RxSM} - \chi^2_{h_{125},SM} < 6.3$ (with $\chi^2_{h_{125},SM} = 159.7$).

4.2 The Two Higgs Doublet model

4.2.1 The model

The Two Higgs Doublet Model (2HDM) is one of the most widely studied extensions of the SM scalar sector. It enlarges the field content of the SM by adding a second complex scalar doublet under $SU(2)_L$ with hypercharge $Y = 1$, so that the scalar sector contains two doublets Φ_1 and Φ_2. After EWSB, three degrees of freedom are eaten by the gauge bosons and five physical scalar states remain: two neutral CP-even scalars h and H, one neutral CP-odd scalar A, and a charged pair $H^\pm$. Throughout this thesis we adopt the convention $m_h < m_H$ and identify h with the observed Higgs boson at $m_h \simeq 125$ GeV.

The most general renormalisable 2HDM contains many parameters and, if both doublets couple to the same fermion species, it generically induces flavour-changing neutral currents (FCNCs) at tree level. This is a large problem since FCNC are severely constrained experimentally [132, 265]. A standard way to forbid tree-level FCNCs is to impose a discrete $\mathbb{Z}_2$ symmetry such that each fermion type couples to only one of the doublets (the Paschos–Glashow–Weinberg condition) [266, 267]. A convenient choice is

$$\Phi_1 \to \Phi_1, \qquad \Phi_2 \to -\Phi_2, \tag{4.14}$$

which can be softly broken by a dimension-two term like $m_{12}^2\,(\Phi_1^\dagger\Phi_2 + \Phi_2^\dagger\Phi_1)$. Depending on the $\mathbb{Z}_2$ charge assignments of the fermions, four Yukawa types (Type I, II, lepton-specific/Type III, and flipped/Type IV) arise; we adopt the common convention in which Φ_2 couples to up-type quarks.

This section is focused on the CP-conserving 2HDM, where all parameters in the scalar potential are taken real [131–133, 268]. The most general tree-level renormalisable $\mathbb{Z}_2$-symmetric potential with soft breaking is:

$$\begin{aligned} V \;=\; & m_{11}^2\,(\Phi_1^\dagger\Phi_1) + m_{22}^2\,(\Phi_2^\dagger\Phi_2) - m_{12}^2\,(\Phi_1^\dagger\Phi_2 + \Phi_2^\dagger\Phi_1) + \frac{\lambda_1}{2}(\Phi_1^\dagger\Phi_1)^2 + \frac{\lambda_2}{2}(\Phi_2^\dagger\Phi_2)^2 \\ & + \lambda_3(\Phi_1^\dagger\Phi_1)(\Phi_2^\dagger\Phi_2) + \lambda_4(\Phi_1^\dagger\Phi_2)(\Phi_2^\dagger\Phi_1) + \frac{\lambda_5}{2}\Big[(\Phi_1^\dagger\Phi_2)^2 + (\Phi_2^\dagger\Phi_1)^2\Big]. \end{aligned} \tag{4.15}$$

After EWSB the doublets can be parametrised as

$$\Phi_1 = \begin{pmatrix} \phi_1^+ \\ \frac{1}{\sqrt{2}}\,(v_1 + \rho_1 + i\eta_1) \end{pmatrix}, \qquad \Phi_2 = \begin{pmatrix} \phi_2^+ \\ \frac{1}{\sqrt{2}}\,(v_2 + \rho_2 + i\eta_2) \end{pmatrix}, \tag{4.16}$$

with vevs v_1 and v_2 satisfying

$$v^2 \equiv v_1^2 + v_2^2 \simeq (246\ \text{GeV})^2, \qquad \tan\beta \equiv t_\beta \equiv \frac{v_2}{v_1}. \tag{4.17}$$

The gauge eigenstates mix to define the mass eigenstates. In the neutral CP-even sector to define the mass eigenstates one introduces a mixing angle α,

$$\begin{pmatrix}\rho_1\\ \rho_2\end{pmatrix} = \begin{pmatrix}\cos\alpha & -\sin\alpha\\ \sin\alpha & \cos\alpha\end{pmatrix}\begin{pmatrix}H\\ h\end{pmatrix}, \tag{4.18}$$

while in the CP-odd and charged sectors the rotation is defined by β,

$$\begin{pmatrix}\eta_1\\ \eta_2\end{pmatrix} = \begin{pmatrix}\cos\beta & -\sin\beta\\ \sin\beta & \cos\beta\end{pmatrix}\begin{pmatrix}G^0\\ A\end{pmatrix}, \qquad \begin{pmatrix}\phi_1^\pm\\ \phi_2^\pm\end{pmatrix} = \begin{pmatrix}\cos\beta & -\sin\beta\\ \sin\beta & \cos\beta\end{pmatrix}\begin{pmatrix}G^\pm\\ H^\pm\end{pmatrix}, \tag{4.19}$$

where G^0 and $G^\pm$ are the would-be Goldstone bosons. It is often convenient to use

$$s_x \equiv \sin x, \qquad c_x \equiv \cos x, \qquad s_{\beta-\alpha} \equiv \sin(\beta-\alpha), \qquad c_{\beta-\alpha} \equiv \cos(\beta-\alpha). \tag{4.20}$$

The minimisation of the tree-level potential fixes two combinations of parameters via the tadpole conditions. At the loop level tadpoles play an important role in renormalisation.

A convenient parameter set, known as the physical basis, is given by the masses, mixing angles, and vev,

$$c_{\beta-\alpha}, \quad t_\beta, \quad v, \quad m_h, \quad m_H, \quad m_A, \quad m_{H^\pm}, \quad m_{12}^2, \tag{4.21}$$

where $m_h, m_H, m_A, m_{H^\pm}$ denote the masses of $h, H, A, H^\pm$, respectively. The m_{12}^2 parameter is usually repleced by:

$$M^2 \equiv \frac{m_{12}^2}{s_\beta c_\beta}, \tag{4.22}$$

which is particularly useful when discussing decoupling properties.

In the 2HDM the heavy Higgs masses can be written schematically as

$$m_\varphi^2 = M^2 + \lambda_\varphi v^2 + \mathcal{O}(v^4/M^2), \qquad \varphi = H,\ A,\ H^\pm, \tag{4.23}$$

where λ_φ denotes a suitable linear combination of quartic couplings. If $M^2 \gg \lambda_\varphi v^2$, the heavy states decouple in the sense of the decoupling theorem [269] and low-energy observables approach their SM values. In contrast, if $M^2 \sim \lambda_\varphi v^2$, non-decoupling effects can occur and lead to sizeable radiative corrections even for heavy additional scalars [72]. A particularly important limit is the *alignment limit*, $c_{\beta-\alpha} \to 0$, in which the light state h has SM-like couplings [70].

The neutral Higgs couplings to fermions can be written compactly in terms of Yukawa coupling modifiers $\xi_f^{h,H,A}$,

$$\begin{aligned}\mathscr{L}_Y \;=\; &-\sum_{f=u,d,\ell}\frac{m_f}{v}\left[\xi_f^h\,\bar f f\,h + \xi_f^H\,\bar f f\,H + \xi_f^A\,\bar f\, i\gamma_5 f\,A\right]\\ &-\frac{\sqrt{2}}{v}\left[\bar u\,(\xi_d\,V_{CKM}\,m_d\,P_R)\,d\,H^+ + \xi_\ell\,\bar\nu\,m_\ell\,P_R\,\ell\,H^+ + \text{h.c.}\right],\end{aligned} \tag{4.24}$$

where V_{CKM} is the CKM matrix and $P_{R,L} = (1 \pm \gamma^5)/2$. The modifiers are given by

$$\xi_f^h = s_{\beta-\alpha} + \xi_f\,c_{\beta-\alpha}, \qquad \xi_f^H = c_{\beta-\alpha} - \xi_f\,s_{\beta-\alpha}, \qquad \xi_u^A = -i\,\xi_u, \qquad \xi_{d,\ell}^A = i\,\xi_{d,\ell}, \tag{4.25}$$

with ξ_f depending on the Yukawa type [132, 268]:

	ξ_u	ξ_d	ξ_ℓ
Type I	$\cot\beta$	$\cot\beta$	$\cot\beta$
Type II	$\cot\beta$	$-\tan\beta$	$-\tan\beta$
Type III (lepton-specific)	$\cot\beta$	$\cot\beta$	$-\tan\beta$
Type IV (flipped)	$\cot\beta$	$-\tan\beta$	$\cot\beta$

In the CP-conserving case the possible trilinear couplings can be expressed in terms of the physical parameters as:

$$\lambda_{hhh} = \frac{1}{2v^2}\left\{m_h^2 s_{\beta-\alpha}^3 + \left(3m_h^2 - 2M^2\right)c_{\beta-\alpha}^2 s_{\beta-\alpha} + 2\cot 2\beta\left(m_h^2 - M^2\right)c_{\beta-\alpha}^3\right\}, \tag{4.26}$$

$$\lambda_{hhH} = -\frac{c_{\beta-\alpha}}{2v^2}\left\{\left(2m_h^2 + m_H^2 - 4M^2\right)s_{\beta-\alpha}^2 + 2\cot 2\beta\left(2m_h^2 + m_H^2 - 3M^2\right)s_{\beta-\alpha}c_{\beta-\alpha} - \left(2m_h^2 + m_H^2 - 2M^2\right)c_{\beta-\alpha}^2\right\}, \tag{4.27}$$

$$\lambda_{hHH} = \frac{s_{\beta-\alpha}}{2v^2}\left\{s_{\beta-\alpha}\left(m_h^2 + 2m_H^2 - 2M^2\right) + 2s_{\beta-\alpha}c_{\beta-\alpha}\cot 2\beta\left(m_h^2 + 2m_H^2 - 3M^2\right)\right\}, \tag{4.28}$$

$$\lambda_{HHH} = \frac{1}{2v^2}\left\{c_{\beta-\alpha}^3 m_H^2 + s_{\beta-\alpha}^2 c_{\beta-\alpha}\left(3m_H^2 - 2M^2\right) - 2s_{\beta-\alpha}^3\cot 2\beta\left(m_H^2 - M^2\right)\right\}, \tag{4.29}$$

$$\lambda_{hAA} = \frac{1}{2v^2}\left\{s_{\beta-\alpha}\left(2m_A^2 + m_h^2 - 2M^2\right) + 2c_{\beta-\alpha}\cot 2\beta\left(m_h^2 - M^2\right)\right\}, \tag{4.30}$$

$$\lambda_{HAA} = \frac{1}{2v^2}\left\{c_{\beta-\alpha}\left(2m_A^2 + m_H^2 - 2M^2\right) - 2s_{\beta-\alpha}\cot 2\beta\left(m_H^2 - M^2\right)\right\}, \tag{4.31}$$

$$\lambda_{hH^+H^-} = \frac{1}{v^2}\left\{s_{\beta-\alpha}\left(m_h^2 + 2m_{H^\pm}^2 - 2M^2\right) + 2c_{\beta-\alpha}\cot 2\beta\left(m_h^2 - M^2\right)\right\}, \tag{4.32}$$

$$\lambda_{HH^+H^-} = \frac{1}{v^2}\left\{c_{\beta-\alpha}\left(m_H^2 + 2m_{H^\pm}^2 - 2M^2\right) - 2s_{\beta-\alpha}\cot 2\beta\left(m_H^2 - M^2\right)\right\}. \tag{4.33}$$

These couplings illustrate that, in the alignment limit, λ_{hhh} approaches its SM value while several BSM trilinear couplings remain non-zero and can therefore enter loop observables.

4.2.2 Theoretical and experimental constraints in the 2HDM

This section summarizes the set of theoretical consistency requirements and experimental bounds that define the viable parameter space of the CP-conserving 2HDM with a softly broken $\mathbb{Z}_2$ symmetry. Again di-Higgs constrains are not considered at this stage.

Boundedness from below and vacuum stability. As in the RxSM a necessary condition for a consistent scalar theory is that the potential is bounded from below (at large field values). For the CP-conserving 2HDM with a softly broken $\mathbb{Z}_2$ symmetry, this requirement translates into a set of inequalities among the quartic couplings ensuring that no field direction exists along which $V \to -\infty$. In the convention of eq. (4.15), a set of sufficient conditions is

$$\begin{aligned} \lambda_1 > 0, \qquad \lambda_2 > 0, \\ \lambda_3 > -\sqrt{\lambda_1\lambda_2}, \\ \lambda_3 + \lambda_4 - |\lambda_5| > -\sqrt{\lambda_1\lambda_2}\,. \end{aligned} \tag{4.34}$$

In the case of the 2HDM even if the potential is bounded from below, it can admit multiple extrema, including charge-breaking and CP-breaking stationary points. A phenomenologically viable parameter point must feature an electroweak vacuum with the correct pattern of symmetry breaking, and one typically imposes that this vacuum is the global minimum (or, more conservatively, that it is sufficiently long-lived).

For the 2HDM, an efficient tree-level test for whether the electroweak stationary point is the global minimum can be formulated in terms of the potential parameters; a widely used condition and its phenomenological implementation are discussed in [270].

Perturbative unitarity. For the 2HDM this yields bounds on combinations of the quartic couplings of the scalar potential, preventing the appearance of unphysically large scattering amplitudes. Widely used tree-level unitarity conditions (in the high-energy limit) can be found in [271–273] and subsequent refinements, including the role of higher-order effects [274, 275] and RG-improvement [276–278]. In numerical analyses, these constraints become particularly relevant in regions with non-decoupling effects, where heavy Higgs masses are enhanced by large quartic couplings rather than by a large soft-breaking scale.

Perturbativity. Closely related to unitarity is the requirement that the quartic couplings remain within a range where perturbation theory is reliable. A common working criterion is to demand that all quartic couplings of the 2HDM potential satisfy

$$|\lambda_i| < 4\pi, \qquad i = 1, \ldots, 5. \tag{4.35}$$

Choice of soft-breaking scale and large-$\tan\beta$ behaviour. The soft-breaking parameter m_{12}^2 (or equivalently $M^2 = m_{12}^2/(s_\beta c_\beta)$) controls decoupling properties and can have a significant impact on radiative corrections. In particular, in scenarios close to alignment and at large $\tan\beta$, an inappropriate choice of m_{12}^2 may induce very large loop corrections to Higgs self-couplings or destabilise perturbativity. These effects and their impact on λ_{hhh} at one and two loops have been studied extensively [71, 72, 93].

Electroweak precision tests and custodial symmetry. Electroweak precision tests are performed by checking the know as ρ parameter [279] which gives information about the status of the custodial symmetry since at tree level this symmetry fixes the value of ρ to the unity. The ρ parameter is defined as the ratio between the neutral and the charged currents in a model. At tree level this is commonly expressed as

$$\rho \;\equiv\; \frac{m_W^2}{m_Z^2 \cos^2\theta_W}\,, \tag{4.36}$$

whose experimental value is consistent with $\rho \simeq 1$ to very high accuracy (see, e.g., the PDG review [280]). At the loop level one would have to compute the loop improved neutral and charged currents [279]. For a general scalar sector containing n scalar multiplets ϕ_i with weak isospin I_i, hypercharge Y_i, and vacuum expectation values v_i for the neutral components, the tree-level value can be written as

$$\rho \;=\; \frac{\sum_{i=1}^{n} \left[I_i(I_i+1) - \frac{1}{4} Y_i^2 \right] v_i^2}{\sum_{i=1}^{n} \frac{1}{2} Y_i^2 \, v_i^2}\,. \tag{4.37}$$

Since the 2HDM contains only $SU(2)_L$ doublets with $I = \frac{1}{2}$ and $Y = 1$, one has $I(I+1) = \frac{3}{4}Y^2$, and therefore $\rho = 1$ holds automatically at tree level. Loop-level corrections (often described in terms of oblique parameters) can nevertheless constrain mass splittings among the additional Higgs states, as discussed below.

Beyond the tree-level statement $\rho = 1$, precision observables constrain loop-induced effects of the extended scalar spectrum. These constraints are frequently phrased in terms of the oblique parameters (S, T, U) [281,282], where T is particularly sensitive to custodial-symmetry breaking mass splittings among $(H, A, H^{\pm})$. At leading order one has $\rho - 1 \simeq \alpha_{em} T$ [281], so precision constraints on T translate directly into restrictions on scalar mass spectra. As a result, electroweak precision data often enforce approximate degeneracies such as $m_{H^{\pm}} \simeq m_A$ (or analogous relations) in sizable parts of the viable parameter space.

To ensure that the studied scenarios fulfil the EW precision measurements one can confront parameter points with the global electroweak precision fits, using as input the standard experimental determinations compiled in [280]. For the 2HDM, dedicated treatments of electroweak precision observables (including improved higher-order predictions for ρ) can be found in [283] and are useful to assess the impact of two-loop corrections in regions with sizeable scalar mass splittings.

Direct searches and Higgs signal strengths. Finally as in the RxSM the experimental constraints have to be taken into account. Collider searches for additional Higgs bosons (H, A, $H^{\pm}$) provide strong and complementary constraints, with the most relevant channels depending on the mass spectrum and Yukawa type. In addition, the observed Higgs boson at 125 GeV exhibits couplings close to the SM expectation, which constrains mixing and favours the alignment limit.

In practice, direct search limits can be tested using `HiggsBounds` [256–258, 260] and the compatibility with Higgs rate measurements using `HiggsSignals` [262–264]. Both are distributed and maintained within the unified framework `HiggsTools` [261].

4.3 Relevant limits in extended scalar sectors

Extended scalar sectors often contain several parametric regimes with distinct phenomenological implications. Among the most important are the alignment limit, the decoupling limit, and the non-decoupling regime. In this section, these limits are discussed in general terms, using the singlet extension of the Standard Model as a simple illustrative example [248, 284, 285].

4.3.1 Alignment limit

The alignment limit is the regime in which one of the neutral scalar mass eigenstates is aligned with the direction of the EW vacuum expectation value in field space. As a result, this state has SM-like couplings to gauge bosons and fermions and also the same observables than the SM. In extended scalar sectors, this means that the observed Higgs boson behaves as the SM Higgs boson, independently of whether additional scalar states are light or heavy [284, 285].

This can be understood most directly in the scalar basis before diagonalisation. After electroweak symmetry breaking, the scalar fields mix, and the mass eigenstates are obtained through an orthogonal transformation. Alignment corresponds to the situation

in which the state pointing along the EW VEV direction remains an eigenstate of the full mass matrix. In that case, its couplings to the SM particles coincide, with the SM predictions [284, 285].

A simple example is provided by the RxSM, where the physical field states are obtained through eq. (4.7) which read as [248]:

$$\begin{pmatrix} \phi \\ s \end{pmatrix} = \begin{pmatrix} \cos\alpha & -\sin\alpha \\ \sin\alpha & \cos\alpha \end{pmatrix} \begin{pmatrix} h \\ H \end{pmatrix} . \tag{4.38}$$

where α is the singlet-doublet mixing angle. If h is identified with the observed Higgs boson, the alignment limit corresponds to

$$\alpha \to 0, \tag{4.39}$$

so that h becomes purely doublet-like and therefore couples to fermions and gauge bosons exactly as in the SM. In this simple case, alignment is equivalent to suppressed singlet-doublet mixing. More generally, in multi-scalar models such as two-Higgs-doublet models [284, 285].

An important point is that alignment does not require the additional scalar states to be heavy. It is therefore possible to realise approximate alignment even in the presence of relatively light extra scalars, provided the mixing with the SM-like direction is sufficiently suppressed [284, 285]. This possibility is phenomenologically relevant, since current Higgs signal strength measurements already favour a near-aligned Higgs boson, while still allowing for observable effects from an extended scalar sector in other channels or observables [14, 248, 286].

4.3.2 Decoupling limit

The decoupling limit is the regime in which the additional states become much heavier than the electroweak scale and their effects on low-energy observables are suppressed [70, 269, 285]. In this limit, the low-energy theory reduces effectively to the SM, up to corrections suppressed by inverse powers of the heavy mass scale. According to the Appelquist–Carazzone decoupling theorem, heavy degrees of freedom decouple from low-energy observables, up to renormalisation effects and corrections suppressed by inverse powers of the heavy mass [269].

Decoupling occurs when the masses of the extra states are controlled by a scale M satisfying

$$M^2 \gg v^2, \tag{4.40}$$

with v the electroweak vacuum expectation value, and when the couplings of the heavy states do not grow in such a way as to compensate the mass suppression in any case limited by perturbativity and perturbative unitarity [70, 72, 269]. In this case, integrating out the heavy fields generates only small corrections to Higgs couplings and other electroweak observables, typically scaling as powers of v^2/M^2 [70, 269].

This can be applied to extended Higgs sector by showing how heavy states can increase their masses. In general terms, if the mass of an additional scalar is of the form

$$m_\Phi^2 \sim M^2 + \lambda_\Phi v^2, \tag{4.41}$$

to decouple the heavy state one has to increase its mass m_Φ^2 by increasing the scale M^2 while maintaining the coupling of the state to the rest of the Higgs sector λ_Φ small [70,72]. If one applies this to a simple scenario like the singlet extension, the decoupling limit is reached when the singlet-like state becomes heavy while its mixing with the doublet remains small [248]. Schematically, if the singlet mass parameter is much larger than the electroweak scale, the mixing angle behaves as

$$\alpha \sim \frac{v}{M}, \tag{4.42}$$

or more generally as a quantity suppressed by the ratio of electroweak to heavy scales. Consequently, the couplings of the observed Higgs boson approach their SM values, and the direct impact of the heavy singlet on low-energy Higgs phenomenology becomes negligible [70, 248].

Alignment also emerges automatically in the decoupling limit. This is because when the non-SM scalar states are sufficiently heavy, the off-diagonal entries of the scalar mass matrix induce only a small admixture of heavy states in the SM-like Higgs boson [70, 284, 285]. It is therefore useful to distinguish between *alignment with decoupling* and *alignment without decoupling*. The former corresponds to the case where SM-like Higgs couplings arise because the extra scalars are heavy, whereas the latter occurs when the scalar sector is arranged in such a way that the SM-like state decouples from the BSM ones even though the additional states remain comparatively light [284, 285].

Phenomenologically, the decoupling limit implies that deviations in Higgs couplings, trilinear scalar couplings, and electroweak precision observables become progressively smaller as the heavy mass scale increases [70, 72, 269]. In this regime, direct production of the new scalars is also suppressed kinematically, which makes the extended scalar sector increasingly difficult to probe at colliders [70, 248].

4.3.3 Non-decoupling effects

Non-decoupling refers to the situation in which heavy scalar states do not become irrelevant, even when their masses are increased [71, 72, 93]. This typically occurs when the masses of the extra scalars are generated predominantly through electroweak symmetry breaking itself, rather than by an independent large mass scale. In that case, the couplings of the heavy states to the Higgs sector can grow with the heavy mass, and this growth can compensate the expected suppression from propagators or loop factors [71, 72].

In general terms, if the mass of an additional scalar is of the form

$$m_\Phi^2 \sim M^2 + \lambda_\Phi v^2, \tag{4.43}$$

the decoupling behaviour depends on which term dominates. If $M^2 \gg \lambda_\Phi v^2$, the heavy mass originates mainly from a scale unrelated to electroweak symmetry breaking, and the scalar typically decouples, defined before as the decoupling limit [70, 269]. By contrast, if

$$M^2 \lesssim \lambda_\Phi v^2, \tag{4.44}$$

the heavy scalar mass is tied to the electroweak vacuum structure itself, and sizeable non-decoupling effects may arise [71, 72]. In such cases, loop corrections to Higgs couplings or to the finite-temperature effective potential can remain important even for comparatively large scalar masses and perturbative regimes of the parameter space [72, 93].

Non-decoupling effects are particularly relevant in studies of Higgs self-interactions. In many extended scalar sectors, loop corrections to the trilinear Higgs couplings can grow with the masses of the additional scalars if these masses originate mainly from symmetry breaking [71, 72, 93]. This implies that heavy states may still induce sizeable deviations from the SM prediction for the Higgs self-coupling, even when their direct production is challenging [72, 93]. Similarly, in finite-temperature analyses, non-decoupling scalar contributions can have a substantial impact on the shape of the effective potential and therefore on the nature of the electroweak phase transition.

It is therefore important to stress that the presence of heavy extra scalars does not automatically imply SM-like phenomenology. Whether the heavy states decouple or not depends on the parametric origin of their masses and couplings. This distinction plays a central role in the interpretation of both collider signatures and cosmological predictions in extended scalar sectors [72, 93, 269].

4.4 Loop corrections in extended Higgs sectors

Up to this point, the discussion has largely focused on the tree-level structure of the models. One might naively expect that the leading phenomenology is already captured at tree level, with loop effects providing only small quantitative refinements. In extended scalar sectors, however, radiative corrections can be numerically sizeable and may even qualitatively alter key predictions. It was first shown in the 2HDM that loop contributions to trilinear Higgs couplings can be very large, with one-loop corrections reaching $\mathcal{O}(100\%)$ [71, 72]. These studies have been refined later at the one-loop level obtaining corrections of $\mathcal{O}(1000\%)$ [138], at the two-loop level reaching $\mathcal{O}(2000\%)$ [87, 93, 94] and in further more studies for any model with an extended scalar sector [73, 76, 78, 89, 287–289]. All the effects observed in these studies were for scenarios that where still inside of the perturbative regime.

Many of the key observables that probe extended Higgs sectors are loop sensitive. Examples include Higgs trilinear self-couplings (relevant for di-Higgs production [138]) or the finite-temperature effective potential governing phase transition dynamics, both studied in this thesis. Consequently, a consistent comparison between model predictions and experimental data requires a controlled treatment of radiative corrections.

A useful way to understand why radiative effects can become so large in extended scalar sectors is to recall that heavy new scalars do not always decouple in a simple manner. In these extensions of the SM one can find large couplings due to splittings in the mass scales of the BSM particles, therefore, the tree-level scalar potential is not sufficient to properly capture the interactions among the particles. This effect is often called mass-splitting effect and enters the radiative correction through the quartic couplings of the form

$$m_\phi^2 = M^2 + g_{hh\phi\phi} v^2 \;\rightarrow\; g_{hh\phi\phi} \;\propto\; \frac{m_\phi^2 - M^2}{v^2}, \tag{4.45}$$

where m_ϕ denotes the physical mass of the BSM scalar ϕ, v is the electroweak vacuum expectation value, and M represents an intrinsic BSM mass scale from the Lagrangian not generated by electroweak symmetry breaking. Importantly, the appearance of large radiative corrections in this scenario does not necessarily indicate a breakdown of perturbation theory; rather, it reflects a well-defined class of heavy-scalar contributions that appear

first only at loop level. This interpretation is supported by explicit higher-order computations, which typically exhibit the expected perturbative behaviour in the parameter regions where the theory remains unitary and perturbative [71, 72, 93–96].

In this thesis we are going to focus on the radiative corrections to the trilinear scalar couplings of BSM models with extended scalar sectors. To do so, firstly we have to define what we understand as trilinear scalar coupling. In this thesis we define the trilinear scalar coupling as an effective coupling extracted from the Lagrangian as

$$\lambda_{ijk} \;=\; \left.\frac{\partial^3 V}{\partial h_i \partial h_j \partial h_k}\right|_{\mathrm{m}in}\,, \tag{4.46}$$

and therefore it dose not have any momentum dependence. Radiative corrections to this couplings can be computed either diagrammatically, by evaluating the relevant one-particle-irreducible (1PI) three-point functions at zero external momentum, or alternatively from the (loop-improved) effective potential.

4.4.1 Effective potential approach

The n-loop effective potential $V^{(n)}_{\mathrm{e}ff}(\phi)$ encodes the quantum-corrected vacuum structure of the theory and provides a compact way to access Higgs masses and self-couplings at zero external momentum, which is an approximation, especially for the masses. In this approach, the trilinear Higgs coupling at n-loop level is obtained by expanding $V^{(n)}_{\mathrm{e}ff}$ around the electroweak vacuum and taking derivatives with respect to the physical Higgs direction (at the n-loop level),

$$\lambda^{(n)}_{ijk} \;=\; \left.\frac{\partial^3 V^{(n)}_{\mathrm{e}ff}}{\partial h_i \partial h_j \partial h_k}\right|_{\mathrm{m}in}\,, \tag{4.47}$$

with the derivatives evaluated at the loop-corrected minimum and where i, j, k make reference to the different Higgs bosons in a model with an extended Higgs sector. The resulting quantity corresponds to the $h_i h_j h_k$ vertex in the zero-momentum limit and captures the non-decoupling effects of heavy scalars in many extended Higgs sectors up to the n loops. In phenomenological applications, this method is particularly convenient because it reduces significantly the complexity of the computation of $\lambda_{h_i h_j h_k}$. The effective potential is constructed adding to the tree level potential ($V^{(0)}$) the loop corrected piece ($V^{(n)}$) and the counterterm potential ($\delta^{\mathrm{CT}} V$):

$$V^{(n)}_{\mathrm{e}ff} = V^{(0)} + V^{(n)} + \delta^{\mathrm{CT}} V. \tag{4.48}$$

The loop corrected piece contains all the bubble diagrams that can be constructed at certain loop level. At the one-loop level this have been deeply studied [290] and one can use the supertrace formula [290] in the $\overline{\mathrm{MS}}$ scheme to compute it:

$$V^{(1)}(\phi) = \sum_i \frac{(-1)^{2s_i} n_i}{64\pi^2}\, m_i^4(\phi) \left[\ln\left(\frac{m_i^2(\phi)}{Q^2}\right) - c_i\right], \tag{4.49}$$

where the sum runs over all particle species contributing to the one-loop effective potential. For each particle i, s_i denotes its spin, n_i the corresponding number of degrees of freedom,

and $m_i^2(\phi)$ the field-dependent squared mass evaluated. The factor $(-1)^{2s_i}$ accounts for the relative minus sign between fermionic and bosonic contributions. Furthermore, Q is the renormalisation scale, and c_i is a scheme-dependent constant, whose value depends on the regularisation and renormalisation prescription adopted. In the $\overline{\text{MS}}$ scheme (which is assumed to compute the effective potential), the constants c_i take the values

$$c_i = \begin{cases} \frac{3}{2}, & \text{for scalars and fermions,} \\ \frac{5}{6}, & \text{for gauge bosons.} \end{cases} \tag{4.50}$$

The counterterm potential will depend on the counterterms of the parameters of the potential (x_i) following:

$$\delta^{\text{CT}} V = \delta^{\text{CT}} x_i \frac{\partial V^{(0)}}{\partial x_i}, \tag{4.51}$$

where $\delta^{\text{CT}} x_i$ are the counterterm of each parameters and they depend on the choice of the renormalisation, where the standard choice is the $\overline{\text{MS}}$ scheme assumed in eq. (4.49).

4.4.2 Diagrammatic approach

A complementary determination of Higgs self-interactions is provided by the diagrammatic approach, which allows, in case is needed (not in our case), to do a full momentum-dependent computation. The diagrammatic computation allows us to compute the loop-corrected three point function with the full momentum dependence

$$\hat{\Gamma}^{(n)}_{h_i,h_j,h_k}(p_1^2, p_2^2, p_3^2)\,, \tag{4.52}$$

where the external momenta satisfy $p_1 + p_2 + p_3 = 0$ and. Then if we want to extract from this function the trilinear scalar coupling as an effective coupling we have to evaluate the three point function at zero external momenta

$$\hat{\lambda}^{(n)}_{ijk} \equiv -\hat{\Gamma}^{(n)}_{h_i,h_j,h_k}(0,0,0). \tag{4.53}$$

At a given loop order, $\hat{\Gamma}_{ijk}$ is obtained by summing all 1PI Feynman diagrams contributing to the ijk vertex ($\delta^{(n)}_{\text{gen}}\lambda_{ijk}$), adding the corrections to the external legs ($\delta^{(n)}_{\text{wfr}}\lambda_{ijk}$), the vertex counterterm contribution ($\delta^{\text{CT}}\lambda_{ijk}$) and finally the sub-loop renormalisation term ($\delta^{(n)}_{\text{sub}}\lambda_{ijk}$) composed by all the Feynman diagrams with a topological structure of $(n-1)$-loop or less but where counterterms are attached either in the propagators or in the vertices:

$$\hat{\lambda}^{(n)}_{ijk} = -\hat{\Gamma}^{(n)}_{h_i,h_j,h_k}(0,0,0) = \lambda^{(0)}_{ijk} + \delta^{(n)}_{\text{gen}}\lambda_{ijk} + \delta^{(n)}_{\text{wfr}}\lambda_{ijk} + \delta^{\text{CT}}\lambda_{ijk} + \delta^{(n)}_{\text{sub}}\lambda_{ijk} =$$

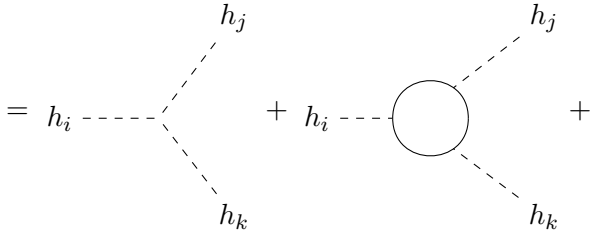

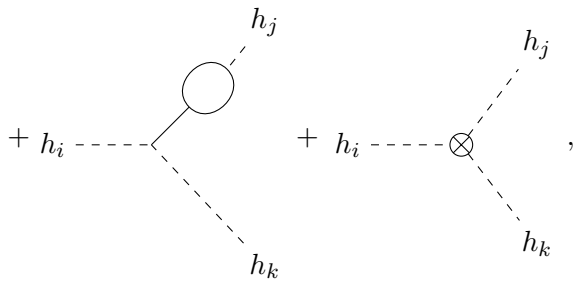

(4.54)

where for simplicity only one-loop diagrams have been shown. The tadpole contributions are included in the vertex corrections in case that they are attached to the vertex or in the external leg corrections in case they are attached to the propagators. Now the only missing piece are the different counterterms for the parameters of the model that arise from the renormalisation scheme.

4.4.3 Renormalisation schemes

Loop calculations in renormalisable quantum field theories require the introduction of counterterms to absorb ultraviolet (UV) divergences and to relate the parameters appearing in the Lagrangian to physical observables. Concretely, one splits bare parameters and fields into renormalised quantities and counterterms, e.g.

$$x_B = \hat{x} + \delta^{\mathrm{CT}} x, \qquad \phi_0 = \left(1 + \frac{1}{2}\delta Z_\phi\right)\hat{\phi}, \tag{4.55}$$

where $\hat{x}$ denotes a generic renormalised parameter (masses, couplings, mixing angles, ...), $\delta^{\mathrm{CT}} x$ the corresponding counterterm, and δZ_ϕ the field renormalisation constant for the field ϕ. While the cancellation of UV divergencies uniquely fixes the divergent parts of the counterterms, their finite parts remain undetermined. The prescription used to fix these finite parts defines the renormalisation scheme. Choosing a scheme is therefore essential to obtain unambiguous numerical predictions for loop-corrected masses and couplings such as the trilinear scalar couplings.

In practice, one has the choice of using renormalisation scheme and at infinite-loop the physical observables are independent of this choice. Different schemes are related by finite parameter redefinitions and agree up to higher-order corrections, but the residual scheme dependence at fixed order provides a useful estimate of theoretical uncertainties from unknown higher-order contributions.

$\overline{\mathrm{MS}}$ scheme. In the modified minimal subtraction scheme, counterterms remove only the UV-divergent part so that

$$\delta^{\mathrm{CT}}_{\overline{\mathrm{MS}}} x \;=\; x^{(n)}|_{\mathrm{div}}\,, \tag{4.56}$$

with no additional finite renormalisation imposed. Since the counterterm only absorbs the divergent part of the loop corrected function there is still a finite contribution coming from the loop corrections that depend on the renormalisation scale μ (introduced in dimensional regularisation to keep the couplings dimensionally consistent) and as a consequence, $\overline{\mathrm{MS}}$ parameters are *running* quantities:

$$\hat{x} \equiv \hat{x}(\mu), \qquad \mu\frac{d}{d\mu}\hat{x}(\mu) = \beta_x, \tag{4.57}$$

and physical observables computed at finite order retain a residual dependence on the renormalisation scale μ, which is compensated (up to higher orders) when including the running parameters at lower orders and that also decreases when higher perturbative orders are included. The $\overline{\text{MS}}$ scheme is particularly convenient for renormalisation-group improvement and for matching calculations, and it often leads to compact expressions for counterterms. In extended Higgs sectors, however, purely $\overline{\text{MS}}$ definitions of masses or mixing angles can sometimes lead to artificially large loop corrections or gauge-sensitive intermediate quantities.

On-shell scheme. In the on-shell (OS) scheme, counterterms are fixed by requiring that selected quantities coincide with physical observable-like quantities. For a scalar field h, OS conditions are typically imposed on the renormalised two-point function such that the position of the pole and its residue match the physical mass and canonical normalisation:

$$\hat{\Sigma}_h(p^2)\big|_{p^2=m_h^2} = 0, \tag{4.58}$$

$$\frac{d}{dp^2}\hat{\Sigma}_h(p^2)\bigg|_{p^2=m_h^2} = 0, \tag{4.59}$$

where $\hat{\Sigma}_h$ denotes the renormalised self-energy. Analogous conditions can be formulated for gauge bosons and fermions. In this way, OS renormalisation ties the input parameters directly to measured masses and couplings and often leads to stable numerical predictions for collider observables. In models with mixing, OS schemes require additional conditions to renormalise mixing angles and off-diagonal field renormalisation constants, which can be defined, for instance, from on-shell transitions or from suitable renormalised vertices, the OS scheme is then not uniquely defined. The OS scheme is therefore related with phenomenological applications, although it may become technically more challenging when many parameters and mixing structures are present. Finally another advance with respect to $\overline{\text{MS}}$ scheme is that effective couplings like the trilinear scalar couplings computed following a full OS scheme will not depend on the renormalisation scale.

Chapter 5

Di-Higgs production at future colliders

No me importa lo que hagas;
solo quiero que seas feliz.

– Ama

In this chapter we present the first results of this thesis, focusing on di-Higgs production as a direct probe of the scalar potential in the real singlet extension of the Standard Model. Higgs-pair production constitutes one of the most promising channels through which information on trilinear Higgs couplings may be accessed experimentally, and it therefore provides a unique link between collider phenomenology and the underlying structure of the scalar sector. In the class of scenarios considered here, this connection is particularly relevant because the same extended scalar dynamics that can strengthen the electroweak phase transition may also induce sizeable modifications in Higgs self-interactions and in the production of Higgs-boson pairs at colliders.

A central aspect of this analysis is that the di-Higgs signal cannot, in general, be described reliably by considering only the heavy-resonance contribution. In the real singlet model, the full process receives contributions from the heavy-Higgs-mediated resonant diagram, the Standard-Model-like light-Higgs triangle diagram, and the box diagram, together with the corresponding interference effects among them. As will be shown in this chapter, these interference terms can substantially distort both the total rate and, even more importantly, the shape of the invariant-mass distribution of the Higgs pair. A consistent phenomenological interpretation therefore requires the inclusion of the complete set of diagrams rather than a simplified resonant approximation.

With this motivation, we analyse Higgs-pair production at the HL-LHC in a benchmark region of the parameter space that is favourable for a strong first-order electroweak phase transition and compatible with current theoretical and experimental constraints. We first study the total production rate and assess the extent to which deviations from the Standard Model prediction may become observable. We then turn to the differential invariant-mass distribution, which provides more detailed information on the interplay between resonant and non-resonant contributions and on the sensitivity to the beyond-

the-Standard-Model trilinear coupling λ_{hhH}. Particular emphasis is placed on the comparison between the full calculation and the approximation in which only the resonant contribution is retained, since this difference has important consequences for the interpretation of present and future experimental searches.

5.1 Benchmark Plane and Points

After applying the minimization conditions the RxSM has seven free parameters: κ_S, κ_{SH}, λ_S, λ_{SH}, λ, v and v_S. Fixing the SM-like Higgs mass m_h and the SM VEV v to their phenomenological values $m_h \approx 125$ GeV and $v \approx 246$ GeV, we are left with five free parameters, κ_S, κ_{SH}, λ_S, λ, and v_S. The aim in this section is to define a benchmark plane with only two degrees of freedom which features a SFOEWPT, and which maximizes the di-Higgs production cross section at the LHC. The authors of [108] scanned the RxSM parameter space and kept points exhibiting a SFOEWPT. Out of these they selected eleven points that maximize the di-Higgs production cross section at the LHC, $\sigma(pp \to H \to hh)$. We have used these results from [108] to define our 2-dimensional benchmark plane.

Out of the eleven points provided in [108] we use eight points which all have $v_S > 30$ GeV.[1] These points are shown in table 5.1.[2] They approximately fulfill the numerical conditions[3]

$$\begin{aligned} \kappa_{SH} &= \frac{-16000}{v_S} \,, \\ \lambda &= 0.36 \,, \\ \kappa_S &= -560\sqrt{2\lambda_S} \,, \end{aligned} \tag{5.1}$$

leaving the singlet vev v_S and the parameter λ_S as our free parameters, so that we arrive at a two-dimensional benchmark plane that features a SFOEWPT. The appearance of "restricted allowed intervals" for the Lagrangian parameters that can be observed in table 5.1 is just a consequence of the requirement of a SFOEWPT as demanded in [108].

All points of the defined benchmark plane are within the range of parameters that were found to feature a FOEWPT, see our analysis below. Calculating the values of κ_{SH}, λ and κ_S from the values of λ_S and v_S in table 5.1 we find a maximum deviation of 7% for κ_{SH}, 6% for λ and 30% for κ_S w.r.t. the values given in table 5.1. We can use the relations of section 4.1.1 to translate the relations in eq. (5.1) into the mass basis. This allows us to take into account the experimental and theoretical constraints as described in the previous subsection. The plane is shown in the upper left plot of fig. 5.1, where the red stars indicate the eight benchmark points, and the blue points are allowed by

[1] We have checked that the remaining three points exhibit a very similar phenomenology (see our analysis below) as the eight chosen points.

[2] We have checked that these eight points also lead to a FOEWPT using the more updated calculation implemented in `BSMPTv3` [83, 85, 91]. This code uses the one-loop corrected effective potential including thermal masses. While lattice simulations allow to complete the incomplete perturbative approach [211, 215, 291, 292], they are computationally demanding preventing an easy investigation of arbitrary BSM models. For lattice treatments of the effective potential, see e.g. [293–296], for lattice simulations of gravitational waves, see e.g. [239]. The code `DRalgo` [297] provides an algorithm for the construction of an effective, dimensionally reduced, high-temperature field theory for generic models, allowing to better describe infrared effects [208] that can only be treated properly by lattice simulations [298].

[3] For the four points with $v_S < 30$ GeV the deviations from our three conditions exceed the few-percent level.

Benchmark	v_S [GeV]	λ	κ_{SH} [GeV]	λ_{SH}	$\kappa_{\tilde{S}}$[GeV]	λ_S	κ_λ	λ_{hhH} [GeV]
B1	60.9	0.34	-245	2.65	-361	0.260	1.42	123
B2	59.6	0.34	-284	3.26	-397	0.380	1.40	153
B3	54.6	0.34	-321	3.80	-214	0.080	1.41	167
B4	47.4	0.36	-354	4.63	-607	0.435	1.47	187
B5	40.7	0.36	-372	5.17	-618	0.410	1.47	182
B6	40.5	0.38	-422	5.85	-151	0.040	1.48	207
B7	36.4	0.36	-449	7.36	-424	0.140	1.43	236
B8	32.9	0.34	-488	8.98	-542	0.265	1.41	266

Table 5.1: Values of v_S, λ, κ_{SH}, λ_{SH}, κ_S, λ_S, κ_λ, and λ_{hhH} of the reference benchmark points from [108].

all constraints. The gray points are excluded by `HiggsBounds`, which found them to be incompatible with a 2020 ATLAS search for a resonance of a heavy Higgs boson, which decays into two Z bosons and ultimately into four leptons [299]. This experimental result was not yet available when [108] was published. We also show the projection of the allowed/excluded regions (blue/grey) in the λ_{hhH}-κ_λ plane in the upper right plot of fig. 5.1. It can be seen how almost the entire plane lies in the area defined by the points of [108], which ensures the SFOEWPT in our plane. One can observe that four reference points are outside the plane, because of their smaller or larger value of κ_λ. However, this does not constitute a problem, since the points are outside our benchmark plane by a maximum of 2% in κ_λ. (In [108] a favorable value of $\kappa_\lambda \sim 1.5$ is found to ensure the SFOEWPT, in agreement with our benchmark plane.) Finally, in the lower plot of fig. 5.1 we show a zoom into the allowed regions in the λ_{hhH}-κ_λ plane.

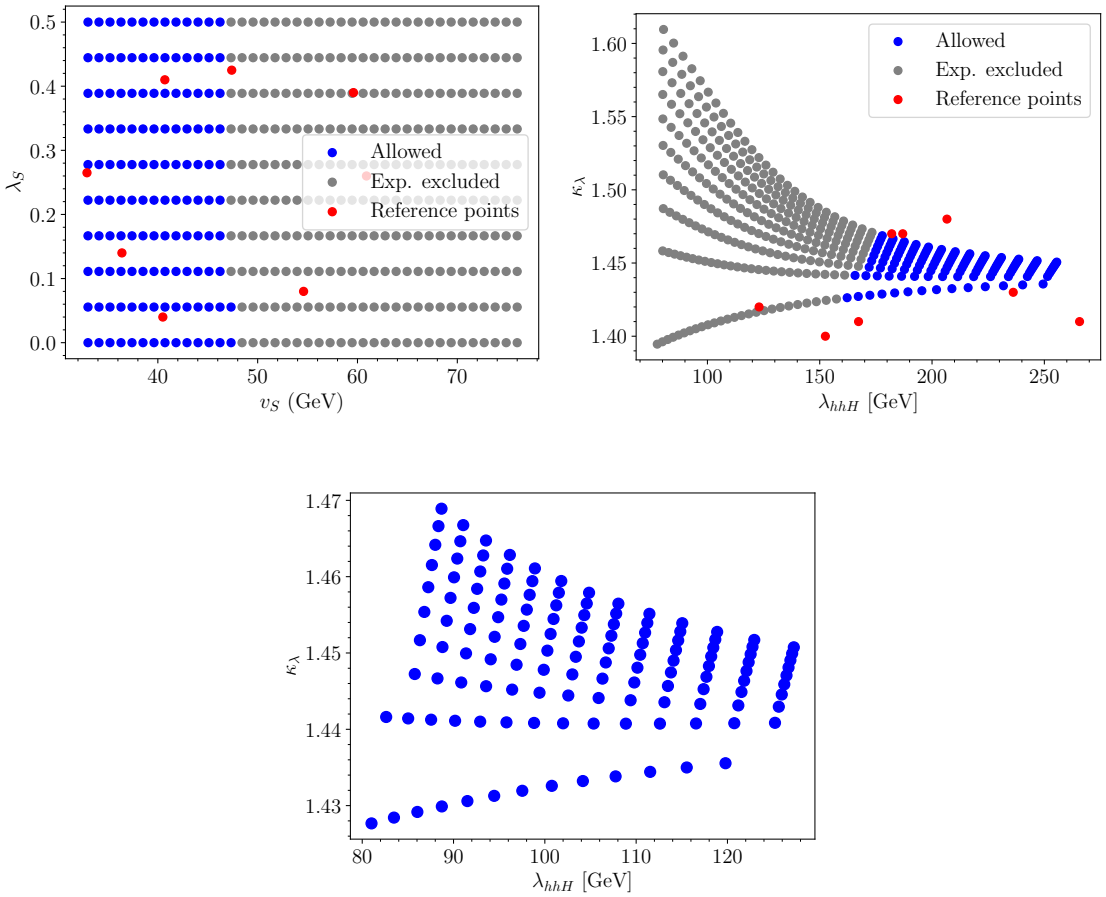

Figure 5.1: The benchmark plane with the experimentally excluded region in grey, the allowed region in blue and the points used to define the plane in red (see text). Upper left: the prediction in the plane v_S-λ_S. Upper right: the projection of the benchmark plane in the λ_{hhH}-κ_λ plane. Lower plot: the final allowed benchmark plane in the λ_{hhH}-κ_λ projection.

In the following we briefly analyze the basic phenomenological features of our benchmark plane. In fig. 5.2 we show the prediction for m_H in the v_S-λ_S plane (left) and in the λ_{hhH}-κ_λ plane (right). It can be seen that the mass of the heavy Higgs boson is inversely proportional to the singlet vev. This is an effect of the definition of the benchmark plane, not a feature of the model. The allowed range of m_H in our plane is $[458, 660]$ GeV. One can also see that λ_{hhH} increases with the heavy Higgs-boson mass. Overall, we find that in our benchmark plane the product of $(\sin\alpha \cdot \lambda_{hhH})$ is approximately constant (within a few percent). In the calculation of $gg \to H \to hh$ in the limit of large m_H one thus finds a suppression with increasing m_H, and in the limit $m_H \to \infty$ the amplitude for this process goes to zero.

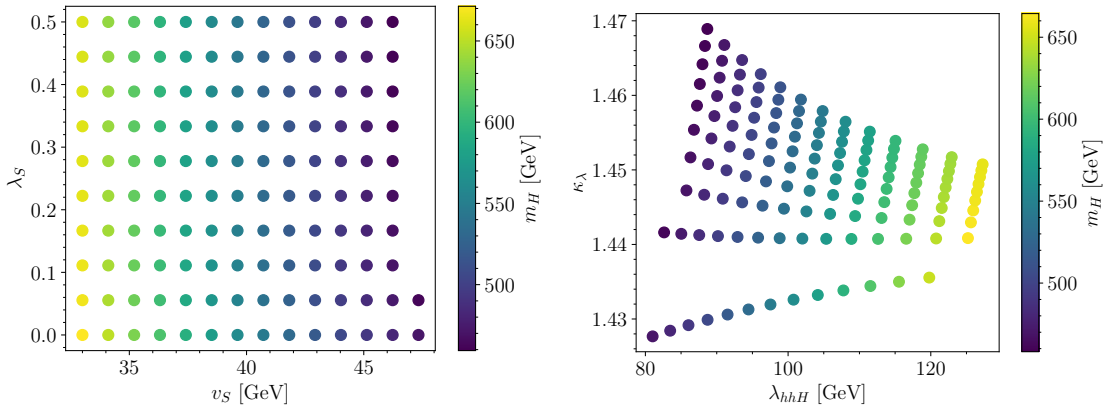

Figure 5.2: The prediction of the heavy Higgs mass m_H in our benchmark scenario. Left: in the v_S-λ_S plane, right: in the λ_{hhH}-κ_λ plane.

In fig. 5.3 we show the prediction of the cosine of the mixing angle α in the v_S-λ_S plane (left) and in the λ_{hhH}-κ_λ plane (right). The cosine tends to 1 for small values of v_S, but $\cos\alpha = 1$ is never reached, which is again an artifact of our benchmark plane. This is consistent since in the alignment limit the SM is recovered, in which no SFOEWPT is found, whereas it is ensured in our benchmark plane by construction. Similarly, $\kappa_\lambda = 1$ is never reached by construction.

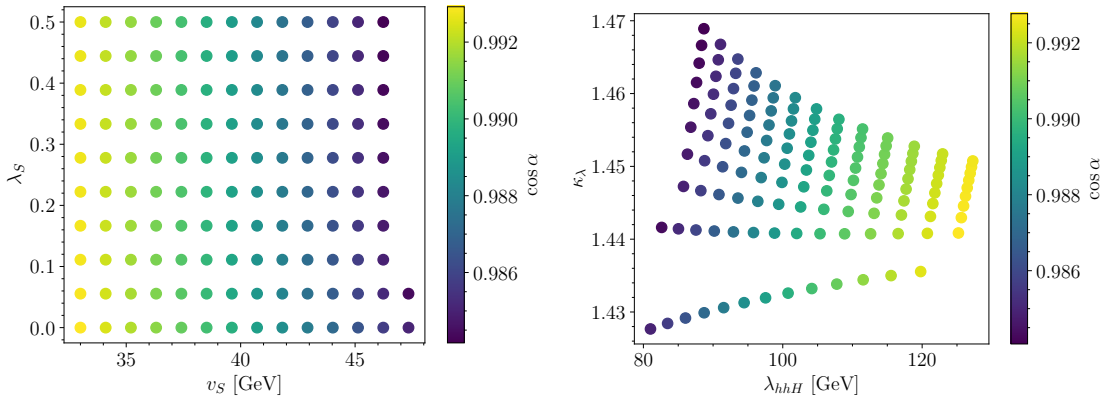

Figure 5.3: The prediction of the mixing angle in the second benchmark plane. Left: in the $v_S - \lambda_S$ plane. Right: in the $\lambda_{hhH} - \kappa_\lambda$ plane.

5.2 HL-LHC Analysis

In this chapter, we first briefly review the set-up for the calculation of $pp \to hh$. We show the results for the cross section in an specific benchmark plane favorable for a SFOEWPT and analyze whether differences w.r.t. the SM predictions will be observable. Finally, we analyze the sensitivity to the heavy Higgs-boson resonance and its THC, λ_{hhH}. The corresponding analysis for high-energy e^+e^- colliders is presented in the subsequent section 6.3.2.

5.2.1 Calculation of $gg \to hh$

Standard Model Higgs-pair production has not been observed yet at the LHC, and therefore di-Higgs production constitutes an interesting window to test new physics in future experiments such as the HL-LHC. The main production channel at the (HL-)LHC is gluon fusion. In the SM at leading order (LO), two diagrams contribute to the process: the box diagram (shown by the lower diagram in fig. 5.4), which is given by a heavy quark loop with two Yukawa couplings, and the triangle diagram (shown by the upper right diagram in fig. 5.4), which is given by a heavy quark loop with a Yukawa coupling and the THC λ_{hhh}.[4] In the RxSM, an additional diagram contributes: the triangle diagram in which a heavy Higgs boson is propagating in the s-channel (shown by the upper left diagram in fig. 5.4). It depends on the Yukawa coupling of the heavy Higgs boson and on the BSM THC λ_{hhH}. The box and the light Higgs triangle diagram are known as the "continuum" or the non-resonant part, while the heavy Higgs triangle diagram is called the "resonant" part (even in the case of $m_H < 2m_h$). It should be noted that in the SM there is a destructive interference between the triangle and the box diagram.[5]

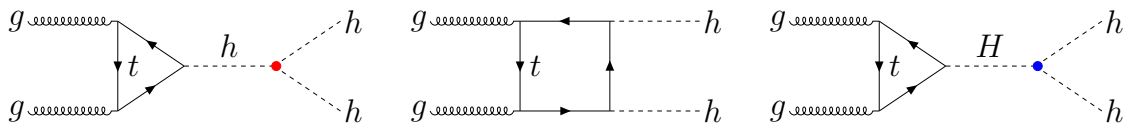

Figure 5.4: Leading-order diagrams contributing to the di-Higgs production process at the (HL-)LHC.The red and blue dots indicate the trilinear scalar couplings λ_{hhh} and λ_{hhH}, respectively. Left: light triangle diagram; centre: box diagram; right: heavy triangle diagram.

For our analysis we calculate the total production cross section as well as the differential cross section with respect to the invariant mass of the two light Higgs bosons, m_{hh}. For both calculations the code `HPAIR` [137] has been used, adapted to the RxSM. The original `Fortran` code `HPAIR` was written to calculate the production cross sections of two neutral Higgs bosons through gluon fusion in the SM and in the Minimal Supersymmetric Extension of the SM (MSSM). In the meantime, it has been extended to other models [64, 69, 137, 300–302]. For our project, we extended the code to include the RxSM. The computation can be performed either at LO or next-to-leading order (NLO) in QCD. In the LO case, the calculation takes into account the top and bottom quark loops with full mass dependence, whereas in the NLO case the heavy top quark mass limit (HTL) is

[4] We only display top-quark loops as in the SM the contributions from bottom-loops are very small.

[5] In principle, also the weak-boson fusion process can contribute. However, within the SM it is suppressed w.r.t. gluon fusion by more than a factor of 10 [100]. The contribution of the heavy Higgs-boson, involving λ_{hhH}, receives an additional reduction due to the suppressed WWH coupling.

used. In this limit, the contributions of all quarks are neglected, except for the top quark, which is assumed to be infinitely heavy. The computation of the NLO QCD corrections in the HTL including the full top-quark mass effects at LO leads to a K-factor, i.e. the ratio of the NLO over the LO cross section, of approximately 2 in the SM [137] and also in other BSM extensions, as found in [64, 69, 137, 300–302].[6] This value approximates the results of the K-factor of the inclusive cross section including the finite top-mass effects at NLO QCD, very well as shown in [303–307] for the SM and [307, 308] for the 2HDM. The QCD corrections are not affected by Higgs mixings, so they can be taken over to the RxSM case.

The code also provides the calculation of differential cross sections with respect to the invariant Higgs-pair mass, m_{hh}, both at LO and in the HTL. However, as has been shown in [309] in the context of non-linear effective field theory, mass effects can be significant in the m_{hh} distributions. Since for BSM models there are no results available for distributions at NLO QCD including the full mass dependence, we will stick to LO distributions in the following. Although we are aware that NLO corrections are important, we do not want to present results for distributions that could be significantly distorted by mass effects, and hence chose to make this compromise. Since not all calculations necessary for our analysis can be performed at NLO, we consistently use LO QCD everywhere.

5.2.2 Analysis of the total cross section

In fig. 5.5 we show the results for the di-Higgs production cross section in the RxSM at LO. We have verified numerically that the results at NLO QCD are larger by a factor ~ 2. From now on, we concentrate on the LO result (keeping in mind the NLO factor). All cross section calculations are done for $\sqrt{s} = 14$ TeV. The corresponding SM cross section is obtained with our RxSM version of `HPAIR` setting the mixing angle $\alpha = 0$, i.e. in the SM limit. Numerically, we find

$$\sigma_{\rm SM}^{LO}\,(pp \to hh) = 19.76\ \text{fb}\,, \quad \sigma_{\rm SM}^{NLO}\,(pp \to hh) = 38.24\ \text{fb}\,. \tag{5.2}$$

In a first step, we compare the results of the RxSM with the SM model ones at the HL-LHC and analyze whether the cross sections of both models can be distinguished experimentally. To do so we define the statistical significance of the RxSM cross section w.r.t. the SM. To calculate the uncertainty of the cross section measurement at the HL-LHC we take the anticipated significance of the SM di-Higgs production cross section at the HL-LHC [183], which has been found to be $s_{SM} = 4.5\sigma$. This significance is rescaled to the cross section of the RxSM (as the number of expected events will be different). Since we are dealing with a Gaussian distribution, the uncertainty scales as the square root of the number of events, or in this case of the cross section. The uncertainty $\Delta\sigma_{hh}^{\rm RxSM}$ on the cross section in the RxSM can then be obtained as,[7]

$$\Delta\sigma_{hh}^{\rm RxSM} = \frac{\sigma_{hh}^{\rm SM}}{s_{\rm SM}}\sqrt{\frac{\sigma_{hh}^{\rm SM}}{\sigma_{hh}^{\rm RxSM}}}, \tag{5.3}$$

[6] In our calculations performed for this work we confirmed a K-factor of ~ 2 for the RxSM, see the next subsection.

[7] Since, as discussed above, also in the RxSM the K-factor is ~ 2 as in the SM, we can safely assume that the NLO QCD corrections, that are not taken into account (see the discussion above), rescale all cross sections and the corresponding uncertainties in the same way.

and the significance of the deviation of the total RxSM di-Higgs production from the SM prediction is defined as,

$$\Delta s = \frac{\sigma_{hh}^{\mathrm{R}xSM} - \sigma_{hh}^{SM}}{\Delta\sigma_{hh}^{\mathrm{R}xSM}} \,. \tag{5.4}$$

With this definition of the significance we are scaling the SM analysis, which properly takes into account the background at the HL-LHC, to the cross section of the RxSM. While this is an approximation, e.g. not taking into account the possibility of a resonant structure, it should capture the main SM background effects. There are previous works that do a more detailed analysis of the impact of the backgrounds in the RxSM, see [108, 126, 310–312], but this goes beyond the scope of our analysis.

In fig. 5.5 we show the λ_{hhH}-κ_λ benchmark plane as defined in the previous section. In the left plot we display as color coding the total cross section of the di-Higgs production in the RxSM and we mark in red when the value of the cross-section in the RxSM is approximately equal to the SM, which we define through the right plot, where we show as color coding the significance of the deviation from the SM, i.e. Δs as defined in eq. (5.4), where red points have $|\Delta s < 0.1|$. For values of $\lambda_{hhH} \lesssim 200$ GeV we find larger RxSM cross section values than in the SM, whereas for larger λ_{hhH} values they are smaller. However, this is not a general feature, but an artifact of our benchmark plane. The figure shows that the cross-section of the process is inversely proportional to the THC λ_{hhH}. Here it is important to keep in mind that λ_{hhH} increases with m_H. However, as argued in the section where the benchmark plane is defined, an overall suppression of the heavy Higgs-boson contribution is expected with increasing λ_{hhH} due to the fact that in our benchmark plane we find that the product of $(\sin\alpha \cdot \lambda_{hhH})$ is approximately constant. Finally, as can be observed in the right plot of fig. 5.5, we find that for the smallest allowed values of λ_{hhH} in our benchmark plane the cross section of the RxSM deviates by more than $5\,\sigma$ from the SM prediction, i.e. from the cross section measurement alone a difference could be observed. For most parts of the parameter space, however, this difference is big enough to be significant.

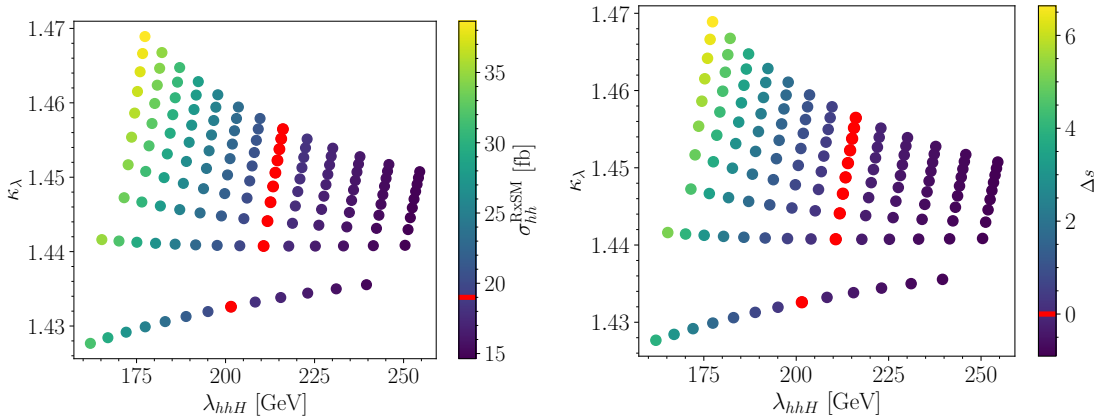

Figure 5.5: The λ_{hhH}-κ_λ benchmark plane. Left: total cross section of the process $gg \to hh$ for the HL-LHC in the RxSM. The red mark on the colorbar corresponds to $\sigma_{hh}^{\mathrm{R}xSM} = \sigma_{hh}^{SM}$. The red colored points are defined via the right plot (see text). Right: the significance of the cross section of the process $gg \to hh$ in the RxSM w.r.t. the SM. The red mark on the colorbar corresponds to $\Delta s = 0$, and the red points have $|\Delta s| < 0.1$.

In the region where $\sigma_{hh}^{SM} \approx \sigma_{hh}^{\mathrm{R}xSM}$, i.e. the region marked in red in the right plot of

fig. 5.5, the RxSM is not in the alignment limit, but the various BSM effects cancel each other. W.r.t. the SM one has $\kappa_\lambda \sim 1.45$, i.e. the destructive interference of the box diagram and the h s-channel contribution is enhanced, leading to a smaller cross section. This, however, is compensated by the resonant H exchange contribution, leading to an accidental numerical cancellation of both effects.

Resonant di-Higgs-boson searches at ATLAS [9, 13] and CMS [14, 313] so far take into account only the resonant diagram, but neglect possible effects from the two continuum diagrams, which will be discussed further in section 5.2.3. Here, in fig. 5.6, we show the total cross section in the RxSM for the case that the continuum diagrams are (incorrectly) not taken into account. It can be observed that this cross section is lower than the SM result by $\sim 30\%$ for small values of λ_{hhH} and by up to $\sim$ % for large values of λ_{hhH}. These numbers differ substantially from the complete calculation taking into account all diagrams, as shown in fig. 5.5. This demonstrates already at the level of the full cross section that the experimental "approximation" of neglecting the continuum diagrams may not be adequate in all cases. This difference in the computation of the cross section makes it complicated to compare the results of this work with results of previous works. These analyse the background further, but apply a different approach in the computation of the signal, as e.g. done in [108].

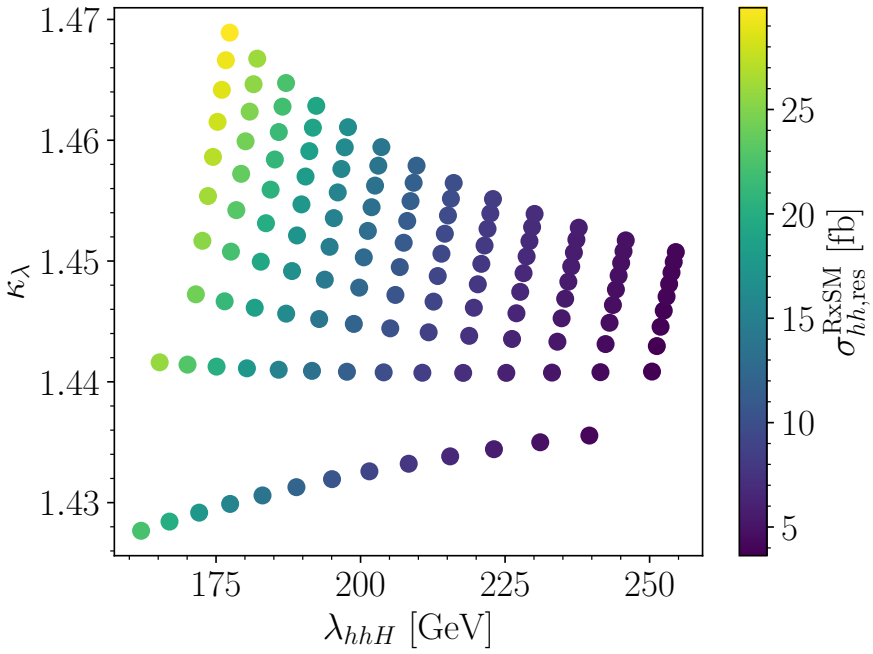

Figure 5.6: The cross section of the process $gg \to hh$ for the HL-LHC in the RxSM only taking into account the heavy Higgs boson triangle diagram, shown in the plane λ_{hhH}-κ_λ.

5.2.3 Analysis of m_{hh}

Definitions and Benchmark Points

Experimental di-Higgs analyses not only rely on the total cross section, but also build substantially on differential distributions like the differential invariant mass distribution of the di-Higgs system, m_{hh} (which we evaluate, as discussed above, also with the code

HPAIR). This will be particularly interesting in parameter regions where $\Delta s > 5$, i.e. the measurement of the total cross section is sufficient to distinguish the RxSM from the SM and one could extract information of the λ_{hhH} coupling from the differential distributions. And it can be particularly relevant in parameter regions with $\Delta s < 5$ i.e. the measurement of the total cross section is not sufficient to distinguish the RxSM from the SM. To facilitate our analysis, we are going to focus on eight benchmark points distributed over the plane. They have been selected to explore parameter regions with different values of the BSM Higgs-boson mass, different couplings and also different values of the statistical significance of the total cross section with respect to the SM. The eight benchmark points that we have defined are shown in fig. 5.7, with their input parameters and other relevant quantities given in table 5.2. In our analysis we will group these benchmark points according to the differences between $\sigma_{hh}^{\mathrm{R}xSM}$ and $\sigma_{hh}^{\mathrm{SM}}$ in each point. Specifically, we define

- **Region 1:** $\Delta s > 5$,
- **Region 2:** $5 > \Delta s > 1$,
- **Region 3:** $1 > \Delta s$.

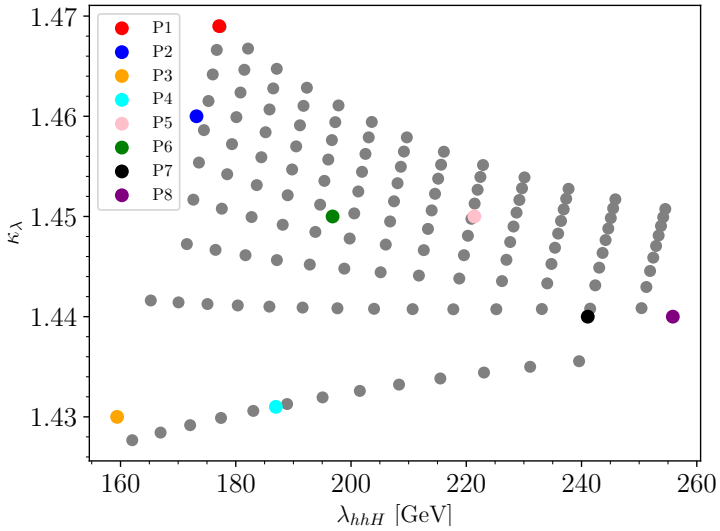

Figure 5.7: The λ_{hhH}-κ_λ plane with the eight benchmark points marked. For details, see table 5.2.

Before we present our m_{hh} analysis, we discuss the impact of the experimental uncertainties, see [64]. In fig. 5.8 we show the theoretical prediction for the m_{hh} distribution in black for the benchmark point P1, as given in table 5.2. It has a dip for low values of the invariant mass, $m_{hh} \sim 290$ GeV. This is caused by a negative interference between the box and the light Higgs-boson triangle diagrams. In the SM with $\kappa_\lambda \sim 1$ this interference occurs at $m_{hh} \sim 250$ GeV. In P1 we have $\kappa_\lambda \sim 1.5$, and the negative interference is shifted to $m_{hh} \sim 290$ GeV. The second important effect is the peak-dip structure observed around the resonance of the heavy Higgs boson, $m_{hh} = m_H \sim 460$ GeV. This peak-dip structure is due to the interference of the heavy Higgs-boson triangle and the two non-resonant diagrams, see the discussion in [64] and references therein. The sign

Id	m_H [GeV]	α	v_S [GeV]	λ_S	λ_{hhH} [GeV]	κ_λ	Γ_H [GeV]	$\sigma_{hh}^{\mathrm{R}xSM}$ [fb]	Δs	R
P1	459.2	0.178	46.3	0.445	177	1.47	2.07	38.1	6.4	318
P2	464.9	0.176	46.3	0.225	172	1.46	2.07	35.3	5.3	293
P3	469.4	0.174	47.4	0.000	157	1.43	2.02	31.7	3.9	255
P4	529.8	0.153	41.9	0.000	187	1.43	2.38	21.7	0.7	156
P5	577.5	0.139	37.5	0.390	221	1.45	2.72	18.0	-0.2	126
P6	531.7	0.152	40.8	0.225	197	1.45	2.46	22.1	0.8	165
P7	642.9	0.125	34.2	0.055	241	1.44	2.99	15.1	-0.8	89
P8	657.9	0.122	33.1	0.390	256	1.44	3.00	15.3	-0.8	93

Table 5.2: Benchmark points: identifier, heavy Higgs mass, mixing angle, singlet vev, b_4, λ_{hhH} coupling, κ_λ modifier, heavy Higgs decay width, di-Higgs production cross section at the HL-LHC, Δs, and the R parameter defined in eq. (5.5), see text.

of the couplings entering the heavy Higgs-boson resonance diagram, $Y_t \cdot \lambda_{hhH}$, where Y_t is the top Yukawa coupling of the heavy Higgs boson, determines whether one finds a peak-dip structure (as in our case), or a dip-peak structure.

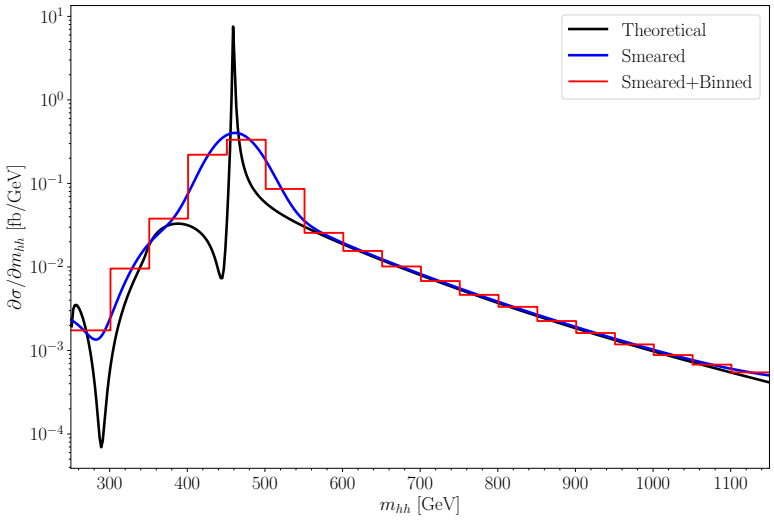

Figure 5.8: Differential cross section of the process $pp \to hh$ at the HL-LHC with $\sqrt{s} =$ 14 GeV as a function of m_{hh} for the point P1, see table 5.2; black: theoretical curve, blue: smeared curve with 15% of smearing, red: smeared and binned curve with 15% of smearing and a bin size of 50 GeV.

The first experimental uncertainty that has to be taken into account is the uncertainty in the m_{hh} measurement, labeled as "smearing". Here we follow the procedure of [64], where each point in m_{hh} is smeared out out as a Gaussian distribution in m_{hh}. We represent each point in m_{hh} as a Gaussian distribution with a full width half maximum (FWHM) of a percentage (p) of the corresponding value of m_{hh}, see [64] for details, where it was argued that the percentage (p) value to perform a realistic analysis is 15%. The effect of smearing on a distribution can be seen in the blue curve in fig. 5.8. It can

be observed how the distribution is smoothened out and does not exhibit a pronounced peak-dip structure anymore, which will make it more difficult to identify the resonance contribution. The second effect to be taken into account is that the detector does not have an infinite resolution in m_{hh}. Instead, the data will be given in bins of 50 GeV width, see again the discussion in [64]. Taking this into account on top of the smearing results in the red curve shown in fig. 5.8. Indentifying the resonance contribution becomes even more difficult taking the finite resolution in m_{hh} into account.

One main objective of our analysis is the question whether we can distinguish the RxSM from the SM via the m_{hh} distributions, i.e. whether the effect of the heavy Higgs-boson resonance can be detected. To this end, we define a theoretical parameter, R, to compare quantitatively the difference between the RxSM and the SM distributions for the different benchmark points. Following [64], we define R as,

$$R = \frac{\sum_i |N_i^R - N_i^C|}{\sqrt{\sum_i N_i^C}}\,, \tag{5.5}$$

where N_i^R is the number of events of the RxSM distribution, and N_i^C is the number of events of the SM distribution in bin i. The window in which the bins are counted is defined by [64],

$$|N^R - N^C| > \mathrm{b}in\ size \cdot 20\ \ \mathrm{GeV}\,, \tag{5.6}$$

i.e., the sum over i in eq. (5.5) runs over all the bins that fulfill the condition in eq. (5.6). With this choice we focus on the region in which there are sizeable differences between the two distributions, i.e. around the resonance. It is important to emphasize that R is a theoretical measure to compare the two distributions with each other. To determine whether via an m_{hh} distribution the measurement the value of the THC λ_{hhH} can be performed, a full experimental analysis is required, which is beyond the scope of this.

Complete Calculation

In this subsection we present our results for the calculation of the differential cross section based on the full set of LO diagrams. In the next subsection we highlight the differences w.r.t. the calculation taking into account only the resonant heavy Higgs-boson diagram, as done by the experimental collaborations to obtain their exclusion limits.

Region 1

In the first region with $\Delta s > 5$ one could observe indications of BSM physics via the total cross-section measurement alone. Two benchmark points, P1 and P2 lie in Region 1. In fig. 5.9 we show the m_{hh} distributions for a smearing of 15% and a bin size of 50 GeV, as discussed in the previous subsection. Compared are the results for the SM (red dashed line), benchmark point P1 (red) and P2 (blue). One can observe that the "original" dip-peak structure, as e.g. visible in fig. 5.8, is not visible anymore, an effect of the smearing and binning. On the other hand, a pronounced peak w.r.t. the SM is visible around $m_{hh} \sim 460$ GeV, which corresponds to a good approximation to the values of m_H in P1 and P2. The values found for R according to eq. (5.5) and (5.6) are $R \sim 300$ (see also table 5.2), where we have indicated in fig. 5.9, which bins are taken into account in the respective evaluation. While R is not representing a true experimental significance, the values are relatively high, giving rise to the expectation that the RxSM and the SM can

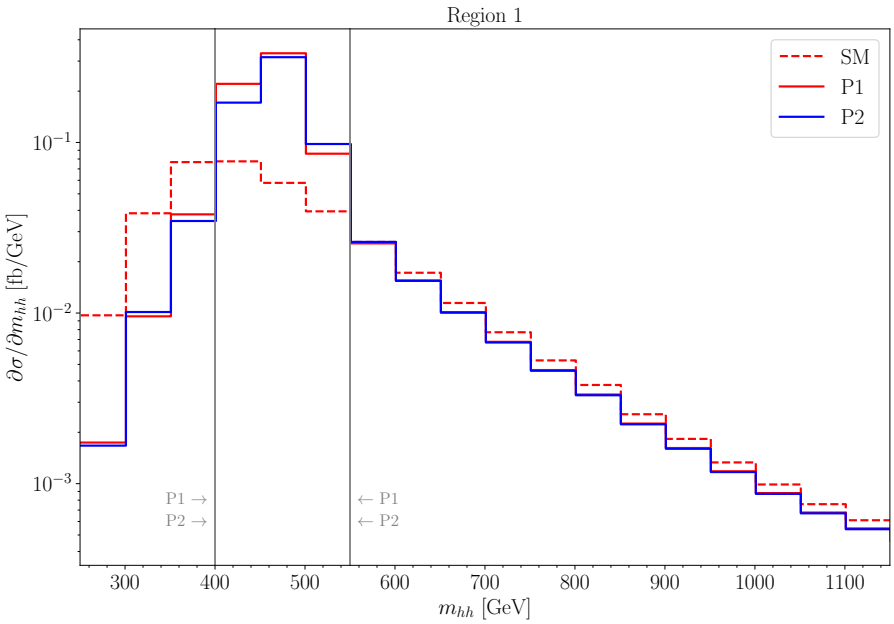

Figure 5.9: Differential cross section of the process $pp \to hh$ at the HL-LHC as a function of m_{hh} for the SM (red dashed line) and for two RxSM benchmark points: P1 (red) and P2 (blue) see table 5.2. Results are shown for a smearing of 15% and a bin size of 50 GeV. The bins that have been used to calculate the R values are indicated by gray vertical lines.

be distinguished not only via a measurement of the total cross section, but also via a measurement of the m_{hh} distributions.

Region 2

In the second region the difference in the total di-Higgs production cross section between the RxSM and the SM is $5 > \Delta s > 1$, i.e. the total cross section measurement would exhibit a significant deviation although it would not be statistically distinguishable from the SM. However, as discussed above, this is due to the cancellation of several BSM effects, as we will demonstrate here. In fig. 5.10 we show the m_{hh} distributions of the benchmark point in region 2, P3 (orange) see table 5.2. As before, they are compared to the SM distribution (dashed red), and a smearing of 15% and a bin size of 50 GeV have been applied. As for region 1, it can be observed how the dip-peak structure is washed out, leaving resonance peaks around the values of m_H, with $m_H \sim 470$ GeV for P3 (see also table 5.2), where we have indicated in fig. 5.10, which bins are taken into account in the respective evaluation. Most importantly, all three RxSM distributions differ substantially from the SM m_{hh} distribution where the differential cross section is large. The values of R found for P3 is ~ 250. These large value give rise to the hope that while the total cross section does not allow to distinguish the RxSM from the SM, such a distinction may be possible via the measurement of the m_{hh} distribution in comparison with the theory prediction for the SM.

Region 3

In the third region the difference in the total di-Higgs production cross section between the RxSM and the SM is $1 > \Delta s$, i.e. the total cross section in the RxSM is effectively identical

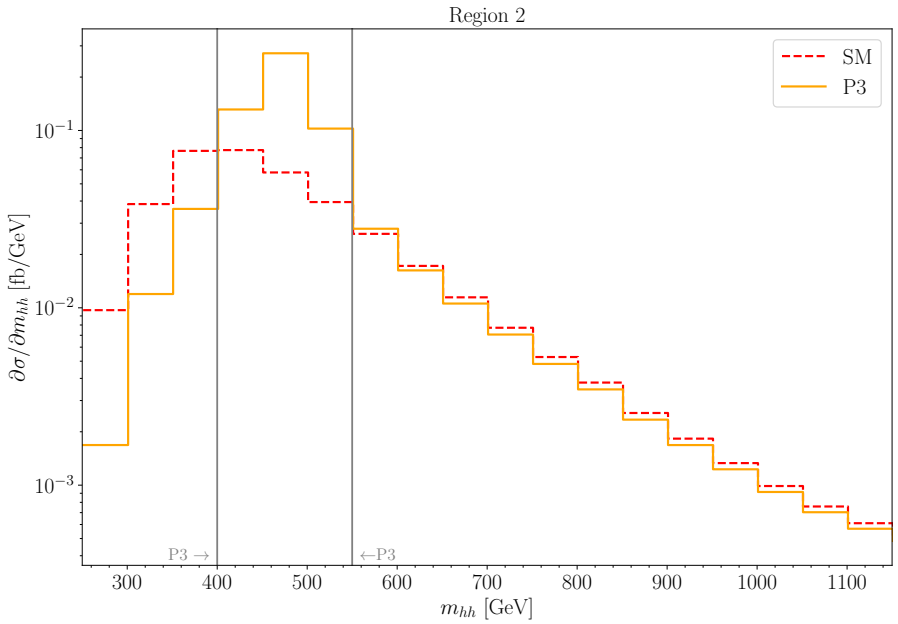

Figure 5.10: Differential cross section of the process $pp \to hh$ at the HL-LHC as a function of m_{hh} for the SM (red dashed line) and for three RxSM benchmark point in region 2: P3 (orange) , see table 5.2. Results are shown for a smearing of 15% and a bin size of 50 GeV. The bins that have been used to calculate the R values are indicated with gray lines.

to the SM prediction. In fig. 5.11 we show the m_{hh} distributions of the benchmark points P4 (cyan) and P5 (green) in region 3 and in fig. 5.12 the benchmark points P6 (pink), P7 (purple) and P8 (black), see table 5.2. As before, they are compared to the SM distribution (dashed red), and a smearing of 15% and a bin size of 50 GeV have been applied. From the original peak-dip structure only a broadly smeared out "resonance peak" remains, again centered around the respective values of the heavy Higgs-boson mass. However, in contrast to regions 1 and 2, the differences w.r.t. the SM m_{hh} distribution around m_H, i.e. where the differential cross section is relatively large, appears much smaller than in the regions 1 and 2. Correspondingly, relatively smaller R values are found between $\sim [90, 150]$ (see also table 5.2), where again we have indicated in fig. 5.11 and fig. 5.12, which bins are taken into account in the respective evaluation. While these values still appear substantial, a more realistic experimental analysis will be needed to determine whether in region 3 the m_{hh} measurement at the HL-LHC will be able to distinguish the RxSM from the SM.

Pure Heavy Resonant Contribution

In view of recent improvements in the experimental sensitivity to resonant di-Higgs production (see, e.g., [9,313]) it is crucial that the experimental limits (and possibly eventually also the experimental measurements) are presented in a way that they can be correctly confronted with theoretical predictions in different models. The resonant limits that have been presented by ATLAS [9] and CMS [313] so far were obtained assuming that only one heavy resonance is contributing to the cross section, neglecting the non-resonant contributions. In [138] it was demonstrated for benchmark points in the 2HDM that the current

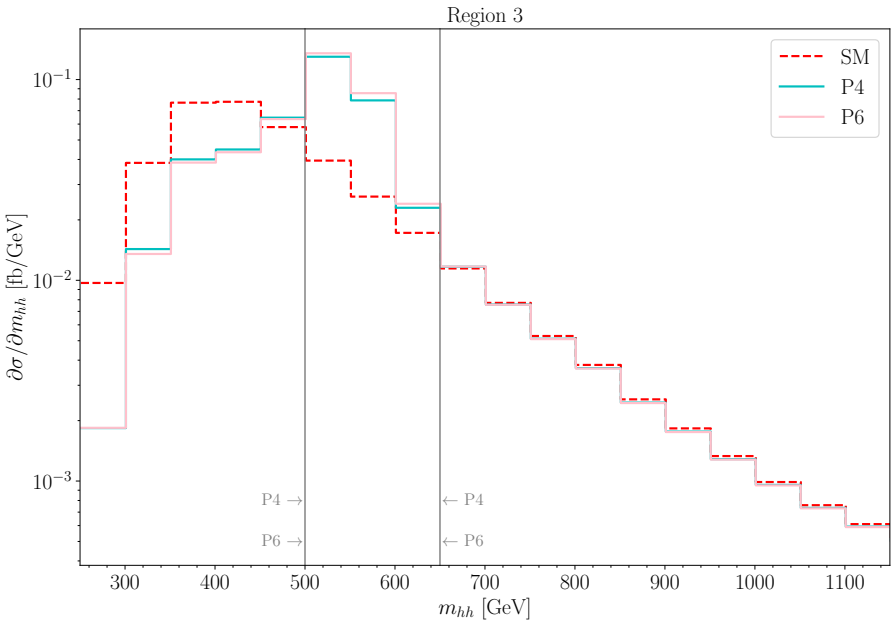

Figure 5.11: Differential cross section of the process $pp \to hh$ at the HL-LHC as a function of m_{hh} for the SM (red dashed line) and for three RxSM benchmark points in region 2: P4 (cyan) and P6 (pink) , see table 5.2. Results are shown for a smearing of 15% and a bin size of 50 GeV. The bins that have been used to calculate the R values are indicated with gray lines.

experimental procedure may not yield reliable resonant di-Higgs exclusion limits. In this subsection we compare the m_{hh} distributions of the full calculation, as presented in the previous subsection, with the distributions obtained neglecting the non-resonant contributions, i.e. m_{hh} distributions of the type employed by the experimental collaborations to obtain their current exclusion bounds. The comparison is shown for one benchmark point in each region.

In fig. 5.13 we show the differential cross section of the process $pp \to hh$ at the HL-LHC as a function of m_{hh} for the SM (red dashed line), compared to the distributions in P1 (region 1, upper plot), P3 (region 2, middle plot) and P7 (region 3, lower plot), see table 5.2. Orange (blue) lines show the result of the full calculation (taking into account only the resonant diagram). For all three depicted benchmark points the pure resonant m_{hh} distribution exhibits, as expected, a clear peak structure around the respective $m_{hh} = m_H$ value. The correct m_{hh} distributions, i.e. taking correctly into account the resonant contribution, the non-resonant diagrams, as well as all interference contributions, have a substantially broader structure. For $m_{hh} \gtrsim m_H$ the m_{hh} distributions are somewhat enhanced w.r.t. the pure resonant result. However, substantially larger effects of the correct full calculation are found for $m_{hh} \lesssim m_H$. In P1 (region 1) the resonant peak is somewhat broadened to smaller m_{hh} values. For P3 (region 2) the peak is broadened already over several bins towards smaller m_{hh} values, where the effect becomes most pronounced for P7 (region 3). As argued in [138], it is plausible to conclude that such (realisticly) broadened peak structures, deviating strongly from the clear peak structure of the pure resonant contribution, could not be identified by the current design of the experimental searches. Conversely, applying a pure resonant m_{hh} distribution to the

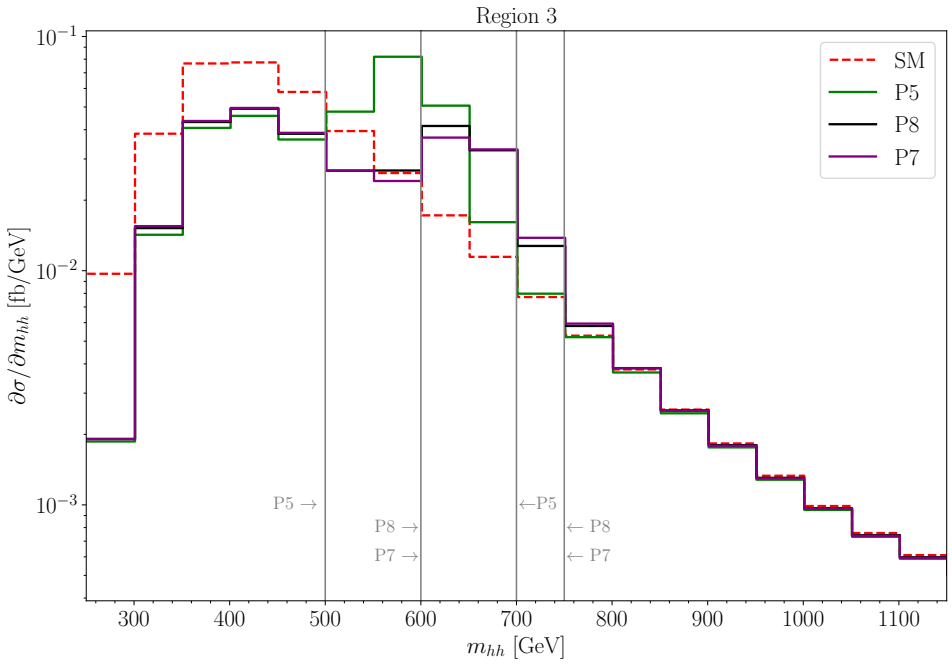

Figure 5.12: Differential cross section of the process $pp \to hh$ at the HL-LHC as a function of m_{hh} for the SM (red dashed line) and for three RxSM benchmark points in region 3: P5 (green), P7 (purple) and P8 (black), see table 5.2. Results are shown for a smearing of 15% and a bin size of 50 GeV. The bins that have been used to calculate the R values are indicated with gray lines.

experimental analysis could lead to an erroneous exclusion of a parameter point, which in reality produces a substantially broadened m_{hh} "peak structure".

5.3 ILC1000 Results

In this section we present our results for the di-Higgs production at future high-energy e^+e^- colliders. We consider the double Higgs-strahlung channel, i.e. $e^+e^- \to Zhh$, which is the dominant production channel of two SM-like Higgs bosons up to a center-of-mass energy slightly above 1 TeV. The Feynman diagrams that contribute to this process at tree level are shown in fig. 5.14. In particular, our study focuses on the effects induced by the two upper diagrams, since these are the ones containing the triple Higgs couplings λ_{hhh} (upper left) and λ_{hhH} (upper right diagram).

Similarly to the previous HL-LHC study, we employ the differential cross section distributions of the invariant mass of the final state Higgs-boson pair, m_{hh}, to study the effects of the two THCs involved in the cross section prediction. The contributions proportional to λ_{hhh} enter via a non-resonant diagram, similar to the SM case. Correspondingly, the largest effects of λ_{hhh} are expected at low values of m_{hh}, close to the kinematic threshold. On the other hand, the contributions proportional to the BSM THC, λ_{hhH}, enter via a (potentially) resonant diagram mediated by the heavy Higgs boson H. Therefore, the sensitivity to λ_{hhH} could be accessed by detecting a resonance structure in the invariant mass distribution around $m_{hh} = m_H$.

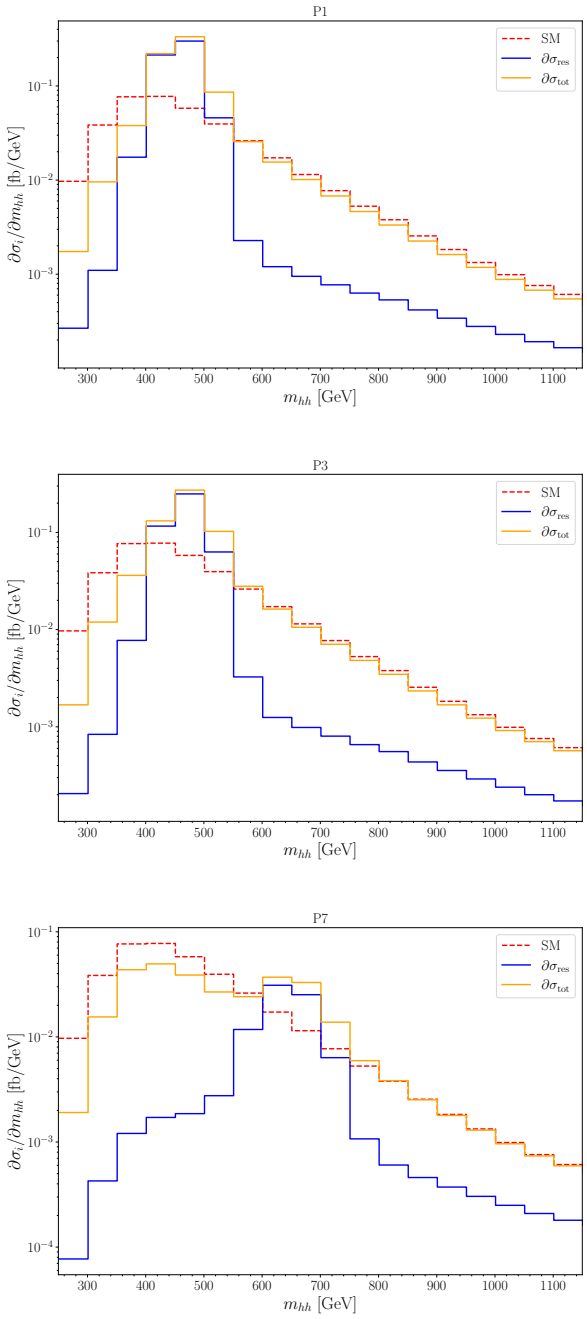

Figure 5.13: Differential cross section of the process $pp \to hh$ at the HL-LHC as a function of m_{hh} for the SM (red dashed line), compared to the distributions in P1 (region 1, upper plot), P3 (region 2, middle plot) and P7 (region 3, lower plot), see table 5.2. Orange (blue) lines show the result of the full calculation (taking into account only the resonant diagram).

5.3.1 Calculation of $e^+e^- \to Zhh$

We compute the unpolarized cross section for the double Higgs-strahlung process at the tree-level with the help of the public code `Madgraph5_aMC v3.5.7` [141]. The input model

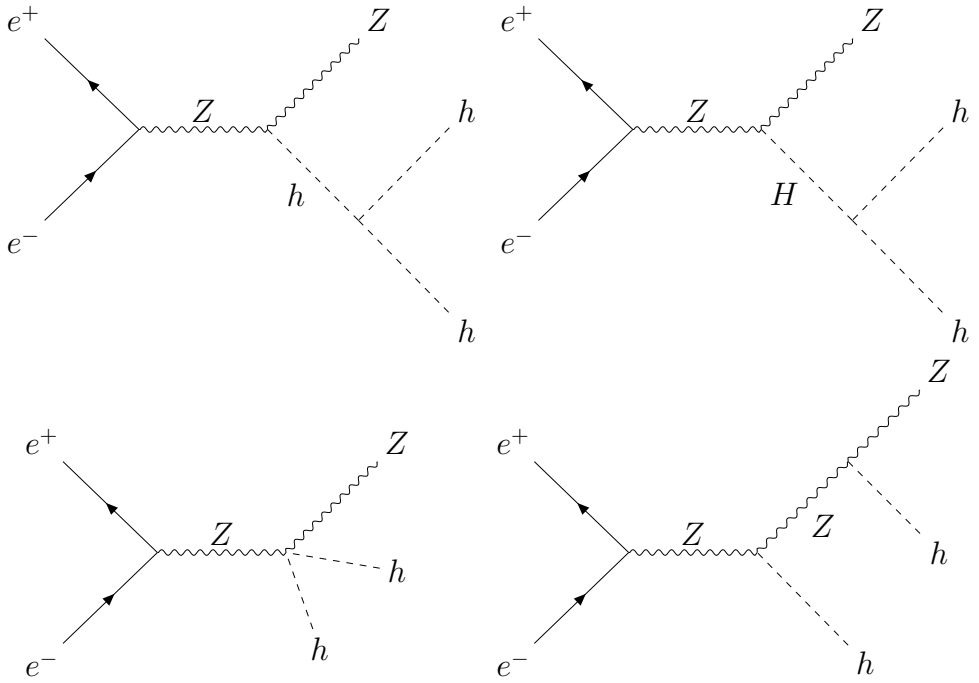

Figure 5.14: Generic Feynman diagrams contributing to the double Higgs-strahlung process $e^+e^- \to Zhh$ in the RxSM.

file of the RxSM required by `Madgraph` was obtained with the `Mathematica` package `SARAH-4.15` [314]. We compute the cross section for the ILC operating at a center-of-mass energy of $\sqrt{s} = 1000$ GeV (ILC1000) [139, 315, 316]. The choice for the large center-of-mass energy is due to the large values of m_H in our selected benchmark points, see table 5.2. In this work we assume an integrated luminosity of 8 ab^{-1}, as projected for the ILC1000 [139] (neglecting the possibility of polarized beams).[8]

Using our computational setup, we obtain a prediction for $\sigma(e^+e^- \to Zhh)$ of 0.12 fb in the SM for a center-of-mass energy of 1 TeV. At $\sqrt{s} = 500$ GeV we find $\sigma(e^+e^- \to Zhh) = 0.16\,\text{fb}$. For this center-of-mass energy it is expected to have a discovery of the di-Higgs-strahlung process at the 8σ level for an integrated luminosity of $4\,\text{ab}^{-1}$ (combining several polarization runs), corresponding to an experimental uncertainty of 16.8% [317]. Applying a simple scaling with the number of events, this yields a relative uncertainty of the cross section at $\sqrt{s} = 1000$ GeV of $\sim 10\%$ for an integrated luminosity of $8\,\text{ab}^{-1}$, which corresponds to a significance of close to 13σ.

5.3.2 Analysis of the total cross section

In fig. 5.15 we show the prediction of $\sigma(e^+e^- \to Zhh)$ in the RxSM in the λ_{hhH}-κ_λ benchmark plane, see section 5.1. It ranges from $\sim 0.16\,\text{fb}$ for smaller κ_λ and larger λ_{hhH}, up to $\sim 0.19\,\text{fb}$ for larger κ_λ and smaller λ_{hhH}. This means an increase of the RxSM pre-

[8] For $\sqrt{s} = 1000$ GeV the cross sections of $e^+e^- \to Zhh$ and $e^+e^- \to \nu\bar{\nu}hh$ are roughly of the same size [140]. Nevertheless, including the weak-boson fusion process (and possibly combining it with the Higgs-strahlung process), in view of the fact that the m_{hh} distributions are very different, is beyond the scope of our work and we focus on the Zhh final state.

diction in our benchmark plane between $\sim 33\%$ up to $\sim 60\%$ w.r.t. the SM. Another observation can be made for the contribution of the heavy Higgs-boson resonance. The size of the H-resonance contribution becomes smaller with increasing λ_{hhH}. The reason behind is the fact that in our benchmark plane the product of $(\sin \cdot \lambda_{hhH})$ is approximately constant. Larger λ_{hhH}, however, corresponds to larger m_H, leading to an overall suppression of $\sigma(e^+e^- \to ZH) \times \mathrm{BR}(H \to hh)$ for larger λ_{hhH}, as can be seen in the blue curves in fig. 5.16 and 5.17 below. On the other hand, the cross section leaving out the H-resonance contribution remains nearly constant over the plane, as can be observed in the green curves in fig. 5.16 and 5.17, below. In combination with the corresponding interference effects, the overall contribution of the heavy Higgs-boson resonance to the total cross section decreases with increasing λ_{hhH}, leading to smaller $\sigma(e^+e^- \to Zhh)$ for larger λ_{hhH} as observed in fig. 5.15. A more detailed analysis of the THC dependencies will be given in the next subsection. But it is interesting to note that a parameter space of the RxSM that was identified to yield a strong FOEWPT and is favorable for the di-Higgs production at the LHC [108] yields possibly detectable deviations from the SM also at e^+e^- colliders.

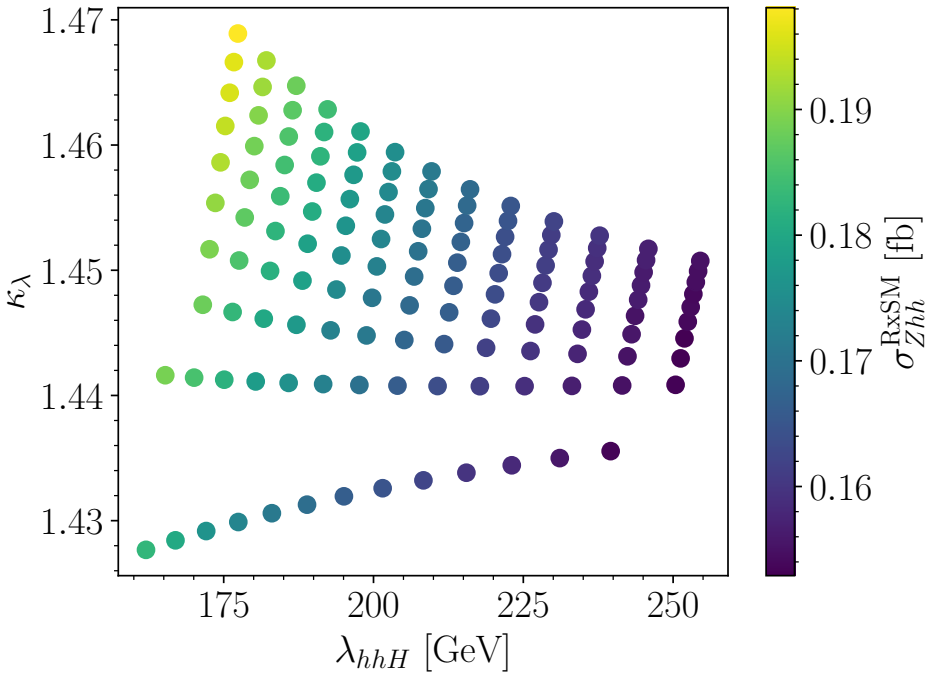

Figure 5.15: κ_λ-λ_{hhH} plane as a function of the total cross section for the process $e^+e^- \to Zhh$ at the ILC1000 in our benchmark plane.

While we also comment on the effects of λ_{hhh} on the total and the differential cross sections in the next subsection, a major focus of this work is to study the potential sensitivity of the ILC1000 to the THC, λ_{hhH}, via an analysis of the H resonance structure. In order to take into account in more detail the experimental analyses (i.e. detector effects, cuts, etc.) we focus on the main light Higgs-boson decay channel, $h \to b\bar{b}$, which in the SM has a BR of ~ 0.58. Consequently, the main experimental signature is given by four b-quark jets together with a Z boson. Therefore, following a similar strategy as in [65], we estimate the expected number of events with four b jets and one Z boson, denoted by $\bar{N}$, that

could be detected at the ILC1000 with the following expression:

$$\bar{N} = N \times \left(\mathrm{BR}(h \to b\bar{b})\right)^2 \times \mathscr{A} \times \epsilon_b^4 \,, \tag{5.7}$$

where N is the inclusive number of Zhh events predicted by the RxSM, as calculated above. We assume a conservative b-tagging efficiency of $\epsilon_b = 80\%$ for each final b-jet. We also assume the SM prediction for the $h \to b\bar{b}$ branching ratio (in good agreement with the LHC measurements). $\mathscr{A}$ is our estimation of the detector acceptance after applying the following pre-selection cuts to detect the final $4b + Z$ events (see [65] for details):

$$p_T^Z > 20 \text{ GeV}, \quad p_T^b > 20 \text{ GeV}, \quad |\eta_b| < 2, \quad \Delta R_{bb} > 0.4 \,, \tag{5.8}$$

where p_T^Z and p_T^b are the transverse momenta of the Z boson and each of the b quarks, respectively, η_b is the pseudo-rapidity of each of the b quarks, and ΔR_{bb} is the angular separation between two b quarks defined by $\Delta R_{ij} = \sqrt{(\eta_i - \eta_j)^2 + (\phi_i - \phi_j)^2}$, with ϕ being the azimuthal angle. We compute the acceptance $\mathscr{A}$ by simulating the process $e^+e^- \to Zhh$ with the subsequent decay $h \to b\bar{b}$ with and without the cuts defined in eq. (6.38) in `MadGraph` at the parton level. Therefore, the acceptance is given by the ratio of the predicted $4b + Z$ events with and without cuts. The obtained values of the acceptances $\mathscr{A}$ for the studied BPs are given in table 5.3.

	P1	P2	P3	P4	P5	P6	P7	P8
$\mathscr{A}$	0.696	0.695	0.697	0.698	0.699	0.698	0.698	0.699

Table 5.3: Detector acceptances at the ILC1000 (see text) for the benchmark points defined in Tab. 5.2.

To evaluate the potential sensitivity to the H resonant peak, and therefore to λ_{hhH}, of the ILC1000 we again use the "theoretical estimator" R defined in 5.5. Analogously to the HL-LHC case, $\bar{N}_i^R$ and $\bar{N}_i^C$ denote the expected events, as defined in 5.7, in the ith bin from the purely resonant diagrams (the one mediated by H and proportional to λ_{hhH}) and the non-resonant ones, respectively.[9] In contrast to the HL-LHC, in the case of the ILC1000 we define the signal region such that the difference between the resonant and non-resonant number of expected events is at least two, i.e.,

$$|\bar{N}_i^R - \bar{N}_i^C| > 2. \tag{5.9}$$

Here it should be kept in mind that, similar to the HL-LHC case, the "theoretical estimator" R gives an idea of how prominent the H resonance peak is relative to the continuum contributions from the non-resonant diagrams. Large values of R indicate more accessible H resonance peaks at the ILC1000, which implies higher chances of obtaining potential experimental information about the λ_{hhH} coupling. As in the case of the HL-LHC, R does not correspond to a true "experimental significance".

5.3.3 Analysis of m_{hh}

In this subsection we analyze the differential m_{hh} distributions for the eight benchmark points as defined in Tab. 5.2 at the ILC1000. In Fig. 5.16 and Fig. 5.17, we present the

[9] Note that the definition of $\bar{N}^C$ slightly differs from the one used in the HL-LHC analysis, where the SM curve was employed for N^C. However, this has a minor numerical impact.

results for P1–P4 and P5–P8, respectively. In each plot the red curve corresponds to the full RxSM prediction ($\sigma_{\mathrm{R}xSM}$), whereas the green and and the blue curves show, respectively, the results leaving out the resonant H diagram ($\sigma_{\mathrm{N}oH}$) and taking into account the resonant H diagram only (σ_{H}). For comparison, the green curve indicates the SM result (σ_{SM}). The values for the total cross sections are given in the legends, as well as the values of m_H, κ_λ and λ_{hhH} for each benchmark point. The binning of 6.7 GeV is chosen according to 5.9.

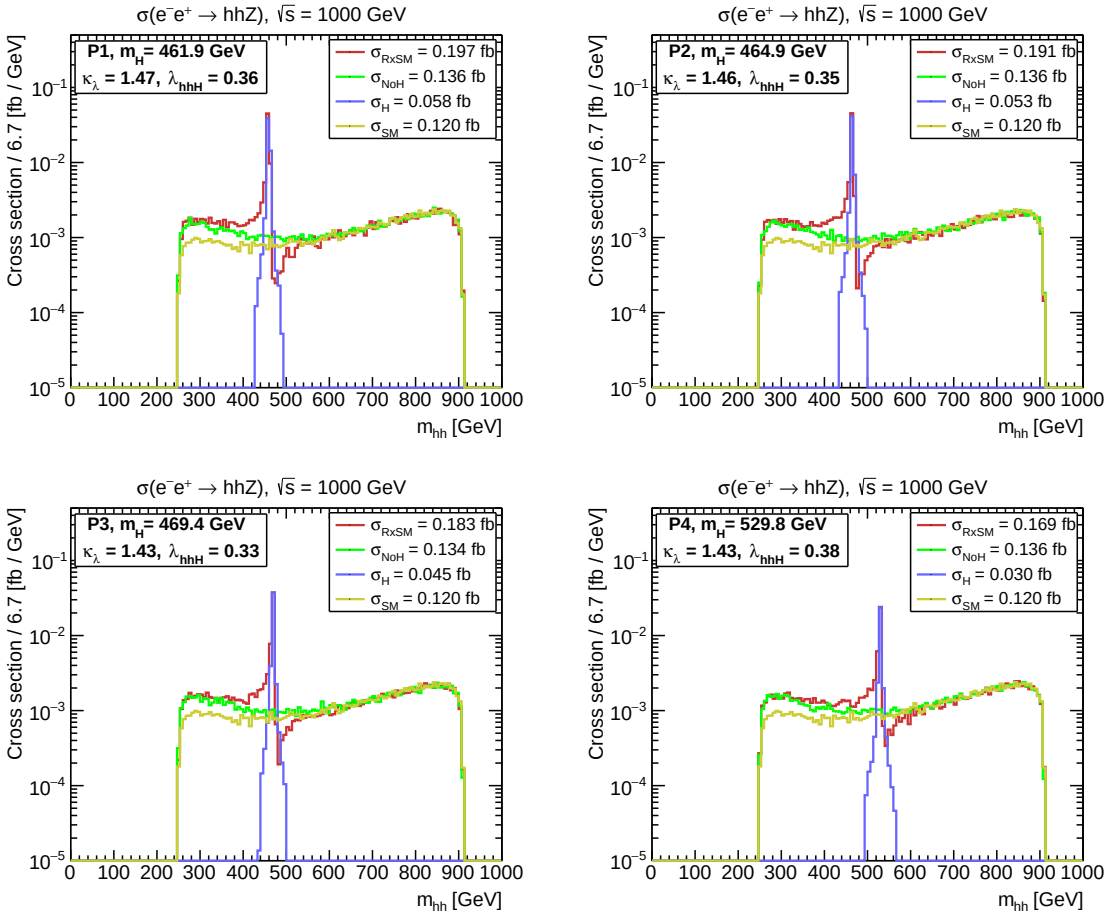

Figure 5.16: Differential cross section of the process $e^+e^- \to Zhh$ at the ILC1000 as a function of m_{hh} for the SM, for the pure heavy Higgs resonant contribution (blue), for the non-resonant contributions (green), and for the full RxSM calculation (red) for benchmark points P1, P2, P3, and P4.

Each benchmark point yields the same qualitative features, but differs in the location of the resonance structure, determined by the respective m_H value, the "height" of the resonance, determined by $\sin\theta \cdot \lambda_{hhH}$ and m_H, where the same holds for σ_{H}. For the two RxSM cross sections involving the h exchange ($\sigma_{\mathrm{R}xSM}$, $\sigma_{\mathrm{N}oH}$) κ_λ plays a significant role. The effects of $\kappa_\lambda \sim 1.45$ are best visible in the comparison of σ_{SM} and $\sigma_{\mathrm{N}oH}$. As expected (and also observed in [65]), the enhancement w.r.t. the SM is most pronounced for small m_{hh} and leads to an enhancement of the differential cross section prediction (corresponding to an enhanced total cross section, as known for $\kappa_\lambda > 1$ in the $e^+e^- \to Zhh$ channel). This effect is nearly identical for all eight benchmark points, as the value of κ_λ

varies only slightly over the whole benchmark plane.

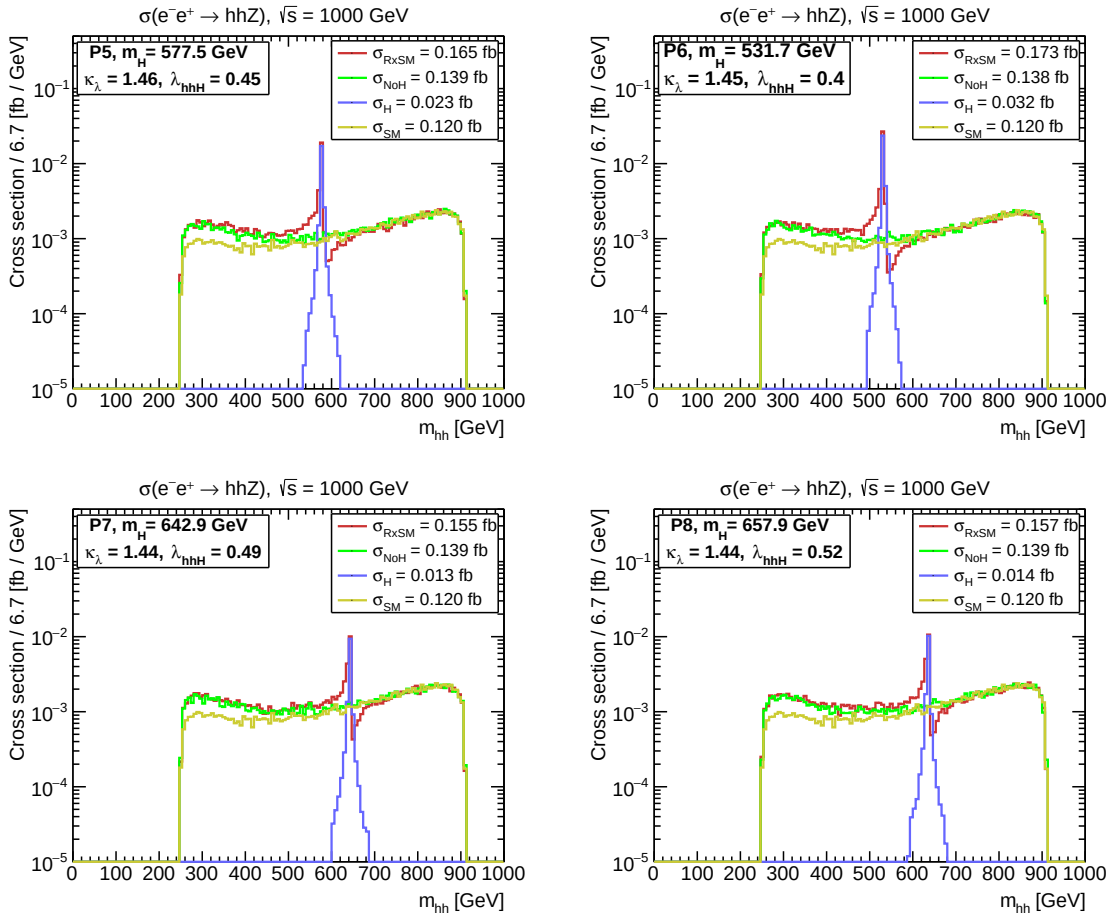

Figure 5.17: m_{hh} distribution for benchmark points P5 - P8, with the color coding as in Fig. 5.16.

The differential cross section that would be given by the pure resonance contribution is shown by the blue curves in Figs. 5.16 and (5.17). One can observe that this cross section is largest for smaller λ_{hhH}. As discussed above, this is due to the fact that in our benchmark plane larger λ_{hhH} corresponds to larger m_H, while $(\sin\theta \cdot \lambda_{hhH})$ remains approximately constant, leading to an overall suppression of the heavy Higgs-boson resonant contribution for larger λ_{hhH}. Taking into account the interference with the non-resonant diagrams, this yields a peak-dip structure around $m_{hh} = m_H$ as clearly visible in the red curves. However, corresponding to the size of the H-resonance contribution, also the peak-dip structure is strongest for smaller λ_{hhH}, which can be seen best in the R values: for each of the points we have evaluated the R value according to 5.5, which are summarized in Tab. 5.4. For an easier comparison, we also repeat in that table the values of m_H and λ_{hhH} for each benchmark point. It can be observed that within our benchmark plane (which is favored by the phenomenology of a strong FOEWPT) smaller values of λ_{hhH} lead (to a good approximation) to a stronger "signal" of the resonant H contribution and thus to a larger R value – in agreement with our discussion above. The overall substantially lower values of R as compared to the HL-LHC result on the one hand from a more realistic set-up including cuts etc., and on the other hand from the overall lower number of events

at the e^+e^- collider.

	P1	P2	P3	P4	P5	P6	P7	P8
R	31.58	29.52	24.09	19.67	14.27	16.68	6.16	7.35
m_H [GeV]	461.9	470.8	469.4	530.9	575.1	529.6	642.5	656.1
λ_{hhH}	0.36	0.35	0.33	0.38	0.45	0.40	0.49	0.52

Table 5.4: Values of the sensitivity R for the eight benchmark points, see Tab. 5.2.

5.4 Discussion of the results

In this chapter we have analyzed the impact of triple Higgs couplings on the production cross section of two ~ 125 GeV Higgs bosons at the HL-LHC and the ILC1000. We have chosen the Higgs singlet extension of the SM without Z_2 symmetry, the RxSM, as an example framework. We have focused on a benchmark plane that is phenomenologically favored, as it yields a strong FOEWPT in the early Universe (based on the original analysis of [108]), a key ingredient to fulfill one of the three Sakharov conditions required for EW baryogenesis to explain the baryon asymmetry of the Universe. We have ensured that the plane under consideration is in agreement with all theoretical and experimental constraints. By the requirement of the FOEWPT the benchmark plane is not in the alignment limit. The main idea of our work is to analyze the effect of the THC, encoded in $\kappa_\lambda \equiv \lambda_{hhh}/\lambda_{\rm SM}$, which is found to be $\kappa_\lambda \sim 1.45$, i.e. far away from the SM value. The second focus is on the impact of the BSM THC λ_{hhH}, which enters via a heavy Higgs-boson exchange with the subsequent decay $H \to hh$, in the di-Higgs production cross section both at the HL-LHC and at the ILC.

For the HL-LHC we calculated $\sigma(gg \to hh)$ as well as $\mathrm{d}\sigma(gg \to hh)/\mathrm{d}m_{hh}$ with the help of the code `HPAIR`, adapted to the RxSM. Within our phenomenologically favored benchmark plane the total cross section can deviate by more than 3σ from the SM cross section. In other parts of the benchmark plane the total cross section would remain experimentally indistinguishable from the SM prediction. Since we are away from the alignment limit, this equality between the RxSM and the SM results is due to (accidental) cancellations of the two BSM effects stemming from $\kappa_\lambda > 1$ and from the contribution of the heavy Higgs-boson resonance, inducing a dependence on λ_{hhH}.

This effect becomes better visible in the second part of the HL-LHC analysis, focusing on the m_{hh} distributions. These have been evaluated for eight benchmark points, distributed over our benchmark plane. For those we take into account a 15% detector smearing and a 50 GeV binning in m_{hh}. The eight benchmark points are compared with the SM expectation. A simple "theoretical significance", R, is employed (as defined and used in an 2HDM HL-LHC analysis in [64]) that allows us to estimate the "visibility" of the H-resonance peak w.r.t. the SM expectation. While this does not constitute a realistic experimental significance, this estimator allows to compare different benchmark points with each other (as well as collider energy and luminosity options). The large values found for R in our eight benchmark points, spanning the whole plane favored by the FOEWPT, give rise to the hope that also in a realistic experimental analysis a clear sign of the H-resonance peak can be observed, giving access to the BSM THC λ_{hhH}.

In the final step of our HL-LHC analysis in the RxSM we compare the m_{hh} distributions evaluated solely from the resonance diagram, but neglecting the two continuum diagrams

with the results from the full calculation (i.e. taking into account all contributing diagrams and in particular the corresponding interferences). This approach of neglecting the continuum diagrams is currently taken by the experimental collaborations, ATLAS and CMS, to obtain their results for resonant di-Higgs production. In the context of the 2HDM, in [138] it was demonstrated that this approach can lead to the erroneous exclusion of parameter points. In our RxSM analysis, comparing the m_{hh} distributions either neglecting or including the continuum diagrams, we find (as expected) strong and relevant differences between the two types of distributions. In particular, in the full calculation the "resonance peak" is substantially broadened. This sheds severe doubts that the current experimental data from resonant di-Higgs production at the LHC can readily be applied to our phenomenologically favored benchmark plane in the RxSM.

The analysis of the RxSM benchmark plane featuring a strong FOEWPT was subsequently extended to future e^+e^- colliders. As a particular example we focused on the ILC with a center-of-mass energy of $\sqrt{s} = 1000$ GeV, the ILC1000. As an integrated luminosity we assume $8\,\text{ab}^{-1}$. The center-of-mass energy is required since our benchmark points have m_H values that yield a resonant contribution (and thus possibly access to λ_{hhH}) only for $\sqrt{s} \gtrsim 600$ GeV (depending on m_H), making the ILC1000 the preferred option. Also for the ILC1000 we calculated the m_{hh} distributions for the eight benchmark points, evaluating the "theory estimator" R adapted to the e^+e^- case (following a corresponding 2HDM analysis in [66]). In this case also experimental cuts were included to take into account detector efficiencies etc. (again following [66]). We find that for the eight benchmark points, to a good approximation, smaller values of λ_{hhH} lead to a stronger "signal" of the resonant H-exchange contribution and thus to a larger R value. Overall substantially lower values of R as compared to the HL-LHC result are found. This results on the one hand from a more realistic set-up including cuts etc., and on the other hand from the overall lower number of events at the e^+e^- collider. Nevertheless, as in the HL-LHC case this gives rise to the hope that also in a realistic experimental analysis a clear sign of the H-resonance peak can be observed, giving access to the BSM THC λ_{hhH} at the ILC1000.

Overall, we conclude from this chapter that within the RxSM, depending on the values of the underlying Lagrangian parameters, a sizable resonant H contribution to the di-Higgs production cross section of two SM-like Higgs bosons can leave possibly visible effects in the m_{hh} distribution. This applies to the HL-LHC or to a future e^+e^- collider (taking the ILC1000 as a concrete example). This would pave the way for a first determination of a BSM THC, a step that is crucial for the reconstruction of the Higgs potential of the underlying BSM model.

Chapter 6

One-loop corrections to the trilinear Higgs coupling

¿Para qué sirve conseguirlo
si no puedes compartirlo
con la gente que quieres?

– Tía Elena

In the previous chapter, we investigated di-Higgs production as a probe of the extended scalar sector in the RxSM. That analysis showed that the process is directly sensitive to the trilinear Higgs couplings λ_{hhh} and λ_{hhH}, and that their interplay with resonant and non-resonant contributions can have a significant impact on both total rates and invariant-mass distributions. However, the discussion there relied on a leading-order treatment of these couplings.

As already discussed earlier in this thesis, such an approximation is not always sufficient in BSM scalar theories. A characteristic feature of extended Higgs sectors is that radiative corrections to Higgs self-couplings can be very large, in some cases even exceeding the corresponding tree-level deviations from the Standard Model. This is particularly relevant in scenarios with sizeable scalar interactions or non-decoupling effects, where loop contributions can substantially modify the phenomenological predictions. It is therefore necessary to go beyond the tree-level description and to compute the one-loop corrections to the trilinear Higgs couplings entering di-Higgs production.

The aim of this chapter is precisely to carry out this programme for the RxSM without an imposed $\mathbb{Z}2$ symmetry. To this end, we construct a complete on-shell renormalisation scheme for the scalar sector of the model and use it to derive one-loop predictions for the couplings λ_{hhh} and λ_{hhH}. A central point is that, to the best of our knowledge, this constitutes the first complete on-shell renormalisation scheme defined for the non-$\mathbb{Z}_2$-symmetric RxSM. In contrast to the $\mathbb{Z}_2$-symmetric case, the general model contains additional Lagrangian trilinear couplings, and these cannot be fully renormalised through the usual on-shell conditions based only on one- and two-point functions.

For this reason, the construction of a complete on-shell setup requires going beyond the standard treatment used in simpler extended scalar models. In particular, we impose

on-shell renormalisation conditions on scalar three-point functions in order to fix the counterterms associated with the $\mathbb{Z}_2$-breaking trilinear couplings of the scalar potential. This step is essential for completing the renormalisation scheme and for obtaining a fully scale-independent prediction for the one-loop-corrected trilinear Higgs couplings. In this sense, the use of on-shell conditions at the level of scalar three-point functions is one of the key theoretical developments of this chapter.

The chapter is organised as follows. We first present the calculational setup and the complete set of renormalisation conditions entering our on-shell scheme, including tadpoles, masses, field renormalisation constants, mixing angle and vacuum expectation values. We then turn to the renormalisation of the $\mathbb{Z}_2$-breaking trilinear parameters of the scalar potential, for which the new three-point on-shell conditions are introduced. After establishing the full renormalisation framework, we compute the one-loop-corrected trilinear Higgs couplings and analyse their numerical impact across the parameter space of the model. Finally, we study the phenomenological implications of these loop corrections for di-Higgs production, thereby extending the previous chapter to a level where the large radiative effects characteristic of BSM scalar models are consistently taken into account.

6.1 Calculational setup and on-shell renormalisation of the RxSM

In this chapter, we describe a setup to obtain one-loop predictions for the trilinear scalar couplings that enter in the calculation of the di-Higgs production cross-section, namely λ_{hhh} and λ_{hhH}, with a complete on-shell (OS) renormalisation of the RxSM.

Following the discussion in section 4.1.1, and taking into account the tadpole parameters, the RxSM contains nine parameters, in the mass basis, given by,

$$m_h^2,\, m_H^2,\, v,\, \alpha,\, v_S,\, \kappa_S,\, \kappa_{SH},\, t_\phi,\, t_S\,, \tag{6.1}$$

As can be seen from eq. (4.11), all nine parameters enter the tree-level expressions of λ_{hhh} and λ_{hhH}, i.e. a calculation at the one-loop level requires a renormalisation of all of them.

To fix our notation, in the rest of this section, for a given parameter x, we denote its bare value as x_B and its counterterm as $\delta_{\rm CT} x$. The tree-level value of x is denoted as $x^{(0)}$ and its one-loop renormalised value as $\hat{x}^{(1)}$. Lastly, $\delta^{(1)}x$ corresponds to the genuine (possibly divergent) one-loop correction to x, i.e. $\delta^{(1)}x \equiv \hat{x}^{(1)} - x^{(0)} - \delta^{(1)}_{\rm CT} x$.

In the following, we begin with the renormalisation of the tadpoles, as the choice of treatment of the tadpoles affects all subsequent steps. Next, we will discuss the renormalisation of the CP-even scalar masses and mixing angles, which relate to scalar two-point functions, before turning to the case of the VEVs. Finally, we will go beyond standard works on the renormalisation of extended Higgs sectors, and we will consider the renormalisation of the Lagrangian trilinear couplings κ_S and κ_{SH} as a necessary ingredient for the calculation of the one-loop corrections to the trilinear Higgs couplings.

6.1.1 Tadpole renormalisation

We employ in this work the standard tadpole scheme [318] (sometimes also referred to as "parameter-renormalised tadpole scheme") and define the tadpole counterterm via an

OS prescription. At one loop, the tadpole equations take the form

$$\hat{t}_i^{(1)} = t_i^{(0)} + \delta^{(1)} t_i + \delta_{\rm CT}^{(1)} t_i = 0 \quad \text{for } i = \phi,\ S\,. \tag{6.2}$$

Our scheme choice for the tadpoles results in

$$\delta_{\rm CT}^{(1)} t_i = -\delta^{(1)} t_i \quad \text{for } i = \phi,\ S\,. \tag{6.3}$$

This implies that the relations between parameters dictated by the tree-level tadpole equations $t_i^{(0)} = 0$ remain valid at the one-loop level, and the values of the VEVs at the minima of the tree-level and one-loop corrected potentials coincide. As a side remark, we note that for scenarios with heavy BSM scalars but very small values of the singlet VEV, unphysical enhancements can occur in the standard tadpole scheme, as pointed out in [319]. However, we will not consider such scenarios in our phenomenological investigations.

Finally, while the tadpole parameters t_ϕ and t_S and their corresponding counterterms are defined in the gauge eigenstate basis, the diagrammatic calculation of one-loop corrections to the tadpoles is most conveniently performed in the mass basis, i.e. $\delta^{(1)} t_h$ and $\delta^{(1)} t_H$. Therefore we need to perform the rotation

$$\begin{aligned} \delta_{\rm CT}^{(1)} t_\phi &= \sin\alpha\ \delta^{(1)} t_H - \cos\alpha\ \delta^{(1)} t_h\,, \\ \delta_{\rm CT}^{(1)} t_S &= -\cos\alpha\ \delta^{(1)} t_H - \sin\alpha\ \delta^{(1)} t_h\,. \end{aligned} \tag{6.4}$$

6.1.2 Two-point function renormalisation

In our work, we renormalise the two-point scalar functions on shell, following Refs. [72,80]. The first step is to renormalise the scalar fields, which are defined in the mass basis in eq. (4.7), by introducing the field renormalisation constant matrix $\sqrt{Z}$ that leads, at the one-loop order, to

$$\begin{pmatrix} h_B \\ H_B \end{pmatrix} = \sqrt{Z} \begin{pmatrix} \hat{h} \\ \hat{H} \end{pmatrix} = \begin{pmatrix} 1 + \frac{1}{2}\delta_{\rm CT}^{(1)} Z_{hh} & \frac{1}{2}\delta_{\rm CT}^{(1)} Z_{hH} \\ \frac{1}{2}\delta_{\rm CT}^{(1)} Z_{Hh} & 1 + \frac{1}{2}\delta_{\rm CT}^{(1)} Z_{HH} \end{pmatrix} \begin{pmatrix} \hat{h} \\ \hat{H} \end{pmatrix}, \tag{6.5}$$

where $\hat{h}$ (h_B) and $\hat{H}$ (H_B) are the renormalised (bare) CP-even scalar fields. For the renormalisation of the two-point function Γ this yields,

$$\begin{aligned} \hat{\Gamma}(p^2) = \begin{pmatrix} \hat{\Gamma}_{hh}(p^2) & \hat{\Gamma}_{hH}(p^2) \\ \hat{\Gamma}_{Hh}(p^2) & \hat{\Gamma}_{HH}(p^2) \end{pmatrix} &= i\sqrt{Z}^\dagger [p^2 1_{2\times 2} - \hat{M}_\phi^2 + \Sigma_{\phi,0}(p^2) - \delta_{\rm CT} M_\phi^2] \sqrt{Z} \\ &\approx i[p^2 1_{2\times 2} - \hat{M}_\phi^2 + \hat{\Sigma}_\phi(p^2)]\,, \end{aligned} \tag{6.6}$$

where in the second line we have only kept terms of one-loop order (hence the "≈"). In this equation, $\hat{\Sigma}_\phi(p^2)$ denotes the 2×2 symmetric matrix of renormalised self-energies, defined as

$$\hat{\Sigma}_\phi(p^2) \equiv \begin{pmatrix} \hat{\Sigma}_{hh}(p^2) & \hat{\Sigma}_{hH}(p^2) \\ \hat{\Sigma}_{Hh}(p^2) & \hat{\Sigma}_{HH}(p^2) \end{pmatrix}, \tag{6.7}$$

while $\hat{M}_\phi^2$ is the renormalised mass matrix. The renormalisation conditions in the OS scheme are as follows:

1. The mixing of particles with the same quantum numbers vanishes at $p^2 = m^2_{h,H}$, so that
$$\mathrm{Re}[\hat{\Sigma}_{hH}(m_h^2)] = \mathrm{Re}[\hat{\Sigma}_{Hh}(m_H^2)] = 0. \tag{6.8}$$

2. The mass parameters $m^2_{h,H}$ are defined as being the real parts of the poles of the renormalised propagator $\hat{G}_\phi(p^2)$ (the inverse of the two-point function). This implies that
$$\mathrm{Re}[\hat{\Sigma}_{hh}(m_h^2)] = \mathrm{Re}[\hat{\Sigma}_{HH}(m_H^2)] = 0. \tag{6.9}$$

3. The physical fields are properly normalised through fixing the residue of the propagator at its pole to i. This gives
$$\mathrm{Re}\left[\frac{\partial\hat{\Sigma}_{hh}(p^2)}{\partial p^2}\,\Big|_{p^2=m_h^2}\right] = \mathrm{Re}\left[\frac{\partial\hat{\Sigma}_{HH}(p^2)}{\partial p^2}\,\Big|_{p^2=m_H^2}\right] = 0. \tag{6.10}$$

From eq. (6.9) the mass counterterms can be derived as

$$\begin{aligned}\delta^{(1)}_{\mathrm{CT}} m_h^2 &= \mathrm{Re}[\Sigma_{hh}(m_h^2)]\,,\\ \delta^{(1)}_{\mathrm{CT}} m_H^2 &= \mathrm{Re}[\Sigma_{HH}(m_H^2)]\,.\end{aligned} \tag{6.11}$$

In turn from eq. (6.8) and eq. (6.10) we can obtain the field counterterms

$$\begin{aligned}\delta^{(1)}_{\mathrm{CT}} Z_{hh} &= -\mathrm{Re}\left[\frac{\partial\Sigma_{hh}(p^2)}{\partial p^2}\right]_{p^2=m_h^2}\,,\\ \delta^{(1)}_{\mathrm{CT}} Z_{HH} &= -\mathrm{Re}\left[\frac{\partial\Sigma_{HH}(p^2)}{\partial p^2}\right]_{p^2=m_H^2}\,,\\ \delta^{(1)}_{\mathrm{CT}} Z_{hH} &= \frac{\mathrm{Re}[\Sigma_{hH}(m_H^2)]}{m_h^2 - m_H^2}\,,\\ \delta^{(1)}_{\mathrm{CT}} Z_{Hh} &= \frac{\mathrm{Re}[\Sigma_{Hh}(m_h^2)]}{m_H^2 - m_h^2}\,.\end{aligned} \tag{6.12}$$

6.1.3 Mixing angle renormalisation

In order to renormalise the mixing angle, we choose in this work to use the KOSY scheme [72,74]. The idea behind this scheme is to renormalise the rotation matrix by temporarily switching to the gauge basis, performing a renormalisation transformation of the fields (in the gauge basis) and of the mixing angle, and then relating this to the renormalisation of the fields in the mass basis — c.f. eq. (6.5). We begin with

$$\begin{aligned}&\begin{pmatrix} h_B \\ H_B \end{pmatrix} = \mathrm{R}^{\mathrm{T}}_{\alpha^0}\begin{pmatrix} s_B \\ \phi_B \end{pmatrix} \to \mathrm{R}^{\mathrm{T}}_{\delta_{\mathrm{CT}}\alpha}\mathrm{R}^{\mathrm{T}}_{\hat{\alpha}}\begin{pmatrix} s_B \\ \phi_B \end{pmatrix} = \mathrm{R}^{\mathrm{T}}_{\delta_{\mathrm{CT}}\alpha}\mathrm{R}^{\mathrm{T}}_{\hat{\alpha}}\sqrt{Z_{\phi,s}}\begin{pmatrix} \hat{s} \\ \hat{\phi} \end{pmatrix} =\\ &= \mathrm{R}^{\mathrm{T}}_{\delta_{\mathrm{CT}}\alpha}\mathrm{R}^{\mathrm{T}}_{\hat{\alpha}}\sqrt{Z_{\phi,s}}\mathrm{R}_{\hat{\alpha}}\mathrm{R}^{\mathrm{T}}_{\hat{\alpha}}\begin{pmatrix} \hat{s} \\ \hat{\phi} \end{pmatrix} = \mathrm{R}^{\mathrm{T}}_{\delta_{\mathrm{CT}}\alpha}\mathrm{R}^{\mathrm{T}}_{\hat{\alpha}}\sqrt{Z_{\phi,s}}\mathrm{R}_{\hat{\alpha}}\begin{pmatrix} \hat{h} \\ \hat{H} \end{pmatrix} = \sqrt{\hat{Z}}\begin{pmatrix} \hat{h} \\ \hat{H} \end{pmatrix}.\end{aligned} \tag{6.13}$$

Expanding in the mass basis the WFR matrix $\mathrm{R}^{\mathrm{T}}_{\hat{\alpha}}\sqrt{Z_{\phi,s}}\mathrm{R}_{\hat{\alpha}}$ and the counterterm rotation matrix $\mathrm{R}^{\mathrm{T}}_{\delta_{\mathrm{CT}}\alpha}$, and then equating this equation to eq. (6.5), we obtain

$$\sqrt{\tilde{Z}} = \mathrm{R}^{\mathrm{T}}_{\delta_{\mathrm{CT}}\alpha}\mathrm{R}^{\mathrm{T}}_{\hat{\alpha}}\sqrt{Z_{\phi,s}}\mathrm{R}_{\hat{\alpha}} = \mathrm{R}^{\mathrm{T}}_{\delta_{\mathrm{CT}}\alpha}\begin{pmatrix} 1+\frac{\delta^{(1)}_{\mathrm{CT}}Z_{hh}}{2} & \delta_{\mathrm{CT}}C_{hH} \\ \delta_{\mathrm{CT}}C_{Hh} & 1+\frac{\delta^{(1)}_{\mathrm{CT}}Z_{HH}}{2}\end{pmatrix} \approx$$
$$\approx \begin{pmatrix} 1+\frac{\delta^{(1)}_{\mathrm{CT}}Z_{hh}}{2} & \delta^{(1)}_{\mathrm{CT}}C_{hH} - \delta^{(1)}_{\mathrm{CT}}\alpha \\ \delta^{(1)}_{\mathrm{CT}}C_{Hh} + \delta^{(1)}_{\mathrm{CT}}\alpha & 1+\frac{\delta^{(1)}_{\mathrm{CT}}Z_{HH}}{2}\end{pmatrix} \equiv \sqrt{Z}\,, \tag{6.14}$$

where $\delta^{(1)}_{\mathrm{CT}}C_{hH}$ and $\delta^{(1)}_{\mathrm{CT}}C_{Hh}$ come from the expansion of the off-diagonal terms of the WFR matrix $\mathrm{R}^{\mathrm{T}}_{\hat{\alpha}}\sqrt{Z_{\phi,s}}\mathrm{R}_{\hat{\alpha}}$. In the second line of the equation above, we have again only kept terms of one-loop order. We can observe that the diagonal terms are identical, while for the non-diagonal terms we find,

$$\begin{aligned}\delta^{(1)}_{\mathrm{CT}}C_{hH} - \delta^{(1)}_{\mathrm{CT}}\alpha &= \frac{\delta^{(1)}_{\mathrm{CT}}Z_{hH}}{2}\,,\\ \delta^{(1)}_{\mathrm{CT}}C_{Hh} + \delta^{(1)}_{\mathrm{CT}}\alpha &= \frac{\delta^{(1)}_{\mathrm{CT}}Z_{Hh}}{2}\,.\end{aligned} \tag{6.15}$$

To extract an expression for $\delta^{(1)}_{\mathrm{CT}}\alpha$ from the equations above, at least one more relation between $\delta^{(1)}_{\mathrm{CT}}C_{hH}$ and $\delta^{(1)}_{\mathrm{CT}}C_{Hh}$ is necessary. Different choices for this have been discussed in the literature: while earlier works [72] imposed that the matrix $Z_{\phi,s}$ be symmetric — thus leading to $\delta^{(1)}_{\mathrm{CT}}C_{hH} = \delta^{(1)}_{\mathrm{CT}}C_{Hh}$ — subsequent work [74] demonstrated that this choice can lead to gauge dependences in renormalised mixing angles. Moreover, these works showed that one can instead use the additional degree of freedom from keeping $\delta^{(1)}_{\mathrm{CT}}C_{hH}$ and $\delta^{(1)}_{\mathrm{CT}}C_{Hh}$ non equal to absorb the gauge dependence. It should however be noted that this issue of gauge dependences only occurs in the renormalisation of extended CP-odd scalar sector, see [74]. Because the RxSM only extends the CP-even scalar sector, but not the CP-odd one, we do not require separate $\delta^{(1)}_{\mathrm{CT}}C_{hH} \neq \delta^{(1)}_{\mathrm{CT}}C_{Hh}$, and we can simply impose that

$$\delta^{(1)}_{\mathrm{CT}}C_{hH} = \delta^{(1)}_{\mathrm{CT}}C_{Hh} \equiv \delta^{(1)}_{\mathrm{CT}}C\,. \tag{6.16}$$

Using the expressions of the field strength counter terms $\delta^{(1)}_{\mathrm{CT}}Z_{hH}$ and $\delta^{(1)}_{\mathrm{CT}}Z_{Hh}$ from eq. (6.12), the following expression can finally be obtained for the mixing angle counterterm

$$\delta^{(1)}_{\mathrm{CT}}\alpha = \frac{1}{2(m_H^2 - m_h^2)}\mathrm{Re}[\Sigma_{hH}(m_h^2) + \Sigma_{hH}(m_H^2)]\,. \tag{6.17}$$

6.1.4 Renormalisation of the VEVs

Electroweak VEV

Since the electroweak sector of the RxSM is identical to the SM one, we use the same procedure to renormalise the EW VEV as in the SM. Following the convention in `anyH3` [89] (which we will use below for the calculation of trilinear scalar couplings), we relate the EW VEV to the W- and Z-boson masses as well as α_{EM} (in the Thompson limit),

$$v^2 = \frac{m_W^2}{\pi\alpha_{\mathrm{EM}}}\left(1 - \frac{m_W^2}{m_Z^2}\right)\,. \tag{6.18}$$

It follows that the EW VEV counterterm can be expressed, like in the SM, as (see also [74])

$$\frac{\delta^{(1)}_{\rm CT} v}{v} = \frac{1}{2}\left[\frac{\delta^{(1)}_{\rm CT} m_W^2}{m_W^2} + \frac{c_{\rm w}^2}{s_{\rm w}^2}\left(\frac{\delta^{(1)}_{\rm CT} m_Z^2}{m_Z^2} - \frac{\delta^{(1)}_{\rm CT} m_W^2}{m_W^2}\right) - \frac{\delta^{(1)}_{\rm CT}\alpha_{\rm EM}}{\alpha_{\rm EM}}\right]. \tag{6.19}$$

where $s_{\rm w}$ and $c_{\rm w}$ are the sine and cosine of the weak mixing angle. Adopting an OS renormalisation of the EW input parameters, we have

$$\delta^{(1)}_{\rm CT} m_V^2 = {\rm Re}\big[\Sigma^T_{VV}(p^2 = m_V^2)\big]\,, \quad \text{for } V = W,\, Z\,, \tag{6.20}$$

where $\Sigma^T_{VV}(p^2)$ is the transverse part of the one-loop gauge boson self-energy, defined through the standard decomposition $\Sigma^{\mu\nu}_{VV}(p^2) = (g^{\mu\nu} - p^\mu p^\nu/p^2)\,\Sigma^T_{VV}(p^2) + p^\mu p^\nu/p^2\,\Sigma^L_{VV}(p^2)$. Moreover,

$$\delta^{(1)}_{\rm CT}\alpha_{\rm EM} = \frac{1}{2}\Pi_{\gamma\gamma}(p^2 = 0) + \frac{2 s_{\rm w}}{c_{\rm w}}\frac{\Sigma^T_{\gamma Z}(p^2 = 0)}{m_Z^2}\,, \tag{6.21}$$

where $\Pi_{\gamma\gamma}$ is defined from the (one-loop) photon self-energy as $\Sigma^{\mu\nu}_{\gamma\gamma}(p^2) = (p^2 g^{\mu\nu} - p^\mu p^\nu)\Pi_{\gamma\gamma}(p^2)$. Combining all these expressions, we obtain

$$\frac{\delta^{(1)}_{\rm CT} v}{v} = \frac{1}{2}\left[\frac{s_{\rm w}^2 - c_{\rm w}^2}{s_W^2}\frac{{\rm Re}\big[\Sigma^T_{WW}(m_W^2)\big]}{m_W^2} + \frac{c_{\rm w}^2}{s_{\rm w}^2}\frac{{\rm Re}\big[\Sigma^T_{ZZ}(m_Z^2)\big]}{m_Z^2} - \Pi_{\gamma\gamma}(0) - \frac{2 s_{\rm w}}{c_{\rm w}}\frac{\Sigma^T_{\gamma Z}(0)}{m_Z^2}\right]. \tag{6.22}$$

Singlet VEV

The one-loop RGE of the singlet VEV can be shown to vanish in the RxSM, which implies that the corresponding counterterm, $\delta_{\rm CT} v_S$, contains no UV divergence. A theoretical understanding for this can be obtained from, e.g., [320], where it was shown that, when the Lagrangian is invariant under a rigid gauge transformation of the field that acquires a VEV, the counterterm of said VEV can at most contain UV-finite contributions. This is precisely the case for the $SU(2)_L$ gauge singlet S in the RxSM. Consequently, $\delta^{(1)}_{\rm CT} v_S$ is UV-finite and, we choose (as we work in the standard tadpole scheme) to set the finite part of this counterterm to zero, i.e.

$$\delta^{(1)}_{\rm CT} v_S = 0\,. \tag{6.23}$$

6.1.5 Diagrammatic calculation of trilinear scalar couplings

Before we turn to the last part of our renormalisation procedure, we have to remember the approach that we are following in this chapter to compute the corrections to the trilinear Higgs couplings. We perform a full one-loop diagrammatric calculations of both λ_{hhh} and λ_{hhH}, employing the public code `anyH3` [89, 99]. We note that, throughout this chapter, we compute predictions for the trilinear scalar couplings with all external momenta set to zero, given that these momentum-independent quantities are passed as modified couplings to `HPAIR`[1] [64, 69, 137, 300–302] to calculate total cross-sections and

[1] `HPAIR` is the code that we use to perform the di-Higgs production cross-section computations in the HL-LHC and is introduced in Sec. 5.

differential distributions for di-Higgs production.[2] The different contributions to the renormalised trilinear Higgs couplings at the one-loop level, which we denote $\hat{\lambda}^{(1)}_{ijk}$ (where $i,j,k = h$ or H), can be divided between the tree level contribution $\lambda^{(0)}_{ijk}$, the one-loop one-particle-irreducible (1PI) vertex correction diagrams $\delta^{(1)}_{\text{gen}}\lambda_{ijk}$, the external-leg corrections $\delta^{(1)}_{\text{wfr}}\lambda_{ijk}$, and the one-loop counterterm $\delta^{(1)}_{\text{CT}}\lambda_{ijk}$. Diagrams with insertions of one-loop tadpoles do not appear in our setup, because we employ an OS renormalisation of tadpoles (as discussed in section 6.1.1). The different contributions can be represented in terms of Feynman diagrams as

$$\hat{\lambda}^{(1)}_{ijk} = -\hat{\Gamma}^{(1)}_{h_i,h_j,h_k}(0,0,0) = \lambda^{(0)}_{ijk} + \delta^{(1)}_{\text{gen}}\lambda_{ijk} + \delta^{(1)}_{\text{wfr}}\lambda_{ijk} + \delta^{(1)}_{\text{CT}}\lambda_{ijk} =$$

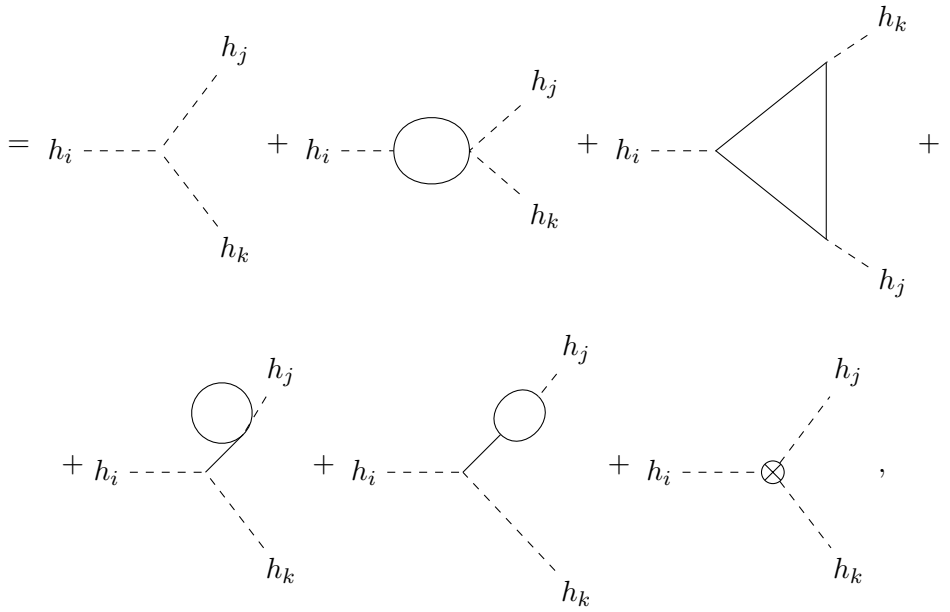

(6.24)

where $\hat{\Gamma}_{ijk}(p_1^2, p_2^2, p_3^2)$ denotes the renormalised scalar three-point function for external states ijk, evaluated for external momenta p_1^2, p_2^2 and p_3^2 (here all taken to zero) respectively. Furthermore, $\lambda^{(0)}_{ijk}$ corresponds to the first diagram, $\delta^{(1)}_{\text{gen}}\lambda_{ijk}$ to the second and third ones (first line), $\delta^{(1)}_{\text{wfr}}\lambda_{ijk}$ to the fourth and fifth diagrams (second line), and $\delta^{(1)}_{\text{CT}}\lambda_{ijk}$ to the last diagram. In the above diagrams the solid lines do not only indicate fermions, but serve to represent *any* possible particle of the RxSM — scalar, fermion, gauge boson or ghost.

The counterterms $\delta_{\text{CT}}\lambda_{ijk}$ can be computed in terms of the counterterms for each of the parameters on which the couplings depend, as

$$\delta^{(1)}_{\text{CT}}\lambda_{ijk} = \sum_x \delta^{(1)}_{\text{CT}} x \frac{\partial \lambda^{(0)}_{ijk}}{\partial x}\,, \tag{6.25}$$

where $x \in \{m_h^2, m_H^2, v, \alpha, \kappa_S, \kappa_{SH}, t_\phi, t_S\}$.

[2] The impact of the momentum dependence in λ_{hhh} and λ_{hhH} on the total di-Higgs cross-section and corresponding distributions is investigated in [99] in the context of various models, including a 2HDM. The effect on distribution shapes is found to be typically moderate [98], while modifications of the total cross-sections can reach up to $\mathcal{O}(20\%)$ — this is to a large extent due to the modification of the height of the resonant peak from the H scalar.

6.1.6 Renormalisation of the $\mathbb{Z}_2$-breaking couplings

At this point, we have already summarised the OS [3] conditions that are commonly used for singlet extensions of the SM (or similarly for the 2HDM). However, two more parameters still need to be renormalised, namely the Lagrangian trilinear couplings κ_S and κ_{SH}. These two additional degrees of freedom constitute a significant difference with the case of the $\mathbb{Z}_2$-symmetric singlet extension of the SM, in which a complete OS renormalisation of the model can be defined exclusively in terms of one- and two-point functions. In contrast, in the RxSM, we have now exhausted the scalar two-point functions that could be use to define OS renormalisation conditions. While an $\overline{\text{MS}}$ renormalisation of κ_S and κ_{SH} is in principle an option (and this is what is generally done in studies of the RxSM [74, 97]), this would leave a renormalisation scale dependence in our results for $\hat{\lambda}^{(1)}_{hhh}$ and $\hat{\lambda}^{(1)}_{hhH}$. Such a renormalisation scale dependence could of course be mitigated by including the renormalisation group running of the $\overline{\text{MS}}$ couplings in our setup. We prefer, however, to avoid this entirely by defining OS renormalisation conditions for κ_S and κ_{SH} in terms of scalar three-point functions, which constitutes one of the main new theoretical aspects of this paper.[4]

The main objective of this calculation is to obtain the leading BSM contributions to the di-Higgs production process at NLO, which only involves the first two out of the four trilinear scalar couplings that exist in the RxSM, namely λ_{hhh}, λ_{hhH}, λ_{hHH} and λ_{HHH}. Therefore, we can use the two trilinear Higgs couplings that do not enter in the di-Higgs production process, i.e. λ_{hHH} and λ_{HHH}, in order to define two on-shell renormalisation conditions for κ_S and κ_{SH}. We choose to impose

$$\hat{\lambda}^{(1)}_{hHH} \stackrel{!}{=} \lambda^{(0)}_{hHH}\,, \tag{6.26}$$

$$\hat{\lambda}^{(1)}_{HHH} \stackrel{!}{=} \lambda^{(0)}_{HHH}\,. \tag{6.27}$$

The two renormalised couplings can be expanded as

$$\begin{aligned}
\hat{\lambda}^{(1)}_{hHH} &= \lambda^{(0)}_{hHH} + \delta^{(1)}_{\text{gen}}\lambda_{hHH} + \delta^{(1)}_{\text{wfr}}\lambda_{hHH} + \delta^{(1)}_{\text{CT},m^2_\varphi}\lambda_{hHH} + \delta^{(1)}_{\text{CT},v}\lambda_{hHH} + \delta^{(1)}_{\text{CT},t_\varphi}\lambda_{hHH} + \\
&\quad + \delta^{(1)}_{\text{CT},\alpha}\lambda_{hHH} + \delta^{(1)}_{\text{CT}}\kappa_S\frac{\partial\lambda^{(0)}_{hHH}}{\partial\kappa_S} + \delta^{(1)}_{\text{CT}}\kappa_{SH}\frac{\partial\lambda^{(0)}_{hHH}}{\partial\kappa_{SH}} \stackrel{!}{=} \lambda^{(0)}_{hHH}\,, \\
\hat{\lambda}^{(1)}_{HHH} &= \lambda^{(0)}_{HHH} + \delta^{(1)}_{\text{gen}}\lambda_{HHH} + \delta^{(1)}_{\text{wfr}}\lambda_{HHH} + \delta^{(1)}_{\text{CT},m^2_\varphi}\lambda_{HHH} + \delta^{(1)}_{\text{CT},v}\lambda_{HHH} + \delta^{(1)}_{\text{CT},t_\varphi}\lambda_{HHH} + \\
&\quad + \delta^{(1)}_{\text{CT},\alpha}\lambda_{HHH} + \delta^{(1)}_{\text{CT}}\kappa_S\frac{\partial\lambda^{(0)}_{HHH}}{\partial\kappa_S} + \delta^{(1)}_{\text{CT}}\kappa_{SH}\frac{\partial\lambda^{(0)}_{HHH}}{\partial\kappa_{SH}} \stackrel{!}{=} \lambda^{(0)}_{HHH}\,,
\end{aligned} \tag{6.28}$$

where $\delta^{(1)}_{\text{CT},x}\lambda_{ijk} \equiv \delta^{(1)}_{\text{CT}}x\frac{\partial\lambda^{(0)}_{ijk}}{\partial x}$ represents the contribution to the total one-loop counterterm for the coupling λ_{ijk} that comes from the parameter x. Furthermore, we have used $\delta^{(1)}_{\text{CT},m^2_\varphi}\lambda_{ijk}$ and $\delta^{(1)}_{\text{CT},t_\varphi}\lambda_{ijk}$ as shorthand notations for the sum of all the contributions

[3] We note that among our chosen renormalisation conditions, all are OS conditions except the one for the singlet VEV v_S. Given that v_S does not require any renormalisation in the RxSM (even the UV divergence of its counterterm vanishes), we will thus refer to our overall renormalisation scheme as an OS scheme, although this constitutes a slight abuse of naming concerning v_S.

[4] Different options for the renormalisation of Lagrangian trilinear couplings were discussed e.g. in the context of the MSSM in [321].

from mass and tadpole counterterms, respectively. The tree level parts on both sides of the equalities cancel with each other, and then we can rewrite the above equations as

$$\begin{aligned}
&\delta^{(1)}_{\text{gen+wfr}}\lambda_{hHH} + \sum_{x\in\{m^2_\varphi,v,t_\varphi,\alpha\}} \delta^{(1)}_{\text{CT},x}\lambda_{hHH} + \delta^{(1)}_{\text{CT}}\kappa_S \frac{\partial\lambda^{(0)}_{hHH}}{\partial\kappa_S} + \delta^{(1)}_{\text{CT}}\kappa_{SH}\frac{\partial\lambda^{(0)}_{hHH}}{\partial\kappa_{SH}} = 0\,,\\
&\delta^{(1)}_{\text{gen+wfr}}\lambda_{HHH} + \sum_{x\in\{m^2_\varphi,v,t_\varphi,\alpha\}} \delta^{(1)}_{\text{CT},x}\lambda_{HHH} + \delta^{(1)}_{\text{CT}}\kappa_S \frac{\partial\lambda^{(0)}_{HHH}}{\partial\kappa_S} + \delta^{(1)}_{\text{CT}}\kappa_{SH}\frac{\partial\lambda^{(0)}_{HHH}}{\partial\kappa_{SH}} = 0\,.
\end{aligned} \tag{6.29}$$

We thus have a system of two equations with two unknowns, $\delta^{(1)}_{\text{CT}}\kappa_S$ and $\delta^{(1)}_{\text{CT}}\kappa_{SH}$, which we can solve to obtain our on-shell counterterms. These read

$$\begin{aligned}
\delta^{(1)}_{\text{CT}}\kappa_S &= \frac{\frac{\partial\lambda^{(0)}_{HHH}}{\partial\kappa_{SH}}(\delta^{(1)}_{\text{gen+wfr}}\lambda_{hHH} + \sum_x \delta^{(1)}_{\text{CT},x}\lambda_{hHH}) - \frac{\partial\lambda^{(0)}_{hHH}}{\partial\kappa_{SH}}(\delta^{(1)}_{\text{gen+wfr}}\lambda_{HHH} + \sum_x \delta^{(1)}_{\text{CT},x}\lambda_{HHH})}{\frac{\partial\lambda^{(0)}_{hHH}}{\partial\kappa_{SH}}\frac{\partial\lambda^{(0)}_{HHH}}{\partial\kappa_S} - \frac{\partial\lambda^{(0)}_{hHH}}{\partial\kappa_S}\frac{\partial\lambda^{(0)}_{HHH}}{\partial\kappa_{SH}}}\,,\\
\delta^{(1)}_{\text{CT}}\kappa_{SH} &= \frac{\frac{\partial\lambda^{(0)}_{hHH}}{\partial\kappa_S}(\delta^{(1)}_{\text{gen+wfr}}\lambda_{HHH} + \sum_x \delta^{(1)}_{\text{CT},x}\lambda_{HHH}) - \frac{\partial\lambda^{(0)}_{HHH}}{\partial\kappa_S}(\delta^{(1)}_{\text{gen+wfr}}\lambda_{hHH} + \sum_x \delta^{(1)}_{\text{CT},x}\lambda_{hHH})}{\frac{\partial\lambda^{(0)}_{hHH}}{\partial\kappa_{SH}}\frac{\partial\lambda^{(0)}_{HHH}}{\partial\kappa_S} - \frac{\partial\lambda^{(0)}_{hHH}}{\partial\kappa_S}\frac{\partial\lambda^{(0)}_{HHH}}{\partial\kappa_{SH}}}\,.
\end{aligned} \tag{6.30}$$

As a final remark, it should be noted that eqs. (6.26) and (6.27) are of course not the only possible choices of renormalisation conditions that could be employed for κ_S and κ_{SH}. In principle, we could have imposed similar conditions on λ_{hhh} and λ_{hhH}. With such a choice, the BSM corrections to the di-Higgs production processes $gg \to hh$ and $e^+e^- \to Zhh$, investigated in section 6.3, would be entirely absorbed into the finite parts of the counterterms $\delta^{(1)}_{\text{CT}}\kappa_S$ and $\delta^{(1)}_{\text{CT}}\kappa_{SH}$. In turn, the investigation of these processes would be identical to the analysis with tree-level couplings in [246].

6.1.7 Dependence on the renormalisation scale Q

Having now determined a complete set of counterterms, we can compute the one-loop corrections to λ_{hhh} and λ_{hhH} in our OS scheme.[5] A powerful check of the consistency of our scheme definition is offered by the renormalisation scale independence of our results, as these should only depend on OS-renormalised quantities that are, by definition, scale independent. To check this we have considered two benchmark points from [246], which are given in table 6.1.

	m_h [GeV]	m_H [GeV]	$\cos\alpha$	v_S [GeV]	κ_S [GeV]	κ_{SH} [GeV]
BPI	125.1	327.0	0.974	60.9	−361.0	−245.0
BPII	125.1	511.0	0.986	40.7	−618.0	−372.0

Table 6.1: Two benchmark points of the RxSM, taken from [246].

We have computed the dependence of each of the contributions entering the calculation of both couplings, as well as their sum, on the renormalisation scale Q, in the range

[5] The `schemes.yml` implementation of our OS scheme for use in `anyH3` can be provided upon request.

$Q \in [m_t, 1500\ \text{GeV}]$. The results are shown in fig. 6.1, where the blue lines show our full one-loop results for λ_{hhh} and λ_{hhH} (for the other colors: see caption). One can observe that they are independent of Q, as expected. (Numerically, this holds up to `Python`'s working accuracy.)

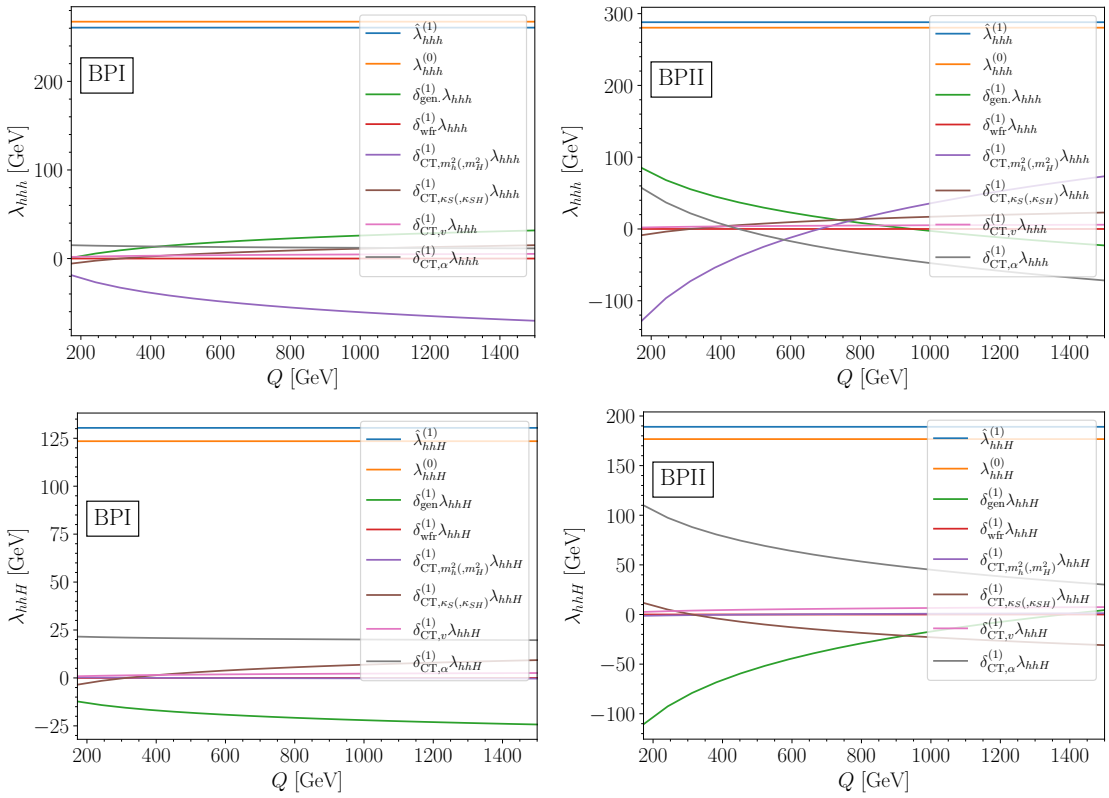

Figure 6.1: Individual contributions — see eq. (6.24) — and total one-loop results for λ_{hhh} and λ_{hhH}, using the OS renormalisation scheme defined in section 6.1. *Upper row*: results for BP1 from table 6.1; *bottom row*: results for BP2 from table 6.1; *left column*: results for λ_{hhh}; *right column*: results for λ_{hhH}. The colour coding is as follows: the blue line is the full one-loop result $\hat{\lambda}^{(1)}_{ijk}$, the orange line is the tree-level contribution $\lambda^{(0)}_{ijk}$, the green curve corresponds to the one-loop 1PI contributions $\delta^{(1)}_{\text{gen}}\lambda_{ijk}$, the red curve represents the external-leg corrections $\delta^{(1)}_{\text{wfr}}\lambda_{ijk}$, the purple curve is the contribution from the mass renormalisation $\delta^{(1)}_{\text{CT},m_h^2(,m_H^2)}\lambda_{ijk}$, the brown curve is the contribution from the renormalisation of κ_S and κ_{SH} $\delta^{(1)}_{\text{CT},\kappa_S(,\kappa_{SH})}\lambda_{ijk}$, the pink curve shows the contribution from the renormalisation of the EW VEV $\delta^{(1)}_{\text{CT},v}\lambda_{ijk}$, and finally the grey curve is the contribution from the α counterterm $\delta^{(1)}_{\text{CT},\alpha}\lambda_{ijk}$.

6.2 One-loop corrections to λ_{ijk}

In this section, we investigate the numerical results for the trilinear Higgs couplings λ_{hhh} and λ_{hhH} that can be obtained at one loop with the OS renormalisation scheme defined in the previous section. The scalar sector of the RxSM contains five free parameters, namely m_H, α v_S, κ_S, and κ_{SH}. To explore this five-dimensional parameter space, we perform parameter scans employing the following scan ranges

$$\begin{aligned} m_H &\in [260, 1000] \text{ GeV}, \\ \cos\alpha &\in [0.95, 1], \\ v_S &\in [1, 800] \text{ GeV}, \\ \kappa_S &\in [-1000, 1000] \text{ GeV}, \\ \kappa_{SH} &\in [-1000, 0] \text{ GeV}. \end{aligned} \tag{6.31}$$

We note that we choose as lower bound for the heavy Higgs mass $m_H > 260$ GeV in order to allow kinematically the decay channel of a heavy Higgs boson into two light ones, i.e. $H \to hh$. We do not start right at the threshold of this decay to avoid numerical instabilities in the calculation of the di-Higgs cross-section (see section 6.3). The requirement of κ_{SH} to be negative comes from the theoretical constraint of boundedness-from-below of the potential, as discussed in section 4.1.1.

6.2.1 Corrections to κ_λ

We begin with the case of the trilinear Higgs coupling of the detected Higgs boson, λ_{hhh}. We present our results in terms of the coupling modifier κ_λ, which is defined as the value of the coupling divided by its prediction in the SM at tree level,

$$\kappa_\lambda = \frac{\lambda_{hhh}}{\lambda_{hhh}^{\text{SM},(0)}} \,. \tag{6.32}$$

In fig. 6.2, we show as colour coding the one-loop predictions of κ_λ (which we denote $\kappa_\lambda^{(1)}$ to indicate the loop order) for our scan points. These results are presented in the $\{\cos\alpha, v_S\}$ plane (left panel) as well as in the $\{\cos\alpha, m_H\}$ plane (right panel). At first, we find that for most of the parameter space of the RxSM the one-loop corrected values of κ_λ are positive with an overall range of $\kappa_\lambda^{(1)} \in [0.91, 6.5]$, which is still fully allowed by the latest experimental constraints on κ_λ [9,10]. We also observe that the large values of κ_λ (red and orange points) are correlated with small values of the singlet VEV, v_S, and large values of the heavy Higgs mass m_H, as well as with values of $\cos\alpha$ close to 1 (i.e. near the alignment limit). The reason being that in these regions of the parameter space the one-loop corrections are enhanced due to large quartic coupling λ_{SH}. From eq. (4.10) one can see that λ_{SH} is inversely proportional to v_S and at the same time grows with m_H.

Next, in order to understand the origin of BSM deviations in κ_λ, between tree-level effects or one-loop corrections, we investigate separately the size of the one-loop corrections to κ_λ. We therefore show in fig. 6.3 the difference between the one-loop and tree-level values of κ_λ, i.e. $\kappa_\lambda^{(1)} - \kappa_\lambda^{(0)}$. The results are shown, as above, in the two planes: $\{\cos\alpha, v_S\}$ (left panel) and $\{\cos\alpha, m_H\}$ (right panel). We find the possible range of $\kappa_\lambda^{(0)} \in [0.97, 2.3]$ and $\kappa_\lambda^{(1)} - \kappa_\lambda^{(0)} \in [-0.26, 5.49]$, where large positive values of the latter are strongly correlated

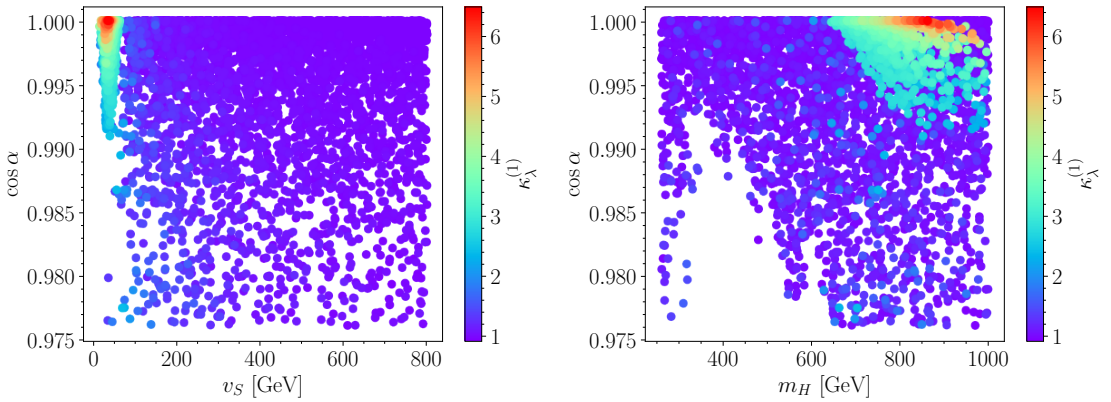

Figure 6.2: Parameter scan results in the RxSM, using the ranges given in eq. (6.31). The colour coding indicates $\kappa_\lambda^{(1)}$. *Left*: results in the $\{\cos\alpha, v_S\}$ plane; *right*: results in the $\{\cos\alpha, m_H\}$ plane.

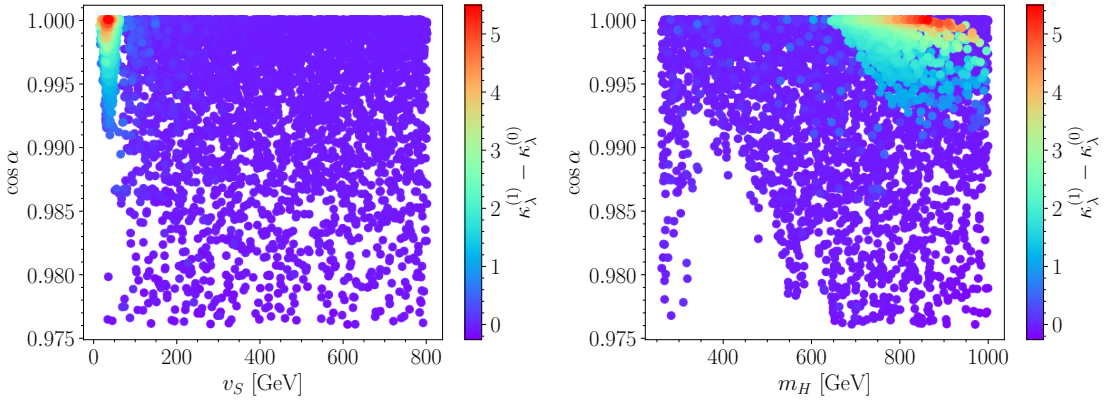

Figure 6.3: Difference between the one-loop and tree-level values of κ_λ, for the same RxSM parameter scan points as in fig. 6.2. *Left*: results in the $\{\cos\alpha, v_S\}$ plane; *right*: results in the $\{\cos\alpha, m_H\}$ plane.

with the values of $\kappa_\lambda^{(1)}$ shown in fig. 6.2. This indicates that, while BSM deviations are possible already at the tree level, the largest BSM deviations arise from loop corrections. By comparing fig. 6.2 and fig. 6.3, we find that for the points with the largest deviations from the SM, i.e. $\kappa_\lambda^{(1)} \in [3, 6.5]$, found in the region with small v_S, large m_H and closer to the alignment limit, the deviation is predominantly due to loop corrections, while the tree-level value is close to the SM, i.e. $\kappa_\lambda^{(0)} \approx 1$. On the other hand for those points with smaller BSM deviations, i.e. $\kappa_\lambda^{(1)} \in [0.91, 3]$ (light blue points in fig. 6.2), which are also further away from the alignment limit $\cos\alpha \in [0.975, 0.990]$, the largest part of the deviation arises already at the tree-level.

6.2.2 Corrections to λ_{hhH}

We turn in this section to the BSM trilinear Higgs coupling involved in di-Higgs production, λ_{hhH}. In fig. 6.4 we present as colour coding the one-loop values of $\hat{\lambda}_{hhH}^{(1)}$ for the RxSM scan points, in the $\{\cos\alpha, v_S\}$ plane (left) and in the $\{\cos\alpha, m_H\}$ plane (right). The two main differences compared to the case of λ_{hhh} is the existence of points with large

negative predictions, reaching even larger absolute values than the points with positive predictions. For points close to the alignment limit, i.e. $\cos\alpha \in [0.995, 1]$, large negative values of $\hat{\lambda}^{(1)}_{hhH}$ only occur for points with small[6] singlet VEVs, $v_S \lesssim 20$ GeV and heavy Higgs masses, $m_H \gtrsim 750$ GeV. On the other hand, for points further from the alignment limit, i.e. $\cos\alpha \in [0.975, 0.995]$, significant positive (red points) and negative (blue points) values of $\hat{\lambda}^{(1)}_{hhH}$ are possible, depending on the values of v_S and m_H. Smaller (larger) values of both v_S and m_H correlate with positive (negative) $\hat{\lambda}^{(1)}_{hhH}$.

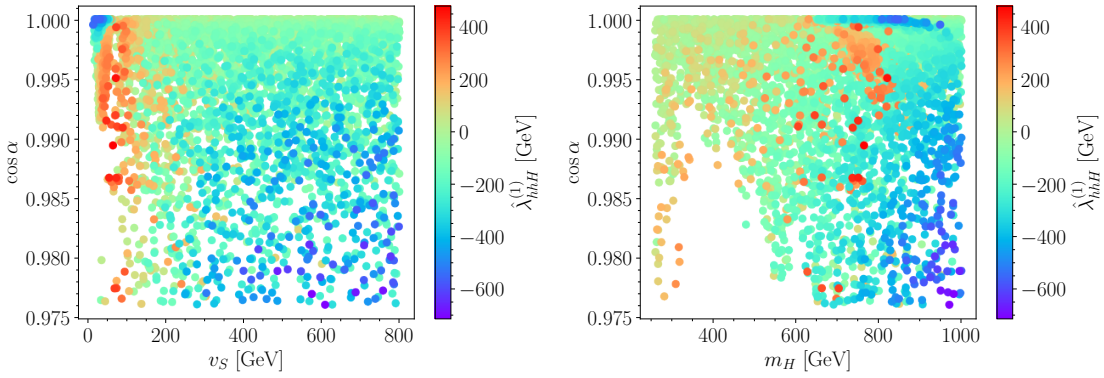

Figure 6.4: Results for $\hat{\lambda}^{(1)}_{hhH}$ of our RxSM parameter scan. *Left*: results in the $\{\cos\alpha, v_S\}$ plane; *right*: results in the $\{\cos\alpha, m_H\}$ plane.

As in the previous section, it is important to understand whether this behaviour stems from tree- or loop-level effects. In fig. 6.5 we present the difference between the one-loop and tree-level values of λ_{hhH} for our scan points in the same two planes as the previous figures. It should be kept in mind that $\lambda^{(0)}_{hhH} = 0$ in the alignment limit. One can observe that in the region of parameter space closer to the alignment limit and for small values of v_S and large values of m_H, the large results for $\hat{\lambda}^{(1)}_{hhH}$ (in absolute values) arise for the most part from radiative corrections driven by large values of λ_{SH}. Inversely, for the points farther from the alignment limit as well as for $v_S \gtrsim 200$ GeV, the tree-level contribution to λ_{hhH} dominates and loop effects are moderate.

As a general conclusion, we find that the largest loop corrections occur for points close to the alignment limit, i.e. $\cos\alpha \in [0.99, 1]$.

[6]While it is known that the standard tadpole scheme can suffer from numerical instabilities stemming from terms $\sim t_S/v_S$ (see e.g. eq. (4.10)), as pointed out in [319], we have checked that no such instability occurs for the points considered in this study.

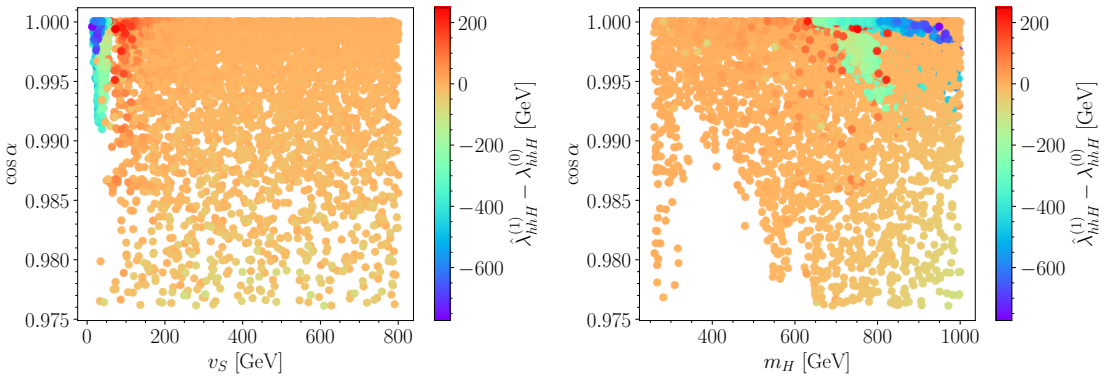

Figure 6.5: Difference between the one-loop and tree-level values of λ_{hhH} for our RxSM parameter scan. *Left*: results in the $\{\cos\alpha, v_S\}$ plane; *right*: results in the $\{\cos\alpha, m_H\}$ plane.

6.3 Predictions for di-Higgs production

In this section we turn to the investigation of the phenomenological implications for di-Higgs production of the potentially large loop corrections in the trilinear Higgs couplings found in the previous section. For this purpose, we consider two possible collider settings, namely the HL-LHC and a e^+e^- collider with centre-of-mass energy of 1 TeV. As a concrete example, we use the specifics for the ILC [139].

6.3.1 HL-LHC

To compute the di-Higgs production at the HL-LHC, we employ a modified version of `HPAIR` [64, 69, 137, 300–302], which was already used in [246]. In this code, the three leading-order (LO) diagrams contributing to the $gg \to hh$ process, shown in fig. 6.6, as well as the interference between them, are taken into account. The code also computes the NLO QCD corrections for the total cross-section, but not for the differential distributions. In order to consistently provide results for the total cross-section and the differential distributions at the same order, we present results for both at LO in QCD only. However, one should remember that these predictions are modified by a QCD K factor close to 2. `HPAIR` takes as inputs the trilinear Higgs couplings λ_{hhh} and λ_{hhH}, so that by providing one-loop corrected versions of these two couplings, we obtain a prediction for the di-Higgs cross-section (and differential distributions) including leading NLO BSM contributions. When comparing results in the RxSM with the SM, one should have in mind that the LO value for the total di-Higgs production cross-section in the SM is $\sigma_{hh}^{\text{SM}} = 19.76$ fb [69].

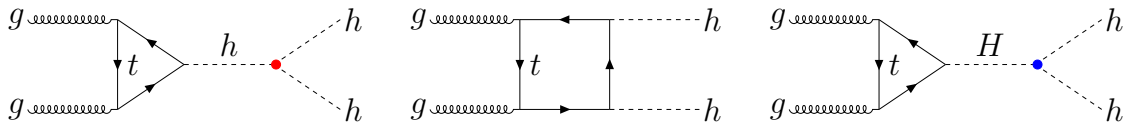

Figure 6.6: Leading-order diagrams contributing to the di-Higgs production process at the (HL-)LHC.The red and blue dots indicate the trilinear scalar couplings λ_{hhh} and λ_{hhH}, respectively.

Total cross-section

Our predictions for the total di-Higgs production cross-section, including one-loop corrections to the trilinear Higgs couplings, for the RxSM scan points are shown in the colour coding of fig. 6.7, for our two benchmark plane projections, the $\{\cos\alpha, v_S\}$ plane (left) and the $\{\cos\alpha, v_S\}$ plane (right). In fig. 6.7, one can see that there is a region, indicated by red points, exhibiting a large enhancement of the cross-section $\sigma_{hh}^{\text{RxSM}} \approx 7.5\,\sigma_{hh}^{\text{SM}}$. This region is located for small values of the heavy Higgs mass, $m_H \lesssim 300$ GeV. We also see that this enhancement increases for values of the mixing angles further away from the alignment limit and that there is not a clear correlation with the value of the singlet VEV. The fact that the large cross-section values found for these points depend only on m_H, but not on changes in the trilinear Higgs couplings, which vary substantially over this part of the parameter space — see figs. 6.2 to 6.5 — indicates that this effect originates from the s-channel heavy Higgs-boson exchange already at the tree-level. There is a second region with smaller but still significant enhancements of the cross-section with respect to the SM, with values reaching $\sigma_{hh}^{\text{RxSM}} \approx 4.5\,\sigma_{hh}^{\text{SM}}$. This region is found for small values of $v_S \lesssim 50$ GeV, large values of $m_H \simeq 850$ GeV, and close to the alignment limit

$\cos\alpha > 0.99$. However, we can also observe for this same region points (in purple) with a decrease in the cross-section w.r.t. the SM, with values as low as $\sigma_{hh}^{\text{RxSM}} \approx 0.5\,\sigma_{hh}^{\text{SM}}$. The second region with significant deviations (both increases and decreases) in the di-Higgs cross-section corresponds exactly to the region for which we observed large deviations in κ_λ in fig. 6.2, which were due to loop contributions. The change in the behaviour of the cross-section, encompassing increase and decrease w.r.t. σ_{hh}^{SM} is well known from the SM with a free λ_{hhh} (see e.g. [100,322] and references therein), due to the negative interference of the h-exchange contribution and the box diagram, see fig. 6.6. Values smaller than the SM are found for $1 \leq \kappa_\lambda \lesssim 3.5$, whereas larger values are found for $\kappa_\lambda \gtrsim 3.5$, with a minimum around $\kappa_\lambda \approx 2.5$.

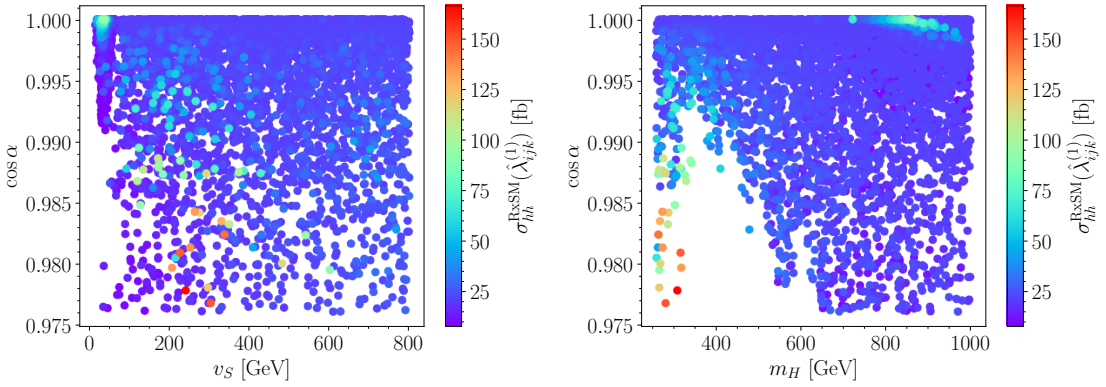

Figure 6.7: Predictions for $\sigma_{hh}^{\text{RxSM}}$ in our RxSM parameter scan. *Left*: results in the $\{\cos\alpha, v_S\}$ plane; *right*: results in the $\{\cos\alpha, m_H\}$ plane.

In fig. 6.8 we present for our RxSM scan points the ratio between the total di-Higgs production cross-section including one-loop corrections to the trilinear Higgs couplings, which we denote $\sigma_{hh}^{\text{RxSM}}(\hat{\lambda}_{ijk}^{(1)})$, and the same cross-section using the tree-level values, $\sigma_{hh}^{\text{RxSM}}(\lambda_{ijk}^{(0)})$. As for the previous figures, the value of the ratio is given by the colour coding of the points and shown for the $\{\cos\alpha, v_S\}$ plane (left panel) and the $\{\cos\alpha, m_H\}$ plane (right panel). From fig. 6.7 we concluded that the large deviations from the SM in the cross-section close to the alignment limit is a loop-induced effect and this is indeed confirmed by fig. 6.8 as the same pattern of deviations can be observed in the ratio $\sigma_{hh}^{\text{RxSM}}(\hat{\lambda}_{ijk}^{(1)})/\sigma_{hh}^{\text{RxSM}}(\lambda_{ijk}^{(0)})$. For the region where we observe the largest deviations from the SM, further from the alignment limit ($\cos\alpha \in [0.975, 0.99]$), we concluded that this is a tree-level effect coming from the propagator of the heavy Higgs boson, and fig. 6.8 also supports this conclusion, as the ratio $\sigma_{hh}^{\text{RxSM}}(\hat{\lambda}_{ijk}^{(1)})/\sigma_{hh}^{\text{RxSM}}(\lambda_{ijk}^{(0)})$ remains close to 1 for these points.

Differential cross-section

The objective of this section is to investigate the impact of the loop corrections to the trilinear Higgs couplings on the differential di-Higgs production cross-section. For this analysis, we have selected six different benchmark points, defined in table 6.2, corresponding to different phenomenological scenarios. We begin by calculating with `HPAIR` theoretical predictions for the di-Higgs invariant mass distributions for the process $gg \to hh$, comparing the results using tree-level or one-loop corrected trilinear couplings. In a second step, we determine for these benchmark points whether the di-Higgs process could be ob-

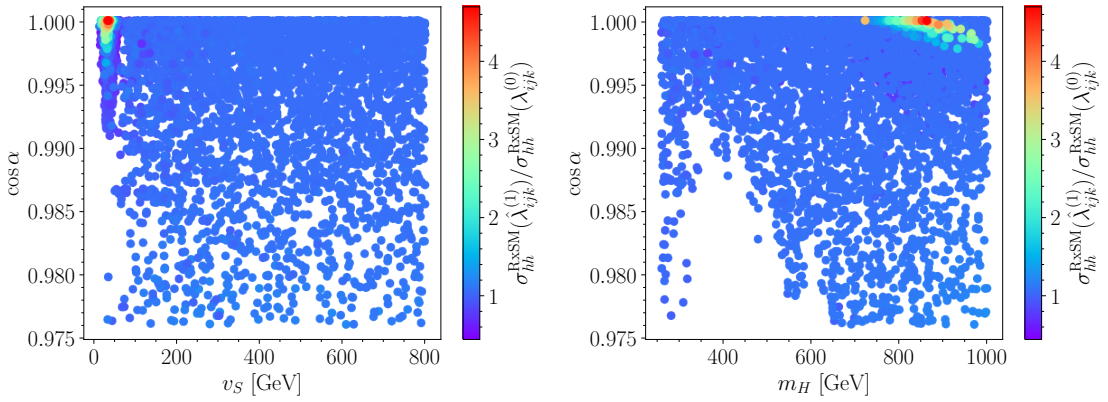

Figure 6.8: The ratio between the total cross-section for di-Higgs production at the (HL-)LHC including one-loop corrections to the trilinear Higgs couplings and using the tree-level value for the points from our parameter scan in the RxSM. *Left*: Results in the $\{\cos\alpha, v_S\}$ plane; *right*: results in the $\{\cos\alpha, m_H\}$ plane.

served at the HL-LHC, taking into account different experimental uncertainties. In order to obtain quantitative results, incorporating also the possibility of statistical fluctuations in experimental signals, we define a statistical significance for the RxSM deviation from the expected SM result. In order to include experimental effects in our analysis, we start by multiplying our cross-section results by the luminosity $\mathscr{L}$ to compute the number of events. We use here the value of $\mathscr{L} = 6\,\mathrm{ab}^{-1}$, obtained by combining the luminosities expected to be collected by ATLAS and CMS at the end of the HL-LHC. Next, following the procedure in [323], we take into account the decays of the Higgs bosons, choosing the channel with the largest branching ratio, $h \to b\bar{b}$. We furthermore take into account the corresponding detector efficiencies, following [324]. The latter are given by the product of $\epsilon = \epsilon_{\mathrm{TOT}}\epsilon_{\mathrm{SR}}$, where ϵ_{TOT} is the efficiency factor of the pre-selection of the events, and ϵ_{SR} is the efficiency of the reconstruction of the $b\bar{b}$ pairs. The total number of events is then given by,

$$N = \sigma(gg \to hh) \times \mathscr{L} \times \left(\mathrm{BR}(h \to b\bar{b})\right)^2 \times \epsilon_{\mathrm{TOT}} \times \epsilon_{\mathrm{SR}}\,. \tag{6.33}$$

Additionally, we have to take into account the smearing and binning of the distributions, which estimate, respectively, the experimental error in the measurement of the four-bottom invariant mass $m_{b\bar{b}b\bar{b}}$ and the finite resolution in $m_{b\bar{b}b\bar{b}}$ of the detector (see e.g. Refs. [64, 246]). We employ, as was done in Refs. [64, 246], experimentally motivated values of 15% for the smearing and 50 GeV for the binning.

One aim of this analysis is to investigate whether there is a realistic chance to distinguish experimentally the di-Higgs distributions in the RxSM, using either tree-level or one-loop trilinear scalar couplings, from the SM. In addition to the experimental effects discussed above, we also include here the statistical uncertainty. For the discrimination of the RxSM (the considered hypothesis to be tested) from the SM (the null hypothesis), we define a statistical significance following [325]. We define our signal and background event numbers for each bin (labelled by the index i) respectively as

$$\begin{aligned} s_i &= N_i^{\mathrm{RxSM}} - N_i^{\mathrm{SM}}, \\ b_i &= N_i^{\mathrm{SM}}\,, \end{aligned} \tag{6.34}$$

BP	m_H [GeV]	$\cos\alpha$	v_S [GeV]	κ_S [GeV]	κ_{SH} [GeV]	$\kappa_\lambda^{(0)}$	$\kappa_\lambda^{(1)}$	$\lambda_{hhH}^{(0)}$ [GeV]	$\hat{\lambda}_{hhH}^{(1)}$ [GeV]
1	659.4	0.9999	56.1	−880	−880	1.01	3.02	96.3	−119.7
2	777.6	1.0000	44.7	−931	−931	1.00	4.87	2.2	−303.6
3	594.5	0.9987	110.7	146	−931	1.08	1.41	127.6	181.9
4	891.1	0.9957	37.0	−993	−993	1.62	3.28	543.2	131.2
5	411.4	0.9878	92.6	−605	−380	1.29	1.31	153.9	165.1
6	625.6	0.9976	96.4	−851	−826	1.14	1.46	163.5	263.8

Table 6.2: Definitions of the RxSM benchmark points for the study of di-Higgs production, in terms of the five free BSM parameters of the model (m_H, $\cos\alpha$, v_S, κ_S and κ_{SH}). Additionally, for each benchmark point, tree-level and one-loop predictions for the trilinear self-coupling modifier κ_λ as well as for the BSM trilinear coupling λ_{hHH} are included. We note that the numbers in this table are rounded; the actual input values to 10 digits, necessary to reproduce the quoted results for the trilinear scalar couplings, are provided in the ancillary file `BPs.csv`.

where $N_i^{\mathrm{RxSM(SM)}}$ is the number of events in the RxSM (SM) in bin i. Assuming Poisson statistics for the distributions, we can use a likelihood ratio method to define a statistical significance [325]

$$Z = \sqrt{\sum_i 2\left[(s_i + b_i)\log\left(1 + \frac{s_i}{b_i}\right) - s_i\right]}, \tag{6.35}$$

summing over all the bins of the distribution. The results for the significances for the RxSM distributions calculated with tree-level and one-loop trilinear scalar couplings are denoted as $Z^{(0)}$ and $Z^{(1)}$, respectively.

In figs. 6.9 and 6.10, we show the results for the theoretical distributions and the distributions including the experimental effects discussed above for the six benchmark points of table 6.2. The blue (red) curves show results using the tree-level (one-loop corrected) trilinear Higgs couplings; the black dashed line shows the corresponding SM result.[7] In the left column we show the distributions without experimental uncertainties; the distributions in the right columns give the number of di-Higgs events in the $b\bar{b}$ final state, taking into account smearing, binning and the experimental efficiencies as discussed above. The error bars indicate Poisson statistical uncertainties in each bin for the signal.

In fig. 6.9, we observe that for BP1 (upper row) the theoretical RxSM distribution with tree-level trilinear scalar couplings (blue curve) is essentially indistinguishable from the SM value for almost the entire range of m_{hh}. At the level of the theoretical curves, only a resonance in the RxSM, for $m_{hh} = m_H$, yields a visible peak-dip structure. After experimental effects are included, the resonance is too small to be distinguished from the SM, which results in a significance $Z^{(0)} = 0.1$. When including loop calculations, the value of κ_λ is increased to $\kappa_\lambda^{(1)} \simeq 3$, while the value of λ_{hhH} effectively switches

[7] We note that for the SM we employ the tree-level value of $\kappa_\lambda = 1$, as the use of an effective trilinear coupling is known not to be a good approximation in the SM [326]. The main reason for this is that momentum effects are significant for $\kappa_\lambda \simeq 1$, while they can be safely neglected for points with BSM deviations in κ_λ (see e.g. the discussion in Ref. [89]). Nevertheless, we emphasise that the SM distributions obtained with $\kappa_\lambda^{(0)} = 1$ or $\kappa_\lambda^{(1)} \simeq 0.94$ are extremely similar, and once experimental effects are included, they are undistinguishable.

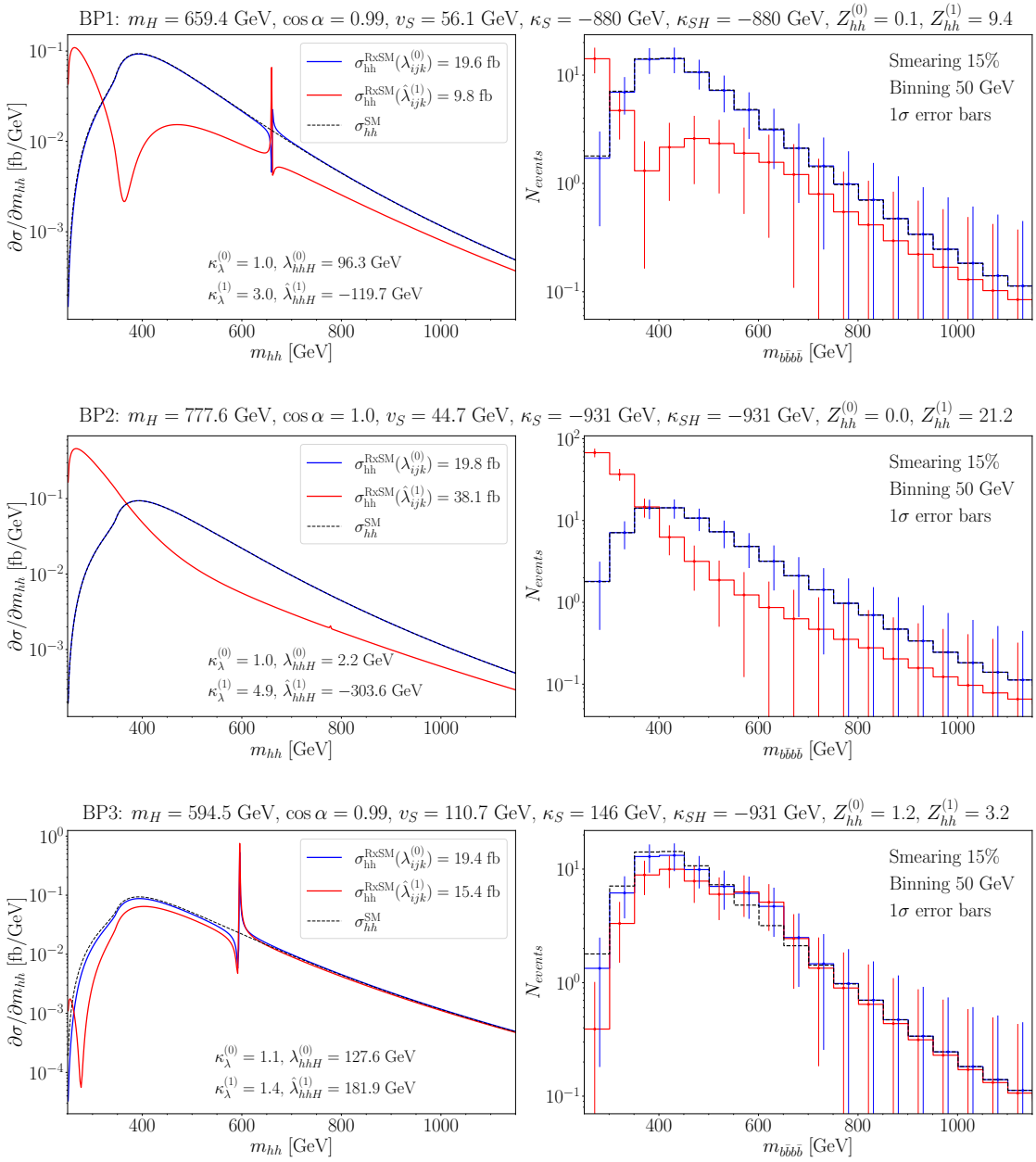

Figure 6.9: Differential m_{hh} di-Higgs production cross-section distributions; blue (red) curves show results using the tree-level (one-loop corrected) trilinear Higgs couplings; the black dashed line shows the corresponding SM result. *Left:* Distribution without experimental uncertainties; *right:* distribution of the number of di-Higgs events in the $b\bar{b}$ final state, taking into account smearing, binning and the experimental efficiencies (see text). Error bars indicate Poisson statistical uncertainties in each bin. *Top:* Results for BP1; *centre:* results for BP2; *bottom:* results for BP3 from table 6.2.

sign. While the former leads to an important modification of the interference pattern for low values of $m_{hh}/m_{b\bar{b}b\bar{b}}$, the latter switches the dip-peak structure to a peak-dip structure. However, after taking into account the experimental uncertainties, this has no visible effect in the distributions due to the very narrow width of the resonance structure. The inclusion of the one-loop effects, particularly in λ_{hhh}, results in a significance of

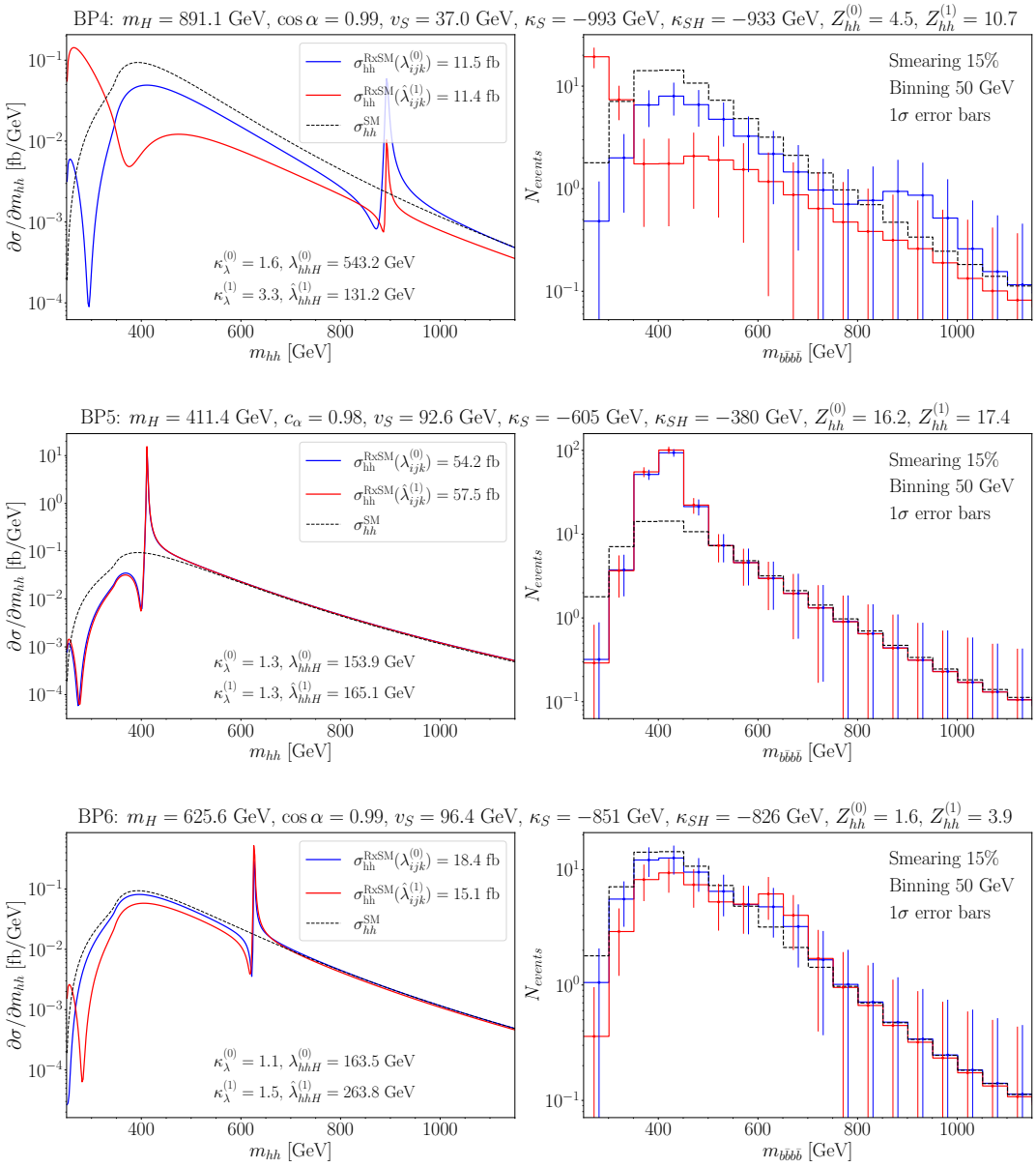

Figure 6.10: Differential m_{hh} di-Higgs production cross-section distributions; line styles and colour coding as in fig. 6.9. *Top:* Results for BP4; *centre:* results for BP5; *bottom:* results for BP6 from table 6.2.

$Z^{(1)} = 9.4$. BP1 is therefore an example scenario for which an analysis using tree-level trilinear scalar couplings would not have allowed distinguishing the RxSM from the SM, while the inclusion of one-loop corrections renders this possible.

BP2 is another example in which one would not expect to be able to distinguish the RxSM from the SM in an analysis using only tree-level trilinear couplings. Indeed, for BP2 $\kappa_\lambda^{(0)} \simeq 1$ and $\lambda_{hhH}^{(0)} \simeq 0$, leading to total and differential cross-sections essentially identical to those of the SM. However, when taking into account the one-loop corrections in $\hat{\lambda}_{ijk}^{(1)}$, we find $\kappa_\lambda^{(1)} \sim 4.9$ and $\lambda_{hhH}^{(1)} \sim -300$ GeV. Using these values, one can already distinguish the RxSM from the SM at the level of the total cross-section, as $\sigma_{hh}^{\mathrm{RxSM}}$ is increased by

$\sim 100\%$ compared to $\sigma_{hh}^{\rm SM}$ — unlike in BP1, where $\sigma_{hh}^{\rm RxSM}$ decreased by $\sim 50\%$. This increase in $\sigma_{hh}^{\rm RxSM}$ is due to the one-loop value of $\kappa_\lambda^{(1)}$. This can be understood well at the level of differential distribution: indeed the interference pattern for such large values of κ_λ yields a large peak for low values of $m_{hh}/m_{b\bar{b}b\bar{b}}$, which results in an increase of the total cross-section. On the other hand, the resonance structure of the heavy Higgs boson remains unobservable, also including the one-loop corrections to λ_{hhH}. The significance at the one-loop level between the RxSM and the SM is found to be $Z^{(1)} = 21.2$.

In BP3, the radiative corrections to the trilinear scalar couplings are moderate. In the case of a tree-level analysis, we are in a similar situation as with BP1, with no deviation in κ_λ and a resonance that is relatively suppressed by experimental effects. This leads to a significance of $Z^{(0)} = 1.2$. At the one-loop level, we have a small correction to λ_{hhh}, yielding $\kappa_\lambda^{(1)} = 1.4$, which modifies slightly the interference for low values of $m_{hh}/m_{b\bar{b}b\bar{b}}$. Nevertheless, the value of κ_λ is still close to 1, and therefore we only observe a dip in the distribution around $m_{hh} \sim 280$ GeV, but no peak (unlike e.g. BP2). The modest correction to λ_{hhH} yields a slightly larger resonance peak with respect to the tree-level case. Combining these two effects, we find an increase in significance to $Z^{(1)} = 3.2$. This remains insufficient to conclude that both curves can be distinguished, but it provides an indication of new physics, which we do not observe at tree level. Possible future improvements in experimental analysis techniques may offer the chance to further improve the significance for scenarios like BP3.

In BP4, with $\kappa_\lambda^{(0)} = 1.6$ there is already a large deviation from the SM in the theoretical distributions employing tree-level trilinear scalar couplings, and this deviation persists even after considering the effects of smearing and binning, leading to $Z^{(0)} = 4.5$, which provides significant indications of new physics. However, the resonance occurs at large masses, and thus once statistical errors are taken into account, the peak in the differential distribution in the RxSM cannot be distinguished from the continuum (i.e. the SM distribution). After including one-loop corrected trilinear scalar couplings, the resonant peak is not modified significantly. However the large loop corrections to λ_{hhh}, leading to $\kappa_\lambda^{(1)} = 3.3$, have a strong impact on the interference pattern at low values of $m_{hh}/m_{b\bar{b}b\bar{b}}$. This yields a large enhancement just above threshold and a dip around ~ 375 GeV. This results in a large deviation from the SM distribution that is not erased by experimental effects, giving a significance of $Z^{(1)} = 10.7$. On the other hand, the increase in κ_λ does not have a significant impact on the total cross-section because the contributions from the peak and the dip cancel each other out. An analysis at the level of differential distributions (and including one-loop corrections to λ_{hhh}) is therefore required to be able to distinguish the RxSM from the SM in BP4.

Turning next to BP5, the tree-level and one-loop distributions are very similar to each other, and, once experimental uncertainties are taken into account, the two would not be distinguishable from each other. BP5 features a small deviation in $\kappa_\lambda^{(0)} \simeq \kappa_\lambda^{(1)} \sim 1.3$, which causes a slight decrease in the differential cross-section for low values of $m_{hh}/m_{b\bar{b}b\bar{b}}$. At the same time, there is also a very large resonant peak allowing to differentiate the RxSM from the SM no matter the order at which the analysis is performed, with significances of $Z^{(0)} \simeq Z^{(1)} \sim 16$. This is due to a combination of a non-negligible value of the trilinear Higgs coupling, $\lambda_{hhH}^{(0)} \sim \lambda_{hhH}^{(1)} \sim 150$ GeV, and of the low value of the BSM Higgs mass, $m_H \sim 400$ GeV, which enhances the interference with the non-resonant contributions. As a general observation from our parameter scans, we find that, for points with a large

resonant peak, found in the range 350 GeV $\lesssim m_H \lesssim$ 500 GeV, there are no significant corrections to λ_{hhH}. Consequently, for this type of scenarios, the one-loop corrections in the RxSM do not enhance the sensitivity to the BSM trilinear Higgs coupling.

Finally, our last scenario, BP6, is similar to BP3 in terms of the trilinear scalar couplings and total di-Higgs cross-sections at tree level and one loop, as well as of the statistical significances. On the other hand, BP6 features a larger resonant peak at the tree level, which is somewhat suppressed by loop corrections to κ_λ. The dip for low values of m_{hh} due to the deviation of κ_λ also pushes down the continuum distribution in the invariant mass region around the resonant peak, therefore the resonant peak is also affected by this interference. To better understand to what extent the resonant peak and, consequently, λ_{hhH} can be resolved experimentally, we have defined a statistical significance, which we denote Z_{peak}, for discriminating the resonant peak (the signal hypothesis) from the continuum (the null hypothesis, $\lambda_{hhH} = 0$) for BP5 and BP6. For BP5, we find for the peak significance $Z^{(0)}_{\text{peak}} = 17.5$ and $Z^{(1)}_{\text{peak}} = 18.4$. In both cases, we can distinguish the resonant peak from the continuum, and therefore, we have sensitivity to the λ_{hhH} coupling. However, as discussed above, the one-loop corrections do not enhance the significance. In the case of BP6, we find $Z^{(0)}_{\text{peak}} = 1.5$ and $Z^{(1)}_{\text{peak}} = 1.2$. In this case, the resonant peak cannot be resolved from the continuum in either case, and the negative one-loop corrections to λ_{hhH} reduce Z_{peak}. All significances are summarised in table 6.3 for our benchmark points.

BP	$\kappa_\lambda^{(0)}$	$\kappa_\lambda^{(1)}$	$\lambda_{hhH}^{(0)}$ [GeV]	$\hat{\lambda}_{hhH}^{(1)}$ [GeV]	$\sigma_{\text{hh}}^{\text{RxSM}}(\lambda_{ijk}^{(0)})$ [fb]	$\sigma_{\text{hh}}^{\text{RxSM}}(\hat{\lambda}_{ijk}^{(1)})$ [fb]	$Z^{(0)}$	$Z^{(1)}$	$Z^{(0)}_{\text{peak}}$	$Z^{(1)}_{\text{peak}}$
1	1.0	3.0	96.3	−119.7	19.6	9.8	0.1	9.4	0.0	0.0
2	1.0	4.9	2.2	−303.6	19.8	38.1	0.0	21.2	0.0	0.0
3	1.1	1.4	127.6	181.9	19.4	15.4	1.2	3.2	0.0	0.0
4	1.6	3.3	543.2	131.2	11.5	11.4	4.5	10.7	0.0	0.0
5	1.3	1.3	153.9	165.1	54.2	57.5	16.2	17.4	17.5	18.4
6	1.1	1.5	163.5	263.8	18.4	15.4	1.6	3.9	1.5	1.2

Table 6.3: Predictions for κ_λ and λ_{hhH} at tree level and one loop, for the total di-Higgs production cross-section at the (HL-)LHC using tree-level or one-loop trilinear couplings, statistical significances to distinguish the di-Higgs invariant mass differential distributions (with tree-level or one-loop trilinear couplings) from the SM and statistical significances to distinguish the di-Higgs invariant mass differential distributions resonant peak (with tree-level or one-loop trilinear couplings) from the continuous distribution, for the benchmark points defined in table 6.2.

6.3.2 e^+e^- colliders

In this section, we present our results for di-Higgs production at future high-energy e^+e^- colliders. We consider the di-Higgs-strahlung channel $e^+e^- \to Zhh$, which is the dominant production channel of two SM-like Higgs bosons up to centre-of-mass energies slightly above 1 TeV. The contributing Feynman diagrams are shown in fig. 6.11. Similarly to the HL-LHC study, we investigate the impact of loop corrections to the trilinear Higgs couplings on the total and differential cross-sections and the experimental sensitivity to possible deviations from the SM. Contributions involving λ_{hhh} arise due to a non-resonant

diagram, shown as the upper right diagram in fig. 6.11. Consequently, the strongest effects of BSM modifications of λ_{hhh} are expected at low values of m_{hh}, close to the kinematic threshold. On the other hand, the contributions proportional to λ_{hhH} come from a (potentially) resonant diagram (lower left diagram in fig. 6.11) mediated by the heavy Higgs boson H. This contribution is expected to have the largest effect around $m_{hh} = m_H$. Consequently, the loop corrections to the two trilinear Higgs couplings will have a different impact for different values of m_{hh}. This makes it crucial to accurately measure the differential distributions over the whole allowed range.

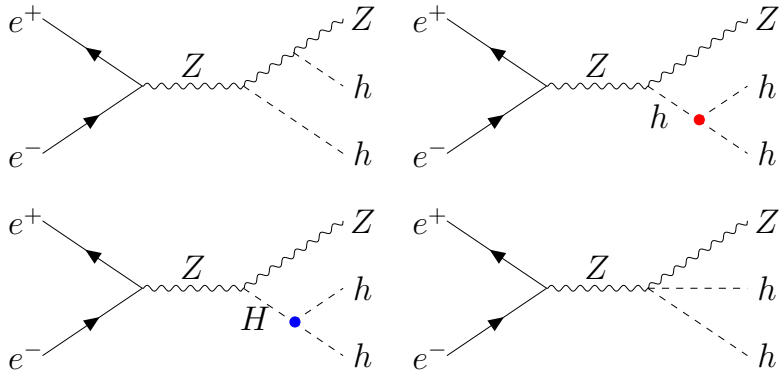

Figure 6.11: Example diagrams contributing to the $e^+e^- \to Zhh$ process at high-energy e^+e^- colliders. The red and blue dots represent, respectively, the trilinear scalar couplings λ_{hhh} and λ_{hhH}.

Calculation of $e^+e^- \to Zhh$

We compute the leading-order unpolarised $e^+e^- \to Zhh$ production cross-section, which we denote σ_{Zhh}, using the public code `Madgraph5_aMC v3.5.7` [141]. The input `UFO` model files for the RxSM required by `Madgraph` were obtained with the `Mathematica` package `SARAH-4.15` [314, 327–330]. We compute the cross-section for future e^+e^- collider at a centre-of-mass energy of $\sqrt{s} = 1000$ GeV, where we take as a concrete example the ILC1000 [139, 315, 316]. We choose a high centre-of-mass energy due to the large masses of our heavy Higgs boson. In this work, we assume an integrated luminosity of 8 ab^{-1}, as projected for the ILC1000 [139]. After computing the unpolarised cross-section we can apply a simple correction factor following [98] to take into account polarised beams as possible at the ILC1000. The optimised polarisation of ILC1000 is an opposite sign polarisation of 80% for electrons and 30% for positrons giving as a result:

$$\sigma(-80\%, +30\%) \simeq 1.476\ \sigma_{\text{unpol}}\,, \tag{6.36}$$

$$\sigma(+80\%, -30\%) \simeq 1.004\ \sigma_{\text{unpol}}\,. \tag{6.37}$$

With our calculational setup, we obtain for the SM di-Higgs production cross-sections of $\sigma^{\text{SM}}_{Zhh} \simeq 0.236$ fb for $\sqrt{s} = 500$ GeV and $\sigma^{\text{SM}}_{Zhh} \simeq 0.177$ fb for $\sqrt{s} = 1$ TeV for the $(-80\%, +30\%)$ polarisation. The observation of the di-Higgs-strahlung process at $\sqrt{s} = 500$ GeV is expected at the 8σ level for an integrated luminosity of 4 ab^{-1} (combining several polarisation runs), corresponding to a relative experimental uncertainty of 16.8% on σ^{SM}_{Zhh} obtained in Ref. [317], and which was recently improved to 12.8% in Refs. [62,331]. Applying a simple scaling of the number of events, this yields a relative uncertainty of the

cross-section at $\sqrt{s} = 1000$ GeV of $\sim 10\%$ for an integrated luminosity of 8 ab^{-1}, which corresponds to a discovery significance of close to 13σ.

Total cross-section

Our predictions for the total di-Higgs production cross-section in the RxSM at $\sqrt{s} = 1$ TeV including one-loop corrections to the trilinear Higgs couplings, which we denote $\sigma^{\text{RxSM}}_{Zhh}(\hat{\lambda}^{(1)}_{ijk})$, are shown in the colour coding of fig. 6.12. Results are projected in two different planes: in the left panel in the $\{\cos\alpha, v_S\}$ plane, and in the right panel in the $\{\cos\alpha, m_H\}$ plane. We find first that values of the total cross-section up to six times larger than the SM result, $\sigma^{\text{RxSM}}_{Zhh} \sim 6\sigma^{\text{SM}}_{Zhh}$, are possible. This would clearly allow to distinguish the corresponding parameter points from the SM. The largest enhancement of $\sigma^{\text{RxSM}}_{Zhh}$ with respect to the SM occurs in the same parameter region as for the $gg \to hh$ process, namely in the region of low values of v_S, high values of m_H, and close to the alignment limit. This is due to the large corrections to κ_λ at the one-loop level. However, comparing fig. 6.2 and fig. 6.12, one can observe a continuous enhancement of $\sigma^{\text{RxSM}}_{Zhh}$ with κ_λ — in contrast to what was found for the $gg \to hh$ process in fig. 6.7. This can be explained by the monotonous increase of the $e^+e^- \to Zhh$ cross-section with κ_λ, which is unlike the $gg \to hh$ cross-section that is non-monotonous, with a minimum around $\kappa_\lambda \sim 2.5$. The total di-Higgs production cross-section of $e^+e^- \to Zhh$ is therefore more sensitive to small changes of κ_λ than that one of $gg \to hh$.

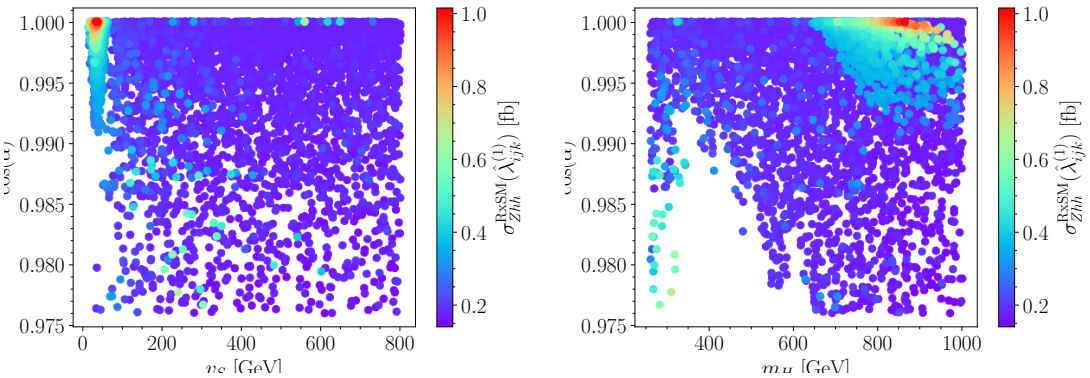

Figure 6.12: Total cross-section for the di-Higgs production process $e^+e^- \to Zhh$ at $\sqrt{s} = 1$ TeV including one-loop corrections to the trilinear scalar couplings for the RxSM scan points. *Left*: Results in the $\{\cos\alpha, v_S\}$ plane; *right*: results in the $\{\cos\alpha, m_H\}$ plane.

In fig. 6.12 we can also find points with smaller deviations from the SM, with $\sigma^{\text{RxSM}}_{Zhh} \sim 3\sigma^{\text{SM}}_{Zhh}$, and that are further from the alignment limit and are not correlated with the loop corrections to κ_λ. In order to understand the behaviour of these points, we present in fig. 6.13 the ratio between $\sigma^{\text{RxSM}}_{Zhh}(\hat{\lambda}^{(1)}_{ijk})$ and the same cross-section using the tree-level values of the trilinear Higgs couplings, $\sigma^{\text{RxSM}}_{Zhh}(\lambda^{(0)}_{ijk})$. The ratio is indicated by the colour coding, shown for the $\{\cos\alpha, v_S\}$ plane (left panel) and the $\{\cos\alpha, m_H\}$ plane (right panel). As can be seen from fig. 6.13, the large enhancement of $\sigma^{\text{RxSM}}_{Zhh}$ for points near the alignment limit arises from $\kappa^{(1)}_\lambda$. On the other hand, for the points with a smaller increase, i.e. $\sigma^{\text{RxSM}}_{Zhh} \sim 3\sigma^{\text{SM}}_{Zhh}$, the increase in the cross-section stems from tree-level effects, e.g. from the heavy Higgs-boson resonance contribution, as $\sigma^{\text{RxSM}}_{Zhh}(\hat{\lambda}^{(1)}_{ijk})/\sigma^{\text{RxSM}}_{Zhh}(\lambda^{(0)}_{ijk})$ is

close to unity.

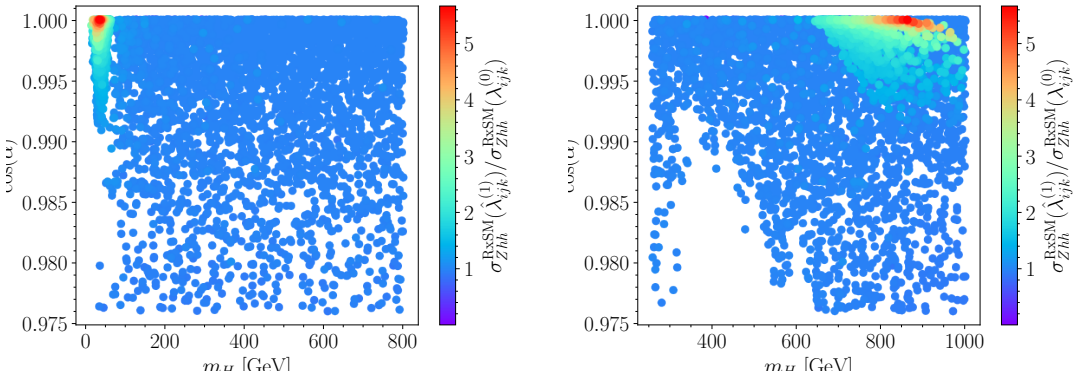

Figure 6.13: $\sigma^{\text{RxSM}}_{Zhh}(\hat{\lambda}^{(1)}_{ijk})/\sigma^{\text{RxSM}}_{Zhh}(\lambda^{(0)}_{ijk})$ (see text). *Left*: Results in the $\{\cos\alpha, v_S\}$ plane; *right*: results in the $\{\cos\alpha, m_H\}$ plane.

Differential cross-section

In this subsection, we analyse the differential di-Higgs production cross-sections with respect to m_{hh} for the six benchmark points defined in table 6.2 at an e^+e^- collider of $\sqrt{s} = 1$ TeV, using additionally polarised beams. As in our study for the HL-LHC case, we want to take into account experimental uncertainties, although in the case of e^+e^- colliders the events are much cleaner than in pp collisions. For this reason, we present in this subsection distributions taking into account the Higgs-boson decays and applying realistic experimental cuts.

We estimate the experimental uncertainties affecting the differential cross-section distributions, following a similar scheme as for the study of the HL-LHC case. Firstly, we consider the decay channel of the SM-like Higgs boson to $b\bar{b}$ by multiplying the differential cross-section by $\text{BR}^2(h \to b\bar{b})$ as well as by the efficiency of the detector in the reconstruction of the b-jets. This efficiency is defined in a different way than that at the HL-LHC, and we follow [98]: we decompose it into the b-tagging efficiency of each b-jet, which we assume to be $\epsilon_b = 80\%$, and the acceptance $\mathscr{A}$ of the detector. We estimate this acceptance by applying the following pre-selection cuts to detect the final $4b + Z$ events [98],

$$E_b > 20 \text{ GeV}, \quad |\eta_b| < 2.5, \quad |\eta_Z| < 2.5, \quad y_{bb} > 0.0010\,, \tag{6.38}$$

where E_b is the energy of the b-jets, $\eta_{b/Z}$ is the pseudo-rapidity of the b/Z respectively and y_{bb} is the difference in the pseudo-rapidity of the b-jets, which represents the distance between two b-jets. In order to estimate the acceptance $\mathscr{A}$, we simulate the $e^+e^- \to Zhh \to Zb\bar{b}b\bar{b}$ process with and without the cuts of eq. (6.38) with `MadGraph` at the parton level. We obtain $\mathscr{A}$ as the ratio of events with and without cuts. Taking also into account the luminosity $\mathscr{L} = 8$ ab^{-1}, we can define the number of events N as

$$N = \sigma(e^+e^- \to Zhh) \times \mathscr{L} \times \left(\text{BR}(h \to b\bar{b})\right)^2 \times \mathscr{A} \times \epsilon_b^4. \tag{6.39}$$

Next, we define the statistical significance very similar as for the HL-LHC case in eq. (6.35). We calculated the significances for both polarisations, denoted as Z_{-+} for eq. (6.36) and

Z_{+-} for eq. (6.37). The luminosity assumed for each polarisation is 40% of the total luminosity, i.e. $\mathscr{L}_{-+} = \mathscr{L}_{+-} = 0.4 \times 8\ \text{ab}^{-1} = 3.2\ \text{ab}^{-1}$. The overall significance is then obtained as $Z := \sqrt{Z_{-+}^2 + Z_{+-}^2}$. The results for the significances are calculated with tree-level and one-loop trilinear scalar couplings, which we denote respectively $Z^{(0)}$ and $Z^{(1)}$. The results for the six benchmark points are summarised in table 6.5. The corresponding results for the differential distributions are presented in figs. 6.17 to 6.19. Considering the Higgs decaying into $b\bar{b}$, the red (green) curves show the distributions for $\sigma_{Zhh}^{\text{RxSM}}$ using $\lambda_{ijk}^{(0)}$ ($\hat{\lambda}_{ijk}^{(1)}$), the blue (orange) curves show the distributions for $\sigma_{H,Zhh}^{\text{RxSM}}$, i.e. only taking into account the heavy Higgs resonance diagram, using $\lambda_{ijk}^{(0)}$ ($\hat{\lambda}_{ijk}^{(1)}$), and the yellow curves show the corresponding SM distribution for σ_{Zhh}^{SM}.

BP	$\kappa_\lambda^{(0)}$	$\kappa_\lambda^{(1)}$	$\lambda_{hhH}^{(0)}$ [GeV]	$\lambda_{hhH}^{(1)}$ [GeV]	$\sigma_{Zhh}^{\text{RxSM}}(\lambda_{ijk}^{(0)})$ [fb]	$\sigma_{Zhh}^{\text{RxSM}}(\hat{\lambda}_{ijk}^{(1)})$ [fb]	$Z^{(0)}$	$Z^{(1)}$	$Z_{\text{peak}}^{(0)}$	$Z_{\text{peak}}^{(1)}$
1	1.01	3.02	96.30	−119.70	0.061	0.125	0.00	6.98	0.00	0.38
2	0.99	4.86	2.30	−303.60	0.060	0.224	0.00	23.98	0.00	0.95
3	1.07	1.41	127.60	181.90	0.064	0.073	1.84	2.29	1.77	2.11
4	1.61	3.27	543.20	131.20	0.078	0.136	0.00	9.90	0.00	0.32
5	1.30	1.30	153.90	165.10	0.100	0.103	18.88	19.80	18.07	18.88
6	1.10	1.50	163.5	263.8	0.066	0.077	3.40	4.44	3.60	0.71

Table 6.4: Predictions for κ_λ and λ_{hhH} at tree level and one loop, for the total $Zhh \to Zb\bar{b}b\bar{b}$ production cross-section at a 1 TeV e^+e^- collider using tree-level or one-loop trilinear couplings and statistical significances to distinguish the di-Higgs invariant mass differential distributions (with tree-level or one-loop trilinear couplings) from the SM, or from the case $\lambda_{hhH} = 0$, for the benchmark points defined in table 6.2.

BP	$\sigma_{Zhh}^{\text{RxSM}}(\lambda_{ijk}^{(0)})$ [fb]	$\sigma_{Zhh}^{\text{RxSM}}(\hat{\lambda}_{ijk}^{(1)})$ [fb]	$Z^{(0)}$	$Z^{(1)}$	$Z_{\text{peak}}^{(0)}$	$Z_{\text{peak}}^{(1)}$
1	0.061	0.125	0.00	6.98	0.00	0.38
2	0.060	0.224	0.00	23.98	0.00	0.95
3	0.064	0.073	1.84	2.29	1.77	2.11
4	0.078	0.136	0.00	9.90	0.00	0.32
5	0.100	0.103	18.88	19.80	18.07	18.88
6	0.066	0.077	3.40	4.44	3.60	4.71

Table 6.5: Predictions for κ_λ and λ_{hhH} at tree level and one loop, for the total Zhh production cross-section for the $(-80\%, +30\%)$ polarisation, considering decay $h \to b\bar{b}$] at a 1 TeV e^+e^- collider using tree-level or one-loop trilinear couplings and statistical significances to distinguish the di-Higgs invariant mass differential distributions (with tree-level or one-loop trilinear couplings) from the SM, or from the case $\lambda_{hhH} = 0$, for the benchmark points defined in table 6.2.

In fig. 6.17, we observe that for BP1 and BP2 the RxSM distribution with tree-level trilinear scalar couplings (red curve) is practically indistinguishable from the SM distributions (yellow curves). In terms of the statistical significance (see table 6.5), BP1 and BP2 both have $Z^{(0)} = 0.0$, meaning that a difference in the number of events cannot be

detected. On the other hand, when we consider the distributions with one-loop trilinear scalar couplings (green curves) and compare them with the SM ones (yellow curves), we find that there is a large enhancement for the RxSM case due to the large loop corrections to κ_λ. We find values of $Z^{(1)} = 6.98$ and $Z^{(1)} = 23.98$ for BP1 and BP2, respectively, which means that these points can be distinguished from the SM when including one-loop corrections to the trilinear scalar couplings.

Turning next to BP3 and BP4, as shown in fig. 6.18, the RxSM distributions using tree-level trilinear scalar couplings (red curves) look slightly different from the SM curve (yellow curve), whether it is the resonance in BP3 or the non-renosant contributions in BP4. However, when we compute the significances we find that for BP3 it is small, whereas for BP4 it is equal to zero, mainly due to the small difference in the number of events after taking into account the Higgs-boson decays and the cuts. For BP3 we do not find large loop corrections for the trilinear scalar couplings and therefore when we consider them in the calculation of the cross-section (green curve), we do not observe an important improvement in the significance comparing it to other BP's values, see table 6.5. For BP4 there is a positive correction of $\mathcal{O}(100\%)$ in κ_λ, which causes a general enhancement of the distribution with respect to the SM one. In turn, the statistical significance including one-loop corrections increases from $Z^{(0)} = 0.00$ to $Z^{(1)} = 9.90$. Consequently, one can distinguish the result of the RxSM from the SM one for BP4 provided that we take into account one-loop corrections to the trilinear scalar couplings.

Finally, for BP5 and BP6, as shown in fig. 6.19, the RxSM distributions using tree-level trilinear scalar couplings (red curve) can already clearly be distinguished from the SM distributions (yellow curves), because of the resonance peak structure from the heavy Higgs boson. For the BP5 we have a significance using tree-level trilinear scalar couplings of $Z^{(0)} = 18.88$, which means that we have evidence of new physics, while for BP6 since the resonance is smaller the significance is only $Z^{(0)} = 3.40$. For these benchmark points when considering one-loop corrected trilinear scalar couplings we can see that the distributions (green curves) are not significantly modified because the loop corrections are not very large. However, we can see that taking into account the loop corrections still does improve slightly the significances for discriminating the RxSM distributions from the SM ones. We have also evaluated for all the benchmark points $Z^{(0)}_{\text{peak}}$ and $Z^{(1)}_{\text{peak}}$, defined analogously to the HL-LHC case — see section 6.3.1. The results are shown the rightmost two columns in table 6.5. While for BP1-4 the sensitivity is small to distinguish the resonant peaks, the numbers for BP5 and BP6 indicate that the main part of the significance to distinguish the RxSM from the SM in in these scenarios originates from the resonance peak, and not from the continuum. For these two benchmark points the statistical significance indicates that the resonance peak structure can possibly be distinguished from the continuum, which may enable a measurement of λ_{hhH}, see [323].

6.4 Discussion of the results

In this chapter, we explored the phenomenology of di-Higgs production in the general Higgs singlet extension of the SM, the RxSM, at the HL-LHC and a possible future high-energy e^+e^- collider. In particular, we investigated the impact of the radiative corrections to the trilinear scalar couplings λ_{hhh} and λ_{hhH}, which are relevant for the di-Higgs processes. At the technical level, we computed the loop-corrected trilinear scalar couplings using `anyH3`, and used these as inputs for calculations of di-Higgs cross-sections

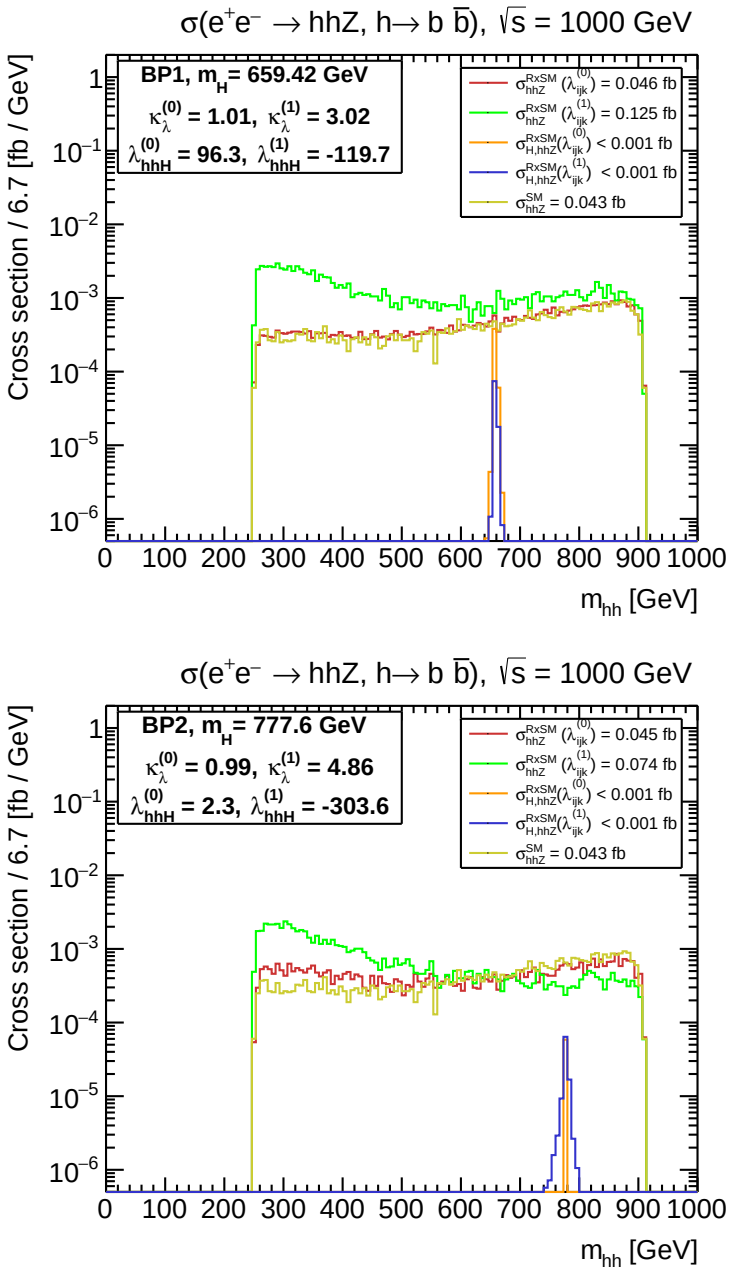

Figure 6.14: Differential polarised di-Higgs production cross-section distributions as a function of the di-Higgs invariant mass m_{hh} for ILC1000. *Top:* Results for BP1; *bottom:* Results for BP2 from table 6.2. We plot the RxSM result using one-loop trilinear scalar couplings (green curve), the RxSM result using tree-level scalar couplings (red), the contribution of the diagram with H in the s-channel using one-loop trilinear scalar couplings (blue curve), the contribution of the diagram with H in the s-channel using tree-level trilinear scalar couplings (orange curve) and the SM result (yellow curve). Values for $\hat{\lambda}^{(1)}_{hhH}$ are shown in GeV.

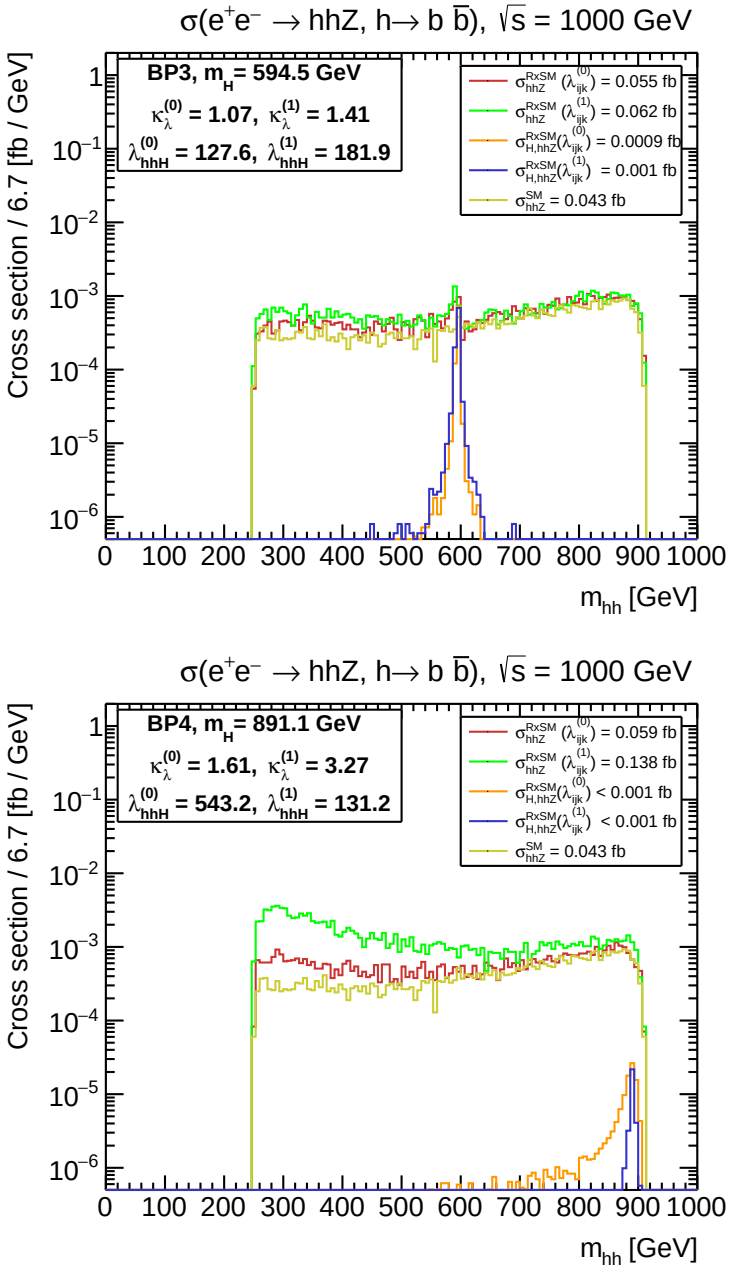

Figure 6.15: Differential polarised di-Higgs production cross-section distributions as a function of the di-Higgs invariant mass m_{hh} for ILC1000. *Top:* Results for BP3; *bottom:* Results for BP4 from table 6.2. We plot the RxSM result using one-loop trilinear scalar couplings (green curve), the RxSM result using tree-level scalar couplings (red), the contribution of the diagram with H in the s-channel using one-loop trilinear scalar couplings (blue curve), the contribution of the diagram with H in the s-channel using tree-level trilinear scalar couplings (orange curve) and the SM result (yellow curve). Values for $\hat{\lambda}^{(1)}_{hhH}$ are shown in GeV.

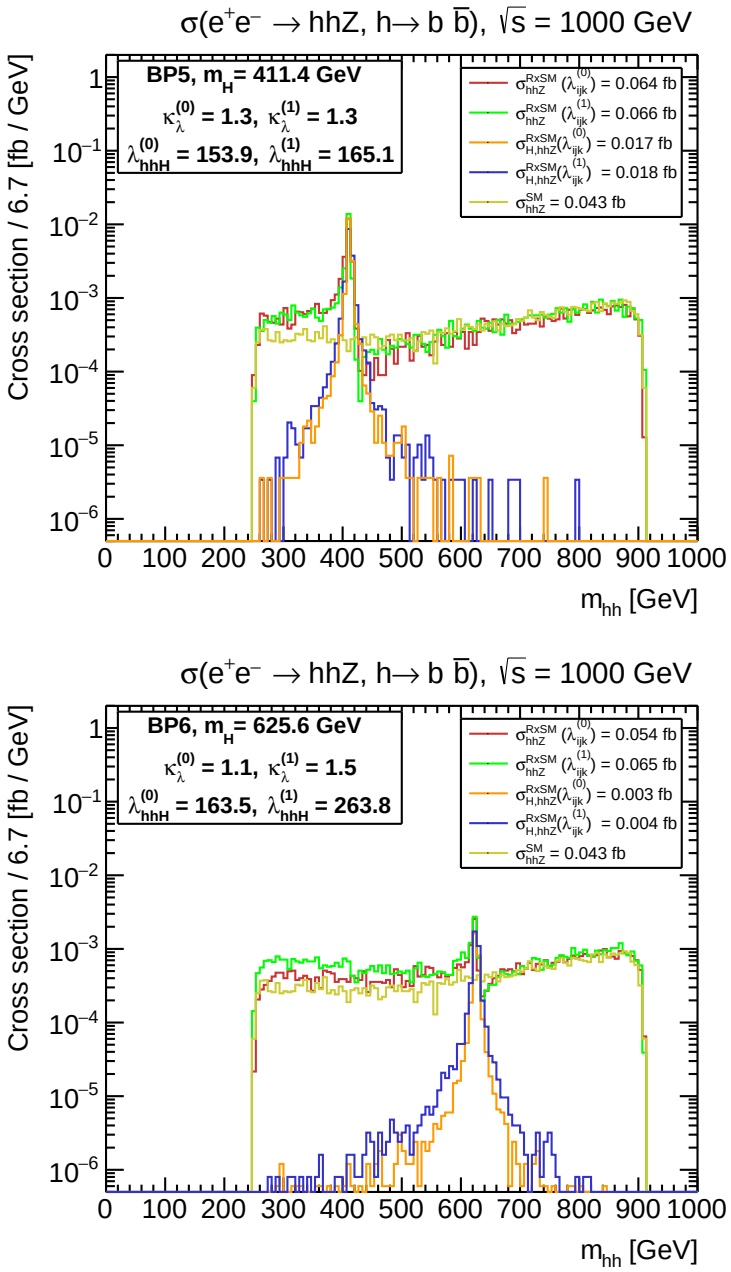

Figure 6.16: Differential polarised di-Higgs production cross-section distributions as a function of the di-Higgs invariant mass m_{hh} for ILC1000. *Top:* Results for BP5; *bottom:* Results for BP6 from table 6.2. We plot the RxSM result using one-loop trilinear scalar couplings (green curve), the RxSM result using tree-level scalar couplings (red), the contribution of the diagram with H in the s-channel using one-loop trilinear scalar couplings (blue curve), the contribution of the diagram with H in the s-channel using tree-level trilinear scalar couplings (orange curve) and the SM result (yellow curve). Values for $\hat{\lambda}^{(1)}_{hhH}$ are shown in GeV.

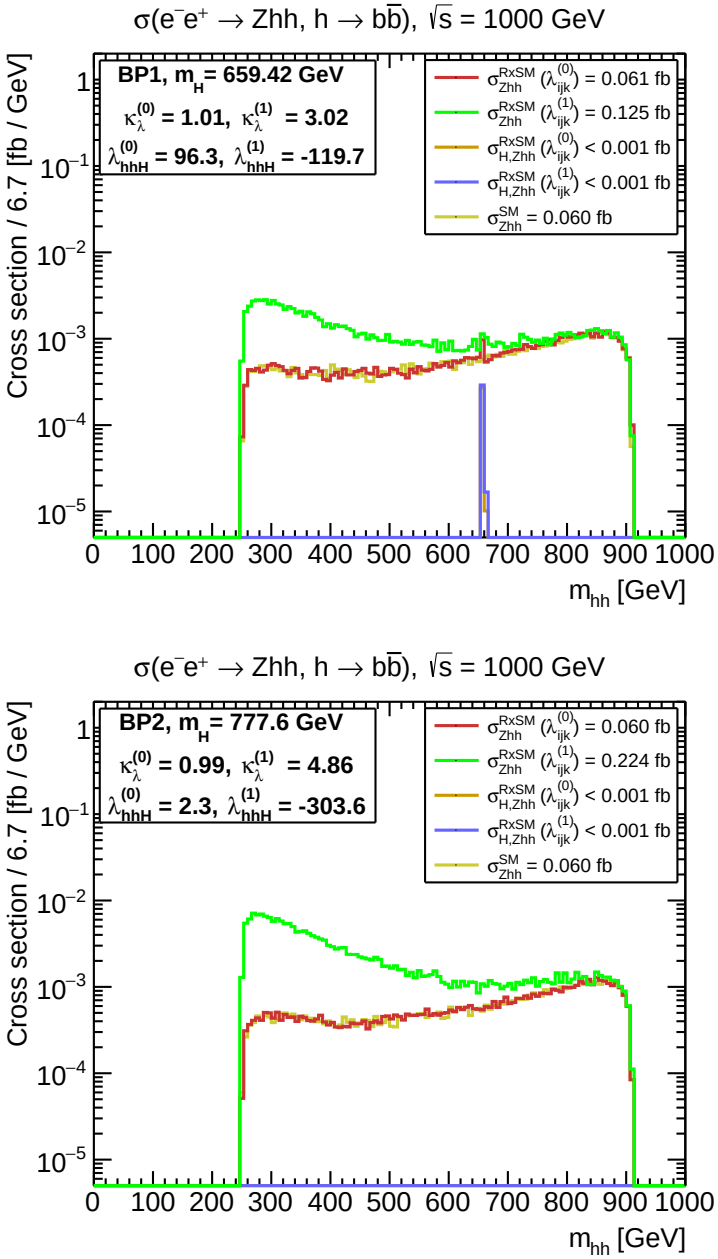

Figure 6.17: Differential polarised di-Higgs production cross-section distributions as a function of the di-Higgs invariant mass m_{hh} for ILC1000. *Top:* Results for BP1; *bottom:* Results for BP2 from table 6.2. We plot the RxSM result using one-loop trilinear scalar couplings (green curve), the RxSM result using tree-level scalar couplings (red), the contribution of the diagram with H in the s-channel using one-loop trilinear scalar couplings (blue curve), the contribution of the diagram with H in the s-channel using tree-level trilinear scalar couplings (orange curve) and the SM result (yellow curve). Values for $\hat{\lambda}^{(1)}_{hhH}$ are shown in GeV.

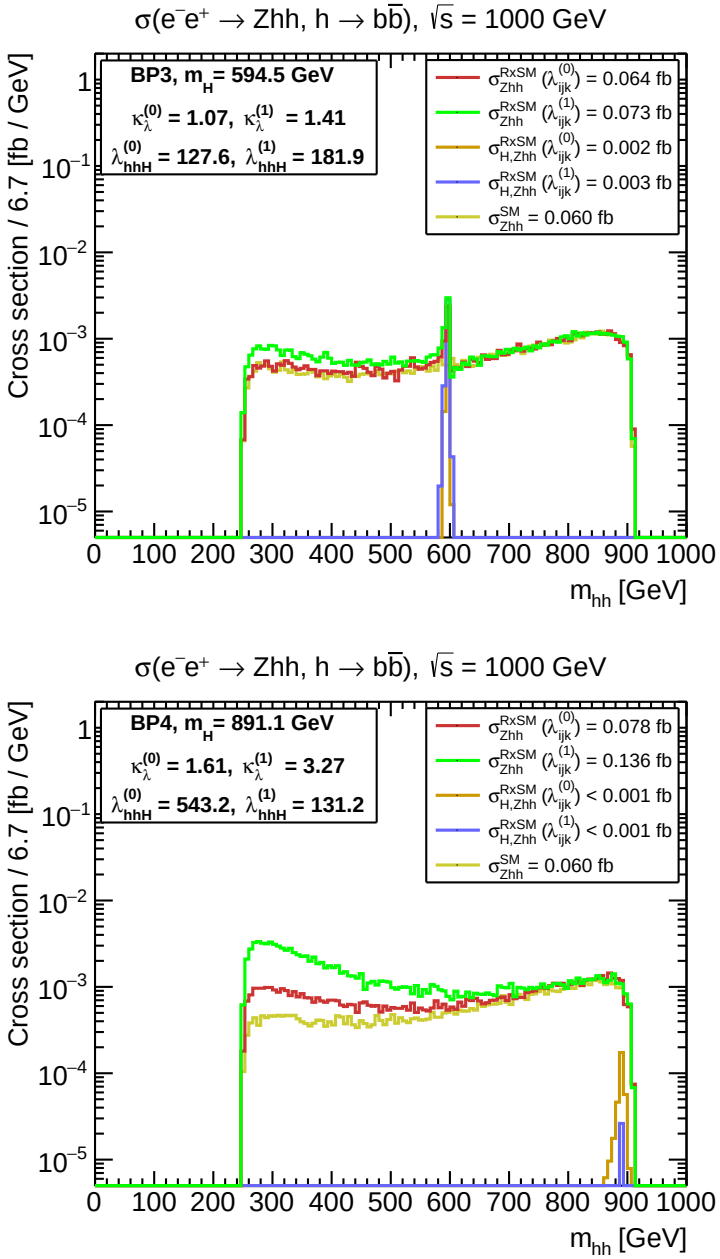

Figure 6.18: Differential polarised di-Higgs production cross-section distributions as a function of the di-Higgs invariant mass m_{hh} for ILC1000. *Top:* Results for BP3; *bottom:* Results for BP4 from table 6.2. We plot the RxSM result using one-loop trilinear scalar couplings (green curve), the RxSM result using tree-level scalar couplings (red), the contribution of the diagram with H in the s-channel using one-loop trilinear scalar couplings (blue curve), the contribution of the diagram with H in the s-channel using tree-level trilinear scalar couplings (orange curve) and the SM result (yellow curve). Values for $\hat{\lambda}^{(1)}_{hhH}$ are shown in GeV.

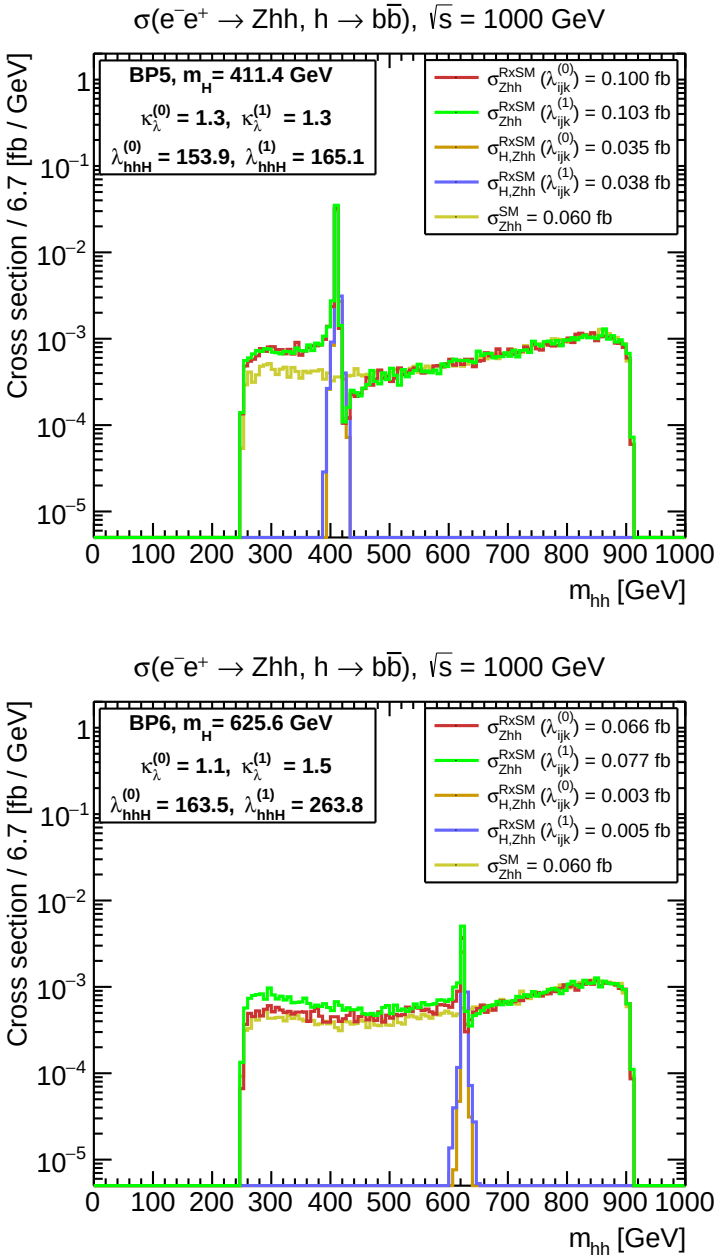

Figure 6.19: Differential polarised di-Higgs production cross-section distributions as a function of the di-Higgs invariant mass m_{hh} for ILC1000. *Top:* Results for BP5; *bottom:* Results for BP6 from table 6.2. We plot the RxSM result using one-loop trilinear scalar couplings (green curve), the RxSM result using tree-level scalar couplings (red), the contribution of the diagram with H in the s-channel using one-loop trilinear scalar couplings (blue curve), the contribution of the diagram with H in the s-channel using tree-level trilinear scalar couplings (orange curve) and the SM result (yellow curve). Values for $\hat{\lambda}^{(1)}_{hhH}$ are shown in GeV.

and distributions with `HPAIR` (for $gg \to hh$) and `Madgraph5_aMC` (for $e^+e^- \to Zhh$). We devised, for the first time, a complete set of on-shell renormalisation conditions for all the parameters of the RxSM scalar sector, including for the $\mathbb{Z}_2$-breaking Lagrangian trilinear couplings κ_{SH} and κ_S that were so far renormalised $\overline{\text{MS}}$ in the existing literature.

We performed an extensive scan of the RxSM parameter space and determined the possible values of λ_{hhh}, λ_{hhH}, $\sigma_{hh}^{\text{RxSM}}$ and $\sigma_{Zhh}^{\text{RxSM}}$ that can be realised for points allowed by state-of-the-art theoretical and experimental constraints. For λ_{hhh}, we find that enhancements up to $\kappa_\lambda \simeq 6$ are possible in the region where $\cos\alpha \gtrsim 0.998$, $m_H \in [800,\ 900]$ GeV and $v_S \lesssim 50$ GeV. In the same region of parameter space λ_{hhH} can receive large negative corrections that can even flip its sign. For this parameter region, the concurrent increase of λ_{hhh} and decrease of λ_{hhH} both contribute to enhancing $\sigma_{hh}^{\text{RxSM}}$, where values up to $\sigma_{hh}^{\text{RxSM}} \sim 4.5\,\sigma_{hh}^{\text{SM}}$ were found. We also compared the magnitude of the enhancements in $\sigma_{hh}^{\text{RxSM}}$ achievable from tree-level or one-loop modifications of the trilinear scalar couplings: while effects are possible already at the tree level, the largest effects arise from radiative corrections.

We next investigated the impact of the loop corrections to the trilinear scalar couplings on the di-Higgs invariant mass distributions. We devised six benchmark scenarios, representative of the RxSM parameter space, and we quantified the ability to distinguish these scenarios from the SM experimentally, using the statistical significance defined in [323]. In particular, we showed that for a number of these scenarios (BPs 1, 2 and 4), only an analysis with one-loop trilinear couplings would allow discriminating the RxSM from the SM. Conversely, we found that for some scenarios with resonant contributions for low m_H (like BP5), the inclusion of loop-corrections in $\hat{\lambda}_{ijk}^{(1)}$ has a smaller impact on the distributions and the conclusions that can be drawn from them.

We performed similar studies of the total and differential cross-sections for the process $e^+e^- \to Zhh$ at a high-energy e^+e^- collider. The largest enhancements of the cross-section are found for the same regions of the parameter space as for the di-Higgs process at the HL-LHC, and values up to $\sigma_{Zhh}^{\text{RxSM}} \sim 4\,\sigma_{Zhh}^{\text{SM}}$ can be attained. For the six benchmark points we have evaluated the differential m_{hh} distributions. We find that the loop corrections to the trilinear scalar couplings can significantly enhance the significance for distinguishing the RxSM from the SM. The resonance peak structure, on the other hand, only contributes significantly in two of the benchmark points. In that case the statistical significance indicates that the resonance peak structure can possibly be distinguished from the continuum, which may enable a measurement of λ_{hhH}.

Our results demonstrate the crucial importance of including, whenever possible, higher-order BSM corrections to analyses of di-Higgs production, in order to draw reliable conclusions from the comparison of experimental data with theoretical predictions. This provides further motivation for the automation of di-Higgs precision calculations, see [99] for recent advancements. Additionally, we concentrated in this work on corrections to trilinear scalar couplings, as these are known (see e.g. [87]) to be the dominant source of BSM corrections to di-Higgs productions. However, for scenarios with total and differential cross-sections undistinguishable from the SM ones, the investigation of corrections to other Higgs couplings entering the process (e.g. Higgs-top or Higgs-Z interactions) becomes relevant. Finally, this work has been focused on probes of RxSM scenarios at high-energy colliders. A next important step is to include into the investigation the dynamics of the EWPT and possible production of cosmological relics of a SFOEWPT.

Chapter 7

SFOEWPT and GW signals

¿Ya no vas a volver a casa nunca?

– Ibontxu

The previous two chapters were devoted to the collider phenomenology of the RxSM. We first showed that di-Higgs production provides a direct probe of the scalar potential through the trilinear Higgs couplings, and that a reliable description of the process requires the complete treatment of resonant and non-resonant contributions, together with their interference. We then demonstrated that, in beyond-the-Standard-Model scalar theories, one-loop corrections to these couplings can be sizeable and may substantially modify the conclusions drawn from a tree-level analysis. Together, these results established a detailed picture of how the extended scalar sector of the RxSM can manifest itself at colliders.

We now shift the emphasis of the discussion towards the cosmological dynamics of the model. In particular, we devote a more detailed analysis to the electroweak phase transition, which constitutes one of the main theoretical motivations for considering scalar extensions of the Standard Model in the first place. The central question is whether the thermal evolution of the RxSM can give rise to a strong first-order electroweak phase transition, and if so, which regions of the RxSM's parameter space realise this possibility.

Addressing this question is important not only from a theoretical perspective, but also from a phenomenological one. A SFOEWPT may leave observable signatures today through a stochastic background of gravitational waves (SBGW). At the same time, the same scalar dynamics responsible for the transition can also affect collider observables, in particular di-Higgs production. This opens the possibility of testing the model through a genuinely complementary strategy, combining information from the early Universe with measurements at high-energy colliders.

A central aspect of this chapter is that, it presents for the first time in the RxSM a simultaneous analysis of these complementary probes: the gravitational-wave signal generated by the phase transition, the prospects at the HL-LHC, and the sensitivity of future high-energy e^+e^- colliders. Moreover, the collider part of this study is not based on simplified estimates, but on a complete calculation of the di-Higgs production cross sections, including the full set of relevant diagrams and the one-loop corrections to the trilinear Higgs couplings discussed in the previous chapter. In this way, the cosmological and collider

analyses are treated on the same footing and connected through a consistent description of the scalar sector.

In this chapter we therefore analyse the one-loop finite-temperature effective potential of the RxSM, classify the different thermal histories that can arise, and identify the regions of parameter space in which a strong first-order electroweak phase transition occurs. We then investigate the associated gravitational-wave spectra and assess their observability, before confronting the same scenarios with the prospects from di-Higgs production at the HL-LHC and at future e^+e^- colliders. The goal is thus to provide a unified view of how the RxSM can be explored through the interplay between cosmological observables and collider signatures.

7.1 Thermodynamics of the RxSM

In this chapter, we review the theoretical setup used to investigate the thermal evolution in the early-Universe of RxSM scenarios. We first introduce the one-loop temperature-dependent effective potential in the RxSM before discussing how we compute the thermal dynamics of the electroweak potential. Finally, we explain our calculation of the stochastic GW background produced in scenarios with a SFOEWPT. For all these steps, we have used the code `BSMPTv3` [83, 85, 91], in which we implemented the general RxSM.

7.1.1 Effective potential

The first step in order to study the thermodynamics of an extended Higgs sector is to compute the temperature-dependent effective potential. In this work, we have used a perturbative 4D approach, where the potential is expanded as

$$V_{\text{eff}}^{(1)}(\phi, T) = V^{(0)}(\phi) + V_{\text{CW}}^{(1)}(\phi) + V_{\text{CT}}^{(1)}(\phi) + V_{\text{T}}^{(1)}(\phi, T) + V_{\text{daisy}}^{(1)}(\phi, T)\,. \tag{7.1}$$

Here $V^{(0)}$ is the tree-level potential, $V_{\text{CW}}^{(1)}$ is the one-loop effective (or Coleman-Weinberg [332]) potential at $T = 0$ (calculated in the $\overline{\text{MS}}$ scheme), $V_{\text{CT}}^{(1)}$ denotes a one-loop counter term (CT) potential (also defined at $T = 0$), while the temperature-dependent parts of the potential are given by the one-loop thermal corrections term $V_{\text{T}}^{(1)}$ and a resummation term $V_{\text{daisy}}^{(1)}$ (discussed below). The notation ϕ is used to denote collectively the scalar field degrees of freedom of the RxSM.

The Coleman-Weinberg potential can be computed straightforwardly in the $\overline{\text{MS}}$ scheme using the supertrace formula [290], it reads

$$V_{\text{CW}}^{(1)}(\phi) = \sum_i \frac{(-1)^{2s_i} n_i}{64\pi^2} m_i^4(\phi) \left[\ln\left(\frac{m_i^2(\phi)}{Q^2} \right) - c_i \right], \tag{7.2}$$

where i runs over the particle content — scalars, fermions, and gauge bosons — of the model (we note that we work here in the Landau gauge, so that ghosts do not contribute to $V_{\text{CW}}^{(1)}$, nor its field derivatives), and Q is the renormalisation scale. The constants c_i are 3/2 for scalars and fermions, and 5/6 for gauge bosons (as we use here the $\overline{\text{MS}}$ scheme). For the rest of this work we choose to take $Q = v$, unless otherwise specified. Although one could in principle use the $\overline{\text{MS}}$ scheme result, we choose instead to convert our expressions to the more convenient and physically-motivated OS-like scheme defined in Refs. [83, 85, 91]. To do so, we add a finite shift to our effective potential, corresponding

to a finite conversion of the parameters entering the tree-level potential. This counterterm potential is defined as

$$V_{\rm CT}^{(1)}(\phi) = \sum_i \frac{\partial V^{(0)}}{\partial x_i}\delta_{\rm CT}^{(1)}x_i + \sum_j(\phi_j + v_j)\delta_{\rm CT}^{(1)}t_j\,, \tag{7.3}$$

where i runs over the parameters of the Lagrangian and j over the scalar particles of the RxSM. The idea of this OS-like scheme is to maintain the location of the minimum of $V_{\rm eff}$ at $T = 0$ as well as the effective-potential masses of all the scalars (also at $T = 0$) to their tree-level values — hence the "OS-like" name of the scheme. In terms of derivatives of the potential, this means that we impose that the first and second derivatives of the zero-temperature effective potential should be equal to the tree-level ones, from which we obtain the following renormalisation conditions

$$\partial_{\phi_i}V_{\rm CT}^{(1)}(\phi)|_{\langle\phi\rangle_{T=0}} = -\partial_{\phi_i}V_{\rm CW}^{(1)}(\phi)|_{\langle\phi\rangle_{T=0}}, \tag{7.4}$$

$$\partial_{\phi_i}\partial_{\phi_j}V_{\rm CT}^{(1)}(\phi)|_{\langle\phi\rangle_{T=0}} = -\partial_{\phi_i}\partial_{\phi_j}V_{\rm CW}^{(1)}(\phi)|_{\langle\phi\rangle_{T=0}}, \tag{7.5}$$

where i and j run over the scalar degrees of freedom. By applying these conditions to the case of the RxSM, one can see that there are not sufficiently many conditions to define a unique set of counterterms and that three additional degrees of freedom remain. Following the original notation of this scheme in [83], we call these degrees of freedom t_1, t_2, t_3, and absorb them into the counterterms (although in the end, we set them to 0). Finally, we obtain the following set of counterterms

$$\begin{aligned}
\delta_{\rm CT}^{(1)}\mu^2 &= 0\,,\\
\delta_{\rm CT}^{(1)}M_S^2 &= 0\,,\\
\delta_{\rm CT}^{(1)}\kappa_S &= \frac{1}{v_S^3}\left(\frac{3v^2}{2}H_{G^0G^0} - \frac{v^2}{2}H_{hh} + \frac{vv_s}{2}H_{hs} + v_S^2H_{ss} - 3v_SN_s\right)\,,\\
\delta_{\rm CT}^{(1)}\kappa_{SH} &= \frac{H_{hh} - 3H_{G^0G^0}}{v_S} + \frac{H_{hs}}{v}\,,\\
\delta_{\rm CT}^{(1)}\lambda &= \frac{H_{G^0G^0} - H_{hh}}{v^2}\,,\\
\delta_{\rm CT}^{(1)}\lambda_S &= \frac{1}{v_S^4}\left(\frac{-3v^2}{4}H_{G^0G^0} + \frac{v^2}{4}H_{hh} - \frac{v_S^2}{2}H_{ss} + v_SN_s\right)\,,\\
\delta_{\rm CT}^{(1)}\lambda_{SH} &= \frac{3H_{G^0G^0} - H_{hh}}{v_S^2} - \frac{2H_{hs}}{vv_S}\,,\\
\delta_{\rm CT}^{(1)}t_{G^0} &= -N_{G^0}\,,\\
\delta_{\rm CT}^{(1)}t_{G^+} &= -N_{G^+}\,,\\
\delta_{\rm CT}^{(1)}t_{G^-} &= -N_{G^-}\,,\\
\delta_{\rm CT}^{(1)}t_h &= H_{G^0G^0}v - N_h\,,\\
\delta_{\rm CT}^{(1)}t_s &= 0\,,
\end{aligned} \tag{7.6}$$

where N_{ϕ_i} and $H_{\phi_i\phi_j}$ are the first and second derivatives of the CW potential evaluated at the minimum of the potential, i.e.

$$N_{\phi_i} = \left.\frac{\partial V_{\rm CW}^{(1)}}{\partial\phi_i}\right|_{\langle\phi\rangle_{T=0}}, \qquad \text{and} \qquad H_{\phi_i\phi_j} = \left.\frac{\partial^2 V_{\rm CW}^{(1)}}{\partial\phi_i\partial\phi_j}\right|_{\langle\phi\rangle_{T=0}}. \tag{7.7}$$

Turning next to the temperature-dependent corrections, the one-loop thermal potential [333, 334] is given by

$$V_{\rm T}^{(1)}(\phi,T)=\sum_i \frac{n_i T^4}{2\pi^2} J_{\pm}\left(\frac{m_i^2(\phi)}{T^2}\right), \tag{7.8}$$

where i runs again over the particle content of the model, and $J_\pm$ are the fermionic and bosonic thermal integrals, respectively, and are defined as:

$$J_{\pm}(x)=\mp\int_0^\infty dz\, z^2 \log\left[1\pm\exp\left(-\sqrt{z^2+x}\right)\right]. \tag{7.9}$$

Finally, we have to solve the IR-divergence problem that arises due to the massless bosonic zero Matsubara modes of finite-temperature field theory and the infrared pole of the propagator of these modes. To solve this problem, there are different ways of resumming relevant higher-order effects in order to dress the propagator of the zero-modes and avoid the pole divergence. The minimal set of higher-order diagrams that must be resummed has been shown to be those known as Daisy diagrams.

There are different methods that one can follow to resum these diagrams. In this work, we have followed the Arnold-Espinosa resummation method [211] to disentangle the UV physics from the IR one. In this method, the mass of the zero Matsubara modes is shifted by the thermal mass and, therefore, substitute the propagator of the zero mode with a dressed propagator, avoiding the divergence of the pole. This leads to a contribution to the potential with the following structure,

$$V_{\rm daisy}^{(1)}(\phi,T)=-\sum_i \frac{T}{12\pi}{\rm Tr}\left\{[m_i^2(\phi_i)+\Pi_i^2(T)]^{\frac{3}{2}}-[m_i^2(\phi_i)]^{\frac{3}{2}}\right\}, \tag{7.10}$$

where i runs over the different bosonic degrees of freedom, and $\Pi_i^2(T)$ is the squared thermal mass of the boson ϕ_i, generated by the thermal potential. The hard thermal masses for the scalars and the longitudinal bosonic fields are defined as:

$$\Pi_\Phi(T)=T^2\left(\frac{3g_2^2+g_1^2}{16}+\frac{\lambda}{2}+\frac{\lambda_{SH}}{12}+\frac{y_t^2}{4}\right), \tag{7.11}$$

$$\Pi_S(T)=T^2\left(\frac{\lambda_{SH}}{3}+\lambda_S\right), \tag{7.12}$$

$$\Pi_{W_L}(T)=\frac{11}{6}\,g_2^2\,T^2, \tag{7.13}$$

$$\Pi_{B_L}(T)=\frac{11}{6}\,g_1^2\,T^2. \tag{7.14}$$

7.1.2 Phase transition dynamics

Employing eq. (7.1) we can compute the thermal evolution of the Higgs potential in order to study the dynamics of the EWPT. Two main ways in which the EWPT could have occurred can be distinguished. On the one hand, it could have proceeded as a second-order phase transition or a cross-over, meaning that the transition from the false vacuum to the EW one is smooth and there is no associated energy gap. On the other hand,

the EWPT could have happened as a first-order phase transition. In the latter case, which we denote as FOEWPT, during the thermal evolution of the potential a barrier forms between the false and the EW minima. The only way to transition is through quantum tunnelling, leading to an energy gap in the transition. This event occurs nearly simultaneously at different points in the Universe as it expands, creating bubbles of the EW vacuum that nucleate and then expand in the background of the false vacuum. The temperature at which this transition occurs is called the nucleation temperature T_n, at which the tunnelling decay rate from the false to the EW minima per Hubble volume matches the Hubble rate.

7.2 Phenomenological implications

In this section, we investigate the dynamics of the EWPT in the RxSM employing the theoretical framework described in the previous section. Numerical computations are performed with the public code `BSMPTv3` [91].

7.2.1 Different thermal histories

We begin by investigating the different possible thermal histories in the RxSM (a similar analysis in the 2HDM can be found in [56]). By scanning of the parameter space of the RxSM, we find six different scenarios, which we label from A to F (similar to [56]), and which we illustrate in fig. 7.1 for selected points listed in table 7.1.

Id	m_H [GeV]	$\cos\alpha$	κ_S [GeV]	κ_{SH} [GeV]	v_S [GeV]
A	342.8	0.9999	−1000	−100	110
B	288.5	0.9949	−900	−54	149
C	285.5	0.9891	−900	−87	125
D	290.7	0.9881	−900	−93	120
E	463.9	0.9955	−24	−992	332
F	600.1	0.9800	−300	−1406	280

Table 7.1: RxSM benchmark points for the investigation of the different thermal histories of the Universe in fig. 7.1.

For each scenario, we trace in fig. 7.1 the evolution of the EW and singlet minima as a function of the temperature in order to understand its specific dynamics.

The blue and orange lines in fig. 7.1 correspond respectively the tracing of the minima of the EW doublet and of the singlet. The parts of the line in solid style indicate the path that the Universe actually follows, i.e. at the temperature where a change from dashed to solid is found, a phase transition takes place. The first scenario (top left, **A**) is a *second-order PT*. The second case (top middle, **B**) is a *weak first-order PT*, where a first-order phase transition occurs along the EW direction while the transition along the singlet field direction is continuous. In case **B**, the first-order PT along the EW direction is so weak — in the sense that the discontinuity in the evolution of the Higgs VEV is so small — that this scenario cannot be phenomenologically distinguished from a second-order PT. The third scenario (top right, **C**) is a *multi-step-first order PT*: specifically the PT occurs in two steps, starting with a first-order PT along the singlet direction at higher temperature, followed by another first-order phase transition where both VEVs experience

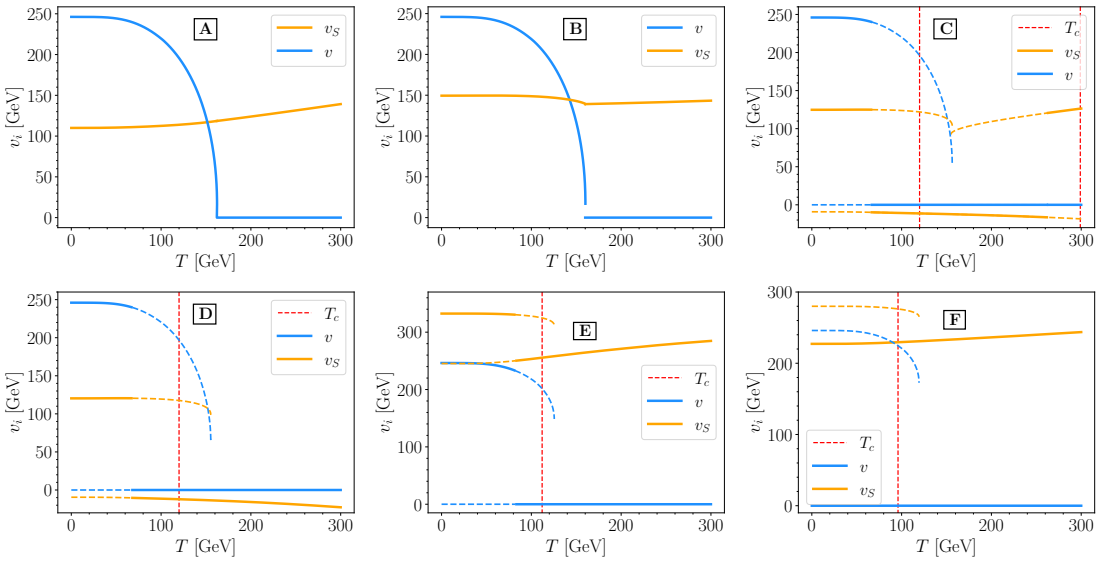

Figure 7.1: The tracing of the different minima of the potential with respect to the temperature for six different thermal histories. In blue we show the minima of the EW doublet and in orange the minima of the singlet field. The solid lines represent the path that the Universe follows. The red dashed line indicates the critical temperature T_c.

a discontinuity. The latter transition corresponds to the EWPT. The fourth scenario (bottom left, **D**) is the *low singlet VEV first-order PT*, where the EWPT occurs as a one-step transition with discontinuities along the EW and singlet directions concurrently. We name the fifth scenario (bottom middle, **E**) *high singlet VEV first-order PT*. This scenario is similar to case **D**, but with the difference that the minimum of the singlet VEV at the moment of the transition is positive. We will see that this leads to weaker transitions than in case **D**. Finally, the last possible history that we find (bottom right, **F**) is *vacuum trapping* [56]. In this scenario, the barrier between the symmetric and EW minima is so large that the tunnelling time is longer than the age of the Universe, meaning that one remains trapped in the symmetric phase. We note that we define here vacuum trapping in terms of the computed tunnelling rate, which is compared to the age of the Universe, rather than in terms of some threshold value of the bounce action.

7.2.2 SFOEWPT

As a first step to search for SFOEWPT scenarios in the RxSM, we perform a parameter scan in the five-dimensional parameter space of the model. We begin by checking theoretical and experimental constraints as outlined in section 4.1.2, and afterwards compute the EWPT dynamics for the allowed points. The scan ranges are as follows,

$$\begin{aligned} m_H &\in [260, 1000] \text{ GeV}, \\ \cos\alpha &\in [0.95, 1], \\ v_S &\in [30, 300] \text{ GeV}, \\ \kappa_S &\in [-1000, 1000] \text{ GeV}, \\ \kappa_{SH} &\in [-1000, 0] \text{ GeV}. \end{aligned} \tag{7.15}$$

We choose as lower bound $m_H > 260$ GeV in order to allow the decay channel $H \to hh$ and enable a complementary analysis of di-Higgs production (including resonant contri-

butions from H) for the scan points — see section 7.3. The requirement of κ_{SH} to be negative comes from the theoretical constraint of boundedness-from-below of the tree-level potential.

In fig. 7.2 we present as colour coding the ratio $\xi_n \equiv v_n/T_n$ in the planes $\{\cos\alpha, m_H\}$ (top left), $\{\cos\alpha, v_S\}$ (top right), $\{\kappa_S, \kappa_{SH}\}$ (bottom left) and $\{m_H, v_S\}$ (bottom right). Our first finding is to confirm the existence of points exhibiting a SFOEWPT, with $\xi_n > 1$, in the scanned region. From the top row in fig. 7.2 we can see that the strongest phase transitions occur further from the alignment limit ($\cos\alpha = 1$), while the weaker ones are closer to it. Another important observation is that we do not find points for large positive values of κ_S. Indeed, for points with large positive values of κ_S, the symmetric minimum of the NLO potential at $T = 0$ is deeper than the EW minimum and therefore the EW vacuum is not stable at NLO. We note that for the potential at NLO, we only check whether the EW minimum is deeper than the minimum of the origin of the potential. Further minima away from the origin of the potential may appear; however, these minima are not reliable because the renormalization scheme is defined in the vicinity of the electroweak vacuum expectation value. When moving far from this minimum, the renormalization scheme ceases to be trustworthy.

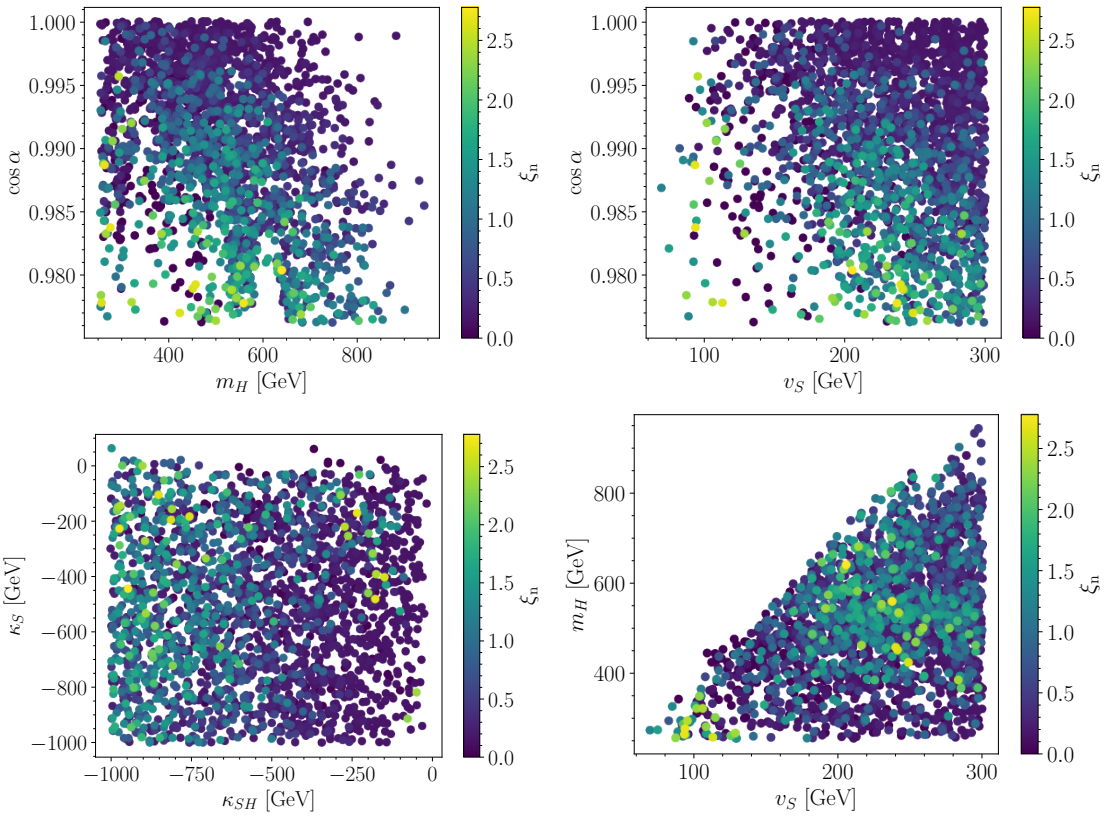

Figure 7.2: Results for $\xi_n \equiv v_n/T_n$ for the points from our RxSM parameter scan. *Top left*: $\{\cos\alpha, m_H\}$ plane; *top right*: $\{\cos\alpha, v_S\}$ plane; *bottom left*: $\{\kappa_S, \kappa_{SH}\}$ plane; *bottom right*: $\{m_H, v_S\}$ plane.

One can also see from fig. 7.2 that the strongest phase transitions (i.e. with $\xi_n > 2$) arise in two distinct regions of the parameter space: a first region with $v_S \lesssim 150$ GeV, $m_H \lesssim 400$ GeV, $\kappa_{SH} \gtrsim -600$ GeV and $\kappa_S \gtrsim -300$ GeV; and a second region for

$v_S \gtrsim 150$ GeV, $m_H \gtrsim 400$ GeV and $\kappa_{SH} \lesssim -500$ GeV. The second region spans the entire range -1000 GeV $< \kappa_S \lesssim 0$ GeV that is populated by allowed points, although the largest values of ξ_n are reached for points with $\kappa_S \gtrsim -600$ GeV.

Investigating the two regions in more detail, one finds that the first region with low v_S corresponds to case **D** in terms of the possible thermal histories of the Universe shown in fig. 7.1, while the second region with larger v_S corresponds to case **E**.

7.2.3 GW signal at LISA

In the following, we focus on the two regions of parameter space found in the previous section that feature the strongest FOEWPT, and we investigate whether they can give rise to GW spectra observable at LISA. Investigating scenarios with five free parameters is however complicated, because of the interplay between effects from different parameters. Instead, we choose to define, for each region, sets of three phenomenological relations between the RxSM parameters that maximise ξ_n, and can then study two-dimensional benchmark planes.

Benchmark plane 1

We begin by considering the region with low values of v_S and m_H. Using the results from the five-dimensional scan in the previous section, we find that the following conditions maximise ξ_n in this region

$$\begin{aligned} \kappa_S &= -900 \text{ GeV}\,, \\ \kappa_{SH} &= (5662.9 \cos\alpha - 5688.4) \text{ GeV}\,, \\ v_S &= (4239.5 \cos\alpha - 4067.6) \text{ GeV}\,. \end{aligned} \tag{7.16}$$

We are then left with only two free parameters, over which we scan with the ranges[1]

$$\begin{aligned} m_H &\in [260, 1000] \text{ GeV}\,, \\ \cos\alpha &\in [0.975, 1]\,. \end{aligned} \tag{7.17}$$

In fig. 7.3 we present the results of the scan in this benchmark plane. The colour coding shows the value of ξ_n for the points allowed by the experimental and theoretical constraints. The region shaded in light blue is excluded by perturbative unitarity. It is important to note that the fact that perturbative unitarity excludes points farther away from the alignment limit is not a general feature of the RxSM, but is only an artefact of the considered plane. We indicate in grey the region where the tree-level potential is stable while at the one-loop level the EW vacuum is unstable (at $T = 0$). Finally, we show in light red the parameter region that is excluded by the direct search of a heavy BSM Higgs boson decaying into a pair of Z bosons in the $l^+l^-l^+l^-$ and $l^+l^-\nu\bar{\nu}$ channels by ATLAS [299].

In fig. 7.3 we can see that in the allowed parameter region three different thermal histories are possible. Following the labels in fig. 7.1, we name the corresponding regions **B**, **C** and **D**. First, in region **B** (dark purple) we find weak first-order phase transitions: these transitions are of first order because there is a small discontinuous transition in the EW

[1] We note that no point allowed by `HiggsSignals` was found below $\cos\alpha = 0.975$, hence the lower bound quoted here.

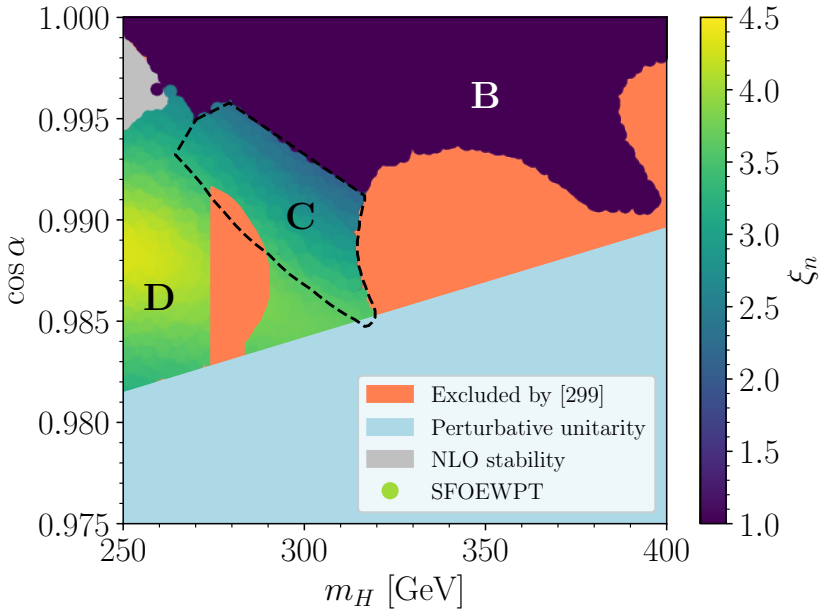

Figure 7.3: Parameter scan results in the RxSM for benchmark plane 1. The colour coding shows the ratio $\xi_n = v_n/T_n$. The different thermal histories are labeled following fig. 7.1. We indicate in light blue the region excluded by perturbative unitarity, in grey the region excluded by the stability of the EW vacuum at NLO and in light red the region excluded by direct searches for heavy Higgs bosons in [299]. We note that in region **B** $0 < \xi_n < 1$.

doublet direction, and the nucleation condition of eq. (3.30) is fulfilled. However, these points are not interesting for phenomenology because the phase transition is too weak. Next, regions **C** and **D** exhibit SFOEWPT — the difference between the two regions is that region **C** features multi-step phase transitions, starting with a weak first-order phase transition followed by the EW phase transition occuring as a SFOEWPT, while in region **D** the phase transitions occur in one step. We can observe that the behaviour of ξ_n at the boundary between both regions is smooth. This is because in region **C** for the calculation of ξ_n we consider the second step of the two-step phase transition, which is the step during which there is tunnelling in the EW doublet direction. Taken separately, this transition corresponds exactly to the single-step transition in region **D**. A similar continuous behaviour of ξ_n is, however, not found at the boundary between regions **B** and **C**. The reason is that at some moment the two branches for positive values of the singlet field in region **C** in fig. 7.1 connect, and the corresponding phase remains deeper than the negative phase. As a consequence, there is then no tunnelling to the negative phase of the singlet field, meaning that the second step of the phase transition of region **C** never occurs, and thus there is no SFOEWPT.

In fig. 7.4 we restrict our attention to the part of benchmark plane 1 where we find a SFOEWPT. In the left and right plots the colour coding represents, respectively, T_n (in GeV) and the SNR at LISA for a bubble wall velocity of $v_w = 0.95$ and 3 years observation time.[2] From the right plot, we find that there is a large region of the parameter space

[2]The shape of the shown areas in both plots is slightly different, because the calculation of the SNR fails for a few points.

for which SNR > 10, i.e. where we find a stochastic GW background detectable at LISA. This result is obtained for $v_w = 0.95$, which as will be discussed in section 7.2.3 is the most pessimistic assumption. Turning next to the left plot of fig. 7.4, we can see that for the points that are observable at LISA T_n is relatively low, $T_n \lesssim 70$ GeV — while the percolation temperature for these same points can be computed to be even significantly lower, $T_p \lesssim 60$ GeV. We can conclude from this that the high GW signals found in benchmark plane 1 are directly related to low values of T_p.

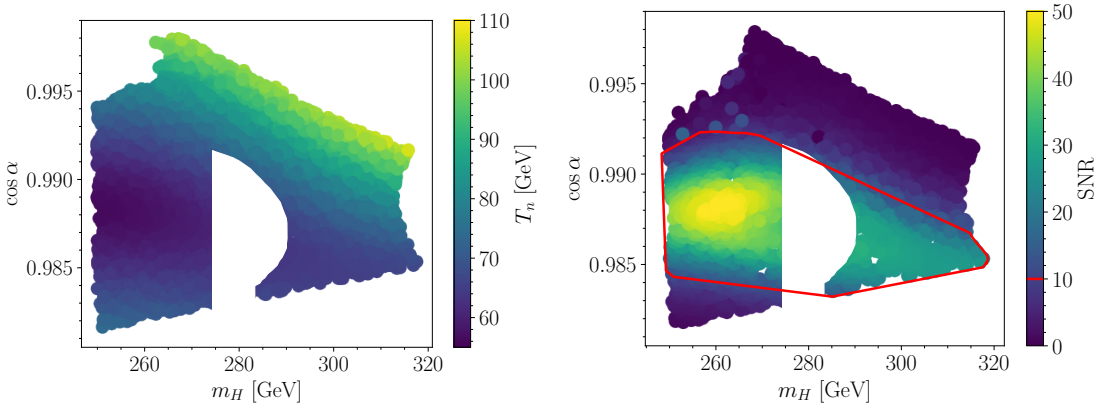

Figure 7.4: Parameter scan results in the RxSM for the points with a SFOEWPT in the benchmark plane 1. *Left*: T_n (in GeV); *right*: SNR at LISA (assuming 3 years of observations) for $v_w = 0.95$, where the region delimited in red represents the observable region (i.e. SNR > 10).

An important characteristic of the SFOEWPT in this benchmark plane (in regions **C** and **D**) is that the transition along the singlet field direction starts from a negative value of v_S. To better visualise this, we display in fig. 7.5 the temperature-dependent effective potential at the nucleation temperature, $V_{\text{eff}}(T_n)$, for a specific benchmark point with an observable SNR > 10 and $T_n = 68$ GeV taken from benchmark plane 1. Because of the negative value of the singlet VEV at the moment of the transition, there is a large difference between the initial and final values of v_S. Another important effect of the negative initial value of the singlet VEV is that it delays the phase transition, thereby lowering the nucleation temperature. This can be observed in the illustration of case **D** in fig. 7.1: one sees that at high temperatures the initial singlet phase is far from the final phase and gradually approaches as the temperature decreases. Starting from a larger negative v_S therefore yields a lower T_n, and in turn a stronger phase transition.

Benchmark plane 2

We now consider the second region, with high values of v_S and m_H, and we define a two-dimensional benchmark plane accordingly. Based on the results from the five-dimensional scan in section 7.2.2, we fix the following conditions

$$\begin{aligned} \cos\alpha &= 0.98\,, \\ \kappa_S &= -300 \text{ GeV}\,, \\ v_S &= 280 \text{ GeV}\,. \end{aligned} \tag{7.18}$$

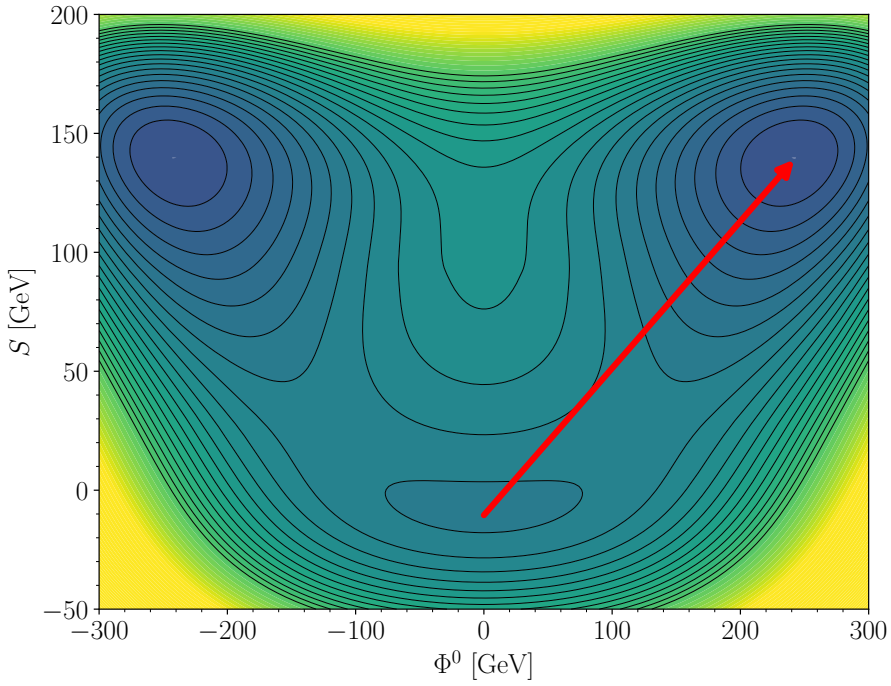

Figure 7.5: Temperature-dependent one-loop effective potential at the nucleation temperature, $V_{\text{eff}}(T_n)$, for a benchmark point featuring a SFOEWPT with a thermal history of type **D** (from fig. 7.1). The BP is defined by $m_H = 262$ GeV, $c_\alpha = 0.9915$, $v_S = 139$ GeV, $\kappa_S = -833$ GeV, $\kappa_{SH} = -72$ GeV, and we obtain $T_n = 68$ GeV as well as a SNR > 10. Φ^0 denotes the CP-even neutral component of the Higgs doublet.

in order to maximise the strength of the SFOEWPT. For the remaining free RxSM parameters, we scan over the following ranges

$$\begin{aligned} m_H &\in [260, 1000]\ \text{GeV}\,, \\ \kappa_{SH} &\in [-2000, -1000]\ \text{GeV}\,. \end{aligned} \tag{7.19}$$

Scan results for this second benchmark plane are shown in fig. 7.6. The colour coding represents the ratio ξ_n for the points allowed by experimental and theoretical constraints. The pink region indicates vacuum trapping, while the grey region corresponds to points for which the potential is stable at tree level but not at NLO (at $T = 0$). The region highlighted in red is excluded by the combination of searches of heavy resonances decaying into bosonic and leptonic final states by ATLAS [335]. Finally, the orange region is excluded by direct searches by CMS of a heavy BSM Higgs boson decaying into two lighter Higgs bosons in the $\tau\tau b\bar{b}$ channel [336].

In fig. 7.6 we can observe that in the allowed parameter space of benchmark plane 2 points with a phase transition only feature one type of thermal history, namely case **E**. Following the labelling in fig. 7.1, we name the corresponding part of the benchmark plane region **E**. With this thermal history, the EWPT is of first order, however, the initial value of v_S at the time of the transition is positive. This leads to weaker phase transitions. From fig. 7.6 we also find that the range of m_H for which a SFOEWPT occurs in benchmark plane 2, namely $m_H \in [550, 950]$ GeV, is significantly larger than in the case of the benchmark plane 1, where it was $m_H \in [250, 320]$ GeV. Additionally, the strength of the

phase transitions increases for lower values of m_H and larger absolute values of κ_{SH} up to a maximum value of $\xi_n \gtrsim 4$, where vacuum trapping occurs. This is the same behaviour as was observed for the 2HDM in Refs. [56, 57]. The explanation for this phenomenon is that the strength of the phase transition grows with the potential barrier between the minima, until the size of the barrier is such that tunnelling cannot happen, leading to the vacuum being trapped in the symmetric minimum.

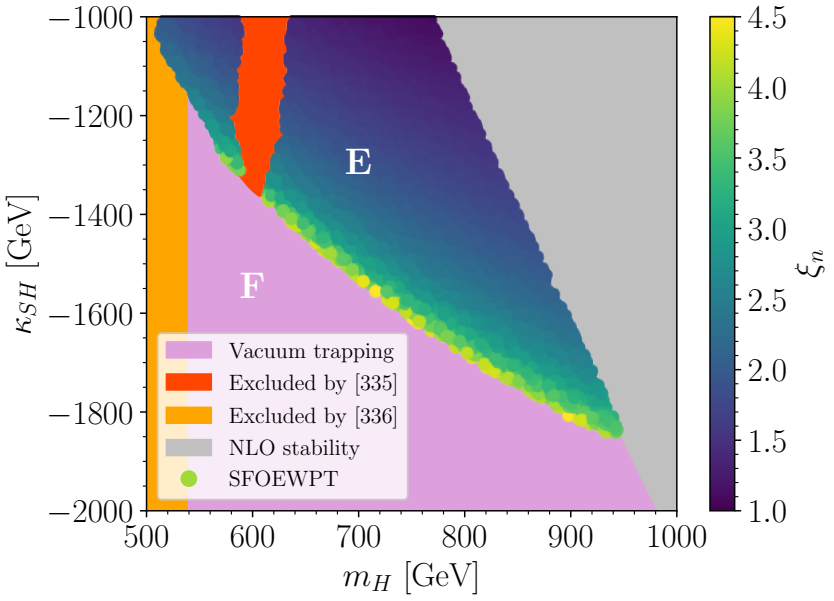

Figure 7.6: Parameter scan results in the RxSM for benchmark plane 2. The colour coding shows the ratio ξ_n. The different thermal histories are labelled following fig. 7.1. The pink region indicates vacuum trapping, while the grey region is excluded by the stability of the potential at NLO. Regions ruled out by experimental searches are shown in red for the region excluded by direct searches of a heavy Higgs boson in [335], and in orange for the region excluded by direct searches of two SM-like Higgs bosons in [336].

We concentrate in fig. 7.7 on the region of the benchmark plane 2 featuring a SFOEWPT. In the left plot the colour coding indicates T_n, while in the right plot it represents the SNR at LISA, calculated for a bubble wall velocity of $v_w = 0.95$ and three years of observation time. At first, we observe from the right plot that for $v_w = 0.95$ no point reaches an SNR larger than 10, even though points at the boundary with the vacuum trapping region are close, with SNR ≈ 8. The observability of these points depends on the uncertainty coming from v_w, which will be discussed in section 7.2.3, as well as on the threshold value of the SNR that one defines as observable. From the left plot, we find that, like in the case of the benchmark plane 1, the strongest phase transitions occur for low values of $T_n \approx 60$ GeV.

Figure 7.8 provides an illustration of the temperature-dependent effective potential evaluated at the nucleation temperature $V_{\text{eff}}(T_n)$ for a point with a SFOEWPT selected from benchmark plane 2 with a SNR $= 4.5$ and $T_n = 64$ GeV. In this scenario, the singlet field direction does not play an important role at the time of the transition, and the difference between the initial and final phases of the singlet VEV is relatively small. On the other hand, the EW doublet direction is the most important one as the tunnelling distance can be seen to be much larger. We can therefore distinguish the situation in benchmark plane

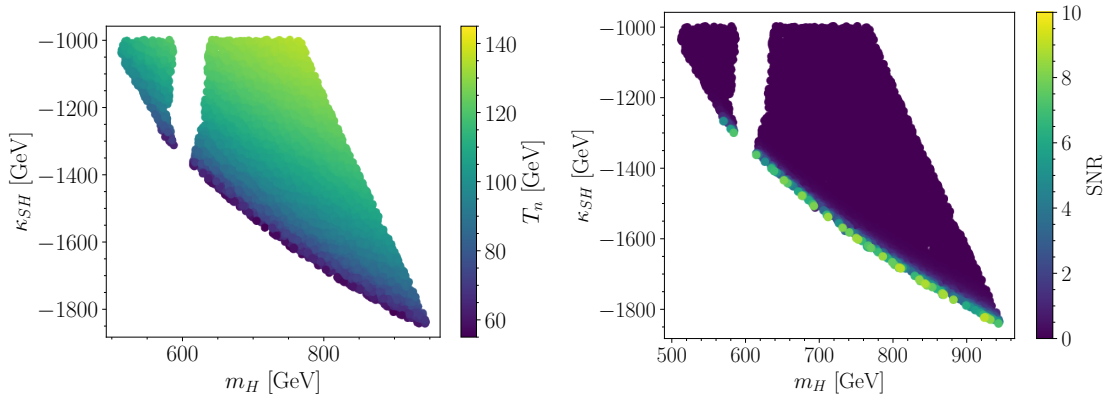

Figure 7.7: Parameter scan results for the points with a SFOEWPT in benchmark plane 2. *Left*: T_n (in GeV); *right*: SNR at LISA for $v_w = 0.95$ and three years of observation time.

2, where the EW doublet direction plays the most important role in the transition, with that of benchmark plane 1, where it is the singlet field direction. This finding also helps understand the behaviour, similar to that of the 2HDM [56], observed for the transition between SFOEWPT and vacuum trapping in fig. 7.6. Indeed, in the 2HDM, the EWPT is driven by the EW VEV, like in our benchmark plane 2. On the contrary, in benchmark plane 1 the singlet phase plays a more important role and we observe different dynamics of the EWPT compared to the 2HDM.

v_w dependence

The objective of this section is to estimate from a qualitative point of view the uncertainty in the computation of the stochastic GW background due to the bubble wall velocity. There have been several investigations of the best way to estimate the velocity of the wall [234, 235], however all of them are associated with large uncertainties, which are propagated to the predictions of GW spectra and in turn to the signal-to-noise ratios. This is illustrated in fig. 7.9, where we show the SNR at LISA (solid lines) after three years of data taking with respect to v_w for the benchmark points BPI, BPII, BPIII and BPIV from table 7.2, which are representative examples of different values of the SNR, while the red dashed line indicates the observability threshold, SNR = 10. As a first observation, the behaviour of the curves for the different BPs demonstrates that the assumption of using $v_w \sim 1$ is in each case nearly the most pessimistic choice possible, whereas a maximum is reached in all four BPs for $v_w \sim 0.7$. We find that any point that is observable at $v_w \sim 1$ is also observable for $v_w \gtrsim 0.2$, with this lower value corresponding to phase transitions with a large degree of supercooling [337]. Next, for points that are close to be observable — i.e. with $6 \lesssim \text{SNR} \lesssim 10$ — for $v_w = 1$, we obtain an observable SNR for $0.3 \lesssim v_w \lesssim 0.9$. If for $v_w = 1$ $1 \lesssim \text{SNR} \lesssim 6$, then the SNR could be observable for some range of values of v_w. Finally, when we obtain a value of $\text{SNR} \lesssim 1$ for $v_w \sim 1$, the signal is not observable for any value of v_w.

Lastly, in fig. 7.10 the colour coding indicates the SNR at LISA after 3 years of data taking and using now a bubble wall velocity of $v_w = 0.6$, in benchmark planes 1 (left) and 2 (right). In benchmark plane 1, while the parameter region producing an observable signal has only grown moderately compared to the case of $v_w = 0.95$ (c.f. fig. 7.4), the maximal

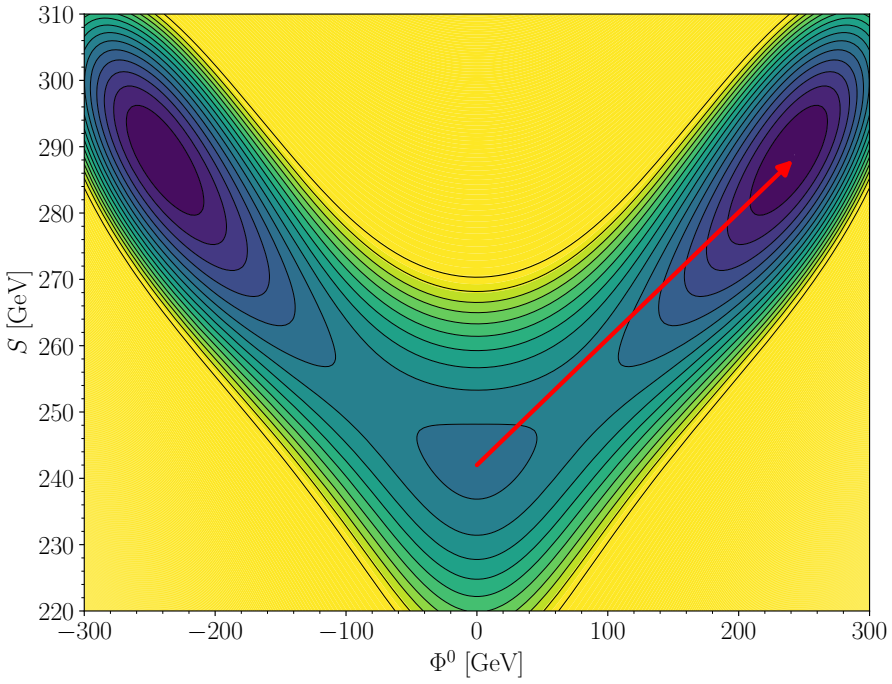

Figure 7.8: Temperature-dependent one-loop effective potential at the nucleation temperature, $V_{\text{eff}}(T_n)$, for a benchmark point featuring a SFOEWPT with a thermal history of type **E** (from fig. 7.1). The point is defined by $m_H = 639$ GeV, $c_\alpha = 0.9777$, $v_S = 289$ GeV, $\kappa_S = -205$ GeV, $\kappa_{SH} = -1403$ GeV and we find $T_n = 64$ GeV and a SNR $= 4.5$. Here S and Φ^0 denote the singlet field and the CP-even neutral component of the doublet, respectively.

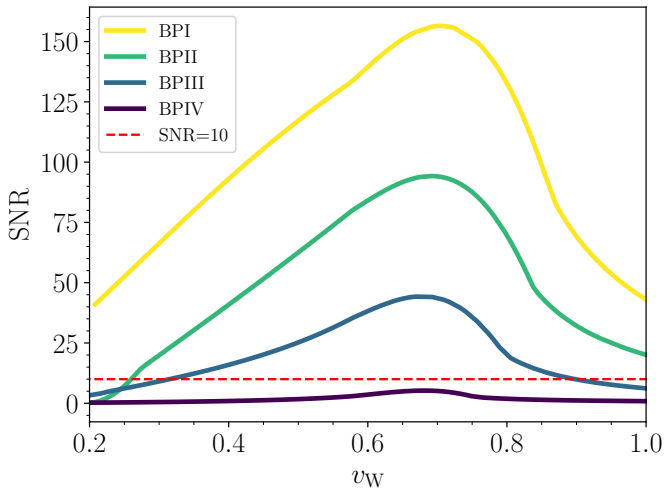

Figure 7.9: SNR at LISA after three years of data taking as a function of v_w for the benchmark points BPI, BPII, BPIII and BPIV from table 7.2. The dashed red line represents the threshold that we consider as observable at LISA, i.e. SNR = 10.

Id	m_H [GeV]	$\cos\alpha$	v_S [GeV]	κ_S [GeV]	κ_{SH} [GeV]
BPI	259.3	0.988	121.5	−900	−91
BPII	289.2	0.987	114.4	−900	−100
BPIII	638.6	0.978	289.4	−204	−1403
BPIV	251.4	0.981	94.2	−900	−127

Table 7.2: RxSM benchmark points for the investigation of the SNR dependence on v_w.

achievable SNR has increased significantly (by a factor of about 3). In benchmark plane 2, the region with the highest values of the SNR (which were however not observable for $v_w = 0.95$) becomes observable for $v_w = 0.6$, as expected from fig. 7.9. On the other hand, the region with a sizeable SNR remains confined to a small strip at the border to the parameter space where vacuum trapping occurs.

7.3 Collider analysis

In this section, we investigate the possibility of probing scenarios with a SFOEWPT at future colliders such as the HL-LHC and future e^+e^- colliders, as well as the complementarity with a GW analysis with data from the future GW observatory LISA. For consistency with the analysis of the EWPT dynamics and GW production in the previous sections, we also include one-loop corrections to the trilinear scalar couplings involved in di-Higgs production in the RxSM, following [142]. To compute the loop corrections, we perform complete one-loop diagrammatic calculations of both λ_{hhh} and λ_{hhH}, employing the public code `anyH3` [89, 99] using the full on-shell (OS) scheme defined in [142].

Here we have to comment on the different choices of renormalisation schemes for the calculation of the EWPT and the collider analyses. The scheme implemented in `BSMPT` [83, 85, 91], often referred to as "OS-like", serves to maintain at the one-loop level the same location of the EW minimum and curvature of the potential around it. It however retains

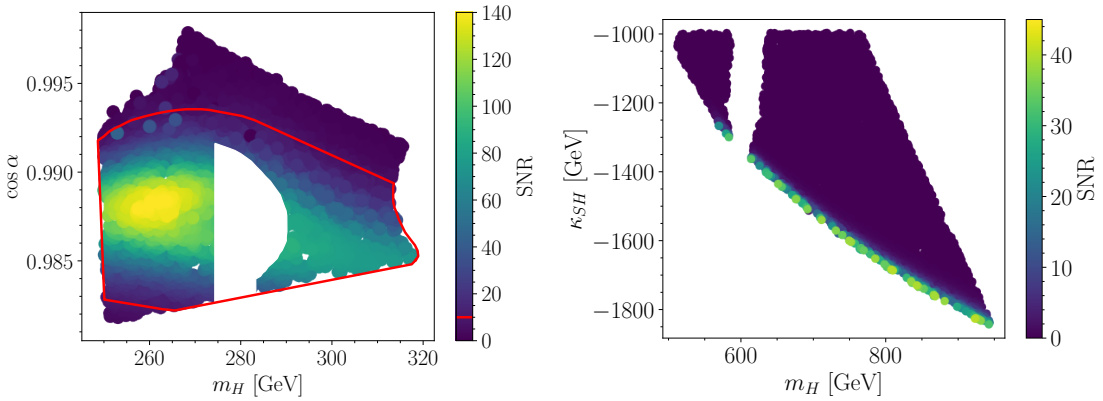

Figure 7.10: SNR at LISA for a bubble wall velocity of $v_w = 0.6$. *Left*: benchmark plane 1, where the region delimited by the red line indicates the region with an observable SNR > 10; *right*: benchmark plane 2.

a significant renormalisation scale dependence, unlike the full OS scheme of [142] employed in our collider analysis (this can be understood from the number of OS conditions that are actually imposed). For the four representative benchmark points of table 6.2 (discussed below), we have extracted the values of the trilinear scalar couplings computed with `BSMPT` and estimated the corresponding theoretical uncertainty by varying the renormalisation from $m_H/2$ to $2m_H$. We have found that, for the same points, the trilinear scalar couplings calculated using the full OS scheme of [142] always lie inside the 1σ uncertainty band from the `BSMPT` results. In other words, the difference between the two schemes is within the renormalisation scale dependence of the `BSMPT` predictions. This result justifies skipping the cumbersome step of performing a parameter conversion between the two schemes, when going from the EWPT study to the collider analysis. It should be noted that the dependence on the renormalisation scale Q does of course affect the results for the dynamics of the EWPT. However, it was shown in [338] that even after improving the calculation of the effective potential to reduce the Q dependence, the phenomenological results in terms of GW productions remain, although potentially shifted in the parameter space of the model. Keeping this observation in mind, we emphasise that our work is meant to be a proof of concept for the opportunity of probing SFOEWPT scenarios using the complementarity of GW signals and collider searches.

7.3.1 Loop corrections to the trilinear scalar couplings

We begin by investigating the size of the loop corrections to the trilinear scalar couplings λ_{hhh} and λ_{hhH}, in the two benchmark planes defined in section 7.2. These corrections have automatically been taken into account in our analysis in the previous section by using the effective potential as defined in eq. (7.1). For benchmark plane 1, we find that the trilinear scalar couplings λ_{hhh} and λ_{hhH} are very close to their SM values, i.e. $\kappa_\lambda = 1$ and $\lambda_{hhH} = 0$, both at tree level and when including one-loop corrections. This can be understood from the fact that, in this plane, the SFOEWPT is driven by the singlet field direction, which is however largely secluded from the direction corresponding to the detected Higgs boson (due to the significant constraints on the amount of mixing allowed by experimental results on properties of the detected Higgs boson). Therefore, the di-Higgs production cross sections in this benchmark plane are essentially undistinguishable from the SM

prediction, and we conclude that benchmark plane 1 is not suited for investigations via di-Higgs production at colliders. On the other hand, for benchmark plane 2, we observe relevant deviations from the SM in the trilinear scalar couplings and the di-Higgs cross section, as illustrated in figs. 7.11 and 7.12.

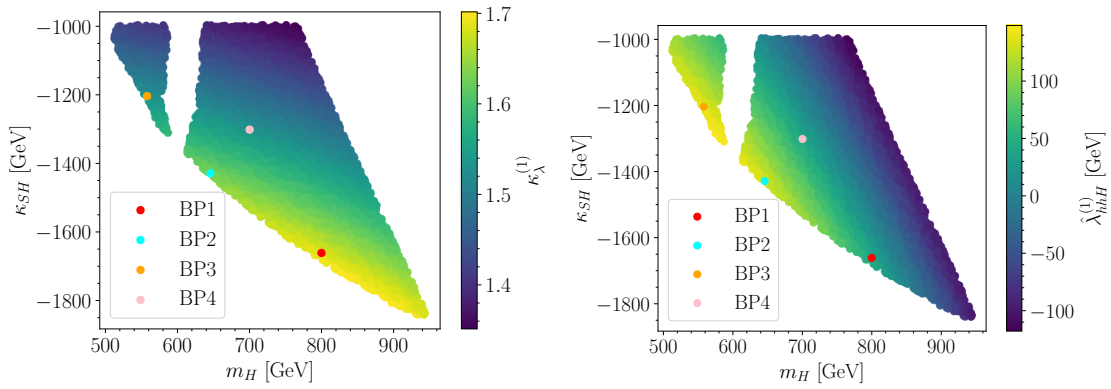

Figure 7.11: One-loop corrected trilinear scalar couplings in the benchmark plane 2. *Left*: $\kappa_\lambda^{(1)}$; *right*: $\hat{\lambda}_{hhH}^{(1)}$ (in GeV).

In fig. 7.11, we show as colour coding the one-loop predictions for κ_λ (left panel) and λ_{hhH} (right panel) in benchmark plane 2. We also indicate with coloured points four benchmark points for which we perform in the next subsections the analysis of the differential cross section distributions; the set of parameters defining these points are given in table 6.2. In the left panel of fig. 7.11, we observe that, across the entire benchmark plane, $\kappa_\lambda^{(1)}$ deviates by $40-70\%$ from its SM value. This is in turn sufficient to induce noticeable changes in di-Higgs production. From the right panel of fig. 7.11, we find that $\hat{\lambda}_{hhH}^{(1)}$ takes both positive and negative values, within the range $[-100, 150]$ GeV. This has an impact on the structure of the interference between resonant and non-resonant contributions. Moreover, for the points with $\hat{\lambda}_{hhH}^{(1)} \simeq 0$, no resonance will be observable.

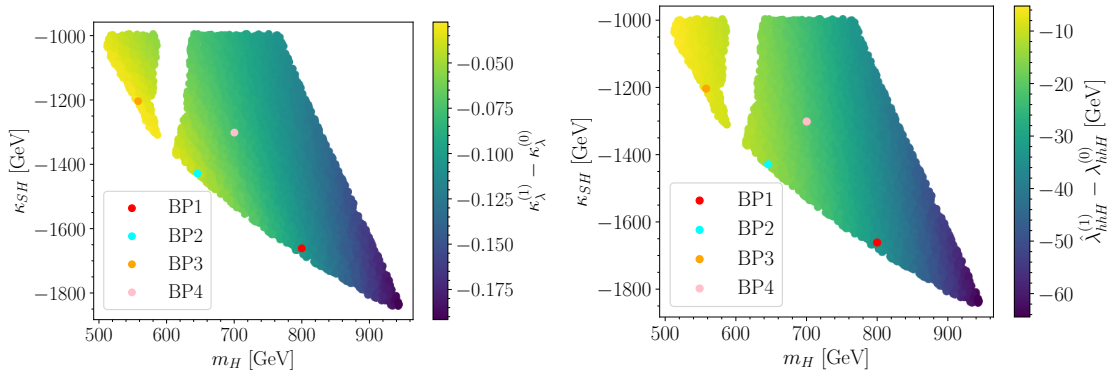

Figure 7.12: One-loop corrections to the trilinear scalar couplings in the benchmark plane 2. *Left*: $\kappa_\lambda^{(1)} - \kappa_\lambda^{(0)}$; *right*: $\hat{\lambda}_{hhH}^{(1)} - \lambda_{hhH}^{(0)}$ (in GeV).

In order to understand whether the BSM deviations originate from tree-level effects or one-loop corrections, we present in the colour coding of fig. 7.12 the differences $\kappa_\lambda^{(1)} - \kappa_\lambda^{(0)}$ (left panel) and $\hat{\lambda}_{hhH}^{(1)} - \lambda_{hhH}^{(0)}$ (right panel) in benchmark plane 2. From the left panel of fig. 7.12, we observe that the one-loop corrections to κ_λ range between -2% and -10% of

the full one-loop values, and that the corrections are negative across the entire benchmark plane. We also find that the largest correction corresponds to the largest value of κ_λ. In the case of λ_{hhH}, the corrections are likewise negative throughout the whole benchmark plane, as can be seen in the right panel of fig. 7.12. However, unlike for κ_λ, the corrections to $\hat{\lambda}^{(1)}_{hhH}$ can become significant in parts of the plane, with values ranging from -6% to -60%. Finally, we note that for λ_{hhH}, the correlation between large radiative corrections and large (negative) values of the coupling is even more important than for κ_λ.

BP	m_H [GeV]	$\cos\alpha$	v_S [GeV]	κ_S [GeV]	κ_{SH} [GeV]	$\kappa_\lambda^{(0)}$	$\kappa_\lambda^{(1)}$	$\lambda_{hhH}^{(0)}$ [GeV]	$\hat{\lambda}_{hhH}^{(1)}$ [GeV]	ξ_n
1	800	0.98	280	-300	-1661	1.8	1.7	72.1	38.6	3.5
2	646	0.98	280	-300	-1429	1.7	1.6	143.9	129.8	3.9
3	558	0.98	280	-300	-1204	1.6	1.5	145.0	137.4	2.7
4	700	0.98	280	-300	-1301	1.6	1.5	61.5	40.0	1.9

Table 7.3: Definitions of the RxSM benchmark points considered for the study of di-Higgs production, in terms of the five free BSM parameters of the model: m_H, $\cos\alpha$, v_S, κ_S and κ_{SH}. Additionally, tree-level and one-loop predictions for κ_λ and λ_{hhH} are included, as well as ξ_n.

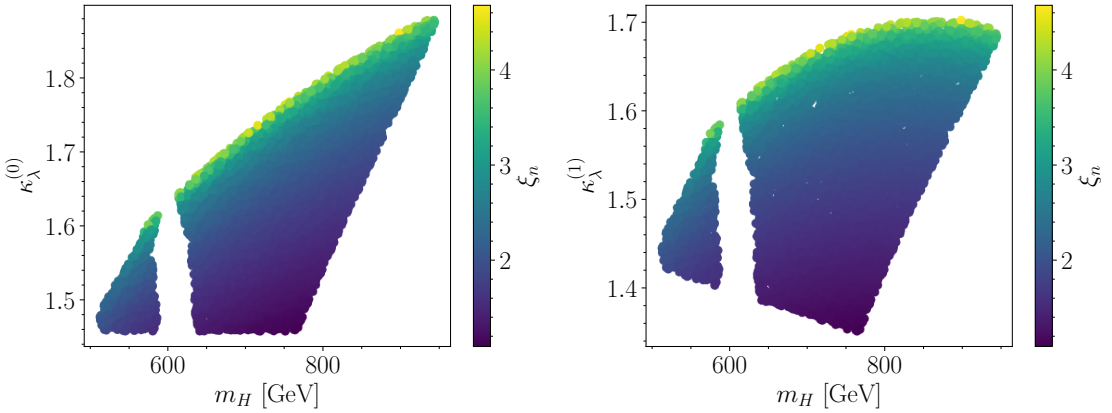

Figure 7.13: Results for ξ_n in benchmark plane 2. *Left*: projected in the plane $\{m_H, \kappa_\lambda^{(0)}\}$; *right*: projected in the plane $\{m_H, \kappa_\lambda^{(1)}\}$.

To investigate the correlation between a BSM deviation in κ_λ and the strength of the phase transition, we show ξ_n in the colour coding of fig. 7.13 for the scan points of benchmark plane 2, projected in the planes $\{m_H, \kappa_\lambda^{(0)}\}$ (left plot) and $\{m_H, \kappa_\lambda^{(1)}\}$ (right plot). For a fixed value of m_H, the strongest EWPT correspond to the largest allowed values of κ_λ, both at tree level and at one loop. Even larger values of κ_λ would be associated with vacuum trapping. Lastly, we observe that for benchmark plane 2, a SFOEWPT is correlated with a BSM deviation of $35\% - 70\%$ at one loop ($45\% - 90\%$ at tree level), as is known to be the case for scenarios where the SFOEWPT is driven by the Higgs doublet (see e.g. Ref [56]).

7.3.2 Di-Higgs production at the HL-LHC

In this section, we present the results obtained for di-Higgs production cross-sections and differential distributions at the HL-LHC using the same framework as in Ref. [142]. For our theoretical predictions, we employ a modified version of `HPAIR` [64, 69, 137, 300–302], which was already used in Ref. [246]. In this code, the three leading-order (LO) diagrams that contribute to the $gg \to hh$ process, as well as the interference between them, are taken into account. We also note that NLO QCD corrections are available for the total cross-section predictions in `HPAIR`, but not for the differential results. To simplify comparisons between results, we choose to work here only with results at LO in QCD (keeping in mind that total cross-sections are modified by a QCD K factor of ≈ 2). On the other hand, `HPAIR` takes numerical values for λ_{hhh} and λ_{hhH} as inputs. Using tree-level or one-loop values for these trilinear scalar couplings therefore allows us to obtain predictions at LO or leading NLO in terms of BSM effects.

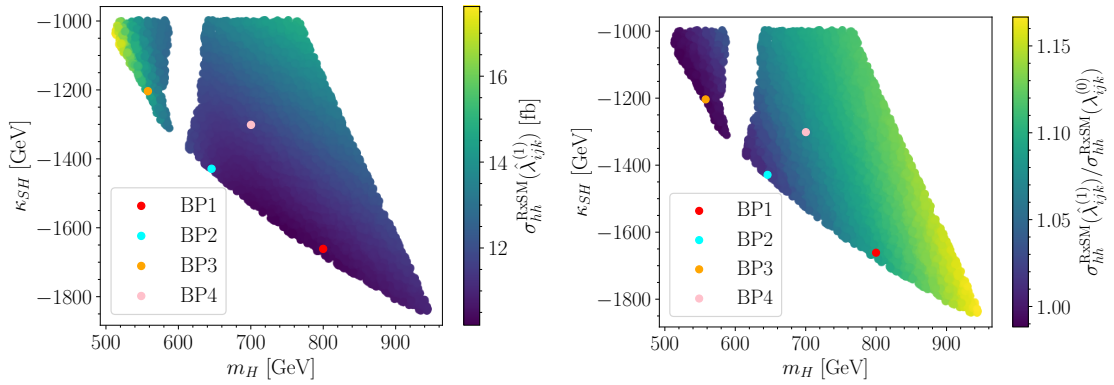

Figure 7.14: Results for the di-Higgs cross-section at the HL-LHC in the benchmark plane 2. *Left*: $\sigma_{hh}^{\mathrm{RxSM}}(\hat{\lambda}_{ijk}^{(1)})$ (in fb); *right*: the ratio between the total di-Higgs production cross section using one-loop and tree-level trilinear Higgs couplings $\sigma_{hh}^{\mathrm{RxSM}}(\hat{\lambda}_{ijk}^{(1)})/\sigma_{hh}^{\mathrm{RxSM}}(\lambda_{ijk}^{(0)})$. The SM prediction is $\sigma_{hh}^{\mathrm{SM}} = 19.76$ fb, above the RxSM results in the entire benchmark plane.

We present in fig. 7.14 our predictions for the total di-Higgs production cross-section in benchmark plane 2. In the left panel, the colour coding indicates the cross-section including one-loop corrections to the trilinear Higgs couplings, which we denote $\sigma_{hh}^{\mathrm{RxSM}}(\hat{\lambda}_{ijk}^{(1)})$, and in the right panel it shows the ratio between the total cross-section including one-loop corrections and the same cross-section using the tree-level values — i.e. $\sigma_{hh}^{\mathrm{RxSM}}(\hat{\lambda}_{ijk}^{(1)})/\sigma_{hh}^{\mathrm{RxSM}}(\lambda_{ijk}^{(0)})$. As can be seen from the left panel of fig. 7.14, over the entire benchmark plane, the predicted total cross-section is lower than its SM value, $\sigma_{hh}^{\mathrm{SM}} = 19.76$ fb [69]. The behaviour of σ_{hh} as a function of κ_λ is well known from studies of the SM with a free λ_{hhh} (see e.g. [100, 322]), and can be explained by the destructive interference between the s-channel Higgs-exchange contribution and the box diagram. The cross-section prediction in the RxSM is affected by the enhancement of λ_{hhh} w.r.t. its SM value, as well as by the contribution of the heavy Higgs-boson resonance. Overall, the values found for κ_λ in benchmark plane 2 lead to an increase of the destructive interference of the SM-type contributions and thus to a decrease in the cross-section prediction. On the other hand, the heavy Higgs-boson resonance leads to an increase in the cross-section, which contributes for momenta in the s-channel around its mass. For all of benchmark plane 2, the first effect dominates, resulting in lower values of the total cross-section compared to the SM.

With decreases in $\sigma_{hh}^{\text{RxSM}}(\hat{\lambda}_{ijk}^{(1)})$ of up to 50%, a measurement of the di-Higgs cross-section could allow distinguishing the RxSM from the SM in parts of benchmark plane 2 (for larger values of $|\kappa_{SH}|$), however, the measurement itself would then be more challenging than in the SM. For the rest of the plane, the RxSM results are close to the SM, meaning that once experimental uncertainties are taken into account it would be difficult to distinguish the two models using the total cross-section alone.

The right panel of fig. 7.14 shows that the largest contribution from the loop corrections to $\hat{\lambda}_{ijk}^{(1)}$ reaches up to 15% of the value obtained with tree-level trilinear scalar couplings, and occurs in the region with the lowest total cross-section. On the other hand, we can see that in the region where the total cross-section is largest in benchmark plane 2, the loop corrections do not appear to have a significant impact on $\sigma_{hh}^{\text{RxSM}}$.

As discussed in previous works [64, 138, 142, 246, 323], the differential cross-section with respect to the di-Higgs invariant mass, m_{hh}, provides much more information for distinguishing BSM models like the RxSM from the SM than the total cross-section alone. For this reason, we have selected four benchmark points with different phenomenological features, which are marked as coloured dots in figs. 7.11 and 7.12. The benchmark points are labelled BP1, BP2, BP3, and BP4, with the parameters summarised in table 6.2.

For these four benchmark points we compute the corresponding differential cross-section distributions, following the framework of [142]. The results for BP1 and BP2 are presented in fig. 7.15, and for BP3 and BP4 in fig. 7.16. The left plots display the theoretical differential cross-section distributions with respect to m_{hh}, while the right plots show the number of events, including experimental uncertainties. Here we assume an integrated luminosity of $\mathscr{L}_{\text{int}} = 6000\,\text{fb}^{-1}$ corresponding to the end of the HL-LHC. We also include the main decay channel, $h \to b\bar{b}$, into the calculation, with $\text{BR}(h \to b\bar{b}) = 0.58$, and the results are displayed as a function of the four-b invariant mass, $m_{b\bar{b}b\bar{b}}$. For these plots we also include a smearing of 15% to take into account the experimental errors, as well as a binning of 50 GeV to account for the detector resolution, see [142] for details. The error bars represent the 1σ statistical uncertainties on the signal (computed as Poisson-distribution errors). The dashed black line corresponds to the SM prediction, the blue line shows the RxSM result using $\lambda_{ijk}^{(0)}$, and the red line is the RxSM prediction including $\hat{\lambda}_{ijk}^{(1)}$.

In fig. 7.15, we observe that for BP1 the theoretical RxSM distributions using $\lambda_{ijk}^{(0)}$ (blue curve) and using $\hat{\lambda}_{ijk}^{(1)}$ (red curve) have similar shapes. When taking into account the experimental uncertainties and error bands, we find in the right plot that the two curves are indistinguishable from each other, but can be distinguished from the SM distribution. Using the definition from Eqs. (47) and (48) of [142], we obtain a significance to discriminate the RxSM distribution using $\hat{\lambda}_{ijk}^{(1)}$ from the SM curve of $Z_{hh}^{(1)} = 4.8$. From this we conclude that using the differential distributions, the RxSM can to a good degree of confidence be distinguished from the SM in BP1. This significance arises from the modification of the interference at low values of $m_{hh} \lesssim 400$ GeV, due to the BSM deviation in κ_λ. It is interesting to note that the resonant peak, visible in the theoretical curve for $m_{hh} \simeq 800$ GeV, is completely washed away once experimental effects are taken into consideration.

In the case of BP2 (lower row of fig. 7.15), the clear resonant peak at $m_{hh} \approx 650$ GeV in the theoretical curves (left plot), is somewhat washed out after the inclusion of experimental

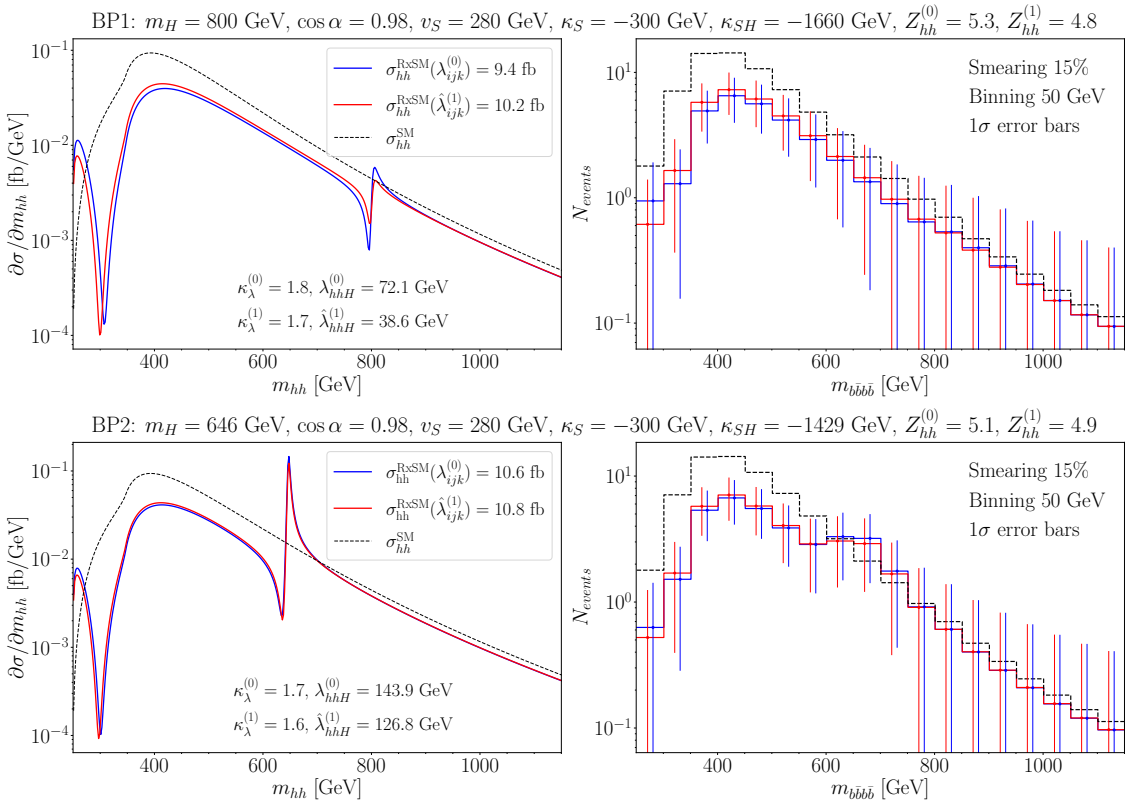

Figure 7.15: *Left:* Differential di-Higgs production cross-section distributions w.r.t. m_{hh}. *Right:* Distribution of the number of di-Higgs events, taking into account the BR($h \to b\bar{b}$), as well as smearing and binning effects, with respect to the invariant mass of the four reconstructed b quarks, $m_{b\bar{b}b\bar{b}}$. The error bars indicate statistical errors, assuming Poisson distributions for the number of events in each bins. Blue curves show results using $\lambda_{ijk}^{(0)}$ in the computation of di-Higgs production, while red curves represent results using $\hat{\lambda}_{ijk}^{(1)}$. The black dashed line indicates the SM result. *Top:* results for BP1; *bottom:* results for BP2 from table 6.2.

uncertainties (right plot) but may remain distinguishable from the continuum, i.e. the SM distribution. The deviation of κ_λ from the SM is smaller in BP2 than in BP1, which reduces the change in the m_{hh} distribution near the di-Higgs threshold and tends to lower the significance. On the other hand, the resonant peak also contributes more noticeably to the significance, resulting in a value of $Z_{hh}^{(1)} = 4.9$. While not sufficient for a discovery, this could already be interpreted as an indication of new physics.

The result for BP3, shown in the upper row of fig. 7.16, is quite similar to that of BP2. In this case, the heavy Higgs mass is smaller, $m_H = 558$ GeV, and therefore the resonant peak is shifted to lower m_{hh}. Due to the slope of the continuum contribution, we observe in the right plot that, after taking into account experimental uncertainties, the peak is enhanced compared to BP2. However, this is compensated the reduction of the significance due to the smaller value of κ_λ, yielding $Z_{hh}^{(1)} = 4.8$. Additionally, the total cross-section is closer to the SM result for BP3 than BP2, which implies that by only considering the total cross-section this scenario might be more complicated to distinguish from the SM. However, the differential cross-section allows us to differentiate the two models.

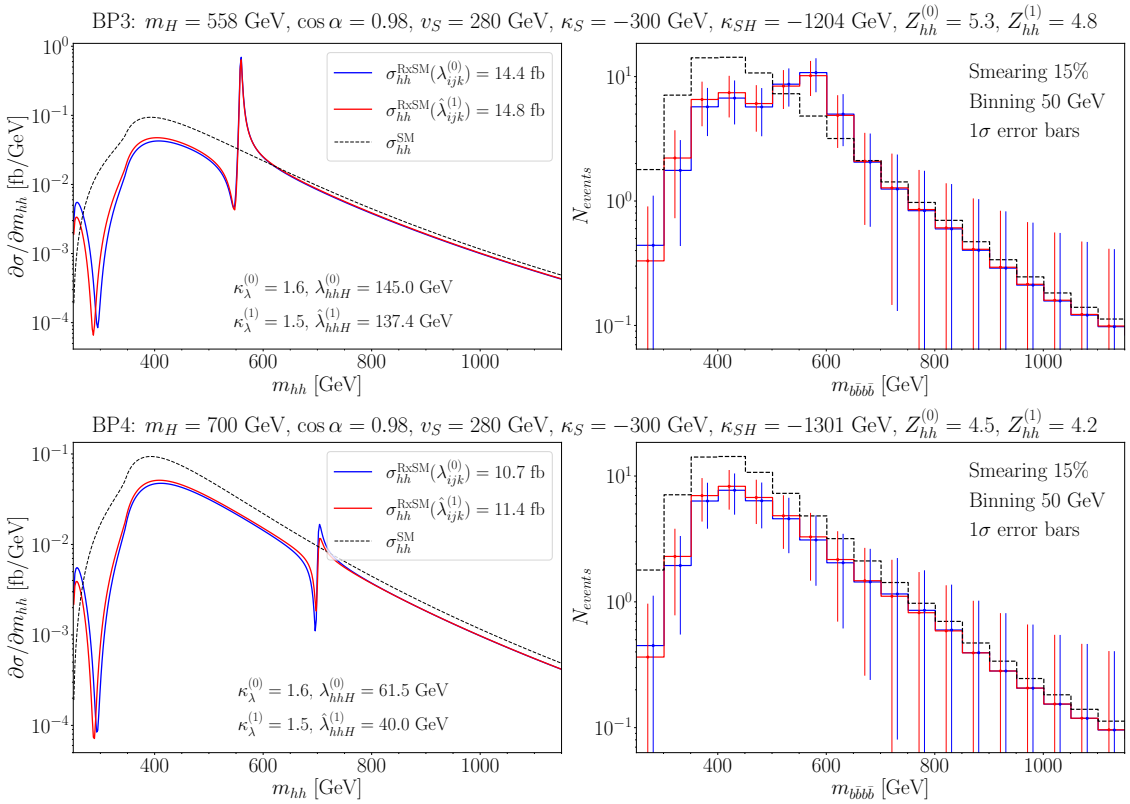

Figure 7.16: Plots and line styles as in fig. 7.15. *Top:* results for BP3; *bottom:* results for BP4 from table 6.2.

Finally, the result for BP4 (lower row of fig. 7.16) is similar to that of BP1. In this case, the coupling λ_{hhH} is negative, which causes the interference around the resonant peak to have a dip–peak structure rather than a peak–dip structure. This suppresses the peak, making it indistinguishable from the continuum once experimental uncertainties are included. Moreover, κ_λ is closer to its SM value, which reduces the modification of interference at low values of $m_{hh} \sim 400$ GeV. In total, these two effects lead to a smaller significance, $Z_{hh}^{(1)} = 4.2$. This result is the lowest among the four considered benchmark points, however, it would still be sufficient to hint at the presence of new physics. A summary of the HL-LHC di-Higgs production cross-sections and the significances can be found in table 7.4.

In summary, while it may be difficult to probe scenarios in the RxSM with a SFOEWPT using the total cross-section $\sigma_{hh}^{\mathrm{RxSM}}$, having access to the differential m_{hh} distributions would allow to investigate some of these scenarios and to distinguish them from the SM.

7.3.3 Di-Higgs production at e^+e^- colliders

In this section, we complement our HL-LHC results with an analysis of di-Higgs production at future high-energy e^+e^- colliders. We consider the double Higgs-strahlung channel, $e^+e^- \to Zhh$, which is the dominant production mode of two SM-like Higgs bosons up to centre-of-mass energies slightly above 1 TeV. In addition, we also consider the WW-fusion channel, $e^+e^- \to \nu\bar{\nu}hh$, which includes the diagrams of the channel Zhh considering that Z decaying to $\nu\bar{\nu}$, and also Vector Boson Fusion (VBF)-like diagrams,

BP	$\sigma_{hh}^{\text{RxSM}}(\lambda_{ijk}^{(0)})$ [fb]	$\sigma_{hh}^{\text{RxSM}}(\hat{\lambda}_{ijk}^{(1)})$ [fb]	$Z_{hh}^{(0)}$	$Z_{hh}^{(1)}$
1	9.4	10.2	5.3	4.8
2	10.6	10.8	5.1	4.9
3	14.4	14.8	5.3	4.8
4	10.7	11.4	4.5	4.2

Table 7.4: Summary of the predictions for di-Higgs production cross-sections and significances at the HL-LHC for the benchmark points in table 6.2.

with W bosons mediating the interaction. To compute the cross-section, which we denote $\sigma_{Zhh}^{\text{RxSM}}$ and $\sigma_{\nu\bar{\nu}hh}^{\text{RxSM}}$, we use the public code `Madgraph5_aMC v3.5.9` [141] (which we will from now on refer to as `MadGraph`). The `UFO` model file for the RxSM required as input by `Madgraph` was generated using the `Mathematica` package `SARAH-4.15` [314, 327–330].

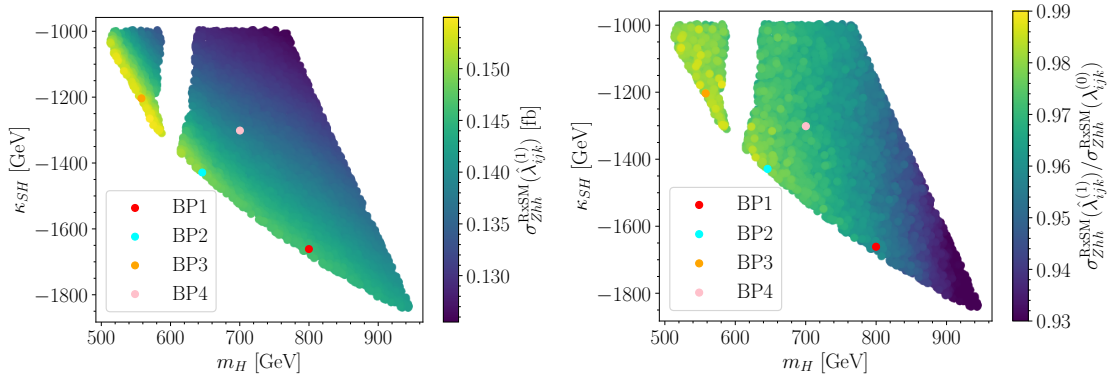

Figure 7.17: Results of the di-Higgs cross-section computation for a 1 TeV e^+e^- collider in the benchmark plane 2. *Left*: $\sigma_{Zhh}^{\text{RxSM}}(\hat{\lambda}_{ijk}^{(1)})$ (in fb); *right*: $\sigma_{Zhh}^{\text{RxSM}}(\hat{\lambda}_{ijk}^{(1)})/\sigma_{Zhh}^{\text{RxSM}}(\lambda_{ijk}^{(0)})$. We note that in the left plot the value of $\sigma_{Zhh}^{\text{SM}} = 0.121$ fb is below the lower bound in the colour bar.

We compute the cross-section for a future e^+e^- collider operating at a centre-of-mass energy of $\sqrt{s} = 1$ TeV, taking as an example the ILC1000 [139, 315, 316]. For other centre-of-mass energies such as $\sqrt{s} = 550$ GeV for the LCF550 [339], we would not expect to see interesting effects since in the benchmark plane studied here, $m_H > 500$ GeV, and effects from λ_{hhH} in the Zhh channel are typically visible for $m_H + m_Z > \sqrt{s}$, so we would not be able to access the resonant effects. Concerning the $\nu\bar{\nu}hh$ channel, due to the energy taken by $\nu\bar{\nu}$ and the experimental cuts on missing energy also no relevant effects from the resonant H-channel diagram are expected. On the other hand, effects of $\kappa_\lambda \neq 1$ would be accessible at LCF550.

In fig. 7.17 we show the benchmark plane 2 where the colour coding indicates our predictions for $\sigma_{Zhh}^{\text{RxSM}}$ using $\hat{\lambda}_{ijk}^{(1)}$ (left panel), and the ratio between the values of $\sigma_{Zhh}^{\text{RxSM}}$ computed using $\hat{\lambda}_{ijk}^{(1)}$ and $\lambda_{ijk}^{(0)}$ (right panel), i.e. $\sigma_{Zhh}^{\text{RxSM}}(\hat{\lambda}_{ijk}^{(1)})/\sigma_{Zhh}^{\text{RxSM}}(\lambda_{ijk}^{(0)})$. In the left panel, we observe that the results lie in the range $\sigma_{Zhh}^{\text{RxSM}}(\hat{\lambda}_{ijk}^{(1)}) \approx [0.125, 0.155]$ fb. Considering that the SM prediction for the same process is $\sigma_{Zhh}^{\text{SM}} = 0.121$ fb[3] the RxSM result

[3]Including a −80% (+30%) polarisation for electrons (positrons), these numbers go up by a factor of

in the benchmark plane 2 is therefore $3\% - 24\%$ larger than the SM value. This enhancement is due to the deviation of κ_λ from its SM value. Unlike the HL-LHC case, where σ_{hh} exhibits a minimum around $\kappa_\lambda \approx 2.5$, at an e^+e^- collider in the process $e^+e^- \to Zhh$ one finds a constructive interference between the SM-type diagrams, and σ_{Zhh} increases monotonically with κ_λ. This feature makes an e^+e^- collider a more promising setting to use the total di-Higgs cross section as a probe of SFOEWPT scenarios. Turning to the right panel of fig. 7.17, we find that including one-loop corrections to the trilinear scalar couplings in the cross-section computation leads to deviations of up to $\sim 7\%$ relative to the result obtained with tree-level couplings.

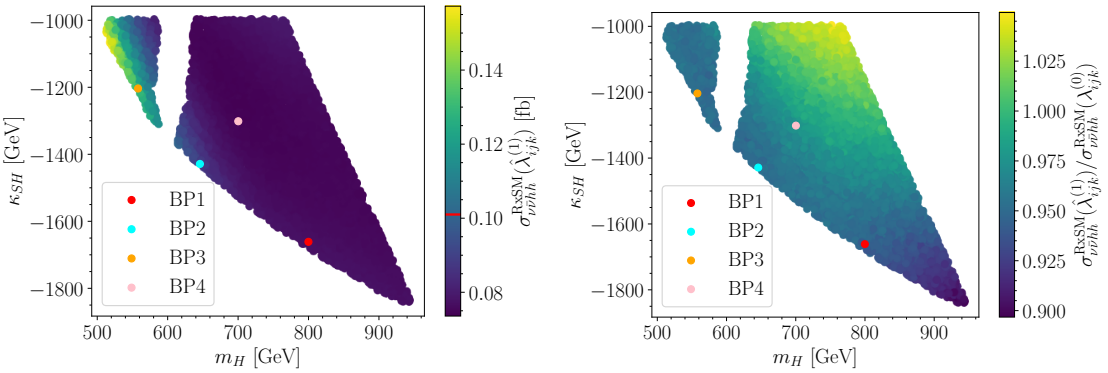

Figure 7.18: Results of the di-Higgs cross-section computation for a 1 TeV e^+e^- collider in the benchmark plane 2. *Left*: $\sigma^{\mathrm{RxSM}}_{\nu\bar{\nu}hh}(\hat{\lambda}^{(1)}_{ijk})$ (in fb); *right*: $\sigma^{\mathrm{RxSM}}_{\nu\bar{\nu}hh}(\hat{\lambda}^{(1)}_{ijk})/\sigma^{\mathrm{RxSM}}_{\nu\bar{\nu}hh}(\lambda^{(0)}_{ijk})$. The red line in the colour bar of the left plot indicates the SM cross-section prediction.

In fig. 7.18, analogously to fig. 7.17, we show the prediction in the benchmark plane 2 for $\sigma^{\mathrm{RxSM}}_{\nu\bar{\nu}hh}$ using $\hat{\lambda}^{(1)}_{ijk}$ (left panel), and the ratio between the value of $\sigma^{\mathrm{RxSM}}_{\nu\bar{\nu}hh}$ using $\hat{\lambda}^{(1)}_{ijk}$ and $\lambda^{(0)}_{ijk}$ (right panel), i.e. $\sigma^{\mathrm{RxSM}}_{\nu\bar{\nu}hh}(\hat{\lambda}^{(1)}_{ijk})/\sigma^{\mathrm{RxSM}}_{\nu\bar{\nu}hh}(\lambda^{(0)}_{ijk})$. The values of $\sigma^{\mathrm{RxSM}}_{\nu\bar{\nu}hh}(\hat{\lambda}^{(1)}_{ijk})$ range between $\approx [0.075, 0.155]$ fb, with a SM value of $\sigma^{\mathrm{SM}}_{\nu\bar{\nu}hh} = 0.101\,\mathrm{fb}$. The κ_λ values in our benchmark plane 2 range around ~ 1.5, see fig. 7.11, where (unlike the Zhh cross-section) the destructive interference of the SM-like diagrams has a maximum, i.e. the corresponding cross-section is smallest. On the other hand, the resonant H-channel diagram yields a positive contribution, which is larger for smaller values of m_H. These two effects partially cancel each other, leading to the cross-section range as found in the left plot of fig. 7.18. Approximately for $m_H \lesssim 600$ GeV we find a $\sigma^{\mathrm{RxSM}}_{\nu\bar{\nu}hh}$ larger than in the SM. This makes this channel promising regarding the sensitivity to resonances, and hence to BSM trilinear scalar couplings, of heavy Higgs bosons in this mass range. In the right panel of fig. 7.18, we see that this ratio between the one-loop and tree-level cross-section predictions is in the range $\approx [0.90, 1.04]$. In parts of the plane (for larger $|\kappa_{SH}|$) we observe a decrease in the one-loop contributions of up to 10%. Nevertheless, unlike in fig. 7.17, there are points in the parameter space where we find higher cross-section values at one loop than at tree level, mainly for smaller $|\kappa_{SH}|$ and larger m_H, with an increase of almost 5%.

Similarly to the HL-LHC case, differential m_{hh} cross-section distributions at e^+e^- colliders provide valuable information to explore SFOEWPT scenarios. We compute these distributions following the procedure described in [142]. As discussed there, we consider the scenario where the Higgs bosons decay as $hh \to b\bar{b}b\bar{b}$. We furthermore take into ac-

1.476, see below.

count the possible polarisations of the electron and positron beams, as described below. Following [98] for the Zhh channel we include experimental cuts as,

$$E_b > 20 \text{ GeV}, \quad |\eta_b| < 2.5, \quad |\eta_Z| < 2.5, \quad y_{bb} > 0.001, \tag{7.20}$$

where E_b is the energy of the b-tagged jets, η_b and η_Z are the pseudo-rapidity of the b-tagged jets and the Z boson, respectively, and y_{bb} is a variable used to perform the jet clustering procedure by the Durham algorithm [340], where y_{bb} gives us a notion of distance between the b-tagged jets, defined as $y_{ij} = 2\text{min}(E_i^2, E_j^2)(1 - \cos\theta_{ij})/s$, where θ_{ij} is the angle between the momenta of the particles i and j. For the $\nu\bar{\nu}hh$ channel, we also consider similar experimental cuts based on [98, 102],

$$E_b > 20 \text{ GeV}, \quad |\eta_b| < 2.5, \quad E^T_{\text{miss}} > 20 \text{ GeV}, \quad y_{bb} > 0.001, \tag{7.21}$$

where we include a cut to the transverse missing energy, $E^T_{\text{miss}} > 20$ GeV [102], due to the presence of the neutrinos. The corresponding number of events is calculated as in [142],

$$N = \mathscr{L}_{\text{int}} \times \sigma \times \text{ BR}(h \to b\bar{b})^2 \times \mathscr{A} \times \epsilon_b, \tag{7.22}$$

where σ is the polarised cross-section for the respective channel. Additionally, we define the acceptance as $\mathscr{A} = N^{\text{with cuts}}/N^{\text{w/o cuts}}$, which is calculated with `Madgraph`. We also consider $\epsilon_b = 0.85$ [317, 341], denoting the b-tagging efficiency for all the b-tagged jets in the final state. $\mathscr{L}_{\text{int}}$ denotes the integrated luminosity, which we define below. Concerning the size of the polarised cross-section, we assume two possible polarisations, 80% for the electrons and 30% for the positrons, with opposite signs, denoted by $(\pm 80\%, \mp 30\%)$. In the case of $\sigma^{\text{RxSM}}_{Zhh}$ this can be taken into account by a simple scaling (see the discussion in [98]), as $\sigma(-80\%, +30\%) \simeq 1.476\,\sigma_{\text{unpol}}$ and $\sigma(+80\%, -30\%) \simeq 1.004\,\sigma_{\text{unpol}}$, with σ_{unpol} the cross-section without polarisation. In the case of $\sigma^{\text{RxSM}}_{\nu\bar{\nu}hh}$ such a simple scaling is not possible, and we calculate the cross-section for each polarisation with `Madgraph`. For this channel, we also found that $(-80\%, +30\%)$ is the most favourable polarisation and its contribution to the m_{hh} distribution is clearly predominant compared to the other polarisation. We additionally found that for each channel the shape of the m_{hh} distributions for each polarisation is virtually the same, with the corresponding rescaling. Therefore, in what follows, for the m_{hh} distributions we show the polarised cross-section for the most favourable polarisation $(-80\%, +30\%)$, while for the number of events we will consider the sum of both polarisations. Here we have assumed an integrated luminosity of $\mathscr{L}_{\text{int}} = 3200\,\text{fb}^{-1}$ for each polarisation [139]. Regarding the binning, for the Zhh channel we set the size of the bins such that for the statistical significance calculations (see below), we meet the condition $N > 2$ for most of the bins for each polarisation. For the $\nu\bar{\nu}hh$ channel, due to the considerably larger contribution of the $(-80\%, +30\%)$ polarisation, we prioritise applying this condition to this polarisation. In addition, we apply a smearing of 5% [98] to the cross-section distributions.

The results for the Zhh channel are shown in fig. 7.19 (BP1 and BP2) and fig. 7.20 (BP3 and BP4). In these plots, the red (green) curve corresponds to the RxSM result using $\hat{\lambda}^{(1)}_{ijk}$ ($\lambda^{(0)}_{ijk}$), the blue (orange) curve represents the contribution, taken alone, of the diagram with H in the s-channel using $\hat{\lambda}^{(1)}_{hhH}$ ($\lambda^{(0)}_{hhH}$), and finally the yellow curve indicates the SM prediction. Here we stress again that the cross-sections, as given in the legends and the left vertical axes, correspond to the case of $(-80\%, +30\%)$ polarisation, whereas the number of events shown on the right vertical axes are obtained as the sum of the two polarisations.

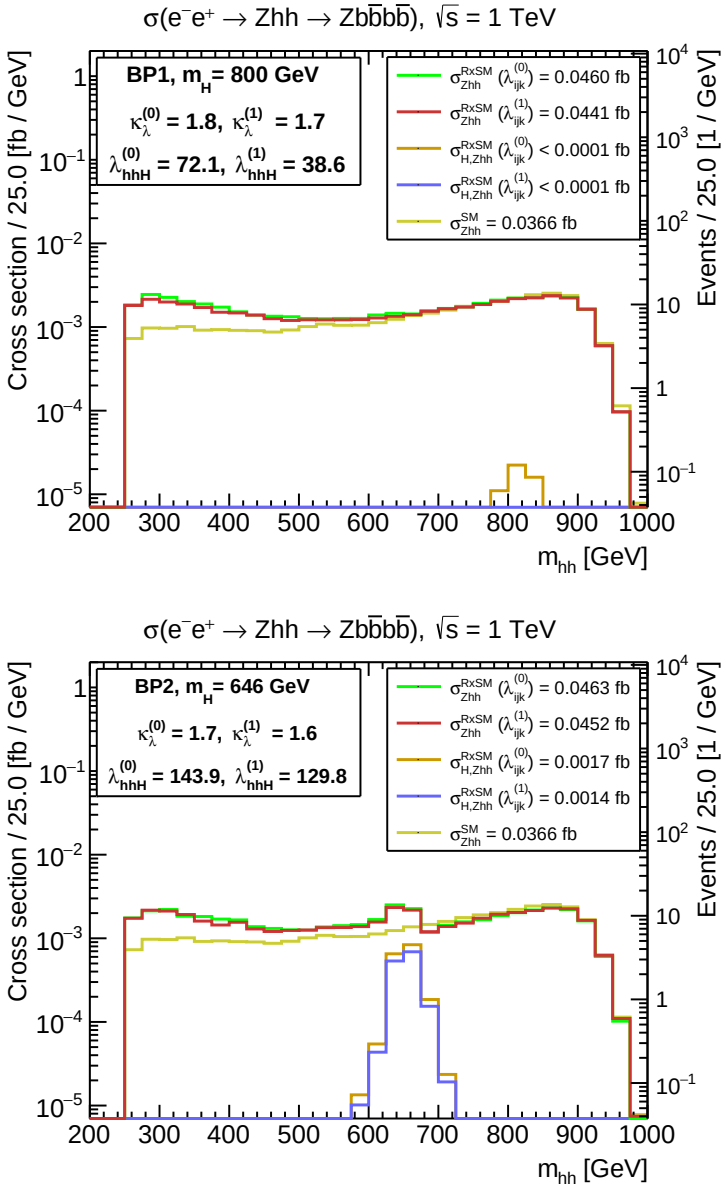

Figure 7.19: Differential polarised di-Higgs production cross-section distributions (for the polarisation $(-80\%, +30\%)$) after applying cuts and smearing (see text) as a function of the di-Higgs invariant mass m_{hh} for the process $e^+e^- \to Zhh \to Zb\bar{b}b\bar{b}$ at the ILC1000. *Top*: Results for BP1. *Bottom*: Results for BP2. We plot the RxSM result using tree-level (one-loop) trilinear scalar couplings in green (red), the contribution of the diagram with H in the s-channel using tree-level (one-loop) trilinear scalar couplings in orange (purple), and the SM result in yellow. On the right axis we show the sum of the number of events for both polarisations considering $\mathscr{L}_{\text{int}} = 3200\,\text{fb}^{-1}$. Values of λ_{hhH} are shown in GeV.

In figs. 7.19 and 7.20, we find larger differential cross-sections in the RxSM than in the SM at low m_{hh}, a significant non-resonant effect. One can furthermore observe a decrease when including trilinear couplings computed at one loop with respect to tree level, as expected from the corresponding small decrease of κ_λ. With regard to each BP, we find

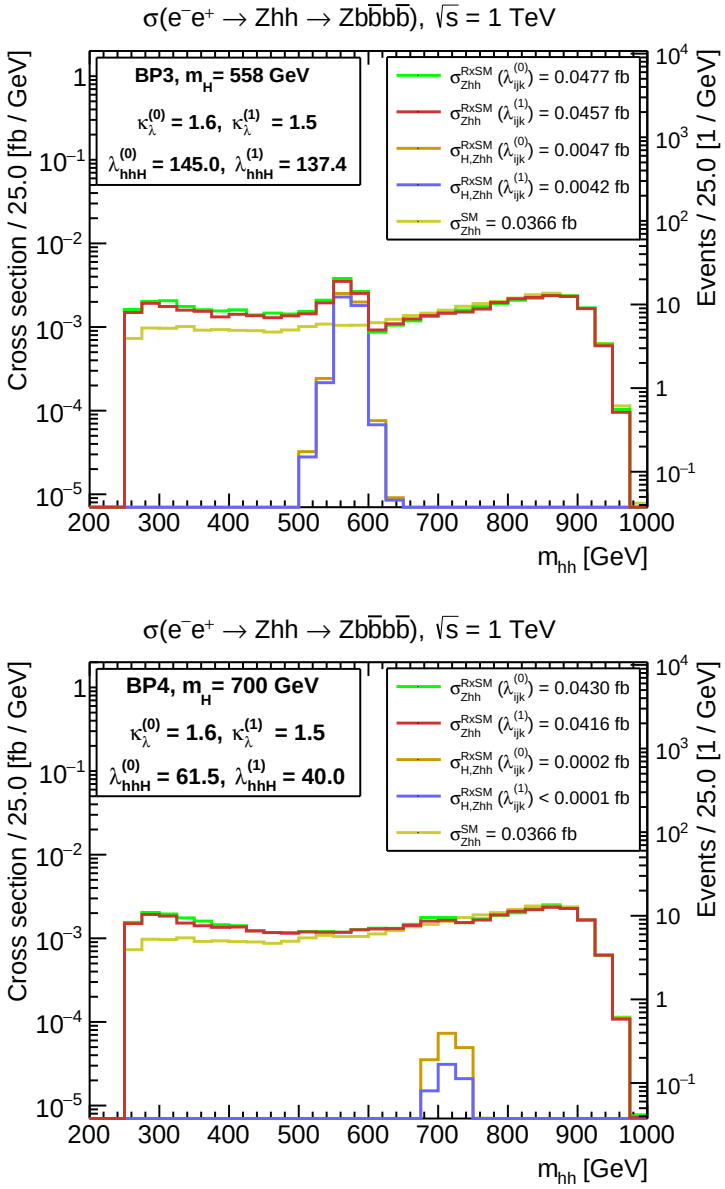

Figure 7.20: Plots and line styles as in fig. 7.19. *Top*: Results for BP3. *Bottom*: Results for BP4.

the highest cross-sections, and also the most pronounced resonances, in BP2 and BP3, which are the benchmark points with lower m_H and higher λ_{hhH}, an effect that is more pronounced in BP3. In these two BPs, we can distinguish a peak-dip structure, caused by the interference of the resonant H-channel diagram with the non-resonant diagrams in this process. This is illustrated by the orange and blue curves, showing the pure heavy Higgs-boson resonance cross-section. On the other hand, for BP1 and BP4 in the full calculation the resonances cannot be resolved, due to the small contribution of the resonance diagrams and the smearing.

In the next step, we calculate a statistical significance for distinguishing the RxSM m_{hh} distribution from the SM prediction following [142], defined as $Z = \sqrt{(Z_{-+})^2 + (Z_{+-})^2}$,

with $Z_{\pm\mp}$ the statistical significance calculated for each polarisation $(\pm 80\%, \mp 30\%)$. The results are summarised in table 7.5, where $Z^{(0)}_{Zhh}$ denotes the tree-level and $Z^{(1)}_{Zhh}$ the one-loop result. In general we find large significances which in the one-loop case lie in the range $[3.9, 6.9]$. One can also see a decrease in the significances from tree level to one loop, in agreement with the total cross-sections. In addition, we find the highest significances for BP3, with 7.8 and 6.9 at tree level and one loop, respectively. Thus, analysing the differential cross-section yields a promising method to study this type of BSM models.

Furthermore, we calculate the statistical significance of the heavy Higgs-boson resonance in the m_{hh} distributions. This gives an indication of the sensitivity to λ_{hhH}. For this calculation we follow the same procedure as before, but now calculating the significance of the full RxSM m_{hh} distribution with respect to the RxSM prediction omitting the heavy Higgs-boson contribution. The results are given in the two right-most columns of table 7.5 as $Z^{(0),\mathrm{r}}_{Zhh}$ at tree level and $Z^{(1),\mathrm{r}}_{Zhh}$ at one loop. As expected from our description of the differential cross-sections, BP1 and BP4 yield only marginal values for this significance. BP2 reaches values slightly below 3, and BP3 yields significances close to 6. The overall differences between the tree-level and one-loop results are small. These results indicate that at least for some parts of the RxSM parameter space favoured by a SFOEWPT a high-energy e^+e^- collider may have access to the BSM trilinear scalar coupling λ_{hhH}. Apart from significances, we also show in table 7.5 our approximation for the detector efficiency, $\mathscr{A}_{Zhh} \times \epsilon_b$. We found that for the considered points at tree level and one loop the difference between the values of $\mathscr{A}_{Zhh} \times \epsilon_b$ for our benchmark points is below the numerical uncertainty of $\sim 0.5\%$ with values around $\sim 60\%$. This is related to the fact that the relative differences between the values of $\sigma^{\mathrm{RxSM}}_{Zhh}$ for the BPs, also before applying cuts, are small.

BP	$\sigma^{\mathrm{RxSM}}_{Zhh}(\lambda^{(0)}_{ijk})$ [fb]	$\sigma^{\mathrm{RxSM}}_{Zhh}(\hat{\lambda}^{(1)}_{ijk})$ [fb]	$Z^{(0)}_{Zhh}$	$Z^{(1)}_{Zhh}$	$\mathscr{A}^{(0)}_{Zhh} \times \epsilon_b$	$\mathscr{A}^{(1)}_{Zhh} \times \epsilon_b$	$Z^{(0),\mathrm{r}}_{Zhh}$	$Z^{(1),\mathrm{r}}_{Zhh}$
1	0.0460	0.0441	5.8	4.8	60.5%	60.6%	0.7	0.7
2	0.0463	0.0452	6.2	5.7	60.6%	60.6%	2.9	2.8
3	0.0477	0.0457	7.8	6.9	60.9%	60.9%	5.8	5.5
4	0.0430	0.0416	4.4	3.9	60.6%	60.6%	1.1	0.8

Table 7.5: Summary of the predictions for $e^+e^- \to Zhh$ cross-sections, significances, and acceptance at the ILC1000 for the benchmark points in table 6.2. From left to right: $(-80\%, +30\%)$ polarised cross-sections $\sigma(e^+e^- \to Zhh \to Zb\bar{b}b\bar{b})$ in the RxSM at tree level and one loop for ILC1000 after applying cuts; statistical significances at tree level and one loop to distinguish the RxSM distribution from the SM; values of acceptances times ϵ_b at tree level and one loop; statistical significances of the resonances, i.e. the RxSM compared to the RxSM process without the resonant heavy Higgs-boson diagram. For the SM, we have $\mathscr{A} \times \epsilon_b = 61.4\%$

As a final step in our analysis, we compute the differential m_{hh} distributions for the $\nu\bar{\nu}hh$ channel, which are shown in fig. 7.21 (BP1 and BP2) and fig. 7.22 (BP3 and BP4). These plots follow the same colour coding and structure as figs. 7.19 and 7.20 for the Zhh channel. The corresponding significances and efficiencies are summarised in table 7.6. For these efficiencies, we have performed the calculation for both polarisations. We have found that the contributions of the polarisation $(-80\%, +30\%)$ are significantly larger that for $(+80\%, -30\%)$, while the acceptances values are virtually the same, with variations of less

than 1%. Therefore, we have used (and listed in table 7.6) the results for the polarisation $(-80\%, +30\%)$.

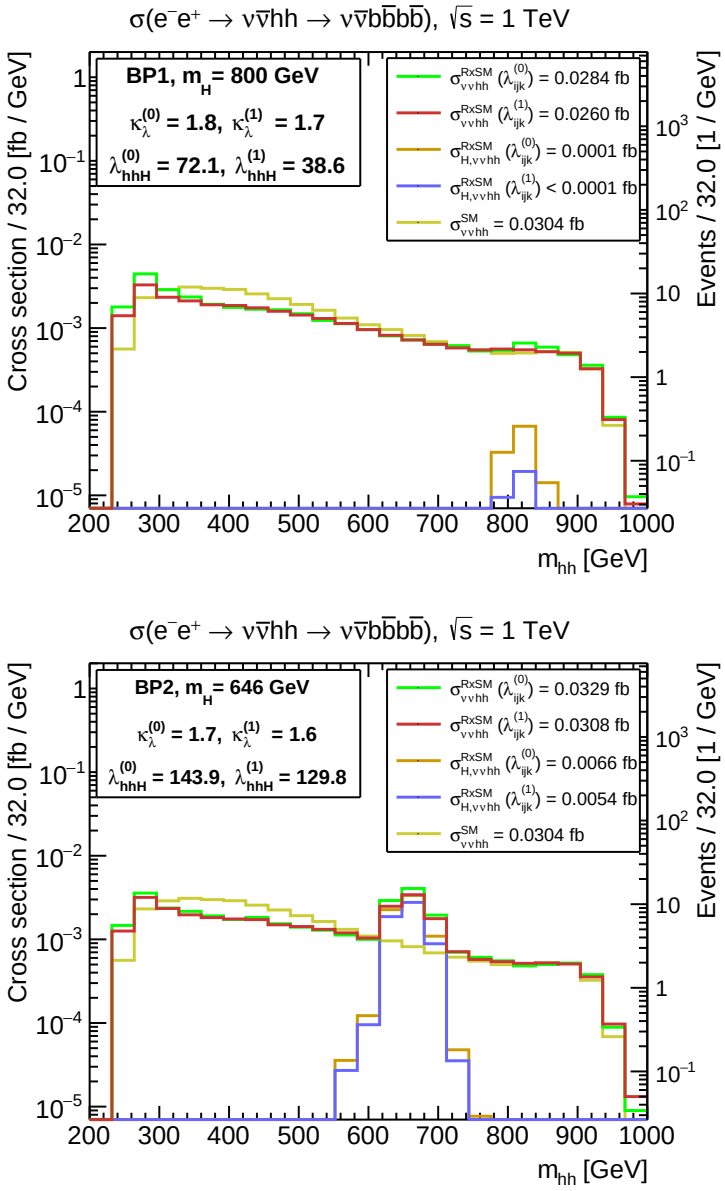

Figure 7.21: Plots and line styles as in fig. 7.19, but for the process $e^+e^- \to \nu\bar{\nu}hh \to \nu\bar{\nu}b\bar{b}b\bar{b}$. *Top*: Results for BP1. *Bottom*: Results for BP2.

In figs. 7.21 and 7.22, unlike figs. 7.19 and 7.20 for the Zhh channel, we find a reduction of the differential cross-sections with respect to the SM prediction in most of the m_{hh} range, observing again significant non-resonant effects in the differential cross-section. Following the analysis of the total cross-section in benchmark plane 2, we obtain lower values of the total cross-sections in the RxSM distributions than for the SM for BP1 and BP4. Meanwhile, for BP2, the cross-section is very close to the SM, and a noticeable increase is only found for BP3. The latter receives the largest enhancement from the heavy Higgs-boson resonance. The sizes and effects of the pure resonant heavy Higgs-exchange contribution follow the same pattern as in the Zhh case, i.e. they yield visible

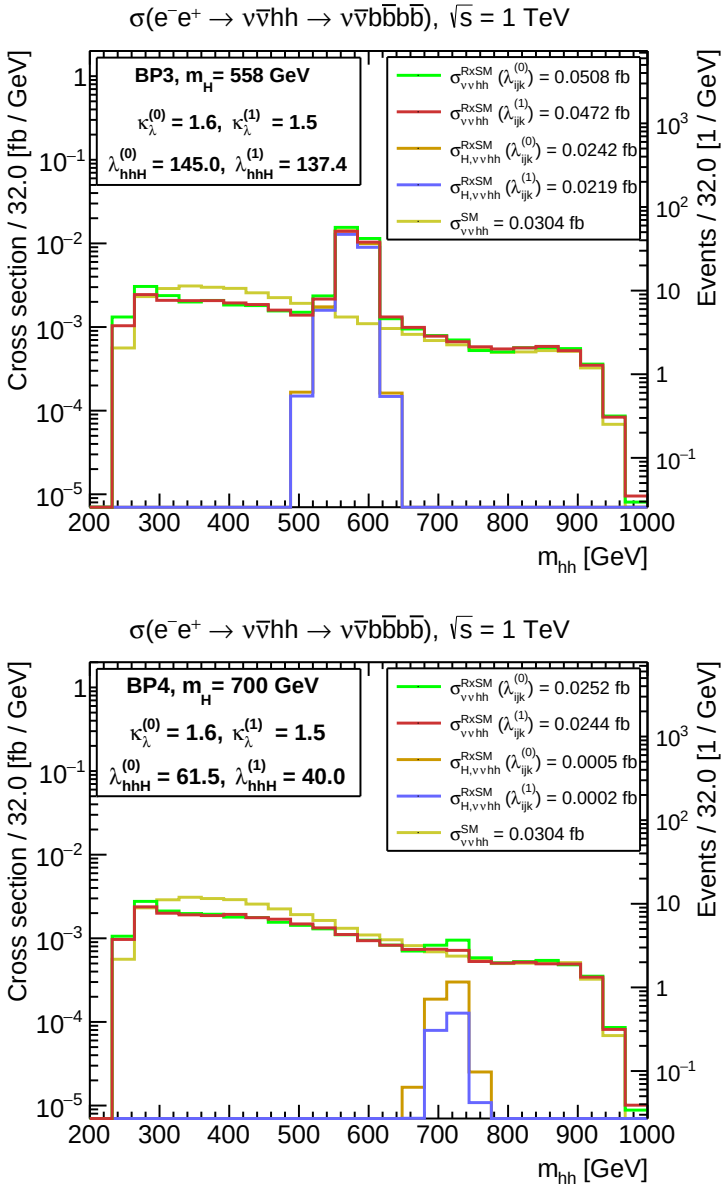

Figure 7.22: Plots and line styles as in fig. 7.20, but for the process $e^+e^- \to \nu\bar{\nu}hh \to \nu\bar{\nu}b\bar{b}b\bar{b}$. *Top*: Results for BP3. *Bottom*: Results for BP4.

results only for BP2 and BP3.

Finally, we compute the statistical significances to distinguish the RxSM differential distributions for this $\nu\bar{\nu}hh$ channel from that in the SM, summarised in table 7.6, following the same procedure used for the results in table 7.5 for the Zhh channel [142]. We denote them as $Z^{(0)}_{\nu\bar{\nu}hh}$ and $Z^{(1)}_{\nu\bar{\nu}hh}$ at tree level and one loop. The overall results for the significances for distinguishing the RxSM from the SM are similar to the Zhh case. However, BP2 and BP3 yield substantially higher values, due to the fact that the differences in the m_{hh} distributions are spread over a larger range in m_{hh}. Concerning the significances for the heavy Higgs-boson resonance, defined as $Z^{(0),\mathrm{r}}_{\nu\bar{\nu}hh}$ and $Z^{(1),\mathrm{r}}_{\nu\bar{\nu}hh}$, there also the results are qualitatively in agreement with the ones of the Zhh channel. Furthermore, BP2 and BP3

yield substantially higher values in the $\nu\bar{\nu}hh$ channel as compared to the Zhh channel. This indicates that the $\nu\bar{\nu}hh$ channel may be better suited to extract information about λ_{hhH} at the ILC1000.

BP	$\sigma^{\mathrm{RxSM}}_{\nu\bar{\nu}hh}(\lambda^{(0)}_{ijk})$ [fb]	$\sigma^{\mathrm{RxSM}}_{\nu\bar{\nu}hh}(\hat{\lambda}^{(1)}_{ijk})$ [fb]	$Z^{(0)}_{\nu\bar{\nu}hh}$	$Z^{(1)}_{\nu\bar{\nu}hh}$	$\mathscr{A}^{(0)}_{\nu\bar{\nu}hh} \times \epsilon_b$	$\mathscr{A}^{(1)}_{\nu\bar{\nu}hh} \times \epsilon_b$	$Z^{(0),\mathrm{r}}_{\nu\bar{\nu}hh}$	$Z^{(1),\mathrm{r}}_{\nu\bar{\nu}hh}$
1	0.0284	0.0260	3.4	2.8	49.8%	48.3%	0.4	0.3
2	0.0329	0.0308	6.5	5.7	49.3%	48.9%	6.0	5.2
3	0.0508	0.0472	16.4	15.0	51.0%	50.5%	16.4	15.0
4	0.0252	0.0244	2.9	2.8	47.7%	47.3%	0.6	0.3

Table 7.6: Summary of the predictions for the benchmark points in table 6.2 as in table 7.5, but for the $\nu\bar{\nu}hh$ channel. For the SM, we have $\mathscr{A} \times \epsilon_b = 45.3\%$.

7.4 Discussion

In this chapter, we have explored the dynamics of the EWPT in the RxSM. Specifically, we analysed the possibility of probing scenarios with a SFOEWPT using the complementarity of GW signals and di-Higgs production at colliders, building on the previous studies in Refs. [142, 246]. A novel aspect of our work is that we included, for consistency, one-loop radiative corrections both in the study of the thermal evolution of the vacuum and in the collider analyses. For the former, this was done using a new implementation of the RxSM into the public code `BSMPTv3`, including also higher-order corrections to the thermal potential. For the latter, we used the public code `anyH3`, employing the full on-shell renormalisation scheme devised in [142], to compute one-loop corrected trilinear scalar couplings. In turn, these served as inputs for the computation of the di-Higgs production cross-sections for $gg \to hh$ at the HL-LHC, using `HPAIR`, and to calculate $e^+e^- \to Zhh$ and $e^+e^- \to \nu\bar{\nu}hh$ at the ILC1000, using `Madgraph5_aMC`.

By performing an extensive scan of the parameter space of the RxSM, we scrutinised the different possible thermal histories in the early Universe of this model. We found that first-order EWPTs are possible and can occur either as single- or multi-step transitions, with potentially various level of strengths. The most favourable scenarios in terms of realising a SFOEWPT are case **C** with a two-step transition, and cases **D** and **E** for a one-step transition (using here the same labelling as in fig. 7.1). Moreover, parts of the RxSM parameter space can be excluded due to vacuum trapping (case **F**).

Inspired by this general scan, we devised two benchmark planes, representative of the specific regions where we found SFOEWPTs, and we investigated in detail their phenomenology. A first such plane features light BSM Higgs-boson masses and low values of v_S, and exhibits SFOEWPTs for an extended range of parameters — both as one-step (case **D**) and two-step (case **C**) transitions. The second plane, with larger v_S and heavy BSM scalar masses, features one-step SFOEWPTs (as well as vacuum trapping). For both benchmark planes we calculated predictions for the spectra of GWs produced during the SFOEWPT and the associated SNR at LISA, using `BSMPT`. We moreover investigated the dependence of the SNR on the bubble wall velocity (which we did not compute in our study), and found that for most scenarios considering $v_\mathrm{w} = 0.95$ is a sufficiently conservative choice, as long as the true $v_\mathrm{w} \gtrsim 0.3$. In benchmark plane 1, the EWPT is largely driven by the singlet field direction, which allows for strong GW signals in significant

parts of the plane. On the other hand, in benchmark plane 2, it is the doublet field direction that plays the most important role in the EWPT, and observable SNR are only found in a narrow band of the plane.

Next, we considered whether searches for di-Higgs production processes at high-energy colliders, the HL-LHC or a 1 TeV e^+e^- collider (ILC1000), can provide additional information to probe these scenarios. In the case of the first benchmark plane, with a singlet-driven EWPT, the BSM effects in trilinear scalar couplings are minute, and essentially no new information would be obtained from di-Higgs production searches. In contrast to this, for the second benchmark plane, with a doublet-driven EWPT, there is a clear correlation between the strength of the SFOEWPT and the BSM deviation in κ_λ — with $1.35 \lesssim \kappa_\lambda^{(1)} \lesssim 1.7$ for points with a SFOEWPT. These values of κ_λ result in a further suppression of the $gg \to hh$ and $e^+e^- \to \nu\bar{\nu}hh$ cross-sections compared to the SM, while the $e^+e^- \to Zhh$ cross-section is increased. Resonant H contributions can yield an increase of the three cross-sections; for the case of $e^+e^- \to \nu\bar{\nu}hh$ this can suffice to exceed the SM prediction, but not for $gg \to hh$. In other words, a high-energy e^+e^- collider could probe these SFOEWPT scenarios via the total di-Higgs production cross-section, but this would be significantly more difficult at the HL-LHC.

Moreover, additional information can be obtained from the study of differential distributions. For this reason, we devised four concrete benchmark points, selected from benchmark plane 2, in order to perform a detailed analysis of differential m_{hh} distributions. While the relative level of significance of the different di-Higgs processes varied between the BPs, we found that all these scenarios could be distinguished from the SM, even though the corresponding total cross-sections were in many cases below the SM predictions. We also illustrated the possibility of discriminating the resonant H contributions from the continuum, provided that the BSM scalar mass is not too heavy ($m_H \lesssim 650$ GeV) — and here the $e^+e^- \to \nu\bar{\nu}hh$ process is clearly the most promising. However, here it should be kept in mind that our study only takes into account parts of the experimental effects and uncertainties; a full experimental study is needed to analyse the sensitivity to the heavy Higgs-boson resonance.

To conclude, in this work we have demonstrated the crucial importance of using complementary sources of experimental data in order to probe SFOEWPT scenarios in the RxSM. Singlet-driven EWPT benchmarks typically feature comparatively stronger signals of GWs, sourced during the phase transition in the early Universe, but close to no signs of BSM effects in di-Higgs production. Meanwhile, the situation in scenarios with a doublet-driven SFOEWPT is more similar to that in models like the 2HDM (see e.g. [56]): i.e. with a significant correlation between ξ_n and κ_λ, BSM effects in di-Higgs production that would likely be observable at colliders — HL-LHC and/or an e^+e^- machine — at least in differential m_{hh} distributions, but detectable GW signals only in a limited fraction of the parameter space. Our results clearly indicate that no single experimental direction can cover the entire parameter space of the RxSM that would give rise to a SFOEWPT — and in particular singlet-driven SFOEWPTs would be extremely difficult to constrain only with collider experiments. This is somewhat in contrast to the results presented in Refs. [63, 342].

Chapter 8

Two loop corrections in the 2HDM

Crecí en el mar y la pobreza me fue fastuosa;
después perdí el mar,
y todos los lujos me parecieron grises,
la miseria intolerable.

– Albert Camus

The previous chapters of this thesis were devoted to the study of extended Higgs sectors from both phenomenological and cosmological perspectives. We first analysed how such models can modify di-Higgs production at colliders and how these effects are shaped by the structure of the scalar potential, including the interplay between resonant and non-resonant contributions. We then showed that, in beyond-the-Standard-Model scalar theories, radiative corrections to trilinear Higgs couplings can be sizeable already at one loop, and that their consistent inclusion can be crucial for reliable predictions. This picture was subsequently connected to the thermal history of the early Universe, where the same extended scalar dynamics can give rise to a strong first-order electroweak phase transition and potentially observable gravitational-wave signals.

A natural next step is therefore to push the study of extended Higgs sectors to a higher level of precision. The purpose of this final chapter is precisely to pursue this direction by going one order further in perturbation theory and investigating two-loop corrections in the Two Higgs Doublet Model. In this way, the chapter completes the programme developed throughout the thesis: starting from the tree-level structure of extended scalar sectors, incorporating one-loop effects in collider and cosmological observables, and finally assessing the impact of higher-order corrections on Higgs self-interactions and their phenomenological consequences.

Our analysis focuses on the CP-conserving 2HDM in the alignment limit, a particularly relevant regime in view of current Higgs data, since in this limit the light scalar h reproduces the Standard-Model-like couplings at tree level. At the same time, the alignment limit has to be properly renormalized at loop-level. For this reason, a central ingredient of this chapter is the consistent treatment of the alignment limit itself, including the

introduction of an on-shell renormalisation prescription for the parameter that controls the departure from alignment. This allows us to define the limit in a renormalised and physically meaningful way when computing higher-order corrections.

Within this framework, we calculate the two-loop corrections to the trilinear Higgs couplings λ_{hhh} and λ_{hhH} and investigate their impact on di-Higgs production at the HL-LHC. An important aspect of the analysis is that the calculation is carried out using two complementary methods in parallel: the diagrammatic approach and the effective-potential approach. This provides a non-trivial consistency check of the calculation, since agreement between the two methods confirms the robustness of the obtained results in the appropriate zero-momentum limit.

The aim of this chapter is therefore twofold. To extends the precision frontier of the study of extended Higgs sectors developed in this thesis by determining the magnitude of the dominant two-loop BSM corrections to the trilinear scalar couplings relevant for Higgs pair production. Therefore, the purely scalar as well as mixed scalar-fermion two-loop contributions to the λ_{hhh} and λ_{hhH} couplings are computed, in the limit of of vanishing external momenta. Additionally, the subleading contributions from light scalars are neglected, and for this purpose m_h is set to 0 and the computation is done in the gaugeless limit. In this sense, the chapter serves as the final step of the thesis, in which a new layer of precision is added to the Higgs self-couplings, and collider phenomenology within a more advanced higher-order framework.

This chapter is motivated by recent advances [97,343,344] in the two-loop computation of trilinear scalar couplings, together with progress in the renormalisation of the alignment condition, provide strong motivation to revisit the earlier results of [93, 94] for λ_{hhh}. In particular, these developments make it possible to relax some of the simplifying assumptions adopted in those works and to extend the analysis to other trilinear couplings, such as λ_{hhH}.

8.1 2HDM in the Higgs Basis

In the Higgs basis, only one of the scalar doublets acquires a vev, while the second doublet is orthogonal to the electroweak symmetry breaking direction. This basis is particularly convenient for phenomenological studies, as it makes the alignment limit transparent and allows for a direct interpretation of the SM-like Higgs state. In this case also helps to take control of the alignment limit at the two-loop level. The two complex scalar doublets are defined as

$$\Phi_{\text{SM}} = \begin{pmatrix} G^{+\prime} \\ \frac{1}{\sqrt{2}}\left(v + \phi_{\text{SM}} + iG^{0\prime}\right) \end{pmatrix}, \qquad \Phi_{\text{BSM}} = \begin{pmatrix} H^{+\prime} \\ \frac{1}{\sqrt{2}}\left(v_{\text{BSM}} + \phi_{\text{BSM}} + iA^{\prime}\right) \end{pmatrix}, \tag{8.1}$$

where $G^{\pm\prime}$ and $G^{0\prime}$ are the Goldstone bosons, $H^{\pm\prime}$ is the charged Higgs boson, $A^{\prime}$ is the CP-odd scalar, which has to be rotated by $\beta^{\prime}$ to define the mass eigenstates $G^{\pm}$,G^{0}, $H^{\pm}$ and A. And ϕ_{SM}, ϕ_{BSM} denote the CP-even interaction eigenstates. By construction, only Φ_{SM} develops a non-zero vev v but we also have to keep track of the BSM doublet vev v_{BSM}. In the Higgs basis, and without imposing a $\mathbb{Z}_2$ symmetry, the most general

renormalisable scalar potential reads

$$\begin{aligned} V(\Phi_{\mathrm{SM}},\Phi_{\mathrm{BSM}}) =& M_{11}^2|\Phi_{\mathrm{SM}}|^2 + M_{22}^2|\Phi_{\mathrm{BSM}}|^2 - M_{12}^2(\Phi_{\mathrm{BSM}}^\dagger\Phi_{\mathrm{SM}} + \mathrm{h.c.}) \\ &+ \frac{\Lambda_1}{2}|\Phi_{\mathrm{SM}}|^4 + \frac{\Lambda_2}{2}|\Phi_{\mathrm{BSM}}|^4 + \Lambda_3|\Phi_{\mathrm{SM}}|^2|\Phi_{\mathrm{BSM}}|^2 + \Lambda_4|\Phi_{\mathrm{BSM}}^\dagger\Phi_{\mathrm{SM}}|^2 \\ &+ \left[\frac{\Lambda_5}{2}(\Phi_{\mathrm{BSM}}^\dagger\Phi_{\mathrm{SM}})^2 + (\Lambda_6|\Phi_{\mathrm{SM}}|^2 + \Lambda_7|\Phi_{\mathrm{BSM}}|^2)\Phi_{\mathrm{SM}}^\dagger\Phi_{\mathrm{BSM}} + \mathrm{h.c.}\right]. \end{aligned} \tag{8.2}$$

The parameters Λ_6 and Λ_7 encode the mixing between the two doublets and are absent in the exact $\mathbb{Z}_2$ symmetric case. In this basis, when setting $v_{\mathrm{BSM}} = 0$, the CP-even mass matrix is obtained from the second derivatives of the potential,

$$\frac{\partial^2 V}{\partial\phi_i\partial\phi_j} = \begin{pmatrix} M_{\mathrm{SM}}^2 & \Lambda_6 v^2 \\ \Lambda_6 v^2 & M_{\mathrm{BSM}}^2 \end{pmatrix}, \tag{8.3}$$

$$M_{\mathrm{SM}}^2 = \Lambda_1 v^2, \tag{8.4}$$

$$M_{\mathrm{BSM}}^2 = M_{22}^2 + \frac{1}{2}(\Lambda_3+\Lambda_4+\Lambda_5)v^2. \tag{8.5}$$

The off-diagonal entry proportional to Λ_6 controls the mixing between the SM-like and BSM-like CP-even states. The CP-even mass matrix is diagonalised by an orthogonal rotation, when setting $v_{\mathrm{BSM}} = 0$ as,

$$\tan(2\alpha') = \frac{2\Lambda_6 v^2}{M_{\mathrm{SM}}^2 - M_{\mathrm{BSM}}^2}. \tag{8.6}$$

After diagonalisation, the physical CP-even masses are

$$m_h^2 = \frac{1}{2}\left(m_A^2 + (\Lambda_1+\Lambda_5)v^2 - \sqrt{(m_A^2 + (\Lambda_5-\Lambda_1)v^2)^2 + 4\Lambda_6^2 v^4}\right), \tag{8.7}$$

$$m_H^2 = \frac{1}{2}\left(m_A^2 + (\Lambda_1+\Lambda_5)v^2 + \sqrt{(m_A^2 + (\Lambda_5-\Lambda_1)v^2)^2 + 4\Lambda_6^2 v^4}\right), \tag{8.8}$$

$$m_A^2 = M_{22}^2 + \frac{1}{2}(\Lambda_3+\Lambda_4-\Lambda_5)v^2, \tag{8.9}$$

$$m_{H^\pm}^2 = M_{22}^2 + \frac{1}{2}\Lambda_3 v^2. \tag{8.10}$$

The interaction eigenstates are related to the mass eigenstates through

$$\begin{pmatrix} H \\ h \end{pmatrix} = R_{\alpha'}^{\mathrm{T}} \begin{pmatrix} \phi_{\mathrm{SM}} \\ \phi_{\mathrm{BSM}} \end{pmatrix}, \quad \begin{pmatrix} G^0 \\ A \end{pmatrix} = R_{\beta'}^{\mathrm{T}} \begin{pmatrix} G^{0\prime} \\ A' \end{pmatrix}, \quad \begin{pmatrix} G^+ \\ H^+ \end{pmatrix} = R_{\beta'}^{\mathrm{T}} \begin{pmatrix} G^{+\prime} \\ H^{+\prime} \end{pmatrix}. \tag{8.11}$$

In the alignment limit, $\Lambda_6 \to 0$, the mixing vanishes and h becomes purely SM-like.

The free parameters in this basis are

$$t_h, t_H, M_{22}^2, m_h, m_H, m_{H^\pm}, m_A, \Lambda_2, \Lambda_6, \Lambda_7, v, v_{\mathrm{BSM}}. \tag{8.12}$$

In order to relate the parameters in the Higgs basis to the parameters in the $\mathbb{Z}_2$ symmetric basis, one has the following relations [285, 345, 346],

$$\Lambda_1 = \lambda_1 c_\beta^4 + \lambda_2 s_\beta^4 + \frac{1}{2}\lambda_{345} s_{2\beta}^2 \,, \tag{8.13}$$

$$\Lambda_2 = \lambda_1 s_\beta^4 + \lambda_2 c_\beta^4 + \frac{1}{2}\lambda_{345} s_{2\beta}^2 \,, \tag{8.14}$$

$$\Lambda_i = \frac{1}{4} s_{2\beta}^2 (\lambda_1 + \lambda_2 - 2\lambda_{345}) + \lambda_i \, (i = 3, 4, 5) \,, \tag{8.15}$$

$$\Lambda_6 = -\frac{1}{2} s_{2\beta} (\lambda_1 c_\beta^2 - \lambda_2 s_\beta^2 - \lambda_{345} c_{2\beta}) \,, \tag{8.16}$$

$$\Lambda_7 = -\frac{1}{2} s_{2\beta} (\lambda_1 s_\beta^2 - \lambda_2 c_\beta^2 + \lambda_{345} c_{2\beta}) \,, \tag{8.17}$$

$$\Lambda_2 = \Lambda_1 + 2(\Lambda_6 + \Lambda_7) \cot 2\beta \,, \tag{8.18}$$

$$\Lambda_3 + \Lambda_4 + \Lambda_5 = \Lambda_1 + 2\Lambda_6 \cot 2\beta - \frac{(\Lambda_6 - \Lambda_7)}{\cot 2\beta} \,, \tag{8.19}$$

$$M_{11}^2 = m_{11}^2 c_\beta^2 + m_{22}^2 s_\beta^2 - m_{12}^2 s_{2\beta} \,, \tag{8.20}$$

$$M_{12}^2 = m_{11}^2 s_\beta^2 + m_{22}^2 c_\beta^2 + m_{12}^2 s_{2\beta} \,, \tag{8.21}$$

$$M_{22}^2 = \frac{1}{2}(m_{22}^2 - m_{11}^2) s_{2\beta} - m_{12}^2 c_{2\beta} \,. \tag{8.22}$$

The Yukawa couplings can be written as

$$Y_{\rm SM}^t = \frac{m_t \sqrt{2}}{v} \frac{1}{1 + \zeta_t \frac{v_{\rm BSM}}{v}} \,, \tag{8.23}$$

$$Y_{\rm BSM}^t = \frac{m_t \sqrt{2}}{v} \frac{\zeta_t}{1 + \zeta_t \frac{v_{\rm BSM}}{v}} \tag{8.24}$$

Comparing with the $\mathbb{Z}_2$ symmetric basis we have

$$\zeta_t = \cot \beta \,. \tag{8.25}$$

This corresponds to eleven independent parameters in the Higgs basis. In contrast, the softly broken $\mathbb{Z}_2$ symmetric model contains ten parameters, since the $\mathbb{Z}_2$ symmetry forbids certain terms responsible for tree-level flavour-changing neutral currents (FCNCs).To avoid it, we define a relation between Λ_2 and Λ_7 using two relations given in [285], which translate between the two bases while avoiding FCNCs:

$$\Lambda_2 = \Lambda_1 + 2(\Lambda_6 + \Lambda_7) \cot 2\beta, \tag{8.26}$$

$$\Lambda_3 + \Lambda_4 + \Lambda_5 = \Lambda_1 + 2\Lambda_6 \cot 2\beta - (\Lambda_6 - \Lambda_7) \tan 2\beta, \tag{8.27}$$

where β comes from the $\mathbb{Z}_2$ symmetric base and is defined as the inverse tangent of the ratio between the vevs of both doublets. We have a system of two equations, and we want to eliminate two variables (β and Λ_2). The second equation does not depend on Λ_2;

therefore, it can be used to obtain a relation between Λ_7 and $\cot 2\beta$, and hence eliminate β. We obtain two possible solutions:

$$\cot 2\beta_\pm = \frac{1}{8\Lambda_6}\left(-\frac{4M_{22}^2 - m_h^2 - m_H^2 - 3\sqrt{(m_h^2-m_H^2)^2 - 4v^4\Lambda_6^2}}{v^2} \right.$$
$$\left. \pm \sqrt{\frac{(4M_{22}^2 - m_h^2 - m_H^2 - 3\sqrt{(m_h^2-m_H^2)^2 - 4v^4\Lambda_6^2})^2}{v^4} - 16\Lambda_6(-2\Lambda_6 + 2\Lambda_7)}\right). \tag{8.28}$$

The idea is to keep track of both branches in order to determine whether one of them is unphysical. We then want to substitute this relation into Eq. (8.26). However, we will see that if we do this directly and then take the alignment limit, the result diverges. On the other hand, if we impose the alignment limit from the beginning and solve the system afterwards, we obtain

$$\Lambda_2\big|_{\text{align}} = \frac{m_h^2}{v^2} - \frac{2v^2\Lambda_7^2}{2M_{22}^2 + m_h^2 - 2m_H^2}. \tag{8.29}$$

This happens because the solution of the full second-order equation in Eq. (8.27) and the solution of the reduced equation obtained from Eq. (8.27) after taking the alignment limit ($\Lambda_6 = 0$) are not compatible. In other words, the order in which one takes the alignment limit and solves the equation matters. To resolve this issue, we substitute Eq. (8.28) into Eq. (8.26) and expand the resulting expression around Λ_6 before taking the alignment limit:

$$\begin{aligned}\Lambda_{2\pm} =& \frac{(-2M_{22}^2 - m_h^2 + 2m_H^2 \pm |2M_{22}^2 + m_h^2 - 2m_H^2|)\Lambda_7}{4v^2\Lambda_6} + \frac{m_h^2}{v^2} \pm \frac{-2v^2\Lambda_7^2}{|2M_{22}^2 + m_h^2 - 2m_H^2|} + \\ &+ \frac{-2M_{22}^2 - m_h^2 + 2m_H^2 \pm |2M_{22}^2 + m_h^2 - 2m_H^2|}{2v^2} + \\ &\left[\pm\frac{-2v^2\Lambda_7}{|2M_{22}^2 + m_h^2 - 2m_H^2|} + \right. \\ &\left. + \frac{\Lambda_7}{4}\left(\frac{6v^2}{m_h^2 - m_H^2} \pm \frac{2v^2\left(4 - \frac{3(2M_{22}^2 + m_h^2 - 2m_H^2)}{m_h^2 - m_H^2} - \frac{16v^8\Lambda_7^2}{(2M_{22}^2 + m_h^2 - 2m_H^2)^4}\right)}{|2M_{22}^2 + m_h^2 - 2m_H^2|}\right)\right]\Lambda_6 \\ &+ \mathcal{O}(\Lambda_6^2).\end{aligned} \tag{8.30}$$

We can see that, depending on the sign of $2M_{22}^2 + m_h^2 - 2m_H^2$, one branch or the other cancels the divergent term. Fortunately, the same branch that cancels the divergence is also the one that reproduces the correct sign in the alignment limit. This means that, away from the alignment limit, the appropriate branch must be chosen depending on the sign of $2M_{22}^2 + m_h^2 - 2m_H^2$, whereas in the alignment limit both branches converge to the same result.

8.2 On-shell renormalisation of the 2HDM at two loops

In this section, we describe a framework to obtain the complete on-shell (OS) renormalisation of the 2HDM required to compute the full set of trilinear scalar couplings in the CP-even scalar sector at two-loop order. The first step is to identify which parameters require one-loop counterterms and which require two-loop counterterms. To this end, we begin by introducing field renormalisation. In the CP-even sector of the 2HDM there are two Higgs fields, h and H, and the standard renormalisation transformation, which we now expand to two-loop order:

$$\begin{pmatrix} H \\ h \end{pmatrix} \to \sqrt{1+\delta_{\mathrm{CT}}Z}\begin{pmatrix} H \\ h \end{pmatrix} \approx \left(1+\frac{\delta_{\mathrm{CT}}Z}{2}-\frac{\delta_{\mathrm{CT}}Z^2}{8}\right)\begin{pmatrix} H \\ h \end{pmatrix}, \tag{8.31}$$

where $\delta_{\mathrm{CT}}Z$ denotes the field-renormalisation counterterm, represented by the matrix

$$\delta_{\mathrm{CT}}Z = \begin{pmatrix} \delta_{\mathrm{CT}}Z_{HH} & \delta_{\mathrm{CT}}Z_{Hh} \\ \delta_{\mathrm{CT}}Z_{hH} & \delta_{\mathrm{CT}}Z_{hh} \end{pmatrix}. \tag{8.32}$$

Having defined the field-renormalisation counterterms, we proceed to the one-point functions (tadpoles), followed by the two-point functions (propagators), and subsequently renormalise the three-point functions, i.e. the trilinear scalar couplings. Once the counterterm expressions for the trilinear couplings are obtained, we can determine which input parameters require renormalisation at a given loop order and impose the corresponding OS conditions. As mentioned above, we perform the renormalisation in the general 2HDM before taking the alignment limit, in order to maintain control over this limit at each loop order. After completing the renormalisation procedure, the alignment limit can be taken.

8.2.1 CP-even tadpole renormalisation

As discussed above, the first step is to renormalise the one-point functions, i.e. the tadpole contributions. We therefore start from the tadpole terms in the Lagrangian. These terms can be written either in terms of the Lagrangian fields (ϕ_{SM}, ϕ_{BSM}) or, equivalently, in the mass basis (h, H):

$$\mathscr{L} \supset \begin{pmatrix} T_1 & T_2 \end{pmatrix}\begin{pmatrix} \phi_{\mathrm{SM}} \\ \phi_{\mathrm{BSM}} \end{pmatrix} = \begin{pmatrix} T_H & T_h \end{pmatrix}\begin{pmatrix} H \\ h \end{pmatrix}, \tag{8.33}$$

where we used the rotation by the mixing angle α' to switch between the two bases:

$$\begin{pmatrix} H \\ h \end{pmatrix} = R^{\mathrm{T}}_{\alpha'}\begin{pmatrix} \phi_{\mathrm{SM}} \\ \phi_{\mathrm{BSM}} \end{pmatrix}, \tag{8.34}$$

$$\begin{pmatrix} T_1 \\ T_2 \end{pmatrix} = R_{\alpha'}\begin{pmatrix} T_H \\ T_h \end{pmatrix}. \tag{8.35}$$

Working in the mass basis, we can now insert the field-renormalisation counterterms according to eq. (8.31):

$$\mathscr{L} \supset \begin{pmatrix} \delta_{\mathrm{CT}}T_H & \delta_{\mathrm{CT}}T_h \end{pmatrix}\left(1+\frac{\delta_{\mathrm{CT}}Z}{2}\right)\begin{pmatrix} H \\ h \end{pmatrix}. \tag{8.36}$$

$$h \text{ - - - - -} \otimes = -i\left(\delta^{(1)}_{\mathrm{CT}} T_h\right) - i\left(\delta^{(2)}_{\mathrm{CT}} T_h + \delta^{(1)}_{\mathrm{CT}} T_h \frac{\delta^{(1)}_{\mathrm{CT}} Z_{hh}}{2} + \delta^{(1)}_{\mathrm{CT}} T_H \frac{\delta^{(1)}_{\mathrm{CT}} Z_{Hh}}{2}\right),$$
$$H \text{ - - - - -} \otimes = -i\left(\delta^{(1)}_{\mathrm{CT}} T_H\right) - i\left(\delta^{(2)}_{\mathrm{CT}} T_H + \delta^{(1)}_{\mathrm{CT}} T_H \frac{\delta^{(1)}_{\mathrm{CT}} Z_{HH}}{2} + \delta^{(1)}_{\mathrm{CT}} T_h \frac{\delta^{(1)}_{\mathrm{CT}} Z_{hH}}{2}\right).$$

At this stage we have to expand the counterterms up to second order and focus in each of the tadpole conunterterms independently:

Since we aim to define a fully OS scheme, we also renormalise the tadpoles on-shell. This amounts to requiring the renormalised tadpoles to vanish. From now on, we use t_h and t_H to denote the (loop) tadpole contributions, i.e.

h - - - -  $= it_h$,
H - - - -  $= it_H$.

Enforcing the vanishing of the renormalised tadpoles further implies the following relations for the tadpole terms:

$$t_h = \left(\delta^{(1)}_{\mathrm{CT}} T_h\right) + \left(\delta^{(2)}_{\mathrm{CT}} T_h + \delta^{(1)}_{\mathrm{CT}} T_h \frac{\delta^{(1)}_{\mathrm{CT}} Z_{hh}}{2} + \delta^{(1)}_{\mathrm{CT}} T_H \frac{\delta^{(1)}_{\mathrm{CT}} Z_{Hh}}{2}\right), \tag{8.37}$$
$$t_H = \left(\delta^{(1)}_{\mathrm{CT}} T_H\right) + \left(\delta^{(2)}_{\mathrm{CT}} T_H + \delta^{(1)}_{\mathrm{CT}} T_H \frac{\delta^{(1)}_{\mathrm{CT}} Z_{HH}}{2} + \delta^{(1)}_{\mathrm{CT}} T_h \frac{\delta^{(1)}_{\mathrm{CT}} Z_{hH}}{2}\right). \tag{8.38}$$

8.2.2 CP-even two point function renormalization

Once the tadpole contributions have been renormalised, we can proceed to the two-point functions, i.e. the propagators. For this purpose, we focus on the quadratic (kinetic and mass) terms of the Lagrangian, which read

$$\mathscr{L} \supset \frac{1}{2}\,\partial^\mu \begin{pmatrix} H & h \end{pmatrix} \partial_\mu \begin{pmatrix} H \\ h \end{pmatrix} - \frac{1}{2} \begin{pmatrix} H & h \end{pmatrix} D \begin{pmatrix} H \\ h \end{pmatrix}, \tag{8.39}$$

where D denotes the (tree-level) mass matrix. As in the tadpole case, we now introduce the field-renormalisation counterterms in the two-point functions via the transformation eq. (8.31) and also the counterterm for the mass matrix $\delta_{\mathrm{CT}} D$:

$$
\begin{aligned}
\mathscr{L} \supset & \frac{1}{2}\partial^\mu \begin{pmatrix} H & h \end{pmatrix} \left(1 + \frac{\delta_{\rm CT} Z^{\rm T}}{2} - \frac{(\delta_{\rm CT} Z^{\rm T})^2}{8}\right) \left(1 + \frac{\delta_{\rm CT} Z}{2} - \frac{\delta_{\rm CT} Z^2}{8}\right) \partial_\mu \begin{pmatrix} H \\ h \end{pmatrix} \\
& - \frac{1}{2} \begin{pmatrix} H & h \end{pmatrix} \left(1 + \frac{\delta_{\rm CT} Z^{\rm T}}{2} - \frac{(\delta_{\rm CT} Z^{\rm T})^2}{8}\right) (D + \delta_{\rm CT} D) \left(1 + \frac{\delta_{\rm CT} Z}{2} - \frac{\delta_{\rm CT} Z^2}{8}\right) \begin{pmatrix} H \\ h \end{pmatrix} \\
= & \frac{1}{2}\partial^\mu \begin{pmatrix} H & h \end{pmatrix} \left(1 + \frac{\delta_{\rm CT} Z + \delta_{\rm CT} Z^{\rm T}}{2} + \frac{2\delta_{\rm CT} Z^{\rm T} \delta_{\rm CT} Z - \delta_{\rm CT} Z^2 - (\delta_{\rm CT} Z^{\rm T})^2}{8}\right) \partial_\mu \begin{pmatrix} H \\ h \end{pmatrix} \\
& - \frac{1}{2} \begin{pmatrix} H & h \end{pmatrix} \Bigg(D + \delta_{\rm CT} D + \frac{D\delta_{\rm CT} Z + \delta_{\rm CT} Z^{\rm T} D}{2} + \frac{2\delta_{\rm CT} Z^{\rm T} D \delta_{\rm CT} Z - D\delta_{\rm CT} Z^2}{8} \\
& - \frac{(\delta_{\rm CT} Z^{\rm T})^2 D}{8} + \frac{\delta_{\rm CT} Z^{\rm T} \delta_{\rm CT} D + \delta_{\rm CT} D \delta_{\rm CT} Z}{2}\Bigg) \begin{pmatrix} H \\ h \end{pmatrix} . \qquad (8.40)
\end{aligned}
$$

Next we have to focus in each of the two-point functions separately. Thus, we obtain

$$
\begin{aligned}
h \xrightarrow{p} \otimes h &= i\Big[\Big(\delta^{(1)}_{\rm CT} Z_{hh}(p^2 - m_h^2) - \delta^{(1)}_{\rm CT} D_{hh}\Big) + \Big(\delta^{(2)}_{\rm CT} Z_{hh}(p^2 - m_h^2) \\
&+ \tfrac{1}{4}(\delta^{(1)}_{\rm CT} Z_{Hh})^2 (p^2 - m_H^2) - \tfrac{1}{4}\delta^{(1)}_{\rm CT} Z_{hH} \delta^{(1)}_{\rm CT} Z_{Hh}(p^2 - m_h^2) - \delta^{(2)}_{\rm CT} D_{hh} - \delta^{(1)}_{\rm CT} D_{hh} \delta^{(1)}_{\rm CT} Z_{hh} \\
&- \delta^{(1)}_{\rm CT} D_{hH} \delta^{(1)}_{\rm CT} Z_{Hh}\Big)\Big] . \\
h \xrightarrow{p} \otimes H &= i\Big[\Big(\tfrac{1}{2}\delta^{(1)}_{\rm CT} Z_{Hh}(p^2 - m_H^2) + \tfrac{1}{2}\delta^{(1)}_{\rm CT} Z_{hH}(p^2 - m_h^2) - \delta^{(1)}_{\rm CT} D_{hH}\Big) + \\
&\Big(\tfrac{1}{2}\delta^{(2)}_{\rm CT} Z_{hH}(p^2 - m_h^2) + \tfrac{1}{2}\delta^{(2)}_{\rm CT} Z_{Hh}(p^2 - m_H^2) + \tfrac{1}{8}\delta^{(1)}_{\rm CT} Z_{HH}(\delta^{(1)}_{\rm CT} Z_{Hh}(p^2 - m_H^2) \\
&- \delta^{(1)}_{\rm CT} Z_{hH}(p^2 - m_h^2)) + \tfrac{1}{8}\delta^{(1)}_{\rm CT} Z_{hh}(\delta^{(1)}_{\rm CT} Z_{hH}(p^2 - m_h^2) - \delta^{(1)}_{\rm CT} Z_{Hh}(p^2 - m_H^2) - \delta^{(2)}_{\rm CT} D_{hH} \\
&- \tfrac{1}{2}\delta^{(1)}_{\rm CT} D_{hh} \delta^{(1)}_{\rm CT} Z_{hH} - \tfrac{1}{2}\delta^{(1)}_{\rm CT} D_{HH} \delta^{(1)}_{\rm CT} Z_{Hh} - \delta^{(1)}_{\rm CT} D_{hH} \left(\tfrac{\delta^{(1)}_{\rm CT} Z_{hh} + \delta^{(1)}_{\rm CT} Z_{HH}}{2}\right)\Big)\Big] . \\
H \xrightarrow{p} \otimes H &= i\Big[\Big(\delta^{(1)}_{\rm CT} Z_{HH}(p^2 - m_H^2) - \delta^{(1)}_{\rm CT} D_{HH}\Big) + \Big(\delta^{(2)}_{\rm CT} Z_{HH}(p^2 - m_H^2) \\
&+ \tfrac{1}{4}(\delta^{(1)}_{\rm CT} Z_{hH})^2 (p^2 - m_h^2) - \tfrac{1}{4}\delta^{(1)}_{\rm CT} Z_{hH} \delta^{(1)}_{\rm CT} Z_{Hh}(p^2 - m_H^2) - \delta^{(2)}_{\rm CT} D_{HH} - \delta^{(1)}_{\rm CT} D_{HH} \delta^{(1)}_{\rm CT} Z_{HH} \\
&- \delta^{(1)}_{\rm CT} D_{hH} \delta^{(1)}_{\rm CT} Z_{hH}\Big)\Big] .
\end{aligned}
$$

Next, we can use again the OS renormalization conditions. We denote again with $\Sigma(p^2)$ the self energies, i.e. we have

$$
\begin{aligned}
h \xrightarrow{p} \bigcirc h &= i\Sigma_{hh}(p^2) , \\
h \xrightarrow{p} \bigcirc H &= i\Sigma_{hH}(p^2) , \\
h \xrightarrow{p} \bigcirc H &= i\Sigma_{HH}(p^2) .
\end{aligned}
$$

We can now take a closer look at the mass matrix. It reads for the scalars h and H,

$$
D_{(Hh)} = R^{\rm T}_{\alpha'} \mathscr{M} R_{\alpha'} = \begin{pmatrix} m_H^2 & 0 \\ 0 & m_h^2 \end{pmatrix} + R^{\rm T}_{\alpha'} \begin{pmatrix} \frac{T_1}{v} - \frac{T_2 v_{\rm BSM}}{v^2} & \frac{T_2}{v} \\ \frac{T_2}{v} & 0 \end{pmatrix} R'_\alpha . \qquad (8.41)
$$

Now, we obtain for the counterterm of the mass matrix,

$$\delta_{\rm CT} D_{(Hh)} = \begin{pmatrix} \delta_{\rm CT} m_H^2 & 0 \\ 0 & \delta_{\rm CT} m_h^2 \end{pmatrix} + \underbrace{R_{\alpha'}^{\rm T} \begin{pmatrix} \frac{\delta_{\rm CT} T_1}{v+\delta_{\rm CT} v} - \frac{\delta_{\rm CT} T_2 (v_{\rm BSM}+\delta_{\rm CT} v_{\rm BSM})}{(v+\delta_{\rm CT} v)^2} & \frac{\delta_{\rm CT} T_2}{v+\delta_{\rm CT} v} \\ \frac{\delta_{\rm CT} T_2}{v+\delta_{\rm CT} v} & 0 \end{pmatrix} R_{\alpha'}}_{\begin{pmatrix} \delta_{\rm CT} T_{HH} & \delta_{\rm CT} T_{hH} \\ \delta_{\rm CT} T_{hH} & \delta_{\rm CT} T_{hh} \end{pmatrix}} . \tag{8.42}$$

We can now expand this expression up to second order and obtain for the tadpole counterterms, in the alignment limit ($\alpha' = -\frac{\pi}{2}$) and in the Higgs basis ($\beta' = 0$),

$$\delta_{\rm CT} T_{hh} = \left(\frac{\delta_{\rm CT}^{(1)} T_h}{v} \right) + \left(-\frac{\delta_{\rm CT}^{(1)} T_h \delta_{\rm CT}^{(1)} v}{v^2} + \frac{\delta_{\rm CT}^{(2)} T_h}{v} \right) , \tag{8.43}$$

$$\delta_{\rm CT} T_{hH} = \left(\frac{\delta_{\rm CT}^{(1)} T_H}{v} \right) + \left(-\frac{\delta_{\rm CT}^{(1)} T_H \delta_{\rm CT}^{(1)} v}{v^2} + \frac{\delta_{\rm CT}^{(2)} T_H}{v} \right) , \tag{8.44}$$

$$\delta_{\rm CT} T_{HH} = (0) . \tag{8.45}$$

Putting everything together, we obtain the following relations for the tadpole counterterms, the mass counterterms and the wave function renormalization counterterms:

$$\delta_{\rm CT}^{(1)} T_h = t_h^{(1)} , \tag{8.46}$$

$$\delta_{\rm CT}^{(2)} T_h = t_h^{(2)} - \delta_{\rm CT}^{(1)} T_h \frac{\delta_{\rm CT}^{(1)} Z_{hh}}{2} - \delta_{\rm CT}^{(1)} T_H \frac{\delta_{\rm CT}^{(1)} Z_{Hh}}{2} , \tag{8.47}$$

$$\delta_{\rm CT}^{(1)} T_H = t_H^{(1)} , \tag{8.48}$$

$$\delta_{\rm CT}^{(2)} T_H = t_H^{(2)} - \delta_{\rm CT}^{(1)} T_H \frac{\delta_{\rm CT}^{(1)} Z_{HH}}{2} - \delta_{\rm CT}^{(1)} T_h \frac{\delta_{\rm CT}^{(1)} Z_{hH}}{2} , \tag{8.49}$$

$$\delta_{\rm CT}^{(1)} m_h^2 = {\rm Re}\Sigma_{hh}^{(1)}(m_h^2) - \delta_{\rm CT}^{(1)} T_{hh} , \tag{8.50}$$

$$\delta_{\rm CT}^{(2)} m_h^2 = {\rm Re}\Sigma_{hh}^{(2)}(m_h^2) - \delta_{\rm CT}^{(2)} T_{hh} - \delta_{\rm CT}^{(1)} D_{hh} \delta_{\rm CT}^{(1)} Z_{hh} - \delta_{\rm CT}^{(1)} D_{hH} \delta_{\rm CT}^{(1)} Z_{Hh} + \frac{1}{4} (\delta_{\rm CT}^{(1)} Z_{Hh})^2 (m_h^2 - m_H^2) , \tag{8.51}$$

$$\delta_{\rm CT}^{(1)} m_H^2 = {\rm Re}\Sigma_{HH}^{(1)}(m_H^2) - \delta_{\rm CT}^{(1)} T_{HH} . \tag{8.52}$$

8.2.3 Renormalization of pseudoscalar and charge scalar sectors

The one-loop counterterms for $\delta_{\rm CT} m_A^2$, $\delta_{\rm CT} m_{H^+}^2$, and the wave function renormalization counterterms are expressed correspondingly. Similarly to the CP-even case, we have for

the pseudoscalar and charge scalar matrices,

$$\delta_{\rm CT} D_{(G^0 A)} = \begin{pmatrix} 0 & 0 \\ 0 & \delta_{\rm CT} m_A^2 \end{pmatrix} + \underbrace{R^{\rm T}_{\beta'} \begin{pmatrix} \frac{\delta_{\rm CT} T_1}{v+\delta_{\rm CT} v} - \frac{\delta_{\rm CT} T_2 (v_{\rm BSM} + \delta_{\rm CT} v_{\rm BSM})}{(v+\delta_{\rm CT} v)^2} & \frac{\delta_{\rm CT} T_2}{v+\delta_{\rm CT} v} \\ \frac{\delta_{\rm CT} T_2}{v+\delta_{\rm CT} v} & 0 \end{pmatrix} R_{\beta'}}_{\begin{pmatrix} \delta_{\rm CT} T_{G^0 G^0} & \delta_{\rm CT} T_{G^0 A} \\ \delta_{\rm CT} T_{G^0 A} & \delta_{\rm CT} T_{AA} \end{pmatrix}} \tag{8.53}$$

$$\delta_{\rm CT} D_{(G^\pm H^\pm)} = \begin{pmatrix} 0 & 0 \\ 0 & \delta_{\rm CT} m_{H^\pm}^2 \end{pmatrix} + \underbrace{R^{\rm T}_{\beta'} \begin{pmatrix} \frac{\delta_{\rm CT} T_1}{v+\delta_{\rm CT} v} - \frac{\delta_{\rm CT} T_2 (v_{\rm BSM} + \delta_{\rm CT} v_{\rm BSM})}{(v+\delta_{\rm CT} v)^2} & \frac{\delta_{\rm CT} T_2}{v+\delta_{\rm CT} v} \\ \frac{\delta_{\rm CT} T_2}{v+\delta_{\rm CT} v} & 0 \end{pmatrix} R_{\beta'}}_{\begin{pmatrix} \delta_{\rm CT} T_{G^\pm G^\pm} & \delta_{\rm CT} T_{G^\pm H^\pm} \\ \delta_{\rm CT} T_{G^\pm H^\pm} & \delta_{\rm CT} T_{H^\pm H^\pm} \end{pmatrix}} . \tag{8.54}$$

Therefore, the tadpole counterterms read

$$\delta_{\rm CT} T_{G^\pm G^\pm} = \delta_{\rm CT} T_{G^0 G^0} = \left(\frac{\delta^{(1)}_{\rm CT} T_h}{v} \right) + \left(-\frac{\delta^{(1)}_{\rm CT} T_h \delta^{(1)}_{\rm CT} v}{v^2} + \frac{\delta^{(2)}_{\rm CT} T_h}{v} \right) , \tag{8.55}$$

$$\delta_{\rm CT} T_{G^+ \pm H^\pm} = \delta_{\rm CT} T_{G^0 A} = \left(-\frac{\delta^{(1)}_{\rm CT} T_H}{v} \right) + \left(\frac{\delta^{(1)}_{\rm CT} T_H \delta^{(1)}_{\rm CT} v}{v^2} - \frac{\delta^{(2)}_{\rm CT} T_H}{v} \right) , \tag{8.56}$$

$$\delta_{\rm CT} T_{H^\pm H^\pm} = \delta_{\rm CT} T_{AA} = (0) . \tag{8.57}$$

8.2.4 Renormalization of the mixing

We define the counterterms for Λ_6 and $v_{\rm BSM}$ by demanding that they cancel the off-diagonal contributions to the mass matrices at zero external momentum. We find, that for the pseudoscalar (and charged) scalar matrix this is automatically the case, and we can therefore set $\delta_{\rm CT} v_{\rm BSM} = 0$ in our setup (this happens due to the Goldstone boson nature of G^0 and $G^\pm$).

Thus, the remaining mass matrices D with $v_{\rm BSM} = 0$ read

$$D_{G^0 A} = \begin{pmatrix} 0 & 0 \\ 0 & m_A^2 \end{pmatrix} + \begin{pmatrix} \frac{T_{\phi_{\rm SM}}}{v} & \frac{T_{\phi_{\rm BSM}}}{v} \\ \frac{T_{\phi_{\rm BSM}}}{v} & 0 \end{pmatrix} \tag{8.58}$$

$$D_{G^\pm H^\pm} = \begin{pmatrix} 0 & 0 \\ 0 & m_{H^\pm}^2 \end{pmatrix} + \begin{pmatrix} \frac{T_{\phi_{\rm SM}}}{v} & \frac{T_{\phi_{\rm BSM}}}{v} \\ \frac{T_{\phi_{\rm BSM}}}{v} & 0 \end{pmatrix} \tag{8.59}$$

$$D_{\phi_{\rm SM}\phi_{\rm BSM}} = \begin{pmatrix} m_h^2 & \Lambda_6 v^2 \\ \Lambda_6 v^2 & m_H^2 \end{pmatrix} + \begin{pmatrix} \frac{T_{\phi_{\rm SM}}}{v} & \frac{T_{\phi_{\rm BSM}}}{v} \\ \frac{T_{\phi_{\rm BSM}}}{v} & 0 \end{pmatrix} \tag{8.60}$$

Applying the replacement $\Phi_{\text{BSM}} \to -H$ and $T_2 \to -T_H$ (i.e. rotating with $-\frac{\pi}{2}$) we have

$$D_{Hh} = \begin{pmatrix} m_H^2 & -\Lambda_6 v^2 \\ -\Lambda_6 v^2 & m_h^2 \end{pmatrix} + \underbrace{\begin{pmatrix} 0 & -\frac{T_H}{v} \\ -\frac{T_H}{v} & \frac{T_h}{v} \end{pmatrix}}_{\equiv T_{Hh}} \tag{8.61}$$

Demanding now that the off-diagonal contributions to the self-energy for the CP-even scalar fields cancel, we obtain expressions that we can solve for Λ_6 and the off-diagonal $\delta_{\text{CT}} Z$. We have some redundancy here, as Λ_6 takes over the role of $\delta_{\text{CT}} Z_{Hh}$ and we can set $\delta_{\text{CT}} Z_{Hh}$ to zero. We then obtain the relations

$$\Sigma^{(1)}_{Hh}(m_h^2) = \delta^{(1)}_{\text{CT}} D_{Hh} \tag{8.62}$$

$$\Sigma^{(2)}_{Hh}(m_h^2) = \delta^{(2)}_{\text{CT}} D_{Hh} + \frac{1}{2}\delta^{(1)}_{\text{CT}} D_{hh} \delta^{(1)}_{\text{CT}} Z_{hH} + \delta^{(1)}_{\text{CT}} D_{Hh} \left(\frac{\delta^{(1)}_{\text{CT}} Z_{hh} + \delta^{(1)}_{\text{CT}} Z_{HH}}{2} \right) \tag{8.63}$$

$$\Sigma^{(1)}_{Hh}(m_H^2) = \delta^{(1)}_{\text{CT}} D_{Hh} - \frac{1}{2} m_H^2 \delta^{(1)}_{\text{CT}} Z_{hH} \tag{8.64}$$

Solving for the counterterms of $\delta\Lambda_6$, we have

$$\delta^{(1)}_{\text{CT}} \Lambda_6 = -\frac{1}{v^2} \left(\Sigma^{(1)}_{Hh}(m_h^2) - \delta^{(1)}_{\text{CT}} T_{Hh} \right) , \tag{8.65}$$

$$\begin{aligned} \delta^{(2)}_{\text{CT}} \Lambda_6 = -\frac{1}{v^2} \Bigg(& \Sigma^{(2)}_{Hh}(m_h^2) - \delta^{(2)}_{\text{CT}} T_{Hh} - (-v^2 \delta^{(1)}_{\text{CT}} \Lambda_6 + \delta^{(1)}_{\text{CT}} T_{Hh}) \left(\frac{\delta^{(1)}_{\text{CT}} Z_{hh} + \delta^{(1)}_{\text{CT}} Z_{HH}}{2} \right) \\ & - \frac{1}{2} \delta^{(1)}_{\text{CT}} D_{hh} \delta^{(1)}_{\text{CT}} Z_{hH} + 2 \delta^{(1)}_{\text{CT}} \Lambda_6 v \delta^{(1)}_{\text{CT}} v \Bigg) . \end{aligned} \tag{8.66}$$

We furthermore have

$$\begin{aligned} \delta^{(1)}_{\text{CT}} Z_{hH} &= \frac{2}{m_h^2 - m_H^2} \left(\Sigma^{(1)}_{Hh}(m_H^2) + \delta^{(1)}_{\text{CT}} \Lambda_6 v^2 - \delta^{(1)}_{\text{CT}} T_{Hh} \right) \\ &= \frac{2}{m_h^2 - m_H^2} \left(\Sigma^{(1)}_{Hh}(m_H^2) - \Sigma^{(1)}_{Hh}(m_h^2) \right) , \end{aligned} \tag{8.67}$$

$$\delta^{(1)}_{\text{CT}} Z_{G^0 A} = \frac{2}{m_Z^2 - m_H^2} \left(\Sigma^{(1)}_{G^0 A}(m_H^2) - \Sigma^{(1)}_{G^0 A}(m_Z^2) \right) \tag{8.68}$$

8.2.5 Trilinear scalar coupling renormalization

After renormalising the one- and two-point functions in detail, we can proceed to the three-point functions of the CP-even sector, i.e. the trilinear scalar couplings. We again start from the Lagrangian:

$$\mathscr{L} \supset -\frac{1}{3!}\lambda_{hhh} h^3 - \frac{1}{2!}\lambda_{hhH} h^2 H - \frac{1}{2!}\lambda_{hHH} h H^2 - \frac{1}{3!}\lambda_{HHH} H^3 . \tag{8.69}$$

As a first step, we insert counterterms for the fields and the couplings in the Lagrangian and expand up to second order to obtain the counterterms for the trilinear scalar couplings. These counterterm contributions to the three-point functions take the form:

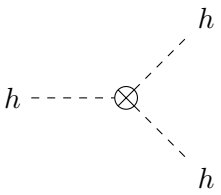

$$= -i\left[\delta^{(1)}_{\rm CT}\lambda_{hhh} + \tfrac{3}{2}(\delta^{(1)}_{\rm CT}Z_{hh}\lambda_{hhh} + \delta^{(1)}_{\rm CT}Z_{Hh}\lambda_{hhH})\right) -$$
$$i\left(\delta^{(2)}_{\rm CT}\lambda_{hhh} + \tfrac{3}{2}\delta^{(1)}_{\rm CT}\lambda_{hhh}\delta^{(1)}_{\rm CT}Z_{hh} + \tfrac{3}{2}\delta^{(1)}_{\rm CT}\lambda_{hhH}\delta^{(1)}_{\rm CT}Z_{Hh} + \tfrac{3}{8}(\delta^{(1)}_{\rm CT}Z_{hh})^2\lambda_{hhh} + \tfrac{3}{2}\delta^{(2)}_{\rm CT}Z_{hh}\lambda_{hhh}\right.$$
$$-\tfrac{3}{8}\delta^{(1)}_{\rm CT}Z_{hH}\delta^{(1)}_{\rm CT}Z_{Hh}\lambda_{hhh} + \tfrac{9}{8}\delta^{(1)}_{\rm CT}Z_{hh}\delta^{(1)}_{\rm CT}Z_{Hh}\lambda_{hhH} + \tfrac{3}{2}\delta^{(2)}_{\rm CT}Z_{Hh}\lambda_{hhH}$$
$$\left.-\tfrac{3}{8}\delta^{(1)}_{\rm CT}Z_{Hh}\delta^{(1)}_{\rm CT}Z_{HH}\lambda_{hhH} + \tfrac{3}{4}(\delta^{(1)}_{\rm CT}Z_{Hh})^2\lambda_{hHH}\right]$$

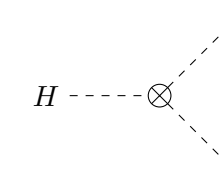

$$= -i\left[\delta^{(1)}_{\rm CT}\lambda_{hhH} + \delta^{(1)}_{\rm CT}Z_{hh}\lambda_{hhH} + \delta^{(1)}_{\rm CT}Z_{Hh}\lambda_{hHH}\right.$$
$$\left.+\tfrac{1}{2}\delta^{(1)}_{\rm CT}Z_{hH}\lambda_{hhh} + \tfrac{1}{2}\delta^{(1)}_{\rm CT}Z_{HH}\lambda_{hhH}\right) -$$
$$i\left(\delta^{(2)}_{\rm CT}\lambda_{hhH} + \tfrac{1}{2}\delta^{(1)}_{\rm CT}\lambda_{hhh}\delta^{(1)}_{\rm CT}Z_{hH} + \delta\lambda^{(1)}_{hHH}\delta^{(1)}_{\rm CT}Z_{Hh} + \delta^{(1)}_{\rm CT}\lambda_{hhH}(\delta^{(1)}_{\rm CT}Z_{hh}\right.$$
$$+\tfrac{1}{2}\delta^{(1)}_{\rm CT}Z_{HH}) + \lambda_{hhh}(\tfrac{3}{8}\delta^{(1)}_{\rm CT}Z_{hh}\delta^{(1)}_{\rm CT}Z_{hH} + \tfrac{1}{2}\delta^{(2)}_{\rm CT}Z_{hH} - \tfrac{1}{8}\delta^{(1)}_{\rm CT}Z_{hH}\delta^{(1)}_{\rm CT}Z_{HH}) + \lambda_{hhH}(\delta^{(2)}_{\rm CT}Z_{hh}$$
$$+\tfrac{1}{8}\delta^{(1)}_{\rm CT}Z_{hH}\delta^{(1)}_{\rm CT}Z_{Hh} + \tfrac{1}{2}\delta^{(1)}_{\rm CT}Z_{hh}\delta^{(1)}_{\rm CT}Z_{HH} - \tfrac{1}{8}(\delta^{(1)}_{\rm CT}Z_{HH})^2 + \tfrac{1}{2}\delta^{(2)}_{\rm CT}Z_{HH})$$
$$\left.+\lambda_{hHH}(\tfrac{1}{4}\delta^{(1)}_{\rm CT}Z_{hh}\delta^{(1)}_{\rm CT}Z_{Hh} + \delta^{(2)}_{\rm CT}Z_{Hh} + \tfrac{1}{4}\delta^{(1)}_{\rm CT}Z_{Hh}\delta^{(1)}_{\rm CT}Z_{HH}) + \tfrac{1}{4}(\delta^{(1)}_{\rm CT}Z_{Hh})^2\lambda_{HHH}\right]$$

We can now substitute the counterterms obtained in the previous sections and obtain the counterterms for the trilinear scalar couplings in terms of the input parameters of the model and their counterterms:

$$\delta\lambda_{hhh} = \left(\frac{3\delta^{(1)}_{\rm CT}m_h^2}{v} - \frac{3\delta^{(1)}_{\rm CT}vm_h^2}{v^2}\right) \tag{8.70}$$
$$+\left(-\frac{3\delta^{(1)}_{\rm CT}m_h^2\delta^{(1)}_{\rm CT}v}{v^2} + \frac{3\delta^{(2)}_{\rm CT}m_h^2}{v} + \frac{3(\delta^{(1)}_{\rm CT}v)^2m_h^2}{v^3} - \frac{3\delta^{(2)}_{\rm CT}vm_h^2}{v^2}\right),$$
$$\delta\lambda_{hhH} = \left(-3\delta^{(1)}_{\rm CT}\Lambda_6 v\right) + \left(-3\delta^{(1)}_{\rm CT}\Lambda_6\delta^{(1)}_{\rm CT}v - 3\delta\Lambda^{(2)}_6 v\right). \tag{8.71}$$

Inspecting these expressions, we find that all counterterms entering the trilinear-coupling counterterms are already fixed by the renormalisation of the one- and two-point functions, with the exception of Λ_7 and M^2_{22}. We therefore proceed to define OS renormalisation condition for the remaining parameter in order to obtain a complete set of OS counterterms.

8.2.6 Renormalization of M^2_{22}

The renormalization of M^2_{22} requires special care beyond one-loop order. As discussed in [93, 94, 343], decoupling of the heavy-scalar contributions may appear automatically at one loop when one rewrites the heavy masses in terms of a soft scale and quartic couplings. However, at two-loop order one must be more careful: parameters renormalized in different schemes enter the same expressions, and using tree-level relations between them may miss genuine two-loop effects.

Following this logic, we define the counterterm of M_{22}^2 through a decoupling-motivated renormalization condition. In our setup, M_{22}^2 plays the role of the heavy mass scale controlling the decoupling of the extra scalar states. We therefore fix the finite part of δM_{22}^2 such that the purely BSM two-loop correction to the trilinear Higgs coupling vanishes in the heavy-mass limit,

$$\delta^{(2)}\lambda_{hhh}|^{\text{BSM}} \xrightarrow[M_{22}\to\infty]{} 0, \qquad m_\Phi^2 \simeq M_{22}^2 + \lambda_\Phi v^2, \qquad (\Phi = H, A, H^\pm). \tag{8.72}$$

This condition is the analogue, in our notation, of the "on-shell" prescription introduced for the soft-breaking mass parameter in the 2HDM in order to make decoupling manifest at two loops.

In practice, the UV-divergent part of δM_{22}^2 is fixed by the standard renormalization procedure, while the finite part remains scheme-dependent. We use this freedom to impose Eq. (8.72). Expanding the two-loop BSM contribution in the heavy-mass limit and requiring the cancellation of the non-decoupling terms determines the finite part uniquely. In our case, we obtain

$$\delta_{\text{CT}}^{(1)} M_{22}^2 = \frac{3M_{22}^2}{16\pi^2}\left[\Lambda_2\left(\frac{1}{\epsilon} + 1 - \log\frac{M_{22}^2}{Q^2}\right) + \frac{2\zeta_t^2 m_t^2}{v^2}\left(\frac{1}{\epsilon} + 2 - \log\frac{M_{22}^2}{Q^2}\right)\right]. \tag{8.73}$$

Let us stress that eq. (8.73) should be understood as a finite renormalization condition for M_{22}^2, i.e. as a prescription that defines an OS-like heavy-mass parameter suited for two-loop calculations. The motivation is exactly the same as in the discussion of the soft-breaking mass: at two loops, using a one-loop relation between mass parameters in different schemes is necessary to preserve the correct decoupling behaviour and avoid spurious non-decoupling terms.

8.2.7 Renormalization of Λ_7

For the parameter Λ_7, an OS condition must be imposed in order to obtain the corresponding one-loop OS counterterm. Once the decoupling behaviour of the model has been ensured at loop level, an additional renormalization condition has to be defined. To this end, we follow the same strategy as in section 6.1.6. In that section, OS conditions were imposed on the trilinear scalar couplings λ_{hHH} and λ_{HHH} of the RxSM by requiring their renormalized one-loop values to coincide with their corresponding tree-level values. This allowed the definition of one-loop OS counterterms for the couplings κ_S and κ_{SH} of the model.

In the present case, for the 2HDM, we fix the renormalized one-loop value of the coupling λ_{HAA} to its tree-level value,

$$\hat{\lambda}_{HAA}^{(1)} \stackrel{!}{=} \lambda_{HAA}^{(0)}. \tag{8.74}$$

Expanding the renormalised one-loop result for $\lambda_{HAA}^{(1)}$, we obtain the following equation, which can be used to extract the expression of $\delta_{\text{CT}}^{(1)}\Lambda_7$,

$$\begin{aligned}&\delta_{\text{gen}}^{(1)}\lambda_{HAA} + \delta_{\text{wfr}}^{(1)}\lambda_{HAA} + \Lambda_7\delta_{\text{CT}}^{(1)}v + \delta_{\text{CT}}^{(1)}\Lambda_7 v + \delta_{\text{CT}}^{(1)}Z_{G^0A}\frac{m_H^2 - m_A^2}{v} \\ &+ \delta_{\text{CT}}^{(1)}Z_{hH}\frac{M_{22}^2 - m_A^2}{v} + \Lambda_7 v\left(\delta_{\text{CT}}^{(1)}Z_{AA} + \frac{1}{2}\delta_{\text{CT}}^{(1)}Z_{HH}\right) \stackrel{!}{=} 0,\end{aligned} \tag{8.75}$$

where $\delta^{(1)}_{\text{gen}}\lambda_{HAA}$ and $\delta^{(1)}_{\text{wfr}}\lambda_{HAA}$ are the one-loop genuine vertex and external-leg corrections to λ_{HAA} respectively. With this counterterm, the OS renormalization of the 2HDM is complete, and the two-loop corrections can be computed in the OS scheme.

8.3 Two-loop corrections to trilinear scalar couplings

Once we have defined a complete OS renormalisation scheme for the model at two-loop order, we can compute the loop corrections to the trilinear scalar couplings λ_{hhh} and λ_{hhH}. As explained earlier in section 4.4, there are two approaches to computing the corrections to the trilinear scalar couplings: the diagrammatic approach and the effective-potential approach. Since the two-loop calculations are more involved than the one-loop ones, in this chapter we follow both approaches in order to cross-check the final result.

8.3.1 Diagrammatic computation

We begin with the diagrammatic approach. This method is more involved, as one has to deal explicitly with the divergent contributions, which can make the calculation more subtle, but it is also better suited to identifying possible errors in the computation. Since all divergent terms must be handled explicitly, this approach allows one to verify the UV finiteness of the final result, which is not possible in the same way within the effective-potential approach. As explained in section 4.4, in this approach we compute the loop corrections directly to the three-point function.

At the two-loop order, $\hat{\Gamma}_{ijk}$ is obtained by summing all 1PI Feynman diagrams contributing to the ijk vertex ($\delta^{(2)}_{\text{gen}}\lambda_{ijk}$), adding the corrections to the external legs ($\delta^{(2)}_{\text{wfr}}\lambda_{ijk}$), the vertex counterterm contribution ($\delta_{\text{CT}}\lambda_{ijk}$), which we have alredy computed in the OS scheme and finally the sub-loop renormalisation term ($\delta^{(2)}_{\text{sub}}\lambda_{ijk}$) composed by all the Feynman diagrams with a one-loop topological structure but with one one-loop counterterm inserted either in the propagators or in the vertices:

$$\hat{\lambda}^{(2)}_{ijk} = -\hat{\Gamma}^{(2)}_{h_i,h_j,h_k}(0,0,0) = \lambda^{(0)}_{ijk} + \delta^{(2)}_{\text{gen}}\lambda_{ijk} + \delta^{(2)}_{\text{wfr}}\lambda_{ijk} + \delta_{\text{CT}}\lambda_{ijk} + \delta^{(2)}_{\text{sub}}\lambda_{ijk} =$$

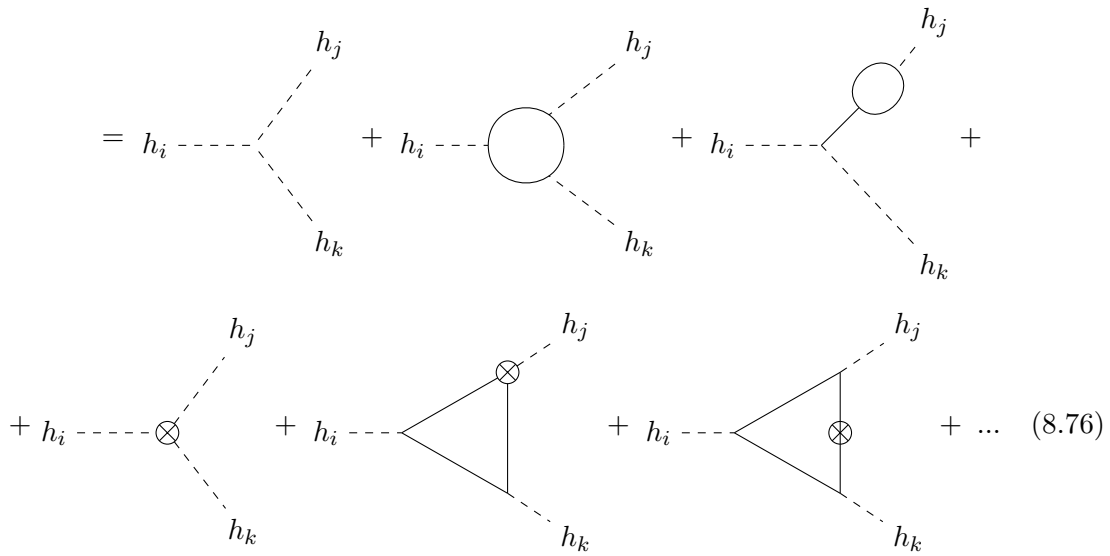

(8.76)

To compute these diagrams, we have used the tools `FeynArts 3.12` [347,348] to construct the diagrams and `FeynHelpers 2.0.0` [349] and `FeynCalc 10.1.0` [350–353] to compute

the diagrams. To define the counterterm $\delta_{\rm CT}\lambda_{ijk}$ we have followed the OS scheme defined in the section 6.1 that allow us to obtain a UV finite and renormalization scale independent result.

8.3.2 Effective potential computation

In order to compute the two-loop corrections to the trilinear scalar couplings, it is particularly convenient to work within the effective-potential framework. In this approach, the relevant CP-even trilinear couplings are obtained from derivatives of the renormalised effective potential $V_{\rm eff}$ with respect to the scalar fields, evaluated at the vacuum expectation values, which provides a compact and systematic organisation of the loop expansion.

$$\lambda_{ijk} \equiv \left.\frac{\partial^3 V_{\rm eff}}{\partial\phi_i\partial\phi_j\partial\phi_k}\right|_{\rm min} \equiv \lambda^{(0)}_{ijk} + \kappa\,\delta^{(1)}\lambda_{ijk} + \kappa^2\,\delta^{(2)}\lambda_{ijk}\,, \tag{8.77}$$

A key advantage is its practical efficiency: compared to an explicit computation of momentum-dependent three-point amplitudes, the effective potential yields the vertices in the zero-external-momentum limit with substantially reduced diagrammatic complexity. On the other hand, the method also has intrinsic limitations: since it targets the $p_i = 0$ limit, it does not directly provide the full momentum dependence of the physical vertices, and at two-loop order the expressions become algebraically involved. In this project, since we are working at the two-loop level, will expand the effective potential and cut it at the two-loop level:

$$V_{\rm eff} \equiv V^{(0)} + \kappa V^{(1)} + \kappa^2 V^{(2)}, \tag{8.78}$$

where κ is the loop factor. The term $V^{(0)}$ denotes the tree-level potential. The term $V^{(1)}$ is the one-loop contribution to the effective potential. It is obtained from the sum of all one-loop vacuum (bubble) diagrams that can be constructed in the model and can be written in the compact supertrace form [354], i.e. the Coleman–Weinberg potential [209]:

$$V^{(1)}(\phi_i) = -3\,m_t^4(\phi_i)\left(\overline{\log}\,m_t^2(\phi_i) - \frac{3}{2}\right) + \sum_{\phi_j}\frac{n_{\phi_j}\,m_{\phi_j}^4(\phi_i)}{4}\left(\overline{\log}\,m_{\phi_j}^2(\phi_i) - \frac{3}{2}\right)\,, \tag{8.79}$$

where the index i runs over the scalar fields of the model and, in the fermionic sector, we only took into account the top-quark contribution. Finally, $V^{(2)}$ denotes the two-loop contribution to the effective potential and is given by the sum of all two-loop vacuum diagrams of the model. In contrast to the one-loop case, there is no universal closed-form expression valid for arbitrary theories, and the relevant contributions must be worked out on a model-by-model basis. In the 2HDM, these diagrams can be organised into three main classes. The first class consists of diagrams with three scalar propagators and two trilinear scalar couplings; we denote their contribution by $V^{(2)}_{SSS}$ and refer to them as scalar sunrise diagrams. The second class contains diagrams with two scalar propagators and one quartic scalar coupling; we denote them by $V^{(2)}_{SS}$ and refer to them as eight-shape scalar diagrams. The third class consists of diagrams with two fermion propagators and one scalar propagator, involving two Yukawa couplings; we denote their contribution by $V^{(2)}_{FFS}$ and refer to them as fermion sunrise diagrams. The full two-loop contribution is obtained by summing these three terms:

$$V^{(2)}(\phi_i) = V^{(2)}_{SSS}(\phi_i) + V^{(2)}_{SS}(\phi_i) + V^{(2)}_{FFS}(\phi_i), \tag{8.80}$$

which diagrammatically would look like:

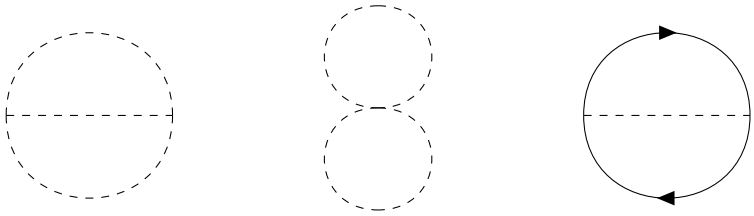

$V^{(2)}_{SSS}$ $V^{(2)}_{SS}$ $V^{(2)}_{FFS}$

We can now use the results of [355] to write general expressions, in the $\overline{\text{MS}}$ scheme, for each of these classes of diagrams. These expressions depend on the field-dependent masses and on the couplings of the particles running in the loops. Some care is required when translating the fermionic contributions, since in our work we employ Dirac fermions, whereas [355] is formulated in terms of two-component Weyl fermions. The analytic expressions for each diagram class are:

$$
\begin{aligned}
V^{(2)}_{SSS} =& \frac{-1}{12}\,(\lambda^{ijk})^2\, I\big(m_i^2, m_j^2, m_k^2\big)\,, \\
V^{(2)}_{SS} =& \frac{1}{8}\,\lambda^{iijj}\, J\big(m_i^2, m_j^2\big)\,, \\
V^{(2)}_{FFS} =& \frac{1}{2}\,|y^{IJk}|^2\,\{J\left(m_I^2, m_J^2\right) - J\left(m_I^2, m_k^2\right) - J\left(m_J^2, m_k^2\right) + \\
&+ \big(m_I^2 + m_J^2 - m_k^2\big)\, I\big(m_I^2, m_J^2, m_k^2\big)\} + \frac{1}{2}\, y^{IJk}\, y^{I'J'k}\, M^*_{II'}\, M^*_{JJ'}\, I\big(m_I^2,\, m_J^2,\, m_k^2\big)\,.
\end{aligned}
\tag{8.81}
$$

The indices i, j, k label scalar mass eigenstates, while I, J, I', J' label fermionic mass eigenstates. The quantities m_a^2 denote the corresponding field-dependent squared masses. The coupling λ^{ijk} is the trilinear scalar coupling and λ^{iijj} is the quartic scalar coupling. The Yukawa coupling y^{IJk} couples the scalar ϕ_k to the fermions $\psi_I\psi_J$ and $|y^{IJk}|^2 \equiv y^{IJk}y^*_{IJk}$. The factors $M_{II'}$ and $M_{JJ'}$ are fermion mass-insertion matrices in the fermion mass-eigenstate basis (they reduce to $M_{II'} = m_I\,\delta_{II'}$ in the absence of fermion mixing), and the asterisks denote complex conjugation. The functions $I(x, y, z)$ and $J(x, y)$ are the standard renormalised two-loop and one-loop vacuum integrals (in the $\overline{\text{MS}}$ scheme), depending only on the squared masses of the particles running in the loops. This functions are summed up in chapter B.

Which in the case of the 2HDM they are expressed as:

$$
\begin{aligned}
V^{(2)}_{SSS}(\phi) = &- \sum_{\Phi=H,A,H^\pm} \frac{n_\Phi}{4}\lambda^2_{h\Phi\Phi} I\big(0,\, m^2_\Phi(\phi),\, m^2_\Phi(\phi)\big) \\
&- \sum_{\Phi=A,H^\pm} \frac{n_\Phi}{4}\lambda^2_{H\Phi\Phi} I\big(m^2_H(\phi),\, m^2_\Phi(\phi),\, m^2_\Phi(\phi)\big) \\
&- \frac{1}{12}\lambda^2_{HHH} I\big(m^2_H(\phi),\, m^2_H(\phi),\, m^2_H(\phi)\big) - \frac{1}{2}\lambda^2_{hHA} I\big(0,\, m^2_H(\phi),\, m^2_A(\phi)\big) \\
&- \lambda^2_{hHH^\pm} I\big(0,\, m^2_H(\phi),\, m^2_{H^\pm}(\phi)\big) - \lambda^2_{hAH^\pm} I\big(0,\, m^2_A(\phi),\, m^2_{H^\pm}(\phi)\big)\,. \qquad (8.82)
\end{aligned}
$$

$$
\begin{aligned}
V^{(2)}_{SS}(\phi) \;=\; &\sum_{\Phi=H,A,H^\pm} \frac{n^2_\Phi \lambda_{\Phi\Phi\Phi\Phi}}{8} J\big(\,m^2_\Phi(\phi),\, m^2_\Phi(\phi)\big) + \frac{\lambda_{HHH^\pm H^\pm}}{2} J\big(\,m^2_H(\phi),\, m^2_{H^\pm}(\phi)\big) \\
&+ \frac{\lambda_{AAH^\pm H^\pm}}{4} J\big(\,m^2_A(\phi),\, m^2_{H^\pm}(\phi)\big) + \frac{\lambda_{AAHH}}{2} J\big(\,m^2_A(\phi),\, m^2_H(\phi)\big)\,. \qquad (8.83)
\end{aligned}
$$

$$
\begin{aligned}
V^{(2)}_{FFS}(\phi) \;=\; &-\frac{3}{2}\, y^2_{t,\mathrm{BSM}} \Big[2\, J(m^2_A(\phi))\, J(m^2_t(\phi)) + 2\, J(m^2_H(\phi))\, J(m^2_t(\phi)) \\
&+ 2\, J(m^2_{H^\pm}(\phi))\, J(m^2_t(\phi)) - 2\, J(m^2_t(\phi))^2 + I(m^2_t(\phi), m^2_t(\phi), m^2_A(\phi))\, m^2_A(\phi) \\
&+ I(m^2_t(\phi), m^2_t(\phi), m^2_H(\phi))\, m^2_H(\phi) + 2\, I(0, m^2_t(\phi), m^2_{H^\pm}(\phi))\, m^2_{H^\pm}(\phi) \\
&- 4\, I(m^2_t(\phi), m^2_t(\phi), m^2_H(\phi))\, m^2_t(\phi) - 2\, I(0, m^2_t(\phi), m^2_{H^\pm}(\phi))\, m^2_t(\phi) \Big]. \qquad (8.84)
\end{aligned}
$$

As we mentioned before, until this point all the expressions are in the $\overline{\mathrm{MS}}$ scheme and therefore we naturally have a UV finite result. If one wants to switch to the OS scheme to obtain an independent result of the renormalization scheme, we have to add a finite shift, which corresponds to the finite part of the OS counterterm obtained in section 6.1, $\delta^{\mathrm{CT,OS}}\lambda_{ijk}|_{\mathrm{fin.}}$.

8.4 Numerical results

In this section we investigate the phenomenological implications of the two-loop corrections to the couplings λ_{hhh} and λ_{hhH} and the impact of this corrections to the di-Higgs production cross section at the HL-LHC. We are going to focus in two specific scenarios:

8.4.1 Impact on λ_{ijk}

In this section, we turn to numerical examples of our two-loop results for λ_{hhh}. Specifically, we consider two different scenarios. In fig. 8.1, we fix $M = m_H = 600$ GeV and vary $m_A = m_{H^\pm}$, while in fig. 8.2, we fix $M = 600$ GeV and vary $m_H = m_A = m_{H^\pm}$. In both scenarios, we choose $\tan\beta = 2$ together with the tree-level alignment condition $\alpha = \beta - \pi/2$. The first case is taken directly from Fig. 2 of Ref. [87], whereas the second is inspired by the numerical analysis of Ref. [94]. The left (right) panels of figs. 8.1 and 8.2 show the results for κ_λ (λ_{hhH}). The black dashed line represents the leading one-loop prediction, while the red solid line denotes our new result including the leading two-loop corrections together with a full OS renormalisation. In the plots for κ_λ, the blue solid line corresponds to the result obtained using the expressions of Refs. [93, 94], where the renormalisation of α (or equivalently Λ_6) is formally performed in the $\overline{\mathrm{MS}}$ scheme.

This implies that the interpretation of α differs between the red and blue curves, and a scheme conversion in the one-loop contributions would in principle be required for a fully consistent comparison between the two results. The grey shaded regions are excluded by perturbative unitarity, for which we use the next-to-leading-order (NLO) results of Refs. [276, 277].

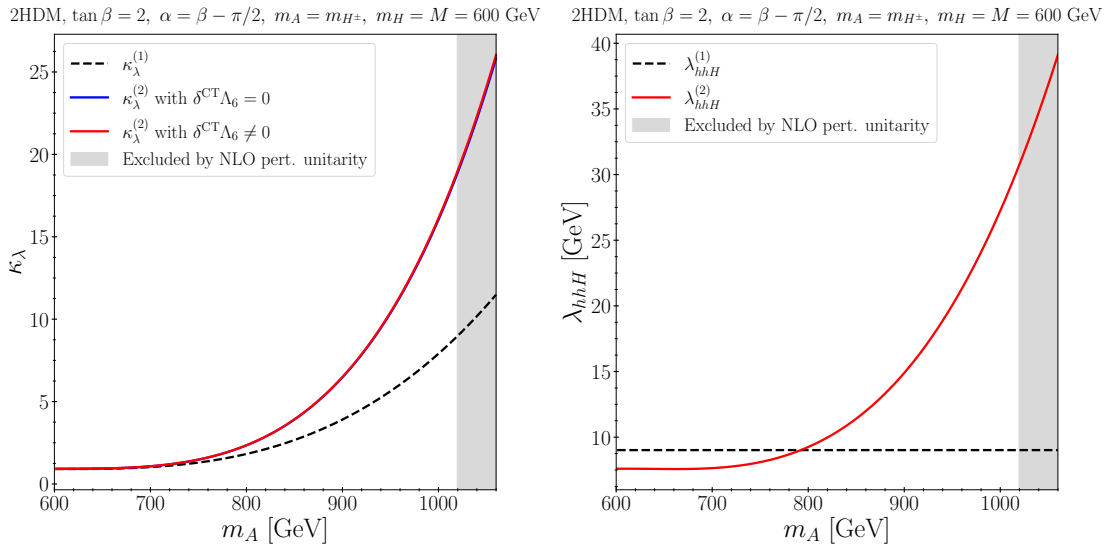

Figure 8.1: Results for κ_λ (*left*) and λ_{hhH} (*right*) in a 2HDM benchmark scenario with $M = m_H = 600$ GeV, $\tan\beta = 2$, $\alpha = \beta - \pi/2$ and varying $m_A = m_{H^\pm}$. The black lines indicate the leading one-loop results, while the red solid lines show our new predictions including the leading one- and two-loop corrections to the trilinear scalar couplings. The blue solid line in the left panel for κ_λ corresponds to the result of Refs. [93, 94], where loop-induced deviations from the alignment condition were neglected.

In the first scenario, shown in fig. 8.1, the results obtained with and without the finite part of the Λ_6 counterterm are almost indistinguishable. The small impact of the Λ_6 counterterm can be explained by the fact that its dominant contribution is proportional to $(M^2 - m_H^2)$ and therefore vanishes in this scenario. This demonstrates that, in this case, the approximation of neglecting deviations from the alignment condition at tree level is well justified, and the conclusions of Ref. [87] remain unchanged, both qualitatively and quantitatively. The two-loop results for λ_{hhH} are also particularly interesting. Indeed, setting $M = m_H$ implies that the couplings λ_{HHH}, λ_{HAA} and $\lambda_{HH^\pm H^\mp}$ all vanish at tree level, so that only the top-quark loop contributes to λ_{hhH} at one loop, while λ_{hhH} itself also vanishes at tree level. Consequently, radiative corrections to λ_{hhH} involving the BSM scalars appear only from the two-loop level onwards. For large mass splittings, $m_A - m_H \gtrsim 300$ GeV, the two-loop corrections can induce a sizeable deviation from the one-loop result. We emphasise that this does not, by itself, signal a breakdown of perturbation theory, since these two-loop effects involve couplings that are absent at one loop and therefore do not constitute a direct perturbative correction to the one-loop result. Rather, they represent a new class of contributions that first appears at the two-loop level and beyond.

Turning to the second scenario, we see from the left panel of fig. 8.2 that the effect of the finite Λ_6 counterterm is much more significant, as expected given that $M \neq m_H$. The proper OS treatment of Λ_6 (or equivalently α) leads to a reduction in the size of the

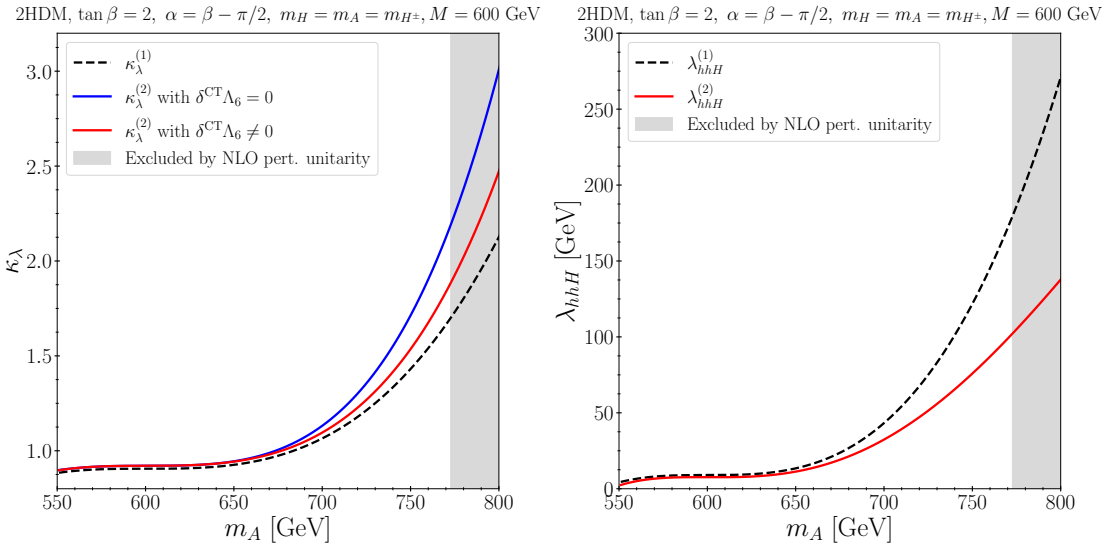

Figure 8.2: Results for κ_λ (*left*) and λ_{hhH} (*right*) in a 2HDM benchmark scenario with $M = 600$ GeV, $\tan\beta = 2$, $\alpha = \beta - \pi/2$ and varying $m_H = m_A = m_{H^\pm}$. The colour coding of the curves is the same as in fig. 8.1.

two-loop corrections to κ_λ. For λ_{hhH}, the one-loop contributions are significantly larger than in the previous scenario, since one-loop diagrams involving BSM scalars no longer vanish. The two-loop corrections to λ_{hhH} are visible, but numerically small, confirming the good perturbative convergence of the predictions.

8.4.2 Impact on di-Higgs production at the HL-LHC

In this section, we consider physical observables involving the trilinear scalar couplings λ_{hhh} and λ_{hhH}, namely the total cross sections and differential m_{hh} distributions for Higgs-pair production in the process $gg \to hh$ at the (HL-)LHC. We compute these predictions at leading order in QCD, while including the dominant BSM corrections to the trilinear scalar couplings up to two-loop order, using the public code `anyHH` [99].

We choose two benchmark points taken from the scenarios discussed in the previous section, both featuring resonances at $m_H = 600$ GeV. Specifically, we define

$$\text{BP1:} \quad M = m_H = 600 \text{ GeV},\ m_A = m_{H^\pm} = 800 \text{ GeV},\ \tan\beta = 2,\ \alpha = \beta - \frac{\pi}{2}, \quad (8.85)$$

and

$$\text{BP2:} \quad M = 400 \text{ GeV},\ m_H = m_A = m_{H^\pm} = 600 \text{ GeV},\ \tan\beta = 2,\ \alpha = \beta - \frac{\pi}{2}. \quad (8.86)$$

The differential cross sections for these two benchmark points are shown in fig. 8.3 as functions of the di-Higgs invariant mass m_{hh}. The blue dotted, yellow dashed, and red solid curves correspond to the predictions obtained with the trilinear scalar couplings computed at tree level, one-loop level, and two-loop level, respectively.

As already observed, for example, in Refs. [138, 142], the inclusion of loop corrections to the trilinear scalar couplings, *i.e.* the change from the blue dotted to the yellow dashed curves, has a dramatic impact on the m_{hh} distributions in alignment scenarios such as

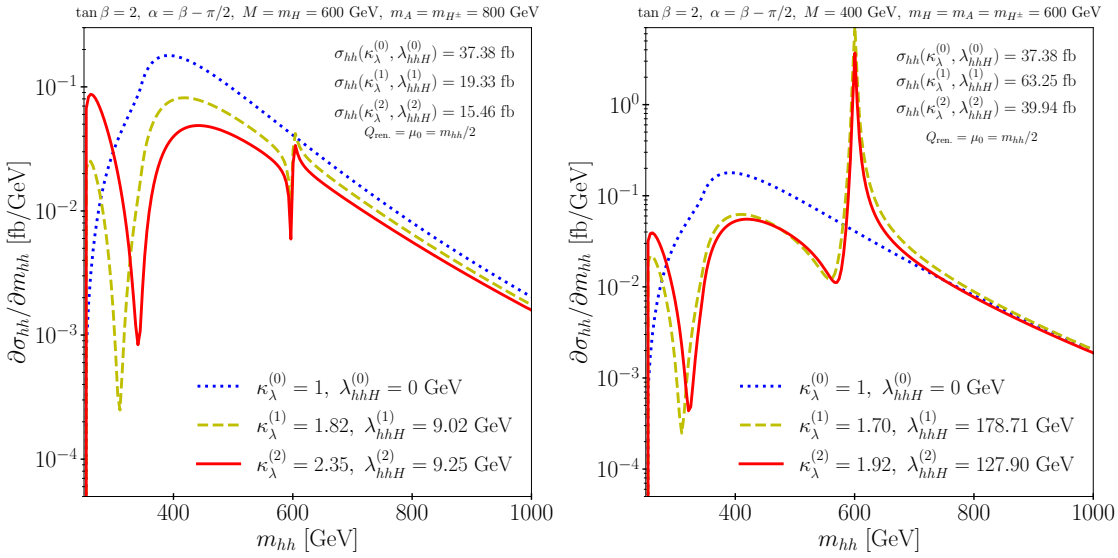

Figure 8.3: Differential cross sections for Higgs-pair production at the (HL-)LHC as a function of the di-Higgs invariant mass m_{hh}. A QCD K-factor of 1 is used, *i.e.* the results are shown at leading order in QCD only, and the PDF factorisation scale is set to $\mu_0 = m_{hh}/2$. *Left:* results for BP1 defined in eq. (8.85); *right:* results for BP2 defined in eq. (8.86). The different lines correspond to the distributions obtained with trilinear scalar couplings computed at tree level (blue dotted), one-loop level (yellow dashed), and two-loop level (red solid).

those considered here. The large BSM effects in κ_λ significantly modify the interference pattern between the box and SM-like triangle diagrams near the di-Higgs production threshold at $m_{hh} \gtrsim 250$ GeV. Furthermore, the non-zero value of λ_{hhH} generated at loop level leads to the appearance of a resonant contribution, with a dip–peak structure, around $m_{hh} = m_H$.

Including the dominant two-loop corrections to the trilinear couplings does not lead to any new qualitative change in the distributions, although the quantitative impact is clearly non-negligible. Most notably, the two-loop corrections further enhance the BSM deviation in κ_λ, leading to an additional shift in the position of the maximal destructive interference between box and triangle contributions towards larger values of m_{hh}, *i.e.* away from threshold. The impact of the two-loop effects on the resonance is less pronounced, especially for BP1, although in BP2 the width and height of the peak are affected by the $\sim 10\%$ increase in λ_{hhH}.

The effect of the two-loop corrections to λ_{hhh} and λ_{hhH} on the total cross sections is of the order of -20% for BP1 and $+14\%$ for BP2. This can be understood from the interplay between the reduction caused by the change in the interference pattern[1] near threshold — which is most pronounced for BP1 — and the effect on the resonant peak — which is largest for BP2. Overall, these results again indicate the perturbative convergence of the calculation, while at the same time demonstrating the importance of including higher-order corrections to the trilinear scalar couplings in precision predictions for Higgs-pair production.

[1]We recall in this context that the minimum of the di-Higgs cross-section prediction with floating κ_λ occurs around $\kappa_\lambda \sim 2$–2.5 [100].

Chapter 9

Conclusions

Tú puedes ofrecer mucho más que eso.

– Ama

The aim of this thesis has been to investigate how extended Higgs sectors can address open questions in particle physics and cosmology, and how these scenarios can be tested through a combined analysis of collider observables, loop corrections, and the thermal history of the early Universe. In particular, the thesis has focused on the scalar potential as the common origin of several key phenomena: Higgs self-interactions, di-Higgs production, the dynamics of the electroweak phase transition, and the generation of stochastic gravitational-wave signals. From this perspective, the central question has been not only whether simple scalar extensions of the SM can realise these effects, but also how reliably they can be studied once higher-order corrections and the full collider dynamics are taken into account.

A first central objective of the thesis was to determine to what extent di-Higgs production can probe the structure of the scalar potential in a simple beyond-the-Standard-Model scenario such as the RxSM, and in particular whether simplified resonant descriptions, where only the s-channel contribution of a BSM Higgs state is taken into account, are sufficient for this purpose as is currently being used by ATLAS and CMS. The analysis carried out in the phenomenological part of the thesis shows that this is in general not the case. In the RxSM, the full di-Higgs production cross section receives contributions not only from resonant heavy-Higgs exchange, but also from non-resonant diagrams and their interference with the resonant part. As a result, restricting the analysis to the resonant contribution alone can lead to an incomplete and in some cases misleading interpretation of the sensitivity to BSM trilinear scalar couplings such as λ_{hhH}. One of the main conclusions of this work is therefore that a reliable extraction of information on the scalar potential from Higgs-pair production requires the complete calculation of the process, rather than a simplified treatment based solely on the resonant topology. This conclusion applies both to the HL-LHC and to future lepton-colliders, where the interplay between different contributions remains phenomenologically important.

A second major objective was to understand how important loop corrections to trilinear scalar couplings can be in extended Higgs sectors, and how these corrections impact collider observables. The one-loop study of the RxSM performed in this thesis shows that

such corrections can indeed be sizeable and can have a substantial effect on the values of the trilinear scalar couplings relevant for di-Higgs production. To address this question consistently, for the first time a fully on-shell renormalisation scheme was constructed for the model, allowing renormalisation-scale-independent predictions for the loop-corrected trilinear couplings. This constitutes one of the original technical results of the thesis. The resulting analysis demonstrates that the impact of one-loop corrections is not merely a small quantitative refinement of the tree-level picture, but can instead modify the predicted di-Higgs cross sections in a phenomenologically relevant way. This is particularly relevant in extended Higgs sectors, where large mass splittings and non-decoupling effects can generate large radiative corrections. In this sense, the thesis answers one of its central motivating questions by concluding that higher-order corrections are indispensable for a realistic interpretation of Higgs self-interactions in BSM scalar theories in.

A third objective of the thesis was to investigate whether parts of the parameter space that modify di-Higgs production can also give rise to a strong first-order electroweak phase transition, and thus provide a possible route towards explaining the baryon asymmetry of the Universe through electroweak baryogenesis. In the RxSM, this question was addressed through a dedicated study of the one-loop finite-temperature effective potential implemented in `BSMPT`. The analysis of the thermal history of the model shows that the RxSM admits a variety of cosmological evolutions, in which a strong first-order electroweak phase transition can indeed be realised. This answers one of the main cosmological questions posed in the thesis: simple Higgs-sector extensions such as the general real singlet model are capable of producing the type of electroweak transition required by the third Sakharov condition, at least at the level of the phase-transition dynamics studied here.

Closely connected to this, the thesis aimed to explore the complementarity between collider probes and early-Universe observables. One of the main goals was to analyse, within the RxSM, the gravitational-wave signal from the phase transition simultaneously with the collider signatures at the HL-LHC and future e^+e^- colliders, while using the full di-Higgs cross sections and including the relevant one-loop corrections to the trilinear scalar couplings. The results of the thesis show that this combined strategy is indeed necessary. No single observable is sufficient to cover the full physically viable parameter space once collider constraints, loop effects, and thermal-history requirements are imposed. Instead, the interplay between di-Higgs phenomenology, electroweak phase-transition dynamics, and gravitational-wave production provides a much more complete picture of the model. The thesis therefore demonstrates in a concrete way that collider and cosmological probes are genuinely complementary tools for testing extended scalar sectors.

Another important objective was to push the analysis of Higgs self-interactions to a higher level of perturbative precision by considering two-loop corrections in the CP-conserving 2HDM. In this part of the thesis, the focus was placed on the trilinear couplings λ_{hhh} and λ_{hhH} in the alignment limit, together with the non-trivial problem of consistently renormalising the parameter that controls the departure from exact alignment. The work carried out here shows that this issue is subtle and that a correct on-shell treatment is required in order to define the alignment limit in a physically meaningful way. This provides a necessary conceptual and technical basis for any precision study of Higgs self-couplings in the 2HDM beyond one loop.

A further question addressed in this context was whether the two-loop calculation is robust. The thesis answers this by performing the calculation simultaneously in the

diagrammatic and effective-potential approaches and cross-checking both results. Their agreement in the appropriate zero-momentum limit provides a non-trivial cross-check of the result and supports the consistency of the renormalisation framework developed in the chapter. This is an important conclusion in its own right, since at this level of perturbative complexity technical consistency checks become essential. The two-loop part of the thesis therefore does not merely extend the calculation to higher order, but also strengthens confidence in the theoretical control over the resulting predictions.

Taken together, the different parts of the thesis support a coherent overall picture. Extended Higgs sectors can simultaneously modify collider observables and alter the thermal history of the Universe in a way that is directly tied to the structure of the scalar potential. Trilinear Higgs couplings occupy a central role in this connection: they affect di-Higgs production at colliders, receive large and sometimes non-decoupling radiative corrections, and are closely linked to the dynamics of the electroweak phase transition. The results obtained here show that a meaningful exploration of this physics requires going beyond simplified treatments on several fronts: beyond resonant approximations in collider phenomenology, beyond tree level in the scalar couplings, and beyond a purely collider-based perspective when assessing the viability of a model.

There are several natural directions for future work. A particularly interesting next step would be to perform a more systematic assessment of the theoretical uncertainties affecting the calculation of the finite-temperature effective potential, the prediction of the strong first-order electroweak phase transition, and the resulting gravitational-wave signal. In this context, methods based on dimensional reduction provide a promising framework to improve the theoretical control over the phase-transition analysis and to reduce the ambiguities inherent in purely perturbative four-dimensional treatments. Another especially interesting direction would be to generalise the analysis to models with explicit or spontaneous CP violation, where the possibility of generating the baryon asymmetry can be addressed more completely. This would open the way to search for regions of parameter space in which collider signatures, gravitational-wave observables, a strong first-order electroweak phase transition, and sufficient CP-violating sources can all be realised simultaneously, thereby moving from the study of favourable phase-transition dynamics to a genuinely complete explanation of electroweak baryogenesis.

In conclusion, this thesis has shown that extended Higgs sectors provide a well-motivated and phenomenologically rich framework in which collider physics and cosmology become deeply interconnected. Within this framework, the RxSM and the 2HDM serve as complementary case studies. The former illustrates how a minimal extension of the scalar sector can simultaneously affect Higgs-pair production and realise a strong first-order electroweak phase transition, while the latter provides a setting in which the precision study of Higgs self-couplings can be pushed to the two-loop level. The overall result is a coherent and quantitative picture in which the Higgs sector emerges as a sensitive probe of physics beyond the Standard Model, both through present and future collider experiments and through relic signatures from the early Universe.

Appendix A

Summary of counterterms for the OS renormalisation of the RxSM

For convenience, we summarise in this appendix the set of expressions for counterterms in our OS renormalisation scheme for the RxSM, which were discussed and derived in section 6.1.

Beginning with one-point functions, we have for the tadpole counterterms,

$$\begin{aligned}\delta^{(1)}_{\mathrm{CT}} t_\phi &= \sin\alpha\ \delta^{(1)} t_H - \cos\alpha\ \delta^{(1)} t_h\,,\\ \delta^{(1)}_{\mathrm{CT}} t_S &= -\cos\alpha\ \delta^{(1)} t_H - \sin\alpha\ \delta^{(1)} t_h\,.\end{aligned} \tag{A.1}$$

Turning next to renormalisation conditions derived from two-point functions, the OS counterterms for the scalar masses and mixing angle are

$$\begin{aligned}\delta^{(1)}_{\mathrm{CT}} m_h^2 &= \mathrm{Re}[\Sigma_{hh}(m_h^2)],\\ \delta^{(1)}_{\mathrm{CT}} m_H^2 &= \mathrm{Re}[\Sigma_{HH}(m_H^2)]\,,\\ \delta^{(1)}_{\mathrm{CT}} \alpha &= \frac{\mathrm{Re}[\Sigma_{hH}(m_h^2) + \Sigma_{hH}(m_H^2)]}{2(m_H^2 - m_h^2)}\,.\end{aligned} \tag{A.2}$$

Additionally, the scalar field renormalisation constants are

$$\begin{aligned}\delta^{(1)}_{\mathrm{CT}} Z_{hh} &= -\mathrm{Re}\left[\frac{\partial\Sigma_{hh}(p^2)}{\partial p^2}\right]_{p^2=m_h^2}\,,\\ \delta^{(1)}_{\mathrm{CT}} Z_{HH} &= -\mathrm{Re}\left[\frac{\partial\Sigma_{HH}(p^2)}{\partial p^2}\right]_{p^2=m_H^2}\,,\\ \delta^{(1)}_{\mathrm{CT}} Z_{hH} &= \frac{\mathrm{Re}[\Sigma_{hH}(m_H^2)]}{m_h^2 - m_H^2}\,,\\ \delta^{(1)}_{\mathrm{CT}} Z_{Hh} &= \frac{\mathrm{Re}[\Sigma_{Hh}(m_h^2)]}{m_H^2 - m_h^2}\end{aligned} \tag{A.3}$$

The EW and singlet VEV counterterms are given by

$$\frac{\delta^{(1)}_{\text{CT}} v}{v} = \frac{1}{2} \left[\frac{s_W^2 - c_W^2}{s_W^2} \frac{\text{Re}\big[\Sigma^T_{WW}(m_W^2)\big]}{m_W^2} + \frac{c_W^2}{s_W^2} \frac{\text{Re}\big[\Sigma^T_{ZZ}(m_Z^2)\big]}{m_Z^2} - \Pi_{\gamma\gamma}(0) - \frac{2 s_W}{c_W} \frac{\Sigma^T_{\gamma Z}(0)}{m_Z^2} \right],$$
$$\delta^{(1)}_{\text{CT}} v_S = 0\,, \tag{A.4}$$

We note that the counterterm for v_S is the only counterterm in our scheme that is technically not an OS counterterm.

Finally, the OS counterterms for the Lagrangian trilinear couplings, κ_S and κ_{SH}, which we determined from conditions on three-point functions, read

$$\delta^{(1)}_{\text{CT}} \kappa_S = \frac{\frac{\partial \lambda^{(0)}_{HHH}}{\partial \kappa_{SH}} (\delta^{(1)}_{\text{gen.+wfr}} \lambda_{hHH} + \sum_x \delta^{(1)}_{\text{CT}x} \lambda_{hHH}) - \frac{\partial \lambda^{(0)}_{hHH}}{\partial \kappa_{SH}} (\delta^{(1)}_{\text{gen.+wfr}} \lambda_{HHH} + \sum_x \delta^{(1)}_{\text{CT}x} \lambda_{HHH})}{\frac{\partial \lambda^{(0)}_{hHH}}{\partial \kappa_{SH}} \frac{\partial \lambda^{(0)}_{HHH}}{\partial \kappa_S} - \frac{\partial \lambda^{(0)}_{hHH}}{\partial \kappa_S} \frac{\partial \lambda^{(0)}_{HHH}}{\partial \kappa_{SH}}},$$
$$\delta^{(1)}_{\text{CT}} \kappa_{SH} = \frac{\frac{\partial \lambda^{(0)}_{hHH}}{\partial \kappa_S} (\delta^{(1)}_{\text{gen.+wfr}} \lambda_{HHH} + \sum_x \delta^{(1)}_{\text{CT}x} \lambda_{HHH}) - \frac{\partial \lambda^{(0)}_{HHH}}{\partial \kappa_S} (\delta^{(1)}_{\text{gen.+wfr}} \lambda_{hHH} + \sum_x \delta^{(1)}_{\text{CT}x} \lambda_{hHH})}{\frac{\partial \lambda^{(0)}_{hHH}}{\partial \kappa_{SH}} \frac{\partial \lambda^{(0)}_{HHH}}{\partial \kappa_S} - \frac{\partial \lambda^{(0)}_{hHH}}{\partial \kappa_S} \frac{\partial \lambda^{(0)}_{HHH}}{\partial \kappa_{SH}}}. \tag{A.5}$$

Appendix B

Loop functions

In this appendix we summarize the loop functions used for the effective-potential computations in Chapter 8, obtained from [355].

$$\overline{\ln}x = \ln\left(\frac{x}{Q^2}\right), \tag{B.1}$$

$$J(x) = x\big(\overline{\ln}x - 1\big), \tag{B.2}$$

$$J(x,y) = x\,y\big(\overline{\ln}x - 1\big)\big(\overline{\ln}y - 1\big), \tag{B.3}$$

$$\begin{aligned} I(x,y,z) = {} & \frac{1}{2}(x-y-z)\,\overline{\ln}y\,\overline{\ln}z + \frac{1}{2}(y-x-z)\,\overline{\ln}x\,\overline{\ln}z + \frac{1}{2}(z-x-y)\,\overline{\ln}x\,\overline{\ln}y \\ & + 2x\,\overline{\ln}x + 2y\,\overline{\ln}y + 2z\,\overline{\ln}z - \frac{5}{2}(x+y+z) - \frac{1}{2}\,\xi(x,y,z)\,. \end{aligned} \tag{B.4}$$

Here $\xi(x,y,z)$ was originally found in terms of Lobachevskiy's function or related integrals in [356] using methods developed in [357–359], but it can also be expressed in terms of dilogarithms according to [360–363] (for $x, y \le z$):

$$\begin{aligned} \xi(x,y,z) = R\Bigg\{ & 2\ln\left(\frac{z+x-y-R}{2z}\right)\ln\left(\frac{z+y-x-R}{2z}\right) - \ln\left(\frac{x}{z}\right)\ln\left(\frac{y}{z}\right) \\ & - 2\,\mathrm{Li}_2\left(\frac{z+x-y-R}{2z}\right) - 2\,\mathrm{Li}_2\left(\frac{z+y-x-R}{2z}\right) + \frac{\pi^2}{3}\Bigg\}, \end{aligned} \tag{B.5}$$

$$R = \big(x^2+y^2+z^2-2xy-2xz-2yz\big)^{1/2}. \tag{B.6}$$

$$\begin{aligned} I(0,x,y) = {} & (x-y)\left[\mathrm{Li}_2\left(\frac{y}{x}\right) - \ln\left(\frac{x}{y}\right)\overline{\ln}(x-y) + \frac{1}{2}\big(\overline{\ln}x\big)^2 - \frac{\pi^2}{6}\right] - \frac{5}{2}(x+y) + \\ & + 2x\,\overline{\ln}x + 2y\,\overline{\ln}y - \overline{\ln}x\,\overline{\ln}y\,, \end{aligned} \tag{B.7}$$

$$I(0,x,x) = 2J(x) - 2x - \frac{1}{x}J(x,x) = -x\big(\overline{\ln}x\big)^2 + 4x\,\overline{\ln}x - 5x\,, \tag{B.8}$$

$$I(0,0,x) = -\frac{1}{2}x\big(\overline{\ln}x\big)^2 + 2x\,\overline{\ln}x - \frac{5}{2}x - \frac{\pi^2}{6}x\,. \tag{B.9}$$

Bibliography

[1] Georges Aad et al. Observation of a new particle in the search for the Standard Model Higgs boson with the ATLAS detector at the LHC. *Phys. Lett. B*, 716:1–29, 2012.

[2] Serguei Chatrchyan et al. Observation of a New Boson at a Mass of 125 GeV with the CMS Experiment at the LHC. *Phys. Lett. B*, 716:30–61, 2012.

[3] Georges Aad et al. Measurements of the Higgs boson production and decay rates and constraints on its couplings from a combined ATLAS and CMS analysis of the LHC pp collision data at $\sqrt{s} = 7$ and 8 TeV. *JHEP*, 08:045, 2016.

[4] F. Englert and R. Brout. Broken Symmetry and the Mass of Gauge Vector Mesons. *Phys. Rev. Lett.*, 13:321–323, 1964.

[5] Peter W. Higgs. Broken Symmetries and the Masses of Gauge Bosons. *Phys. Rev. Lett.*, 13:508–509, 1964.

[6] G. S. Guralnik, C. R. Hagen, and T. W. B. Kibble. Global Conservation Laws and Massless Particles. *Phys. Rev. Lett.*, 13:585–587, 1964.

[7] Peter W. Higgs. Broken symmetries, massless particles and gauge fields. *Phys. Lett.*, 12:132–133, 1964.

[8] T. W. B. Kibble. Symmetry breaking in nonAbelian gauge theories. *Phys. Rev.*, 155:1554–1561, 1967.

[9] Georges Aad et al. Combination of Searches for Higgs Boson Pair Production in pp Collisions at s=13 TeV with the ATLAS Detector. *Phys. Rev. Lett.*, 133(10):101801, 2024.

[10] Aram Hayrapetyan et al. Constraints on the Higgs boson self-coupling from the combination of single and double Higgs boson production in proton-proton collisions at s=13TeV. *Phys. Lett. B*, 861:139210, 2025.

[11] Study of Higgs boson pair production in the $HH \to bb\gamma\gamma$ final state with 308 fb^{-1} of data collected at $\sqrt{s} = 13$ TeV and 13.6 TeV by the ATLAS experiment. 2025.

[12] Georges Aad et al. Constraints on the Higgs boson self-coupling from single- and double-Higgs production with the ATLAS detector using pp collisions at s=13 TeV. *Phys. Lett. B*, 843:137745, 2023.

[13] Constraining the Higgs boson self-coupling from single- and double-Higgs production with the ATLAS detector using *pp* collisions at $\sqrt{s} = 13$ TeV. 2022.

[14] Armen Tumasyan et al. A portrait of the Higgs boson by the CMS experiment ten years after the discovery. *Nature*, 607(7917):60–68, 2022. [Erratum: Nature 623, (2023)].

[15] A. D. Sakharov. Violation of CP Invariance, C asymmetry, and baryon asymmetry of the universe. *Pisma Zh. Eksp. Teor. Fiz.*, 5:32–35, 1967.

[16] V. A. Kuzmin, V. A. Rubakov, and M. E. Shaposhnikov. On the Anomalous Electroweak Baryon Number Nonconservation in the Early Universe. *Phys. Lett. B*, 155:36, 1985.

[17] Andrew G. Cohen, D. B. Kaplan, and A. E. Nelson. Progress in electroweak baryogenesis. *Ann. Rev. Nucl. Part. Sci.*, 43:27–70, 1993.

[18] Antonio Riotto and Mark Trodden. Recent progress in baryogenesis. *Ann. Rev. Nucl. Part. Sci.*, 49:35–75, 1999.

[19] Mark Trodden. Electroweak baryogenesis. *Rev. Mod. Phys.*, 71:1463–1500, 1999.

[20] Michael Dine and Alexander Kusenko. The Origin of the matter - antimatter asymmetry. *Rev. Mod. Phys.*, 76:1, 2003.

[21] David E. Morrissey and Michael J. Ramsey-Musolf. Electroweak baryogenesis. *New J. Phys.*, 14:125003, 2012.

[22] Laurent Canetti, Marco Drewes, and Mikhail Shaposhnikov. Matter and Antimatter in the Universe. *New J. Phys.*, 14:095012, 2012.

[23] Michael J. Ramsey-Musolf. The electroweak phase transition: a collider target. *JHEP*, 09:179, 2020.

[24] Gianfranco Bertone, Dan Hooper, and Joseph Silk. Particle dark matter: Evidence, candidates and constraints. *Phys. Rept.*, 405:279–390, 2005.

[25] Jonathan L. Feng. Dark Matter Candidates from Particle Physics and Methods of Detection. *Ann. Rev. Astron. Astrophys.*, 48:495–545, 2010.

[26] Giorgio Arcadi, Maíra Dutra, Pradipta Ghosh, Manfred Lindner, Yann Mambrini, Mathias Pierre, Stefano Profumo, and Farinaldo S. Queiroz. The waning of the WIMP? A review of models, searches, and constraints. *Eur. Phys. J. C*, 78(3):203, 2018.

[27] Leszek Roszkowski, Enrico Maria Sessolo, and Sebastian Trojanowski. WIMP dark matter candidates and searches—current status and future prospects. *Rept. Prog. Phys.*, 81(6):066201, 2018.

[28] Peter Minkowski. $\mu \to e\gamma$ at a Rate of One Out of 10^9 Muon Decays? *Phys. Lett. B*, 67:421–428, 1977.

[29] Tsutomu Yanagida. Horizontal gauge symmetry and masses of neutrinos. *Conf. Proc. C*, 7902131:95–99, 1979.

[30] Murray Gell-Mann, Pierre Ramond, and Richard Slansky. Complex Spinors and Unified Theories. *Conf. Proc. C*, 790927:315–321, 1979.

[31] Rabindra N. Mohapatra and Goran Senjanovic. Neutrino Mass and Spontaneous Parity Nonconservation. *Phys. Rev. Lett.*, 44:912, 1980.

[32] J. Schechter and J. W. F. Valle. Neutrino Masses in SU(2) x U(1) Theories. *Phys. Rev. D*, 22:2227, 1980.

[33] R. N. Mohapatra et al. Theory of Neutrinos: A White Paper. *Rept. Prog. Phys.*, 70:1757–1867, 2007.

[34] Alessandro Strumia and Francesco Vissani. Neutrino masses and mixings and... 6 2006.

[35] J. R. Espinosa and M. Quiros. The Electroweak phase transition with a singlet. *Phys. Lett. B*, 305:98–105, 1993.

[36] S. W. Ham, Y. S. Jeong, and S. K. Oh. Electroweak phase transition in an extension of the standard model with a real Higgs singlet. *J. Phys. G*, 31(8):857–871, 2005.

[37] Stefano Profumo, Michael J. Ramsey-Musolf, and Gabe Shaughnessy. Singlet Higgs phenomenology and the electroweak phase transition. *JHEP*, 08:010, 2007.

[38] Jose Ramon Espinosa and Mariano Quiros. Novel Effects in Electroweak Breaking from a Hidden Sector. *Phys. Rev. D*, 76:076004, 2007.

[39] Vernon Barger, Paul Langacker, Mathew McCaskey, Michael Ramsey-Musolf, and Gabe Shaughnessy. Complex Singlet Extension of the Standard Model. *Phys. Rev. D*, 79:015018, 2009.

[40] Jose R. Espinosa, Thomas Konstandin, and Francesco Riva. Strong Electroweak Phase Transitions in the Standard Model with a Singlet. *Nucl. Phys. B*, 854:592–630, 2012.

[41] David Curtin, Patrick Meade, and Chiu-Tien Yu. Testing Electroweak Baryogenesis with Future Colliders. *JHEP*, 11:127, 2014.

[42] Gowri Kurup and Maxim Perelstein. Dynamics of Electroweak Phase Transition In Singlet-Scalar Extension of the Standard Model. *Phys. Rev. D*, 96(1):015036, 2017.

[43] Edward Witten. Cosmic Separation of Phases. *Phys. Rev. D*, 30:272–285, 1984.

[44] C. J. Hogan. Gravitational radiation from cosmological phase transitions. *Mon. Not. Roy. Astron. Soc.*, 218:629–636, 1986.

[45] Marc Kamionkowski, Arthur Kosowsky, and Michael S. Turner. Gravitational radiation from first order phase transitions. *Phys. Rev. D*, 49:2837–2851, 1994.

[46] Chiara Caprini et al. Science with the space-based interferometer eLISA. II: Gravitational waves from cosmological phase transitions. *JCAP*, 04:001, 2016.

[47] David J. Weir. Gravitational waves from a first order electroweak phase transition: a brief review. *Phil. Trans. Roy. Soc. Lond. A*, 376(2114):20170126, 2018. [Erratum: Phil.Trans.Roy.Soc.Lond.A 381, 20230212 (2023)].

[48] Chiara Caprini et al. Detecting gravitational waves from cosmological phase transitions with LISA: an update. *JCAP*, 03:024, 2020.

[49] K. Kajantie, M. Laine, K. Rummukainen, and Mikhail E. Shaposhnikov. Is there a hot electroweak phase transition at $m_H \gtrsim m_W$? *Phys. Rev. Lett.*, 77:2887–2890, 1996.

[50] Christophe Grojean, Geraldine Servant, and James D. Wells. First-order electroweak phase transition in the standard model with a low cutoff. *Phys. Rev. D*, 71:036001, 2005.

[51] Shinya Kanemura, Yasuhiro Okada, and Eibun Senaha. Electroweak baryogenesis and quantum corrections to the triple Higgs boson coupling. *Phys. Lett. B*, 606:361–366, 2005.

[52] Mitsuru Kakizaki, Shinya Kanemura, and Toshinori Matsui. Gravitational waves as a probe of extended scalar sectors with the first order electroweak phase transition. *Phys. Rev. D*, 92(11):115007, 2015.

[53] Katsuya Hashino, Mitsuru Kakizaki, Shinya Kanemura, and Toshinori Matsui. Synergy between measurements of gravitational waves and the triple-Higgs coupling in probing the first-order electroweak phase transition. *Phys. Rev. D*, 94(1):015005, 2016.

[54] Katsuya Hashino, Mitsuru Kakizaki, Shinya Kanemura, Pyungwon Ko, and Toshinori Matsui. Gravitational waves and Higgs boson couplings for exploring first order phase transition in the model with a singlet scalar field. *Phys. Lett. B*, 766:49–54, 2017.

[55] Philipp Basler, Margarete Mühlleitner, and Jonas Wittbrodt. The CP-Violating 2HDM in Light of a Strong First Order Electroweak Phase Transition and Implications for Higgs Pair Production. *JHEP*, 03:061, 2018.

[56] Thomas Biekötter, Sven Heinemeyer, José Miguel No, María Olalla Olea-Romacho, and Georg Weiglein. The trap in the early Universe: impact on the interplay between gravitational waves and LHC physics in the 2HDM. *JCAP*, 03:031, 2023.

[57] Pedro Bittar, Subhojit Roy, and Carlos E. M. Wagner. Self consistent thermal resummation: a case study of the phase transition in 2HDM. *JHEP*, 12:021, 2025.

[58] J. de Blas et al. Higgs Boson Studies at Future Particle Colliders. *JHEP*, 01:139, 2020.

[59] J. Alison et al. Higgs boson potential at colliders: Status and perspectives. *Rev. Phys.*, 5:100045, 2020.

[60] Tim Barklow, Keisuke Fujii, Sunghoon Jung, Michael E. Peskin, and Junping Tian. Model-Independent Determination of the Triple Higgs Coupling at e+e- Colliders. *Phys. Rev. D*, 97(5):053004, 2018.

[61] H. Abramowicz et al. A Linear Collider Vision for the Future of Particle Physics. 3 2025.

[62] J. Altmann et al. *ECFA Higgs, electroweak, and top Factory Study*, volume 5/2025 of *CERN Yellow Reports: Monographs*. 6 2025.

[63] Georges Aad et al. Highlights of the HL-LHC physics projections by ATLAS and CMS. 4 2025.

[64] F. Arco, S. Heinemeyer, M. Mühlleitner, and K. Radchenko. Sensitivity to triple Higgs couplings via di-Higgs production in the 2HDM at the (HL-)LHC. *Eur. Phys. J. C*, 83(11):1019, 2023.

[65] F. Arco, S. Heinemeyer, and M. J. Herrero. Sensitivity to triple Higgs couplings via di-Higgs production in the 2HDM at e^+e^- colliders. *Eur. Phys. J. C*, 81(10):913, 2021.

[66] F. Arco, S. Heinemeyer, and M. J. Herrero. Triple Higgs couplings in the 2HDM: the complete picture. *Eur. Phys. J. C*, 82(6):536, 2022.

[67] A. Djouadi, W. Kilian, M. Muhlleitner, and P. M. Zerwas. Production of neutral Higgs boson pairs at LHC. *Eur. Phys. J. C*, 10:45–49, 1999.

[68] Philipp Basler, Margarete Mühlleitner, and Jonas Müller. Electroweak Phase Transition in Non-Minimal Higgs Sectors. *JHEP*, 05:016, 2020.

[69] Hamza Abouabid, Abdesslam Arhrib, Duarte Azevedo, Jaouad El Falaki, Pedro. M. Ferreira, Margarete Mühlleitner, and Rui Santos. Benchmarking di-Higgs production in various extended Higgs sector models. *JHEP*, 09:011, 2022.

[70] John F. Gunion and Howard E. Haber. The CP conserving two Higgs doublet model: The Approach to the decoupling limit. *Phys. Rev. D*, 67:075019, 2003.

[71] Shinya Kanemura, Shingo Kiyoura, Yasuhiro Okada, Eibun Senaha, and C. P. Yuan. New physics effect on the Higgs selfcoupling. *Phys. Lett. B*, 558:157–164, 2003.

[72] Shinya Kanemura, Yasuhiro Okada, Eibun Senaha, and C. P. Yuan. Higgs coupling constants as a probe of new physics. *Phys. Rev. D*, 70:115002, 2004.

[73] Mayumi Aoki, Shinya Kanemura, Mariko Kikuchi, and Kei Yagyu. Radiative corrections to the Higgs boson couplings in the triplet model. *Phys. Rev. D*, 87(1):015012, 2013.

[74] Shinya Kanemura, Mariko Kikuchi, and Kei Yagyu. Radiative corrections to the Higgs boson couplings in the model with an additional real singlet scalar field. *Nucl. Phys. B*, 907:286–322, 2016.

[75] Shinya Kanemura, Mariko Kikuchi, and Kei Yagyu. Fingerprinting the extended Higgs sector using one-loop corrected Higgs boson couplings and future precision measurements. *Nucl. Phys. B*, 896:80–137, 2015.

[76] Abdesslam Arhrib, Rachid Benbrik, Jaouad El Falaki, and Adil Jueid. Radiative corrections to the Triple Higgs Coupling in the Inert Higgs Doublet Model. *JHEP*, 12:007, 2015.

[77] Shinya Kanemura, Mariko Kikuchi, and Kodai Sakurai. Testing the dark matter scenario in the inert doublet model by future precision measurements of the Higgs boson couplings. *Phys. Rev. D*, 94(11):115011, 2016.

[78] Shinya Kanemura, Mariko Kikuchi, and Kei Yagyu. One-loop corrections to the Higgs self-couplings in the singlet extension. *Nucl. Phys. B*, 917:154–177, 2017.

[79] Shi-Ping He and Shou-hua Zhu. One-loop radiative correction to the triple Higgs coupling in the Higgs singlet model. *Phys. Lett. B*, 764:31–37, 2017. [Erratum: Phys.Lett.B 797, 134782 (2019)].

[80] Shinya Kanemura, Mariko Kikuchi, Kodai Sakurai, and Kei Yagyu. Gauge invariant one-loop corrections to Higgs boson couplings in non-minimal Higgs models. *Phys. Rev. D*, 96(3):035014, 2017.

[81] Shinya Kanemura, Mariko Kikuchi, Kodai Sakurai, and Kei Yagyu. H-COUP: a program for one-loop corrected Higgs boson couplings in non-minimal Higgs sectors. *Comput. Phys. Commun.*, 233:134–144, 2018.

[82] Cheng-Wei Chiang, An-Li Kuo, and Kei Yagyu. One-loop renormalized Higgs boson vertices in the Georgi-Machacek model. *Phys. Rev. D*, 98(1):013008, 2018.

[83] Philipp Basler and Margarete Mühlleitner. BSMPT (Beyond the Standard Model Phase Transitions): A tool for the electroweak phase transition in extended Higgs sectors. *Comput. Phys. Commun.*, 237:62–85, 2019.

[84] Shinya Kanemura, Mariko Kikuchi, Kentarou Mawatari, Kodai Sakurai, and Kei Yagyu. H-COUP Version 2: a program for one-loop corrected Higgs boson decays in non-minimal Higgs sectors. *Comput. Phys. Commun.*, 257:107512, 2020.

[85] Philipp Basler, Margarete Mühlleitner, and Jonas Müller. BSMPT v2 a tool for the electroweak phase transition and the baryon asymmetry of the universe in extended Higgs Sectors. *Comput. Phys. Commun.*, 269:108124, 2021.

[86] Jaouad El Falaki. Revisiting one-loop corrections to the trilinear Higgs boson self-coupling in the inert doublet model. *Phys. Lett. B*, 840:137879, 2023.

[87] Henning Bahl, Johannes Braathen, and Georg Weiglein. New Constraints on Extended Higgs Sectors from the Trilinear Higgs Coupling. *Phys. Rev. Lett.*, 129(23):231802, 2022.

[88] Henning Bahl, Wen Han Chiu, Christina Gao, Lian-Tao Wang, and Yi-Ming Zhong. Tripling down on the W boson mass. *Eur. Phys. J. C*, 82(10):944, 2022.

[89] Henning Bahl, Johannes Braathen, Martin Gabelmann, and Georg Weiglein. anyH3: precise predictions for the trilinear Higgs coupling in the Standard Model and beyond. *Eur. Phys. J. C*, 83(12):1156, 2023. [Erratum: Eur.Phys.J.C 84, 498 (2024)].

[90] Adriano Cherchiglia and Leonardo J. Ferreira Leite. Maximal value for trilinear Higgs coupling in a 3-3-1 EFT. *JHEP*, 09:101, 2025.

[91] Philipp Basler, Lisa Biermann, Margarete Mühlleitner, Jonas Müller, Rui Santos, and João Viana. BSMPT v3 a tool for phase transitions and primordial gravitational waves in extended Higgs sectors. *Comput. Phys. Commun.*, 316:109766, 2025.

[92] Eibun Senaha. Radiative Corrections to Triple Higgs Coupling and Electroweak Phase Transition: Beyond One-loop Analysis. *Phys. Rev. D*, 100(5):055034, 2019.

[93] Johannes Braathen and Shinya Kanemura. On two-loop corrections to the Higgs trilinear coupling in models with extended scalar sectors. *Phys. Lett. B*, 796:38–46, 2019.

[94] Johannes Braathen and Shinya Kanemura. Leading two-loop corrections to the Higgs boson self-couplings in models with extended scalar sectors. *Eur. Phys. J. C*, 80(3):227, 2020.

[95] Johannes Braathen, Shinya Kanemura, and Makoto Shimoda. Two-loop analysis of classically scale-invariant models with extended Higgs sectors. *JHEP*, 03:297, 2021.

[96] Masashi Aiko, Johannes Braathen, and Shinya Kanemura. Leading two-loop corrections to the Higgs di-photon decay in the inert doublet model. *Eur. Phys. J. C*, 85(5):489, 2025.

[97] Henning Bahl, Johannes Braathen, Martin Gabelmann, and Sebastian Paßehr. Generic two-loop results for trilinear and quartic scalar self-interactions. *JHEP*, 11:161, 2025.

[98] F. Arco, S. Heinemeyer, and M. Mühlleitner. Large One-Loop Effects of BSM Triple Higgs Couplings on Double Higgs Production at e^+e^- Colliders. 5 2025.

[99] Henning Bahl, Johannes Braathen, Markus Gabelmann, Kirill Radchenko, and Georg Weiglein. anyhh: A general framework for higgs pair production in extended higgs sectors. In preparation. See https://gitlab.com/anybsm/anybsm.

[100] D. de Florian et al. Handbook of LHC Higgs Cross Sections: 4. Deciphering the Nature of the Higgs Sector. *CERN Yellow Rep. Monogr.*, 2:1–869, 2017.

[101] A. Djouadi, W. Kilian, M. Muhlleitner, and P. M. Zerwas. Testing Higgs selfcouplings at e+ e- linear colliders. *Eur. Phys. J. C*, 10:27–43, 1999.

[102] H. Abramowicz et al. Higgs physics at the CLIC electron–positron linear collider. *Eur. Phys. J. C*, 77(7):475, 2017.

[103] Jan Strube. Measurement of the Higgs Boson Coupling to the Top Quark and the Higgs Boson Self-coupling at the ILC. *Nucl. Part. Phys. Proc.*, 273-275:2463–2465, 2016.

[104] Philipp Roloff, Ulrike Schnoor, Rosa Simoniello, and Boruo Xu. Double Higgs boson production and Higgs self-coupling extraction at CLIC. *Eur. Phys. J. C*, 80(11):1010, 2020.

[105] Raul Costa, Margarete Mühlleitner, Marco O. P. Sampaio, and Rui Santos. Singlet Extensions of the Standard Model at LHC Run 2: Benchmarks and Comparison with the NMSSM. *JHEP*, 06:034, 2016.

[106] Vernon Barger, Paul Langacker, Mathew McCaskey, Michael J. Ramsey-Musolf, and Gabe Shaughnessy. LHC Phenomenology of an Extended Standard Model with a Real Scalar Singlet. *Phys. Rev. D*, 77:035005, 2008.

[107] Rose Natalie Lerner and John McDonald. Gauge singlet scalar as inflaton and thermal relic dark matter. *Phys. Rev. D*, 80:123507, 2009.

[108] Hao-Lin Li, Michael Ramsey-Musolf, and Stéphane Willocq. Probing a scalar singlet-catalyzed electroweak phase transition with resonant di-Higgs boson production in the 4b channel. *Phys. Rev. D*, 100(7):075035, 2019.

[109] Mihailo Backovic, Kyoungchul Kong, and Mathew McCaskey. MadDM v.1.0: Computation of Dark Matter Relic Abundance Using MadGraph5. *Physics of the Dark Universe*, 5-6:18–28, 2014.

[110] José Eliel Camargo-Molina, António P. Morais, Roman Pasechnik, Marco O. P. Sampaio, and Jonas Wessén. All one-loop scalar vertices in the effective potential approach. *JHEP*, 08:073, 2016.

[111] Raul Costa, Marco O. P. Sampaio, and Rui Santos. NLO electroweak corrections in general scalar singlet models. *JHEP*, 07:081, 2017.

[112] Alexandre Alves, Tathagata Ghosh, Huai-Ke Guo, Kuver Sinha, and Daniel Vagie. Collider and Gravitational Wave Complementarity in Exploring the Singlet Extension of the Standard Model. *JHEP*, 04:052, 2019.

[113] Peisi Huang, Andrew J. Long, and Lian-Tao Wang. Probing the Electroweak Phase Transition with Higgs Factories and Gravitational Waves. *Phys. Rev. D*, 94(7):075008, 2016.

[114] John Ellis, Marek Lewicki, Marco Merchand, José Miguel No, and Mateusz Zych. The scalar singlet extension of the Standard Model: gravitational waves versus baryogenesis. *JHEP*, 01:093, 2023.

[115] Robert Caldwell et al. Detection of early-universe gravitational-wave signatures and fundamental physics. *Gen. Rel. Grav.*, 54(12):156, 2022.

[116] Michael J. Ramsey-Musolf, Tuomas V. I. Tenkanen, and Van Que Tran. Refining Gravitational Wave and Collider Physics Dialogue via Singlet Scalar Extension. 9 2024.

[117] Lauri Niemi and Tuomas V. I. Tenkanen. Investigating two-loop effects for first-order electroweak phase transitions. *Phys. Rev. D*, 111(7):075034, 2025.

[118] Oliver Gould and Paul M. Saffin. Perturbative gravitational wave predictions for the real-scalar extended Standard Model. *JHEP*, 03:105, 2025.

[119] Apostolos Giovanakis. Enhancing electroweak baryogenesis: The role of dimension-six operators in the real singlet extension of the Standard Model. *Phys. Dark Univ.*, 46:101682, 2024.

[120] Lauri Niemi, Michael J. Ramsey-Musolf, and Guotao Xia. Nonperturbative study of the electroweak phase transition in the real scalar singlet extended standard model. *Phys. Rev. D*, 110(11):115016, 2024.

[121] Wei Liu and Ke-Pan Xie. Probing electroweak phase transition with multi-TeV muon colliders and gravitational waves. *JHEP*, 04:015, 2021.

[122] Simone Blasi, Ryusuke Jinno, Thomas Konstandin, Henrique Rubira, and Isak Stomberg. Gravitational waves from defect-driven phase transitions: domain walls. *JCAP*, 10:051, 2023.

[123] Purusottam Ghosh, Tathagata Ghosh, and Subhojit Roy. Interplay among gravitational waves, dark matter and collider signals in the singlet scalar extended type-II seesaw model. *JHEP*, 10:057, 2023.

[124] Subhojit Roy. Dilution of dark matter relic abundance due to first order electroweak phase transition in the singlet scalar extended type-II seesaw model. *Phys. Rev. D*, 111(1):015037, 2025.

[125] Dorival Gonçalves, Ajay Kaladharan, and Yongcheng Wu. Primordial black holes from first-order phase transition in the singlet-extended SM. *Phys. Rev. D*, 111(3):035009, 2025.

[126] Wenxing Zhang, Hao-Lin Li, Kun Liu, Michael J. Ramsey-Musolf, Yonghao Zeng, and Suntharan Arunasalam. Probing electroweak phase transition in the singlet Standard Model via bb$\gamma\gamma$ and 4l channels. *JHEP*, 12:018, 2023.

[127] Pritam Palit and Sujay Shil. Probing electroweak phase transition in extended singlet scalar model with resonant HH production in bbZZ channel using parameterized machine learning. *J. Phys. G*, 51(9):095005, 2024.

[128] Finn Feuerstake, Elina Fuchs, Tania Robens, and Daniel Winterbottom. Interference effects in resonant di-Higgs production at the LHC in the Higgs singlet extension. *JHEP*, 04:094, 2025.

[129] Ian M. Lewis, Jacob L. Scott, Miguel A. Soto Alcaraz, and Matthew Sullivan. Real singlet scalar benchmarks in the multi-TeV resonance regime. *Phys. Rev. D*, 112(9):095024, 2025.

[130] Mohamed Aboudonia, Csaba Balazs, Andreas Papaefstathiou, and Graham White. Investigating the Electroweak phase transition with a real scalar singlet at a muon collider. *JHEP*, 04:093, 2025.

[131] T. D. Lee. A Theory of Spontaneous T Violation. *Phys. Rev. D*, 8:1226–1239, 1973.

[132] G. C. Branco, P. M. Ferreira, L. Lavoura, M. N. Rebelo, Marc Sher, and Joao P. Silva. Theory and phenomenology of two-Higgs-doublet models. *Phys. Rept.*, 516:1–102, 2012.

[133] John F. Gunion, Howard E. Haber, Gordon L. Kane, and Sally Dawson. *The Higgs Hunter's Guide*, volume 80. 2000.

[134] Howard E. Haber and Ralf Hempfling. The Renormalization group improved Higgs sector of the minimal supersymmetric model. *Phys. Rev. D*, 48:4280–4309, 1993.

[135] Abdelhak Djouadi. The Anatomy of electro-weak symmetry breaking. II. The Higgs bosons in the minimal supersymmetric model. *Phys. Rept.*, 459:1–241, 2008.

[136] T. Plehn, M. Spira, and P. M. Zerwas. Pair production of neutral Higgs particles in gluon-gluon collisions. *Nucl. Phys. B*, 479:46–64, 1996. [Erratum: Nucl.Phys.B 531, 655–655 (1998)].

[137] S. Dawson, S. Dittmaier, and M. Spira. Neutral Higgs boson pair production at hadron colliders: QCD corrections. *Phys. Rev. D*, 58:115012, 1998.

[138] S. Heinemeyer, M. Mühlleitner, K. Radchenko, and G. Weiglein. Higgs pair production in the 2HDM: impact of loop corrections to the trilinear Higgs couplings and interference effects on experimental limits. *Eur. Phys. J. C*, 85(4):437, 2025.

[139] Philip Bambade et al. The International Linear Collider: A Global Project. 3 2019.

[140] T. K. Charles et al. The Compact Linear Collider (CLIC) - 2018 Summary Report. *CERN Yellow Rep. Monogr.*, 2:1–112, 2018.

[141] J. Alwall, R. Frederix, S. Frixione, V. Hirschi, F. Maltoni, O. Mattelaer, H. S. Shao, T. Stelzer, P. Torrielli, and M. Zaro. The automated computation of tree-level and next-to-leading order differential cross sections, and their matching to parton shower simulations. *JHEP*, 07:079, 2014.

[142] Johannes Braathen, Sven Heinemeyer, Andrea Parra Arnay, and Alain Verduras Schaeidt. Impact of one-loop corrections to trilinear scalar couplings on di-Higgs production in the RxSM. *Eur. Phys. J. C*, 85(10):1153, 2025.

[143] Pierre Auclair et al. Cosmology with the Laser Interferometer Space Antenna. *Living Rev. Rel.*, 26(1):5, 2023.

[144] Seiji Kawamura et al. The Japanese space gravitational wave antenna: DECIGO. *Class. Quant. Grav.*, 28:094011, 2011.

[145] Vincent Corbin and Neil J. Cornish. Detecting the cosmic gravitational wave background with the big bang observer. *Class. Quant. Grav.*, 23:2435–2446, 2006.

[146] Michael E. Peskin and Daniel V. Schroeder. *An Introduction to quantum field theory.* Addison-Wesley, Reading, USA, 1995.

[147] David J. Gross and Frank Wilczek. Ultraviolet Behavior of Nonabelian Gauge Theories. *Phys. Rev. Lett.*, 30:1343–1346, 1973.

[148] H. David Politzer. Reliable Perturbative Results for Strong Interactions? *Phys. Rev. Lett.*, 30:1346–1349, 1973.

[149] Gerard 't Hooft. Renormalizable Lagrangians for Massive Yang-Mills Fields. *Nucl. Phys. B*, 35:167–188, 1971.

[150] L. D. Faddeev and V. N. Popov. Feynman Diagrams for the Yang-Mills Field. *Phys. Lett. B*, 25:29–30, 1967.

[151] N. Aghanim et al. Planck 2018 results. VI. Cosmological parameters. *Astron. Astrophys.*, 641:A6, 2020. [Erratum: Astron.Astrophys. 652, C4 (2021)].

[152] V. C. Rubin, N. Thonnard, and W. K. Ford, Jr. Rotational properties of 21 SC galaxies with a large range of luminosities and radii, from NGC 4605 /R = 4kpc/ to UGC 2885 /R = 122 kpc/. *Astrophys. J.*, 238:471, 1980.

[153] Douglas Clowe, Marusa Bradac, Anthony H. Gonzalez, Maxim Markevitch, Scott W. Randall, Christine Jones, and Dennis Zaritsky. A direct empirical proof of the existence of dark matter. *Astrophys. J. Lett.*, 648:L109–L113, 2006.

[154] Julien Lesgourgues and Sergio Pastor. Massive neutrinos and cosmology. *Phys. Rept.*, 429:307–379, 2006.

[155] Vanda Silveira and A. Zee. SCALAR PHANTOMS. *Phys. Lett. B*, 161:136–140, 1985.

[156] John McDonald. Gauge singlet scalars as cold dark matter. *Phys. Rev. D*, 50:3637–3649, 1994.

[157] Richard H. Cyburt, Brian D. Fields, Keith A. Olive, and Tsung-Han Yeh. Big Bang Nucleosynthesis: 2015. *Rev. Mod. Phys.*, 88:015004, 2016.

[158] Frans R. Klinkhamer and N. S. Manton. A Saddle Point Solution in the Weinberg-Salam Theory. *Phys. Rev. D*, 30:2212, 1984.

[159] M. B. Gavela, P. Hernandez, J. Orloff, O. Pene, and C. Quimbay. Standard model CP violation and baryon asymmetry. Part 2: Finite temperature. *Nucl. Phys. B*, 430:382–426, 1994.

[160] M. B. Gavela, M. Lozano, J. Orloff, and O. Pene. Standard model CP violation and baryon asymmetry. Part 1: Zero temperature. *Nucl. Phys. B*, 430:345–381, 1994.

[161] M. Laine and K. Rummukainen. The MSSM electroweak phase transition on the lattice. *Nucl. Phys. B*, 535:423–457, 1998.

[162] Y. Fukuda et al. Evidence for oscillation of atmospheric neutrinos. *Phys. Rev. Lett.*, 81:1562–1567, 1998.

[163] Q. R. Ahmad et al. Direct evidence for neutrino flavor transformation from neutral current interactions in the Sudbury Neutrino Observatory. *Phys. Rev. Lett.*, 89:011301, 2002.

[164] Steven Weinberg. Baryon and Lepton Nonconserving Processes. *Phys. Rev. Lett.*, 43:1566–1570, 1979.

[165] C. A. Baker et al. An Improved experimental limit on the electric dipole moment of the neutron. *Phys. Rev. Lett.*, 97:131801, 2006.

[166] C. Abel et al. Measurement of the Permanent Electric Dipole Moment of the Neutron. *Phys. Rev. Lett.*, 124(8):081803, 2020.

[167] Gerard 't Hooft. Computation of the Quantum Effects Due to a Four-Dimensional Pseudoparticle. *Phys. Rev. D*, 14:3432–3450, 1976. [Erratum: Phys.Rev.D 18, 2199 (1978)].

[168] R. D. Peccei and Helen R. Quinn. CP Conservation in the Presence of Instantons. *Phys. Rev. Lett.*, 38:1440–1443, 1977.

[169] R. D. Peccei and Helen R. Quinn. Constraints Imposed by CP Conservation in the Presence of Instantons. *Phys. Rev. D*, 16:1791–1797, 1977.

[170] Steven Weinberg. A New Light Boson? *Phys. Rev. Lett.*, 40:223–226, 1978.

[171] Frank Wilczek. Problem of Strong P and T Invariance in the Presence of Instantons. *Phys. Rev. Lett.*, 40:279–282, 1978.

[172] John Preskill, Mark B. Wise, and Frank Wilczek. Cosmology of the Invisible Axion. *Phys. Lett. B*, 120:127–132, 1983.

[173] L. F. Abbott and P. Sikivie. A Cosmological Bound on the Invisible Axion. *Phys. Lett. B*, 120:133–136, 1983.

[174] Michael Dine and Willy Fischler. The Not So Harmless Axion. *Phys. Lett. B*, 120:137–141, 1983.

[175] Steven Weinberg. The Cosmological Constant Problem. *Rev. Mod. Phys.*, 61:1–23, 1989.

[176] Giuseppe Degrassi, Stefano Di Vita, Joan Elias-Miro, Jose R. Espinosa, Gian F. Giudice, Gino Isidori, and Alessandro Strumia. Higgs mass and vacuum stability in the Standard Model at NNLO. *JHEP*, 08:098, 2012.

[177] Dario Buttazzo, Giuseppe Degrassi, Pier Paolo Giardino, Gian F. Giudice, Filippo Sala, Alberto Salvio, and Alessandro Strumia. Investigating the near-criticality of the Higgs boson. *JHEP*, 12:089, 2013.

[178] Gino Isidori, Giovanni Ridolfi, and Alessandro Strumia. On the metastability of the standard model vacuum. *Nucl. Phys. B*, 609:387–409, 2001.

[179] Oleg Lebedev. On Stability of the Electroweak Vacuum and the Higgs Portal. *Eur. Phys. J. C*, 72:2058, 2012.

[180] Joan Elias-Miro, Jose R. Espinosa, Gian F. Giudice, Hyun Min Lee, and Alessandro Strumia. Stabilization of the Electroweak Vacuum by a Scalar Threshold Effect. *JHEP*, 06:031, 2012.

[181] M. J. G. Veltman. The Infrared - Ultraviolet Connection. *Acta Phys. Polon. B*, 12:437, 1981.

[182] Gerard 't Hooft. Naturalness, chiral symmetry, and spontaneous chiral symmetry breaking. *NATO Sci. Ser. B*, 59:135–157, 1980.

[183] M. Cepeda et al. Report from Working Group 2: Higgs Physics at the HL-LHC and HE-LHC. *CERN Yellow Rep. Monogr.*, 7:221–584, 2019.

[184] G. Aad et al. The ATLAS Experiment at the CERN Large Hadron Collider. *JINST*, 3:S08003, 2008.

[185] A combination of measurements of Higgs boson production and decay using up to 139 fb^{-1} of proton–proton collision data at $\sqrt{s} = 13$ TeV collected with the ATLAS experiment. 8 2020.

[186] S. Chatrchyan et al. The CMS Experiment at the CERN LHC. *JINST*, 3:S08004, 2008.

[187] Combined Higgs boson production and decay measurements with up to 137 fb^{-1} of proton-proton collision data at $\sqrt{s} = 13$ TeV. 2020.

[188] Georges Aad et al. Characterising the Higgs boson with ATLAS data from the LHC Run-2. *Phys. Rept.*, 1116:4–56, 2025.

[189] H. P. Robertson. Kinematics and World-Structure. *Astrophys. J.*, 82:284–301, 1935.

[190] A. G. Walker. On Milne's Theory of World-Structure. *Proc. Lond. Math. Soc. s*, 2-42(1):90–127, 1937.

[191] Edward W. Kolb and Michael S. Turner. *The Early Universe*, volume 69. Taylor and Francis, 5 2019.

[192] A. Friedmann. Über die Krümmung des Raumes. *Zeitschrift für Physik*, 10(1):377–386, 1922.

[193] Steven Weinberg. *Cosmology.* 2008.

[194] V. Mukhanov. *Physical Foundations of Cosmology.* Cambridge University Press, Oxford, 2005.

[195] Mariano Quiros. Finite temperature field theory and phase transitions. In *ICTP Summer School in High-Energy Physics and Cosmology*, pages 187–259, 1 1999.

[196] K. Kajantie, M. Laine, K. Rummukainen, and Mikhail E. Shaposhnikov. A Non-perturbative analysis of the finite T phase transition in SU(2) x U(1) electroweak theory. *Nucl. Phys. B*, 493:413–438, 1997.

[197] Scott Dodelson. *Modern Cosmology*. Academic Press, Amsterdam, 2003.

[198] James M. Cline. Baryogenesis. In *Les Houches Summer School - Session 86: Particle Physics and Cosmology: The Fabric of Spacetime*, 9 2006.

[199] Cyril Pitrou, Alain Coc, Jean-Philippe Uzan, and Elisabeth Vangioni. Precision big bang nucleosynthesis with improved Helium-4 predictions. *Phys. Rept.*, 754:1–66, 2018.

[200] Makoto Kobayashi and Toshihide Maskawa. CP Violation in the Renormalizable Theory of Weak Interaction. *Prog. Theor. Phys.*, 49:652–657, 1973.

[201] Glennys R. Farrar and M. E. Shaposhnikov. Baryon asymmetry of the universe in the standard electroweak theory. *Phys. Rev. D*, 50:774, 1994.

[202] Patrick Huet and Eric Sather. Electroweak baryogenesis and standard model CP violation. *Phys. Rev. D*, 51:379–394, 1995.

[203] Ian Affleck and Michael Dine. A New Mechanism for Baryogenesis. *Nucl. Phys. B*, 249:361–380, 1985.

[204] M. Fukugita and T. Yanagida. Baryogenesis Without Grand Unification. *Phys. Lett. B*, 174:45–47, 1986.

[205] Ettore Majorana. Teoria simmetrica dell'elettrone e del positrone. *Nuovo Cim.*, 14:171–184, 1937.

[206] L. Dolan and R. Jackiw. Symmetry Behavior at Finite Temperature. *Phys. Rev. D*, 9:3320–3341, 1974.

[207] J. I. Kapusta and Charles Gale. *Finite-temperature field theory: Principles and applications*. Cambridge Monographs on Mathematical Physics. Cambridge University Press, 2011.

[208] Andrei D. Linde. Infrared Problem in Thermodynamics of the Yang-Mills Gas. *Phys. Lett. B*, 96:289–292, 1980.

[209] Sidney R. Coleman and Erick J. Weinberg. Radiative Corrections as the Origin of Spontaneous Symmetry Breaking. *Phys. Rev. D*, 7:1888–1910, 1973.

[210] Rajesh R. Parwani. Resummation in a hot scalar field theory. *Phys. Rev. D*, 45:4695, 1992. [Erratum: Phys.Rev.D 48, 5965 (1993)].

[211] Peter Brockway Arnold and Olivier Espinosa. The Effective potential and first order phase transitions: Beyond leading-order. *Phys. Rev. D*, 47:3546, 1993. [Erratum: Phys.Rev.D 50, 6662 (1994)].

[212] M. E. Carrington. The Effective potential at finite temperature in the Standard Model. *Phys. Rev. D*, 45:2933–2944, 1992.

[213] Peter Athron, Csaba Balázs, Andrew Fowlie, Lachlan Morris, and Lei Wu. Cosmological phase transitions: From perturbative particle physics to gravitational waves. *Prog. Part. Nucl. Phys.*, 135:104094, 2024.

[214] Eibun Senaha. Symmetry Restoration and Breaking at Finite Temperature: An Introductory Review. *Symmetry*, 12(5):733, 2020.

[215] Oliver Gould and Tuomas V. I. Tenkanen. On the perturbative expansion at high temperature and implications for cosmological phase transitions. *JHEP*, 06:069, 2021.

[216] Paul H. Ginsparg. First Order and Second Order Phase Transitions in Gauge Theories at Finite Temperature. *Nucl. Phys. B*, 170:388–408, 1980.

[217] Thomas Appelquist and Robert D. Pisarski. High-Temperature Yang-Mills Theories and Three-Dimensional Quantum Chromodynamics. *Phys. Rev. D*, 23:2305, 1981.

[218] Eric Braaten and Agustin Nieto. Effective field theory approach to high temperature thermodynamics. *Phys. Rev. D*, 51:6990–7006, 1995.

[219] Eric Braaten and Agustin Nieto. Free energy of QCD at high temperature. *Phys. Rev. D*, 53:3421–3437, 1996.

[220] Mikko Laine and Aleksi Vuorinen. *Basics of Thermal Field Theory*, volume 925. Springer, 2016.

[221] Tom Banks, Carl M. Bender, and Tai Tsun Wu. Coupled anharmonic oscillators. i. equal-mass case. *Phys. Rev. D*, 8:3346, 1973.

[222] Andrei D. Linde. Phase transitions in gauge theories and cosmology. *Phys. Lett. B*, 100:37–40, 1981.

[223] Sidney Coleman. The fate of the false vacuum. 1. semiclassical theory. *Phys. Rev. D*, 15, 1977.

[224] Andrei D. Linde. Fate of the False Vacuum at Finite Temperature: Theory and Applications. *Phys. Lett. B*, 100:37–40, 1981.

[225] Carroll L. Wainwright. CosmoTransitions: Computing Cosmological Phase Transition Temperatures and Bubble Profiles with Multiple Fields. *Comput. Phys. Commun.*, 183:2006–2013, 2012.

[226] S. R. Broadbent and J. M. Hammersley. Percolation processes: I. Crystals and mazes. *Proc. Cambridge Phil. Soc.*, 53:629–641, 1957.

[227] Jose R. Espinosa, Thomas Konstandin, Jose M. No, and Geraldine Servant. Energy Budget of Cosmological First-order Phase Transitions. *JCAP*, 06:028, 2010.

[228] Carlo Branchina, Angela Conaci, Stefania De Curtis, Luigi Delle Rose, Andrea Guiggiani, Angel Gil Muyor, and Giuliano Panico. New calculation of collision integrals for cosmological phase transitions. *EPJ Web Conf.*, 314:00031, 2024.

[229] Stefania De Curtis, Luigi Delle Rose, Andrea Guiggiani, Ángel Gil Muyor, and Giuliano Panico. Non-linearities in cosmological bubble wall dynamics. *JHEP*, 05:009, 2024.

[230] Stefania De Curtis, Luigi Delle Rose, Andrea Guiggiani, Ángel Gil Muyor, and Giuliano Panico. Collision integrals for cosmological phase transitions. *JHEP*, 05:194, 2023.

[231] Stefania De Curtis, Luigi Delle Rose, Andrea Guiggiani, Ángel Gil Muyor, and Giuliano Panico. Bubble wall dynamics at the electroweak phase transition. *JHEP*, 03:163, 2022.

[232] Carlo Branchina, Angela Conaci, Stefania De Curtis, and Luigi Delle Rose. Bubble wall velocity with out-of-equilibrium corrections. 10 2025.

[233] Thomas Biekötter, Andrii Dashko, Maximilian Löschner, and Georg Weiglein. Precision studies of extended higgs sectors, 2026. In preparation, DESY-25-131, IFT-UAM/CSIC-25-104.

[234] Wen-Yuan Ai, Benoit Laurent, and Jorinde van de Vis. Model-independent bubble wall velocities in local thermal equilibrium. *JCAP*, 07:002, 2023.

[235] Andreas Ekstedt, Oliver Gould, Joonas Hirvonen, Benoit Laurent, Lauri Niemi, Philipp Schicho, and Jorinde van de Vis. How fast does the WallGo? A package for computing wall velocities in first-order phase transitions. *JHEP*, 04:101, 2025.

[236] Arthur Kosowsky, Michael S. Turner, and Richard Watkins. Gravitational Waves from First Order Cosmological Phase Transitions. *Phys. Rev. Lett.*, 69:2026–2029, 1992.

[237] Arthur Kosowsky and Michael S. Turner. Gravitational radiation from colliding vacuum bubbles: envelope approximation to many bubble collisions. *Phys. Rev. D*, 47:4372–4391, 1993.

[238] Mark Hindmarsh, Stephan J. Huber, Kari Rummukainen, and David J. Weir. Gravitational waves from the sound of a first order phase transition. *Phys. Rev. Lett.*, 112:041301, 2014.

[239] Mark Hindmarsh, Stephan J. Huber, Kari Rummukainen, and David J. Weir. Numerical simulations of acoustically generated gravitational waves at a first order phase transition. *Phys. Rev. D*, 92(12):123009, 2015.

[240] Mark Hindmarsh, Stephan J. Huber, Kari Rummukainen, and David J. Weir. Shape of the acoustic gravitational wave power spectrum from a first order phase transition. *Phys. Rev. D*, 96(10):103520, 2017. [Erratum: Phys.Rev.D 101, 089902 (2020)].

[241] Chiara Caprini, Ruth Durrer, and Geraldine Servant. The stochastic gravitational wave background from turbulence and magnetic fields generated by a first-order phase transition. *JCAP*, 12:024, 2009.

[242] Michele Maggiore. Gravitational wave experiments and early universe cosmology. *Phys. Rept.*, 331:283–367, 2000.

[243] Dietrich Bodeker and Guy D. Moore. Can electroweak bubble walls run away? *JCAP*, 05:009, 2009.

[244] Wen-Yuan Ai, Xander Nagels, and Miguel Vanvlasselaer. Criterion for ultra-fast bubble walls: the impact of hydrodynamic obstruction. *JCAP*, 03:037, 2024.

[245] Matthew Gonderinger, Yingchuan Li, Hiren Patel, and Michael J. Ramsey-Musolf. Vacuum Stability, Perturbativity, and Scalar Singlet Dark Matter. *JHEP*, 01:053, 2010.

[246] F. Arco, S. Heinemeyer, M. Mühlleitner, A. Parra Arnay, N. Rivero González, and A. Verduras Schaeidt. Sensitivity to triple Higgs couplings via di-Higgs production in the RxSM at the (HL-)LHC and future e^+e colliders. *JHEP*, 06:211, 2025.

[247] Donal O'Connell, Michael J. Ramsey-Musolf, and Mark B. Wise. Minimal Extension of the Standard Model Scalar Sector. *Phys. Rev. D*, 75:037701, 2007.

[248] Tania Robens and Tim Stefaniak. Status of the Higgs Singlet Extension of the Standard Model after LHC Run 1. *Eur. Phys. J. C*, 75:104, 2015.

[249] Adam Falkowski, Christian Gross, and Oleg Lebedev. A second Higgs from the Higgs portal. *JHEP*, 05:057, 2015.

[250] Peter Athron, Jonathan M. Cornell, Felix Kahlhoefer, James Mckay, Pat Scott, and Sebastian Wild. Impact of vacuum stability, perturbativity and XENON1T on global fits of $\mathbb{Z}_2$ and $\mathbb{Z}_3$ scalar singlet dark matter. *Eur. Phys. J. C*, 78(10):830, 2018.

[251] Valery A. Rubakov and Dmitry S. Gorbunov. *Introduction to the Theory of the Early Universe: Hot big bang theory.* World Scientific, Singapore, 2017.

[252] Wolfgang G. Hollik, Georg Weiglein, and Jonas Wittbrodt. Impact of Vacuum Stability Constraints on the Phenomenology of Supersymmetric Models. *JHEP*, 03:109, 2019.

[253] Benjamin W. Lee, C. Quigg, and H. B. Thacker. Weak Interactions at Very High-Energies: The Role of the Higgs Boson Mass. *Phys. Rev. D*, 16:1519, 1977.

[254] Benjamin W. Lee, C. Quigg, and H. B. Thacker. The Strength of Weak Interactions at Very High-Energies and the Higgs Boson Mass. *Phys. Rev. Lett.*, 38:883–885, 1977.

[255] Johannes Braathen, Mark D. Goodsell, Manuel E. Krauss, Toby Opferkuch, and Florian Staub. N-loop running should be combined with N-loop matching. *Phys. Rev. D*, 97(1):015011, 2018.

[256] Philip Bechtle, Oliver Brein, Sven Heinemeyer, Georg Weiglein, and Karina E. Williams. HiggsBounds: Confronting Arbitrary Higgs Sectors with Exclusion Bounds from LEP and the Tevatron. *Comput. Phys. Commun.*, 181:138–167, 2010.

[257] Philip Bechtle, Oliver Brein, Sven Heinemeyer, Georg Weiglein, and Karina E. Williams. HiggsBounds 2.0.0: Confronting Neutral and Charged Higgs Sector Predictions with Exclusion Bounds from LEP and the Tevatron. *Comput. Phys. Commun.*, 182:2605–2631, 2011.

[258] Philip Bechtle, Oliver Brein, Sven Heinemeyer, Oscar Stål, Tim Stefaniak, Georg Weiglein, and Karina E. Williams. HiggsBounds – 4: Improved Tests of Extended Higgs Sectors against Exclusion Bounds from LEP, the Tevatron and the LHC. *Eur. Phys. J. C*, 74(3):2693, 2014.

[259] Philip Bechtle, Sven Heinemeyer, Oscar Stal, Tim Stefaniak, and Georg Weiglein. Applying Exclusion Likelihoods from LHC Searches to Extended Higgs Sectors. *Eur. Phys. J. C*, 75(9):421, 2015.

[260] Philip Bechtle, Daniel Dercks, Sven Heinemeyer, Tobias Klingl, Tim Stefaniak, Georg Weiglein, and Jonas Wittbrodt. HiggsBounds-5: Testing Higgs Sectors in the LHC 13 TeV Era. *Eur. Phys. J. C*, 80(12):1211, 2020.

[261] Henning Bahl, Thomas Biekötter, Sven Heinemeyer, Cheng Li, Steven Paasch, Georg Weiglein, and Jonas Wittbrodt. HiggsTools: BSM scalar phenomenology

with new versions of HiggsBounds and HiggsSignals. *Comput. Phys. Commun.*, 291:108803, 2023.

[262] Philip Bechtle, Sven Heinemeyer, Oscar Stål, Tim Stefaniak, and Georg Weiglein. *HiggsSignals*: Confronting arbitrary Higgs sectors with measurements at the Tevatron and the LHC. *Eur. Phys. J. C*, 74(2):2711, 2014.

[263] Philip Bechtle, Sven Heinemeyer, Oscar Stål, Tim Stefaniak, and Georg Weiglein. Probing the Standard Model with Higgs signal rates from the Tevatron, the LHC and a future ILC. *JHEP*, 11:039, 2014.

[264] Philip Bechtle, Sven Heinemeyer, Tobias Klingl, Tim Stefaniak, Georg Weiglein, and Jonas Wittbrodt. HiggsSignals-2: Probing new physics with precision Higgs measurements in the LHC 13 TeV era. *Eur. Phys. J. C*, 81(2):145, 2021.

[265] Tetsuya Enomoto and Ryoutaro Watanabe. Flavor constraints on the Two Higgs Doublet Models of Z_2 symmetric and aligned types. *JHEP*, 05:002, 2016.

[266] Sheldon L. Glashow and Steven Weinberg. Natural Conservation Laws for Neutral Currents. *Phys. Rev. D*, 15:1958, 1977.

[267] E. A. Paschos. Diagonal Neutral Currents. *Phys. Rev. D*, 15:1966, 1977.

[268] Mayumi Aoki, Shinya Kanemura, Koji Tsumura, and Kei Yagyu. Models of Yukawa interaction in the two Higgs doublet model, and their collider phenomenology. *Phys. Rev. D*, 80:015017, 2009.

[269] Thomas Appelquist and J. Carazzone. Infrared Singularities and Massive Fields. *Phys. Rev. D*, 11:2856, 1975.

[270] A. Barroso, P. M. Ferreira, I. P. Ivanov, and Rui Santos. Metastability bounds on the two Higgs doublet model. *JHEP*, 06:045, 2013.

[271] Shinya Kanemura, Takahiro Kubota, and Eiichi Takasugi. Lee-Quigg-Thacker bounds for Higgs boson masses in a two doublet model. *Phys. Lett. B*, 313:155–160, 1993.

[272] I. F. Ginzburg and I. P. Ivanov. Tree-level unitarity constraints in the most general 2HDM. *Phys. Rev. D*, 72:115010, 2005.

[273] Andrew G. Akeroyd, Abdesslam Arhrib, and El-Mokhtar Naimi. Note on tree level unitarity in the general two Higgs doublet model. *Phys. Lett. B*, 490:119–124, 2000.

[274] Mark D. Goodsell and Florian Staub. Unitarity constraints on general scalar couplings with SARAH. *Eur. Phys. J. C*, 78(8):649, 2018.

[275] Manuel E. Krauss, Toby Opferkuch, and Florian Staub. Spontaneous Charge Breaking in the NMSSM - Dangerous or not? *Eur. Phys. J. C*, 77(5):331, 2017.

[276] Benjamín Grinstein, Christopher W. Murphy, and Patipan Uttayarat. One-loop corrections to the perturbative unitarity bounds in the CP-conserving two-Higgs doublet model with a softly broken $\mathbb{Z}_2$ symmetry. *JHEP*, 06:070, 2016.

[277] Vincenzo Cacchio, Debtosh Chowdhury, Otto Eberhardt, and Christopher W. Murphy. Next-to-leading order unitarity fits in Two-Higgs-Doublet models with soft $\mathbb{Z}_2$ breaking. *JHEP*, 11:026, 2016.

[278] Jing Ren, Rui-Qing Xiao, Maosen Zhou, Yaquan Fang, Hong-Jian He, and Weiming Yao. LHC Search of New Higgs Boson via Resonant Di-Higgs Production with Decays into 4W. *JHEP*, 06:090, 2018.

[279] Stephan Hessenberger. *Two-loop corrections to electroweak precision observables in Two-Higgs-Doublet-Models*. PhD thesis, Munich, Tech. U., 2018.

[280] S. Navas et al. Review of particle physics. *Phys. Rev. D*, 110(3):030001, 2024.

[281] Michael E. Peskin and Tatsu Takeuchi. A New constraint on a strongly interacting Higgs sector. *Phys. Rev. Lett.*, 65:964–967, 1990.

[282] Michael E. Peskin and Tatsu Takeuchi. Estimation of oblique electroweak corrections. *Phys. Rev. D*, 46:381–409, 1992.

[283] Stephan Hessenberger and Wolfgang Hollik. Two-loop improved predictions for $\mathbf{M_W}$ and $\mathbf{\sin^2\theta_{eff}}$ in Two-Higgs-Doublet models. *Eur. Phys. J. C*, 82(10):970, 2022.

[284] Marcela Carena, Ian Low, Nausheen R. Shah, and Carlos E. M. Wagner. Impersonating the Standard Model Higgs Boson: Alignment without Decoupling. *JHEP*, 04:015, 2014.

[285] Jérémy Bernon, John F. Gunion, Howard E. Haber, Yun Jiang, and Sabine Kraml. Scrutinizing the alignment limit in two-Higgs-doublet models: m_h=125 GeV. *Phys. Rev. D*, 92(7):075004, 2015.

[286] Georges Aad et al. A detailed map of Higgs boson interactions by the ATLAS experiment ten years after the discovery. *Nature*, 607(7917):52–59, 2022. [Erratum: Nature 612, E24 (2022)].

[287] Mathias Brucherseifer, Ryan Gavin, and Michael Spira. Minimal supersymmetric Higgs boson self-couplings: Two-loop $O(\alpha_t\alpha_s)$ corrections. *Phys. Rev. D*, 90(11):117701, 2014.

[288] Wolfgang Hollik and Siannah Penaranda. Yukawa coupling quantum corrections to the selfcouplings of the lightest MSSM Higgs boson. *Eur. Phys. J. C*, 23:163–172, 2002.

[289] Marcel Krause, Margarete Muhlleitner, Rui Santos, and Hanna Ziesche. Higgs-to-Higgs boson decays in a 2HDM at next-to-leading order. *Phys. Rev. D*, 95(7):075019, 2017.

[290] Roman Jackiw. Functional evaluation of the effective potential. *Phys. Rev. D*, 9:1686, 1974.

[291] K. Farakos, K. Kajantie, K. Rummukainen, and Mikhail E. Shaposhnikov. 3-D physics and the electroweak phase transition: Perturbation theory. *Nucl. Phys. B*, 425:67–109, 1994.

[292] Djuna Croon, Oliver Gould, Philipp Schicho, Tuomas V. I. Tenkanen, and Graham White. Theoretical uncertainties for cosmological first-order phase transitions. *JHEP*, 04:055, 2021.

[293] Kimmo Kainulainen, Venus Keus, Lauri Niemi, Kari Rummukainen, Tuomas V. I. Tenkanen, and Ville Vaskonen. On the validity of perturbative studies of the electroweak phase transition in the Two Higgs Doublet model. *JHEP*, 06:075, 2019.

[294] Lauri Niemi, Michael J. Ramsey-Musolf, Tuomas V. I. Tenkanen, and David J. Weir. Thermodynamics of a Two-Step Electroweak Phase Transition. *Phys. Rev. Lett.*, 126(17):171802, 2021.

[295] Oliver Gould. Real scalar phase transitions: a nonperturbative analysis. *JHEP*, 04:057, 2021.

[296] Oliver Gould, Sinan Güyer, and Kari Rummukainen. First-order electroweak phase transitions: A nonperturbative update. *Phys. Rev. D*, 106(11):114507, 2022. [Erratum: Phys.Rev.D 110, 119903 (2024)].

[297] Andreas Ekstedt, Philipp Schicho, and Tuomas V. I. Tenkanen. DRalgo: A package for effective field theory approach for thermal phase transitions. *Comput. Phys. Commun.*, 288:108725, 2023.

[298] Eric Braaten. Solution to the perturbative infrared catastrophe of hot gauge theories. *Phys. Rev. Lett.*, 74:2164–2167, 1995.

[299] Georges Aad et al. Search for heavy resonances decaying into a pair of Z bosons in the $\ell^+\ell^-\ell'^+\ell'^-$ and $\ell^+\ell^-\nu\bar{\nu}$ final states using 139 fb^{-1} of proton–proton collisions at $\sqrt{s} = 13\,\text{TeV}$ with the ATLAS detector. *Eur. Phys. J. C*, 81(4):332, 2021.

[300] Dao Thi Nhung, Margarete Muhlleitner, Juraj Streicher, and Kathrin Walz. Higher Order Corrections to the Trilinear Higgs Self-Couplings in the Real NMSSM. *JHEP*, 11:181, 2013.

[301] R. Grober, M. Muhlleitner, and M. Spira. Higgs Pair Production at NLO QCD for CP-violating Higgs Sectors. *Nucl. Phys. B*, 925:1–27, 2017.

[302] Ramona Grober, Margarete Muhlleitner, Michael Spira, and Juraj Streicher. NLO QCD Corrections to Higgs Pair Production including Dimension-6 Operators. *JHEP*, 09:092, 2015.

[303] S. Borowka, N. Greiner, G. Heinrich, S. P. Jones, M. Kerner, J. Schlenk, U. Schubert, and T. Zirke. Higgs Boson Pair Production in Gluon Fusion at Next-to-Leading Order with Full Top-Quark Mass Dependence. *Phys. Rev. Lett.*, 117(1):012001, 2016. [Erratum: Phys.Rev.Lett. 117, 079901 (2016)].

[304] S. Borowka, N. Greiner, G. Heinrich, S. P. Jones, M. Kerner, J. Schlenk, and T. Zirke. Full top quark mass dependence in Higgs boson pair production at NLO. *JHEP*, 10:107, 2016.

[305] Julien Baglio, Francisco Campanario, Seraina Glaus, Margarete Mühlleitner, Michael Spira, and Juraj Streicher. Gluon fusion into Higgs pairs at NLO QCD and the top mass scheme. *Eur. Phys. J. C*, 79(6):459, 2019.

[306] J. Baglio, F. Campanario, S. Glaus, M. Mühlleitner, J. Ronca, M. Spira, and J. Streicher. Higgs-Pair Production via Gluon Fusion at Hadron Colliders: NLO QCD Corrections. *JHEP*, 04:181, 2020.

[307] J. Baglio, F. Campanario, S. Glaus, M. Mühlleitner, J. Ronca, and M. Spira. $gg \to HH$: Combined uncertainties. *Phys. Rev. D*, 103(5):056002, 2021.

[308] J. Baglio, F. Campanario, S. Glaus, M. Mühlleitner, J. Ronca, and M. Spira. Full NLO QCD predictions for Higgs-pair production in the 2-Higgs-doublet model. *Eur. Phys. J. C*, 83(9):826, 2023.

[309] G. Buchalla, M. Capozi, A. Celis, G. Heinrich, and L. Scyboz. Higgs boson pair production in non-linear Effective Field Theory with full m_t-dependence at NLO QCD. *JHEP*, 09:057, 2018. [Erratum: JHEP 06, 094 (2025)].

[310] Ashutosh V. Kotwal, Michael J. Ramsey-Musolf, Jose Miguel No, and Peter Winslow. Singlet-catalyzed electroweak phase transitions in the 100 TeV frontier. *Phys. Rev. D*, 94(3):035022, 2016.

[311] T. Huang, J. M. No, L. Pernié, M. Ramsey-Musolf, A. Safonov, M. Spannowsky, and P. Winslow. Resonant di-Higgs boson production in the $b\bar{b}WW$ channel: Probing the electroweak phase transition at the LHC. *Phys. Rev. D*, 96(3):035007, 2017.

[312] Jose M. No and Michael Ramsey-Musolf. Probing the Higgs Portal at the LHC Through Resonant di-Higgs Production. *Phys. Rev. D*, 89(9):095031, 2014.

[313] Combination of searches for nonresonant Higgs boson pair production in proton-proton collisions at sqrt(s) = 13 TeV. 2024.

[314] Florian Staub. SARAH 4 : A tool for (not only SUSY) model builders. *Comput. Phys. Commun.*, 185:1773–1790, 2014.

[315] The International Linear Collider Technical Design Report - Volume 2: Physics. 6 2013.

[316] A. Arbey et al. Physics at the e+ e- Linear Collider. *Eur. Phys. J. C*, 75(8):371, 2015.

[317] Claude Fabienne Dürig. *Measuring the Higgs Self-coupling at the International Linear Collider*. PhD thesis, Hamburg U., Hamburg, 2016.

[318] Ansgar Denner. Techniques for calculation of electroweak radiative corrections at the one loop level and results for W physics at LEP-200. *Fortsch. Phys.*, 41:307–420, 1993.

[319] Johannes Braathen, Mark D. Goodsell, Sebastian Paßehr, and Emanuelle Pinsard. Expectation management. *Eur. Phys. J. C*, 81(6):498, 2021.

[320] Marcus Sperling, Dominik Stöckinger, and Alexander Voigt. Renormalization of vacuum expectation values in spontaneously broken gauge theories. *JHEP*, 07:132, 2013.

[321] Henning Bahl, Johannes Braathen, and Georg Weiglein. Theoretical concepts and measurement prospects for BSM trilinear couplings: a case study for scalar top quarks. *Eur. Phys. J. C*, 83(7):685, 2023.

[322] J. Baglio, A. Djouadi, R. Gröber, M. M. Mühlleitner, J. Quevillon, and M. Spira. The measurement of the Higgs self-coupling at the LHC: theoretical status. *JHEP*, 04:151, 2013.

[323] Markus Frank, Sven Heinemeyer, Margarete Mühlleitner, and Kateryna Radchenko. Experimental Determination of BSM Triple Higgs Couplings at the HL-LHC with Neural Networks. 6 2025.

[324] Georges Aad et al. Search for resonant pair production of Higgs bosons in the $b\bar{b}b\bar{b}$ final state using pp collisions at $\sqrt{s} = 13$ TeV with the ATLAS detector. *Phys. Rev. D*, 105(9):092002, 2022.

[325] Glen Cowan, Kyle Cranmer, Eilam Gross, and Ofer Vitells. Asymptotic formulae for likelihood-based tests of new physics. *Eur. Phys. J. C*, 71:1554, 2011. [Erratum: Eur.Phys.J.C 73, 2501 (2013)].

[326] Margarete Mühlleitner, Johannes Schlenk, and Michael Spira. Top-Yukawa-induced corrections to Higgs pair production. *JHEP*, 10:185, 2022.

[327] F. Staub. SARAH. 6 2008.

[328] Florian Staub. From Superpotential to Model Files for FeynArts and CalcHep/-CompHep. *Comput. Phys. Commun.*, 181:1077–1086, 2010.

[329] Florian Staub. Automatic Calculation of supersymmetric Renormalization Group Equations and Self Energies. *Comput. Phys. Commun.*, 182:808–833, 2011.

[330] Florian Staub. SARAH 3.2: Dirac Gauginos, UFO output, and more. *Comput. Phys. Commun.*, 184:1792–1809, 2013.

[331] Mikael Berggren, Bryan Bliewert, Jenny List, Dimitris Ntounis, Taikan Suehara, Junping Tian, Julie Munch Torndal, and Caterina Vernieri. Update of the Higgs Self-coupling Projections from Di-Higgs Production in Detailed Simulation of the ILD Concept. 9 2025.

[332] Sidney R. Coleman and Erick J. Weinberg. Radiative corrections as the origin of spontaneous symmetry breaking. *Phys. Rev. D*, 7:1888, 1973.

[333] Mariano Quiros. Finite temperature field theory and phase transitions. 1999.

[334] L. Dolan and R. Jackiw. Symmetry behavior at finite temperature. *Phys. Rev. D*, 9:3320, 1974.

[335] Morad Aaboud et al. Combination of searches for heavy resonances decaying into bosonic and leptonic final states using 36 fb^{-1} of proton-proton collision data at $\sqrt{s} = 13$ TeV with the ATLAS detector. *Phys. Rev. D*, 98(5):052008, 2018.

[336] Armen Tumasyan et al. Search for a heavy Higgs boson decaying into two lighter Higgs bosons in the $\tau\tau$bb final state at 13 TeV. *JHEP*, 11:057, 2021.

[337] Alan H. Guth and S. H. H. Tye. Phase Transitions and Magnetic Monopole Production in the Very Early Universe. *Phys. Rev. Lett.*, 44:631, 1980. [Erratum: Phys.Rev.Lett. 44, 963 (1980)].

[338] Marek Lewicki, Marco Merchand, Laura Sagunski, Philipp Schicho, and Daniel Schmitt. Impact of theoretical uncertainties on model parameter reconstruction from GW signals sourced by cosmological phase transitions. *Phys. Rev. D*, 110(2):023538, 2024.

[339] H. Abramowicz et al. The Linear Collider Facility (LCF) at CERN. 3 2025.

[340] S. Catani, Yuri L. Dokshitzer, M. Olsson, G. Turnock, and B. R. Webber. New clustering algorithm for multi - jet cross-sections in e+ e- annihilation. *Phys. Lett. B*, 269:432–438, 1991.

[341] Junping Tian. Study of Higgs self-coupling at the ILC based on the full detector simulation at $\sqrt{}$ s = 500 GeV and $\sqrt{}$ s = 1 TeV. In *3rd Linear Collider Forum*, pages 224–247, Hamburg, 2013. DESY.

[342] Jorge de Blas et al. Cern ecfa higgs/ew/top factory briefing book. `https://cds.cern.ch/record/2944678`, 2025. CERN-ESU-2025-001.

[343] Giuseppe Degrassi and Pietro Slavich. On the two-loop BSM corrections to $h \longrightarrow \gamma\gamma$ in the aligned THDM. *Eur. Phys. J. C*, 83(10):941, 2023.

[344] Giuseppe Degrassi, Ramona Gröber, and Pietro Slavich. Two-loop BSM contributions to Higgs pair production in the aligned THDM. *JHEP*, 01:041, 2026.

[345] Sacha Davidson and Howard E. Haber. Basis-independent methods for the two-Higgs-doublet model. *Phys. Rev. D*, 72:035004, 2005. [Erratum: Phys.Rev.D 72, 099902 (2005)].

[346] Howard E. Haber and Oscar Stål. New LHC benchmarks for the $\mathscr{CP}$ - conserving two-Higgs-doublet model. *Eur. Phys. J. C*, 75(10):491, 2015. [Erratum: Eur.Phys.J.C 76, 312 (2016)].

[347] J. Küblbeck, M. Böhm, and A. Denner. Feyn arts — computer-algebraic generation of feynman graphs and amplitudes. *Computer Physics Communications*, 60(2):165–180, 1990.

[348] Thomas Hahn. Generating Feynman diagrams and amplitudes with FeynArts 3. *Comput. Phys. Commun.*, 140:418–431, 2001.

[349] Vladyslav Shtabovenko. FeynHelpers: Connecting FeynCalc to FIRE and Package-X. *Comput. Phys. Commun.*, 218:48–65, 2017.

[350] R. Mertig, M. Böhm, and A. Denner. Feyn calc - computer-algebraic calculation of feynman amplitudes. *Computer Physics Communications*, 64(3):345–359, 1991.

[351] Vladyslav Shtabovenko, Rolf Mertig, and Frederik Orellana. New Developments in FeynCalc 9.0. *Comput. Phys. Commun.*, 207:432–444, 2016.

[352] Vladyslav Shtabovenko, Rolf Mertig, and Frederik Orellana. FeynCalc 9.3: New features and improvements. *Comput. Phys. Commun.*, 256:107478, 2020.

[353] Vladyslav Shtabovenko, Rolf Mertig, and Frederik Orellana. FeynCalc 10: Do multiloop integrals dream of computer codes? *Comput. Phys. Commun.*, 306:109357, 2025.

[354] R. Jackiw. Functional evaluation of the effective potential. *Phys. Rev. D*, 9:1686, 1974.

[355] Stephen P. Martin. Two Loop Effective Potential for a General Renormalizable Theory and Softly Broken Supersymmetry. *Phys. Rev. D*, 65:116003, 2002.

[356] C. Ford, I. Jack, and D. R. T. Jones. The Standard model effective potential at two loops. *Nucl. Phys. B*, 387:373–390, 1992. [Erratum: Nucl.Phys.B 504, 551–552 (1997)].

[357] A. V. Kotikov. Differential equation method: The Calculation of N point Feynman diagrams. *Phys. Lett. B*, 267:123–127, 1991. [Erratum: Phys.Lett.B 295, 409–409 (1992)].

[358] A. V. Kotikov. Differential equations method: The Calculation of vertex type Feynman diagrams. *Phys. Lett. B*, 259:314–322, 1991.

[359] C. Ford, D. R. T. Jones, P. W. Stephenson, and M. B. Einhorn. The Effective potential and the renormalization group. *Nucl. Phys. B*, 395:17–34, 1993.

[360] Andrei I. Davydychev and J. B. Tausk. Two loop selfenergy diagrams with different masses and the momentum expansion. *Nucl. Phys. B*, 397:123–142, 1993.

[361] Frits A. Berends and J. B. Tausk. On the numerical evaluation of scalar two loop selfenergy diagrams. *Nucl. Phys. B*, 421:456–470, 1994.

[362] Michele Caffo, H. Czyz, S. Laporta, and E. Remiddi. The Master differential equations for the two loop sunrise selfmass amplitudes. *Nuovo Cim. A*, 111:365–389, 1998.

[363] Jose Ramon Espinosa and Ren-Jie Zhang. Complete two loop dominant corrections to the mass of the lightest CP even Higgs boson in the minimal supersymmetric standard model. *Nucl. Phys. B*, 586:3–38, 2000.